R-12-17

Potential alkaline conditions for deposition holes of a repository in Forsmark as a consequence of OPC grouting

Revised final report after review

Magnus Sidborn, Niko Marsic, James Crawford
Kemakta Konsult AB

Steven Joyce, Lee Hartley, Amec Foster Wheeler plc

Andrés Idiart, Luis Manuel de Vries, Flávia Maia, Jorge Molinero
Amphos21

Urban Svensson, Computer-aided Fluid Engineering AB

Patrik Vidstrand, TerraSolve AB

Russell Alexander, Bedrock Geosciences

November 2014

Svensk Kärnbränslehantering AB
Swedish Nuclear Fuel
and Waste Management Co

Box 250, SE-101 24 Stockholm
Phone +46 8 459 84 00

ISSN 1402-3091
SKB R-12-17
ID 1336507

Potential alkaline conditions for deposition holes of a repository in Forsmark as a consequence of OPC grouting

Revised final report after review

Magnus Sidborn, Niko Marsic, James Crawford
Kemakta Konsult AB

Steven Joyce, Lee Hartley, Amec Foster Wheeler plc

Andrés Idiart, Luis Manuel de Vries, Flávia Maia, Jorge Molinero
Amphos21

Urban Svensson, Computer-aided Fluid Engineering AB

Patrik Vidstrand, TerraSolve AB

Russell Alexander, Bedrock Geosciences

November 2014

Preface

This report consists of several parts for which different authors and organisations have contributed material in a collaborative effort. A short description of the main contributors to the different parts of this report follows:

Magnus Sidborn and Niko Marsic (project coordinators), Kemakta Konsult AB
(Chapters 1, 3, 8, and 9)

Russell Alexander, Bedrock Geosciences
(Chapters 1, 2, and 9)

Steven Joyce and Lee Hartley, Amec Foster Wheeler plc
(Sections 3.1, 4.1, 5.1, 5.2, 5.3, 6.2, 6.4, and 6.5)

Andrés Idiart, Luis Manuel de Vries, Flávia Maia, Jorge Molinero, Amphos21
(Sections 3.2, 4.2, 5.4, 5.5, and 7)

Urban Svensson, Computer-aided Fluid Engineering AB
(Section 6.1)

Patrik Vidstrand, TerraSolve AB
(Section 6.3)

James Crawford, Kemakta Konsult AB
(Appendix A)

Some common abbreviations used throughout the report

ACZ	Analogue Cement Zone
AD	Anno Domini
ADZ	Alkali Disturbed Zone
AFM	Atomic Force Microscopy
ATEM	Analytical Transmission Electron Microscopy
BC	Before Christ
BET	Brunauer Emmet Teller; A method for determining the specific surface area
DFN	Discrete Fracture Network
CEC	Cation Exchange Capacity
CPM	Continuous Porous Medium
EBS	Engineered Barrier System
EC	Electrical Conductivity
ECPM	Equivalent Continuous Porous Medium
EDXA	Energy Dispersive X-ray Analysis
EDZ	Excavation Damaged Zone
EFPC	Extended Full Perimeter Criteria
EPMA	Electron Probe Micro Analysis
FFM	Identification code prefix for deterministically modelled fracture domains at Forsmark
FPC	Full Perimeter Criteria
HCD	Hydraulic Conductor Domain
HLW	High-Level Radioactive Waste
HPF	Hyperalkaline Plume in Fractured Rock
HRD	Hydraulic Rock mass Domain
HSD	Hydraulic Soil Domain
ILW	Intermediate-Level Nuclear Waste
LCS	Long-Term Cement Study
LLW	Low-Level Radioactive Waste
L/ILW	Low- and Intermediate-Level Radioactive Waste
NA	Natural Analogue
OPC	Ordinary Portland Cement
PA	Performance Assessment
P_{32}	Fracture intensity expressed as fracture area per unit rock volume
RHB70	Coordinate system used for elevation
SA	Safety Assessment
SCM	Supplementary Cementitious Materials
SDM	Site Descriptive Model
SF	Spent Nuclear Fuel
SFR	Repository for low- and intermediate level radioactive waste at Forsmark
TST	Transition State Theory
URL	Underground Rock Laboratory
XRD	X-Ray Diffraction

NS, NE, NW, EW, HZ and GdFracture sets characterised by their main strike direction (compass direction). HZ and Gd denote sub-horizontal and gently dipping fracture sets respectively.

CCN (cement chemists' notation, a "short hand" way of writing the chemical formula of oxides of calcium, silicon, and various metals and their hydration products, e.g. CH, C-S-H, C-A-S-H etc where hyphens indicate phases of variable composition):

C	CaO	Calcium oxide
S	SiO_2	Silicon dioxide
H	H_2O	Water
A	Al_2O_3	Aluminium oxide
K	K_2O	Potassium oxide

Contents

1 Introduction

1.1 Background

SKB is considering the possibility of using OPC (Ordinary Portland Cement) grouting during the construction of the planned spent nuclear fuel repository in Forsmark above the depth of the "qualified" sealing level i.e. where the low conductive clay will be emplaced in the ramp (see e.g. SKB 2010a, Chapter 3). Two alternatives for depths of the usage of OPC grout are considered. Alternative 1 allows OPC to be used from the surface down to –200 m, and Alternative 2 allows OPC to be used from the surface down to –370 m. The repository layout and the two alternative grouting levels are illustrated in Figure 1-1.

Injection of cement grout is a common practice in civil engineering construction works in fractured rocks. Cement grout penetrates fractures occurring in the immediate vicinity of the tunnel and shafts and, consequently, allows a significant reduction of the overall rock conductivity which leads to an important decrease of the water inflow into the tunnel. This fact has obvious practical advantages for tunnel construction and safety, and it also minimises groundwater drawdown and upconing of deep saline waters.

Concretes and cements will be used in the near-fields of all repository designs, although by far the largest volumes will be found in LLW and ILW repositories. They will be present as:

- rock supports and reinforcements in most repository excavations,
- as plugs and seals in shafts and tunnels,
- a solidification matrix for some LLW and ILW,
- reinforced concrete structures such as silos in ILW repositories (e.g. in the SFR-1 repository: see Figure 1-2 and Figure 1-3),
- concrete waste packages and 'tanks' for certain L/ILWs (Figure 1-3),
- as a cementitious buffer and backfill in some L/ILW repositories.

The actual quantities of cement to be used in some repositories are huge; for example, the near-field of a particular Swiss L/ILW repository design will contain up to 1.5 million tonnes of cement, which will be approximately 90% of the total mass of all materials emplaced in the repository (Alexander 1995). However, for a SF repository at Forsmark, the amount of cementitious material will naturally be much smaller. The total amount of grouting needed (900–3,600 m^3) as estimated in Brantberger and Janson (2009, Table 7-6) for the upper 200 metres of ramp and shafts is uncertain, which is reflected in the wide range in the estimated volumes.

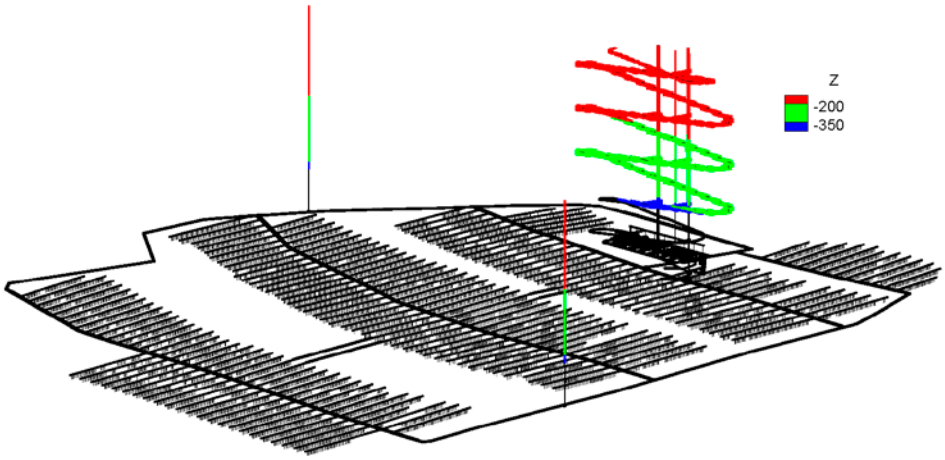

Figure 1-1. *Illustration of the nuclear fuel repository with coloured tunnels and shafts approximately indicating levels –200 m and –370 m proposed to be grouted by OPC.*

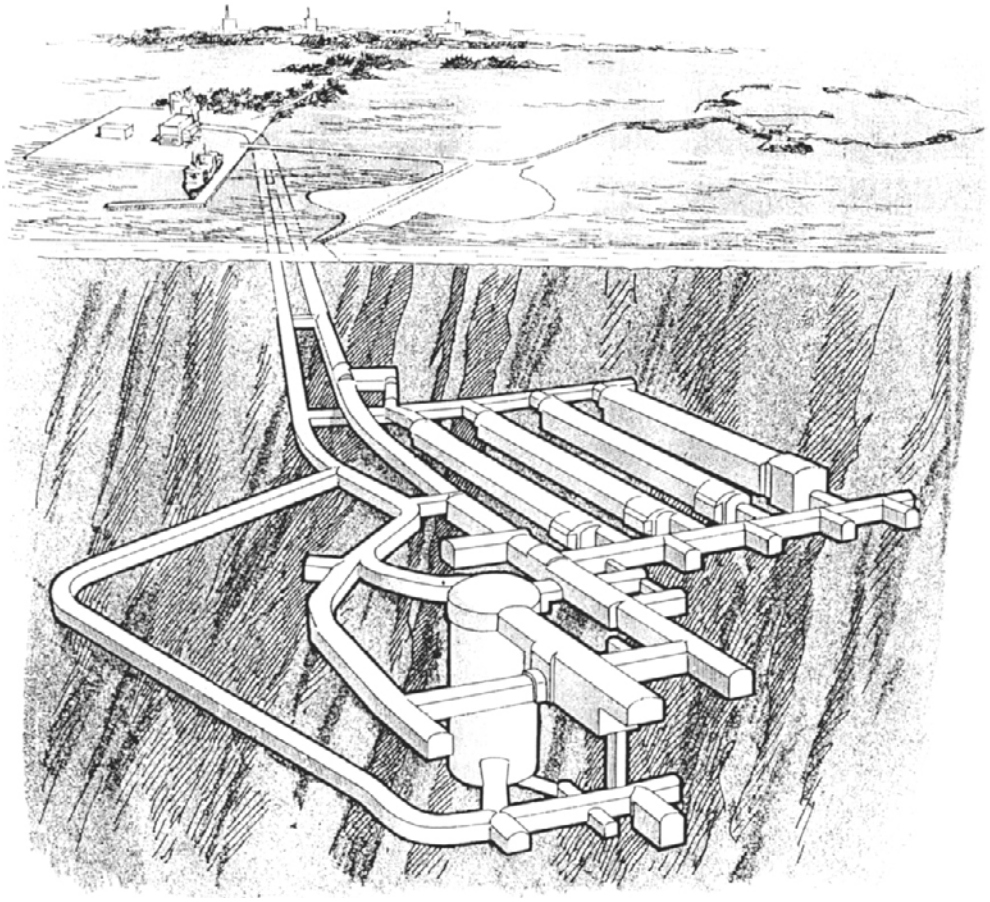

Figure 1-2. *Sketch of the SFR-1 silo and vaults.*

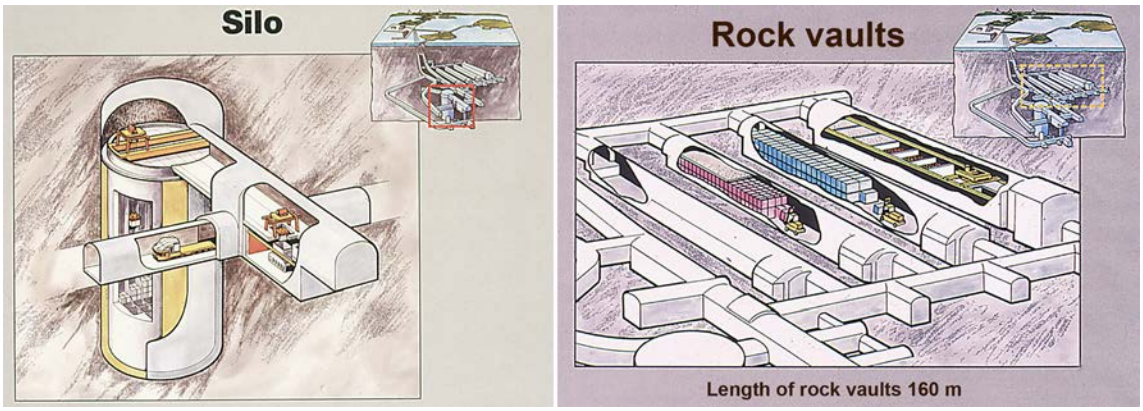

Figure 1-3. *The SFR-1 waste caverns in detail. Left, the silo and, right, the vaults for other waste streams (see SKB 2008 for details).*

It has long been recognised (e.g. Ewart et al. 1985) that the use of cementitious materials in an underground waste repository could, in the long term, give rise to a plume of alkaline water displaced by groundwater flow from the cement into the host rock and EBS. Interaction of the rock and EBS with this alkaline porewater could be detrimental to the performance of the host rock and the EBS as a barrier to radionuclide migration. While some potential processes, such as enhancement of fracture porosity by dissolution of host rock minerals and sealing of matrix porosity due to secondary mineral precipitation, are likely to be deleterious, other simultaneous processes may counteract these or even outweigh them to produce a positive effect on repository performance. Such positive processes include precipitation of secondary minerals with improved sorption characteristics compared to the primary mineralogy and sealing of fractures by secondary minerals, inhibiting water movement and radionuclide transport.

These very large quantities of cement will strongly buffer the pH conditions. According to models of cement evolution (e.g. Atkinson 1985, Berner 1990, Neall 1994), the hydration by groundwater of the cementitious materials will produce an initial stage of alkaline leachates dominated by alkali hydroxides, with a pH of around 13.5, followed by a longer period of portlandite buffered leachates with a pH of around 12 to 12.5. Under such alkaline conditions, most radionuclides will exhibit very low solubilities. Furthermore, the cementitious minerals and gels will provide a very large surface area for sorption (Hodgkinson and Robinson 1987).

In addition to the concrete and cement emplaced in the near-field as part of the engineered barriers, it is likely that concrete will also comprise part of the waste itself in L/ILW repositories, particularly waste from reactor decommissioning operations.

In addition to the potential use of cement grouts noted above, cement will also be used in some HLW and spent fuel repository designs, as structural supports, tunnel and shaft seals etc, although in much smaller amounts than will be used in L/ILW repositories. Although this cement will also hydrate in the groundwaters, it is not assigned any pH buffering capacity role in performance assessments.

Modern concretes of the type that would be used in a repository are based on Portland cement, of which calcium silicate hydrate (C-S-H) compounds are the main hydration products. These C-S-H compounds form an amorphous gel which provides the bonding strength between aggregate particles. The C-S-H gels are thermodynamically unstable and are generally thought to transform spontaneously into stable crystalline forms (e.g. Steadman 1986), although potentially very old gels have been reported in natural cements from Scawt Hill, Northern Ireland and Maqarin, Jordan (Milodowski et al. 1989, 1998a).

From the moment a cement/aggregate mixture hydrates to form concrete, it is subject to leaching, which may be viewed as equilibration between the cement minerals/gels/porewater and any percolating groundwaters. A review of leaching models by Lagerblad (2001) noted that, after initial dissolution of primary phases (such as CH and C-S-H)[1] and concomitant precipitation of secondary phases (such as calcite), concrete/cement degradation is diffusion controlled (e.g. case 2 in Figure 1-4). It is clear, therefore, that any cement (including the grouts – although the long-term stability of most grouts is relatively unknown, see discussion in Alexander and Neall (2007)) remaining in the Forsmark SF repository following closure is likely to degrade to some degree or another and may affect the repository EBS at some time in the distant future.

The rate of this process is too slow to be easily measured experimentally and cannot easily be calculated. It is likely that any conversion product would still bond the aggregate together, but there is no possible way of predicting the resultant bond strength (something of great importance in grouts). It follows that the most appropriate way to study the long-term stability of C-S-H-bearing cements and concretes is through combining data from laboratory, underground rock laboratory (URL) and natural and archaeological analogue (NA) studies and using this information to inform and guide modelling efforts aimed at assessing the potential long-term impact on the repository performance.

When alkali leachates from cement interact with the repository host rock, primary silicate minerals such as quartz and feldspar are dissolved and secondary calcium silicate hydrate (C-S-H) phases are precipitated at the same time as hydroxide ions are consumed (Holgersson et al. 1998, Savage 1998). The specific surface area of the reacted minerals increases in the first instance and this has generally been assumed to mean increased retardation of radionuclides (SKB 2008) within the ADZ (Alkali Disturbed Zone). This is somewhat simplistic, however, as it ignores the fact that reaction of the primary silicates produces secondary reaction products which will complicate matters. There are now data available on the reaction of a wide range of host rocks (some examples are presented in Chapter 2) with alkaline leachates, with the most common observation being the production of a range of secondary C-S-H/C-A-S-H/zeolite phases.

[1] From CCN (cement chemists' notation) shorthand for C=CaO, A=Al_2O_3, S=SiO_2, H=H_2O etc.

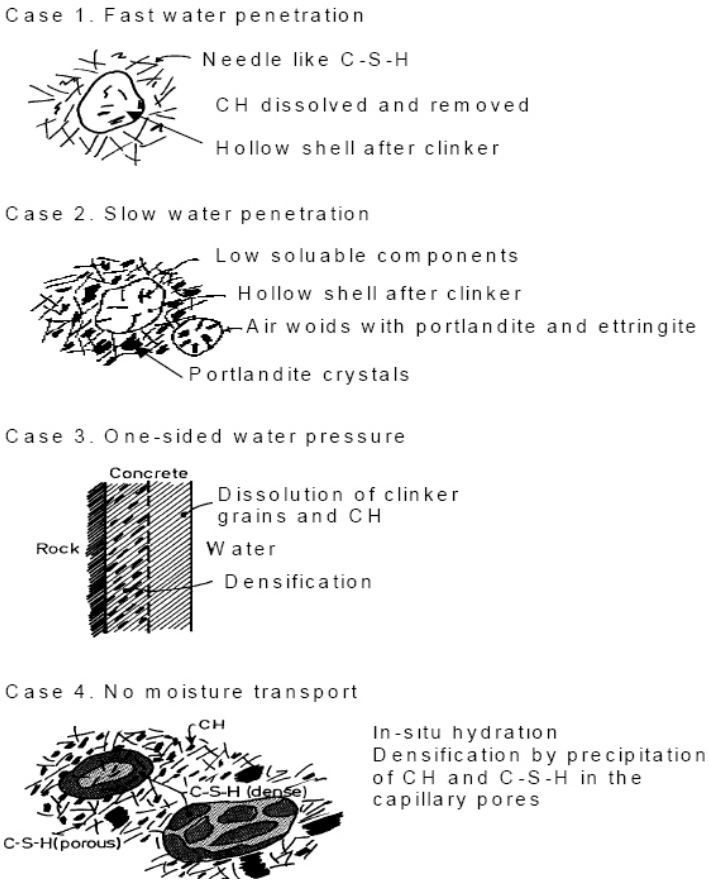

Figure 1-4. *Examples of concrete leaching mechanisms.*

Bentonites have been studied for almost as long as modern OPC has existed, but interest in cement leachate/bentonite is much more recent. Before looking any further at possible bentonite reaction, it is important to clarify the terminology surrounding the material and also the use of the term in this report. The term bentonite was first proposed in the 19th century by Knight (1898) and the name is from the Benton Shale in which the clay was thought at that time to occur. Once the origins of bentonite were understood, several updated definitions followed, but all have limitations. The strict geological definition of "bentonite" is a soft, plastic, porous light-coloured rock composed essentially of clay minerals from the smectite group plus colloidal silica, and produced by chemical alteration of volcanic ash (cf. Hallsworth and Knox 1999). The name implies a definite genetic origin from alteration of volcanic ash, either *in situ* or transported material. The non-genetic term "smectite-claystone" is now recommended where the origin of the smectite-rich clay sediment is uncertain (Hallsworth and Knox 1999).

Industrial bentonite, such as the "bentonite" used in the EBS of a radioactive waste repository, is derived from natural bentonite rock but may be processed to improve the smectite content (i.e. beneficiated) of the material and/or chemically treated to enhance its cation exchange, swelling or other physico-chemical properties (e.g. conversion or "activation" of natural calcium montmorillonite to sodium montmorillonite by treatment with sodium carbonate). As such, the physical and chemical properties of industrial bentonite may differ significantly from that of the natural rock and, therefore, care must be taken when comparing industrial and natural bentonites.

Leaching of concrete can cause changes in pH in the bentonite buffer and backfill. The uncertainties in how bentonite reacts at high pH remain significant (Alexander et al. 2012, Metcalfe and Walker 2004, Savage et al. 2007, 2010b, Savage 2011), and the future evolution of pH in these barriers is therefore difficult to predict. According to two recent studies of the degradation of the bentonite around the SFR-1 silo, only a small increase of the pH in the bentonite immediately adjacent to the concrete is obtained during the first thousand years (Cronstrand 2007, Gaucher et al. 2005). This, however, assumes that the bentonite functions perfectly (i.e. functions as a diffusive barrier) and this

requires a high degree of quality control during original emplacement. Generally, the study of reaction of bentonites in alkali solutions is a younger science than that of cement degradation and so, to some degree, the uncertainties are somewhat greater. When this is combined with the fact that experimental study of bentonite reaction is difficult due to a range of reasons including the very fine grained nature of the primary bentonite minerals and the secondary reaction phases and that even definition of bentonite porewater chemistry is relatively novel (e.g. Bradbury and Baeyens 2003), it is clear that the body of evidence available to constrain models of bentonite reaction remains highly limited.

1.2 Aim and Scope

The main aim of this project is to determine the potential effects of OPC grout within the near-surface rock on the long-time performance of the planned KBS-3 repository at Forsmark. The study must assess possible effects both during repository operation as well as the long-term period after closure assessed in the SR-Site report (SKB 2011), that is, one million years. The beneficial properties of bentonite as a buffer material may be considerably affected by interaction with cement leachates. Alteration of smectites and precipitation of secondary minerals may reduce the swelling capacity and plasticity, thereby reducing the self-sealing properties of bentonite and increasing permeability. In addition, the sorption capacity may be changed. The scope of this report is to evaluate the risk for alkaline OPC leachate to reach bentonite backfilled repository parts by means of hydrogeological and reactive-transport modelling supported with data from natural analogue and experimental studies reported in the literature. The final aim is to provide an analysis that may support decision making regarding the choice of grouting materials in the spent nuclear fuel repository at Forsmark.

1.3 Structure of the report

Following a general introduction with a problem description and background here in Chapter 1, an overview of relevant observations and experiments that are related to the processes of importance for this report (including cement durability, likely cement leachate/host rock reaction, potential impact on the host rock flow system and potential changes to the bentonite following reaction with alkali leachates) is presented in Chapter 2.

In Chapter 3 in the report, processes deemed to be of major importance for the extent of ingress of alkaline water along flowpaths in the fractured rock at Forsmark are briefly described. Transport related processes and chemical processes are described separately in two different subsections. This section also includes processes that may influence the transient behaviour of the OPC leachate composition that serves as a boundary condition in the reactive-transport modelling.

In Chapter 4, the problem of alkaline water ingress is conceptualised based on the transport and chemical processes and observations in previous sections. This conceptualisation forms the basis for the various model implementations in subsequent sections.

Chapter 5 summarises the data available that is used in the parameterisation of the various model implementations and modelled cases.

In Chapter 6, the implementations of the various hydrogeological models are described, and their results are presented. These models include discrete fracture network (DFN) models and equivalent porous medium models (ECPM). The section is divided into four subsections according to characteristically prevailing hydraulic properties for different time periods; an initial period with an open repository and unsaturated conditions, a temperate climate period, a period with periglacial permafrost, and a glacial period. Results for the DFN implementations are presented in terms of performance measures for individual flow paths connecting grouted volumes with bentonite backfilled repository parts. Results obtained from the ECPM implementations are presented also as the extent of alkaline plume ingress purely as a consequence of advective transport and mixing of different waters in the network of fractures.

In Chapter 7, the implementations of the various numerical reactive-transport models and modelled cases are described, and their results for generic fractures with averaged properties are presented. Complementary numerical and analytical reactive-transport calculations and some additional considerations regarding the OPC leachate ingress are presented in Appendix A.

In Chapter 8, the reactive-transport results for the generic fracture with averaged properties are mapped to the flow paths obtained from the hydrogeological DFN models by means of coupling, with the flow related transport resistance, or F-factor, as the coupling variable. Thus, in this section the hydrogeological and reactive transport model results are firstly coupled, and an overall evaluation of the modelled alkaline water breakthrough in bentonite backfilled repository parts is presented.

At the end of the report, Chapter 9 tries to bring together the range of evidence available and recommend the approach taken in utilising the information provided by this integration. Finally, some comments will be made on how the current knowledge gaps on the likely impact of cement alkali leachates on the Forsmark EBS can be sensibly filled, in a way which will improve the current treatment in as robust a manner as possible.

2 Observations and natural analogues

2.1 Introduction

The interaction between bentonite and cement was initially reviewed by Duerden (1992) who covered cation exchange, illitisation, beidellitisation/silica cementation and the formation of zeolites. In this chapter, it is intended to provide an overview of the current knowledge base on the likely long-term behaviour of OPC and potential impacts of alkali leachates on bentonite. The main aim is to provide an overview of the physical evidence for OPC degradation, host rock interaction and bentonite reaction which can be used within the modelling studies. However, no detailed review of existing mineral databases (covering thermodynamic, kinetic and surface area characteristics) will be provided here as the modelling groups are already utilising a variety of data sources.

This project is predominantly focussed on modelling and, obviously, these model predictions must be tested to assess the true significance of the predicted alkaline leachate/host rock interaction. Traditionally, safety assessment (SA) modellers have placed too much weight on laboratory data for the construction and testing of the safety case and, with only a few exceptions (see examples in Alexander and McKinley 1999), have ignored data from natural analogues and *in situ* experiments (see additional comments in Smellie et al. (1997) and Alexander et al. (1998)). The over-dependence on laboratory data is understandable in that the information is produced under well understood, fully controlled conditions and thus the modellers feel they can place a high degree of confidence in the results obtained. Unfortunately, a repository is not like a laboratory and it is necessary to address processes which are influenced by natural heterogeneities, which include large degrees of uncertainty and which operate over very long timescales. In this case, it is necessary to supplement laboratory data with information from *in situ* field experiments (generally from URLs) and natural analogues.

Alexander et al. (1998) noted that "The advantage of natural analogues over short-term laboratory experiments is that they enable study of repository-like systems which have evolved over the geological timescales of relevance to a radwaste repository safety assessment (rather than the days to months usual in laboratory tests). However, by their very nature, natural analogues often have ill-defined boundary conditions which may be better assessed under the well constrained (if less relevant) conditions of a laboratory. Well designed, realistic *in situ* field experiments can bridge the gap between the laboratory and natural analogues by offering repository relevant natural conditions with some of the constraints of the laboratory (and intermediate timescales). In short, combining information from the three sources (long-term and realistic, if poorly defined, natural analogues, medium-term, better constrained, *in situ* field experiments and short-term, less realistic but well defined laboratory studies) can provide greater confidence in the extrapolation of laboratory derived data to repository relevant timescales and conditions."

More and more laboratory data of relevance have been produced recently (e.g. Bateman et al. 2001a, b, Chermak 1992, 1993, Wieland et al. 2004) and this information will be included where appropriate in this report. Unfortunately, what little that has been done in URLs (e.g. Mäder et al. 2006, Mäder and Traber 2005, Soler and Mäder 2010) has not yet been published in enough detail to allow full inclusion here, but the available information will be integrated where appropriate. There are also few natural analogue studies of bentonite reaction in alkaline environments, but the available data will be presented and comment made on the relevance where possible.

The chapter will be broken down so:

Section 2.1: introduction to the chapter including aims of the project and the place of the chapter within the overall project report, structure of the chapter and boundary conditions.

Section 2.2: information from natural analogue (NA) studies on potential engineered barrier system (EBS) and geosphere perturbations by cementitious alkaline leachates.

Section 2.3: information from underground rock laboratory (URL) studies on potential EBS and geosphere perturbations by cementitious alkaline leachates.

Section 2.4: information from laboratory studies on potential EBS and geosphere perturbations by cementitious alkaline leachates.

Section 2.5: integrating the available information from natural analogues, URL and laboratory experiments.

Section 2.6: what remains to be done? How can knowledge gaps of relevance to Forsmark be filled?

Section 2.7: short conclusions, summarising the main points of the chapter.

2.2 Natural and archaeological analogue studies on potential EBS and geosphere perturbations by cementitious alkaline leachates

2.2.1 Background

Before the more recent advent of in situ studies, SKB, Nagra, Ontario Hydro, UKHMIP, Nirex, ANDRA, CEA and JAEA, in collaboration with the University of Jordan, sought additional means of supporting the laboratory data (so producing better tests for the models) by comparison with observations of similar processes which have occurred in nature, i.e. the so-called natural analogue approach (see Miller et al. 2000 and www.natural-analogues.com for discussions on natural analogues). Several sites in Jordan (Figure 2-1 and Figure 2-2) have been studied over the last 15 years (see e.g. Alexander 1992, Kamei et al. 2005, Linklater 1998, Milodowski et al. 2001, Pitty and Alexander 2011, Smellie 1998, Trotignon et al. 2006 for details). In northern and central Jordan, natural cements occur as a result of high temperature, and low pressure metamorphism of kerogen-rich clay biomicrites (see Figure 2-3). These pyrometamorphic rocks are surprisingly widespread, stretching from Turkey in the north, down through Syria, Israel, Jordan and on to northern Saudi Arabia. The rehydrated and recarbonated reaction products are analogous to the mineralogy of Portland cement (Table 2-1), so providing an extremely good natural analogue of cementitious materials in repositories, including OPC grouts.

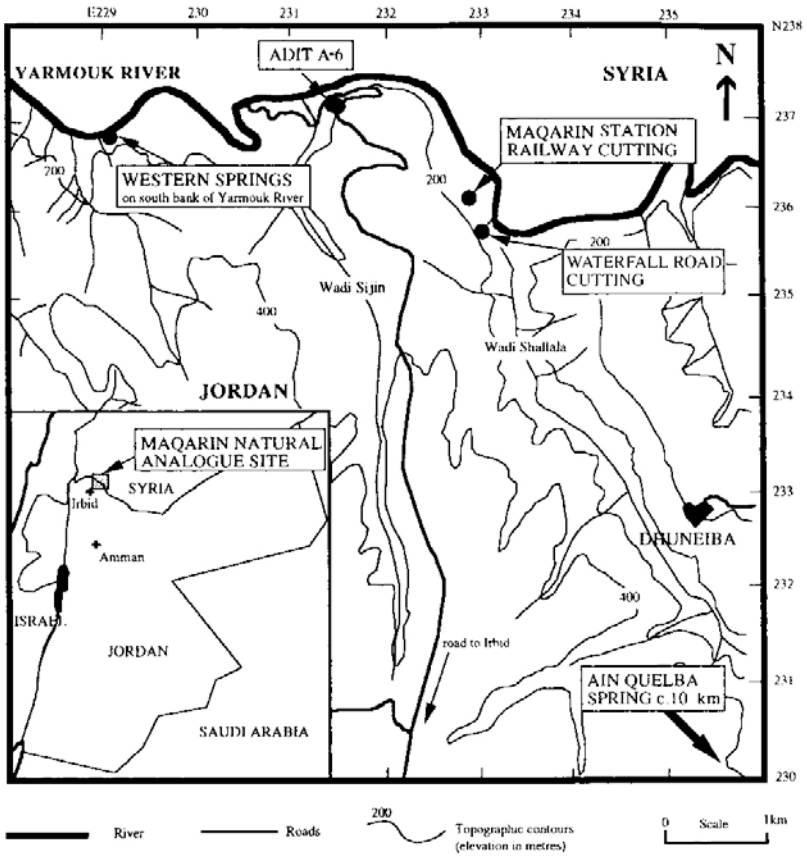

Figure 2-1. *The Maqarin study site in northern Jordan (Alexander 1992).*

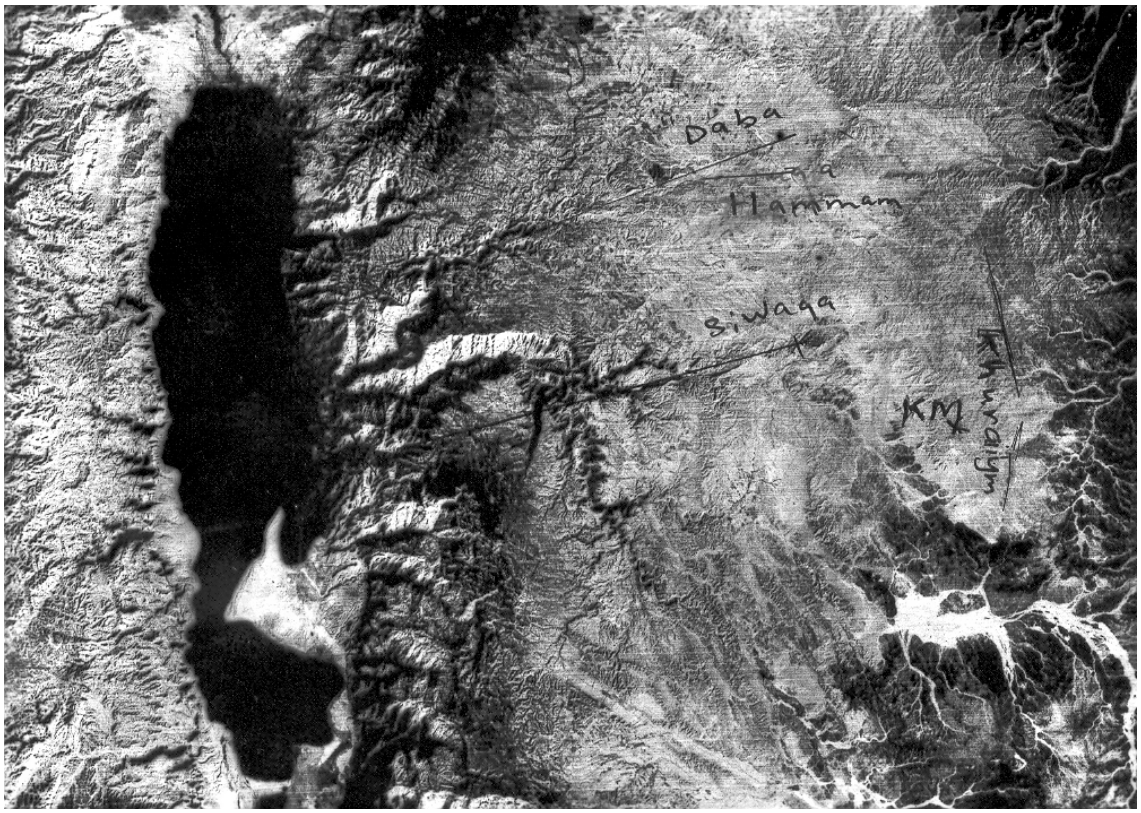

Figure 2-2. *The Khushaym Matruk (KM on right of image) site, central Jordan. The Dead Sea sits on the far left (Pitty and Alexander 2011).*

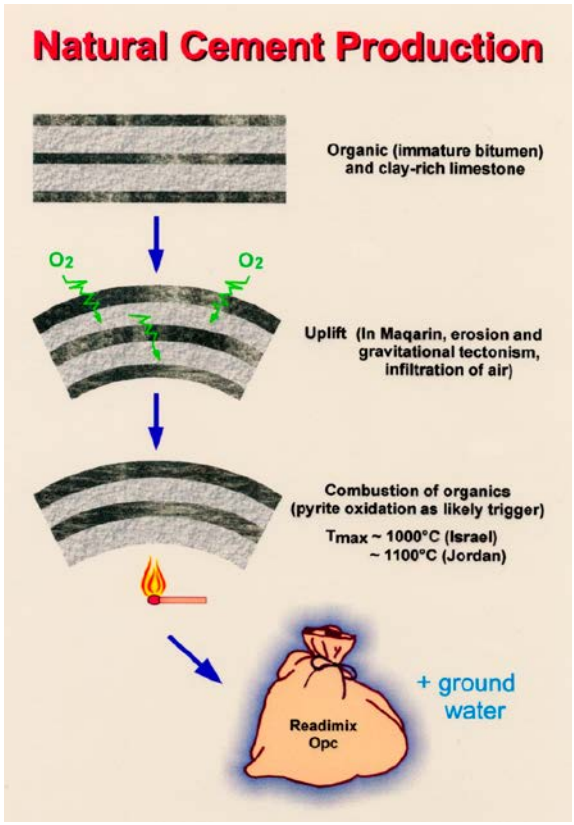

Figure 2-3. *Schematic representation of the production of the natural cements in Jordan (Pitty and Alexander 2011).*

Table 2-1. Primary metamorphic minerals from the Marble Zone (ACS), Maqarin site (after Milodowski et al. 1992, 1998a, b).

Mineralogy	General Formulae	Abundance
CARBONATES		
Calcite	$CaCO_3$	MAJOR
U-Ca-oxycarbonate?	Ca:U = 2:1	TRACE
SIMPLE OXIDES		
Lime	CaO	MINOR to TRACE
Periclase	MgO	TRACE
Hematite or ferric oxide	α-Fe_2O_3	MINOR to TRACE
Magnetite (?)	Fe_3O_4	MINOR to TRACE
Maghemite (?)	γ-Fe_2O_3	
FERRITES, ALUMINATES AND MIXED OXIDES		
Ca-aluminate	Undefined	MINOR
Calcium ferrite,	$CaFe_2O_3$	MINOR
Brownmillerite	$Ca_2(Al,Fe)_2O_5$	MINOR
Multiple element ferrites	$(Ca,Ba,Cr,Al,Ti,Mg,Zn,Mn)Fe_2O_3$ Undefined	TRACE
APATITE GROUP		
Fluorapatite	$Ca_{10}(PO_4)_6F_2$	MAJOR
Francolite	$Ca_{10-x-y}(Na,K)_xMg_x(PO_4)_{6-z}(CO_3)_zF_{0.4z}F_2$	MAJOR
Ellestadite	$Ca_{10}(SiO_4)_3(SO_4)_3O_{24}(Cl,OH,F)_2$	MAJOR
SILICATES		
Larnite	β-Ca_2SiO_4	MAJOR
Wollastonite	$CaSiO_3$	MINOR
Anorthtite	$CaAl_2Si_2O_8$	MINOR
Rankinite (?)	$Ca_3Si_2O_7$ (significant Zn substitution for Ca)	TRACE
Diopside-hedenbergite	$Ca(Al,Fe)Si_2O_6$	MINOR
COMPLEX SILICATES AND SILICATES WITH OTHER OXYANIONS		
Spurrite	$Ca_5(SiO_4)_2(CO_3)$	MAJOR
Parraspurrite	$Ca_5(SiO_4)_2(CO_3)$	MAJOR
Calcium silicate (unknown mineral)	$Ca_5(SiO_4)_2(SO_4)$	MAJOR
Ba-Ca-sulphate-silicate	Undefined	TRACE
Ba-Ca-Zr-Mo-silicate	Undefined	TRACE
CARBONS		
Graphite	C	MINOR to TRACE
SULPHIDES AND SELENIDES		
Oldhamite	CaS to $CaS_{0.9}Se_{0.1}$	TRACE
Cu-K-Na-Selenide	$Cu_{10.2}K_3Na_{0.2}Se_{7.7}S_{2..3\ (approx.)}$	TRACE
Krutaite	$CuSe_2$	TRACE

The Maqarin site in north-west Jordan appears to be unique in that the highly alkaline groundwaters in the area result from the interaction of normal (pH~7) recharge waters with these metamorphosed 'cement' zones producing similar water/rock reactions and mineralogy to that predicted for a cementitious materials in a respository environment. At least three different highly alkaline groundwater environments have been identified in Jordan and they appear to represent, by analogy, three different stages in the theoretical evolution of leachates from cementitious materials (cf. Berner 1987, 1990). These stages are:

- *Early Stage;* alkali hydroxide groundwaters (Western Springs, Maqarin – see Figure 2-1). The pH (maximum observed 12.9[2]) and the high Na/KOH content with relatively high Ca suggests that this site represents a slightly evolved (i.e. high pH, Na/KOH) leachate.
- *Intermediate Stage;* portlandite buffered system (Eastern Springs, Maqarin – see Figure 2-1, Daba and Khushaym Matruk in central Jordan – see Figure 2-2). A pH of ~12.5 and portlandite saturation indicate an intermediate stage (i.e. lower pH, $Ca(OH)_2$ buffered) leachate.
- *Late Stage;* lower pH, silica dominated system (Daba and Khushaym Matruk). The present water table is at least one hundred metres below the cement zone, but the fossil mineral assemblage strongly suggests a late stage (pH 10–11) leachate in parts of both sites.

The basis of the analogy between the natural cement sites in Jordan and cementitious materials in a repository is quite simple as illustrated in Figure 2-4.

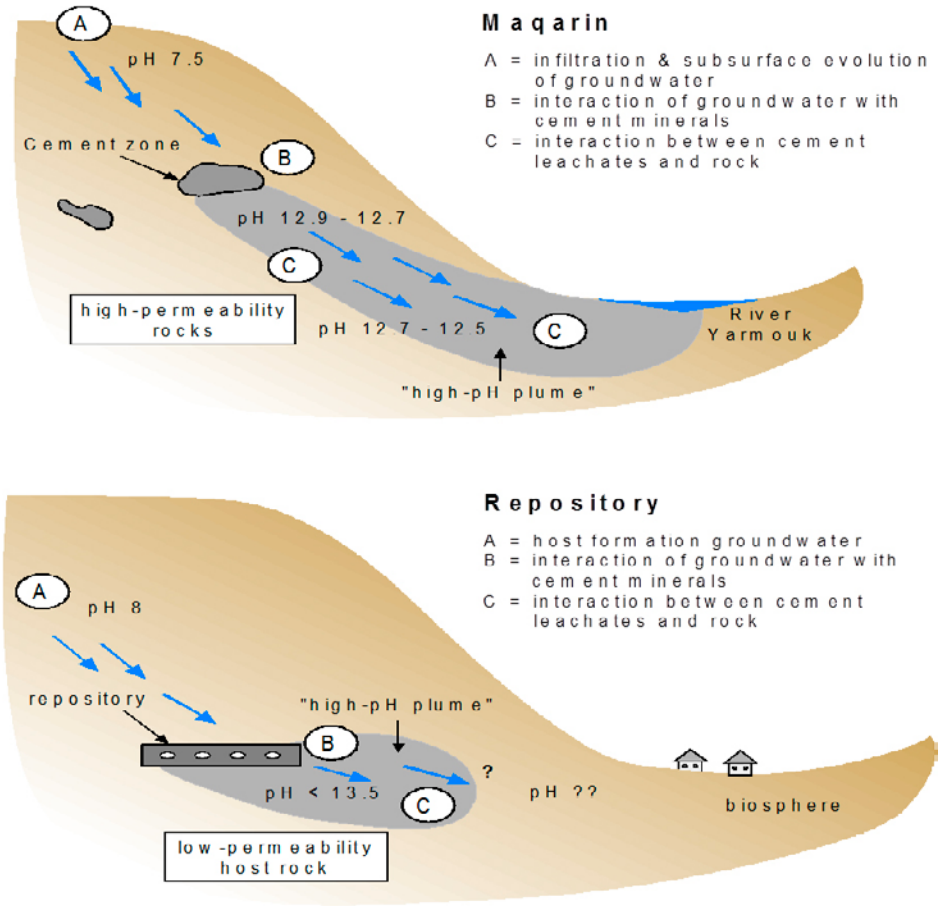

Figure 2-4. *The basis of the analogy. Maqarin (top) contains pods of natural OPC-like concrete and produces a natural alkali disturbed zone (ADZ) in the host rock. Any mass of man-made concrete (in this image a repository, but a block of grout will behave similarly) will likely produce an ADZ downstream from itself following leaching by groundwater (Smellie 1998).*

[2] This is the highest ever reported for a natural groundwater.

Before moving on to assess potential perturbations to the repository EBS, it is useful to consider the general impact of the cement leachates on the host rock. Effectively, the cement leachates will react with the aluminosilicates present, producing a so-called alkaline plume (also known as the Alkali Disturbed Zone (ADZ), the Hyperalkaline Disturbed Zone (HDZ) and the Hyperalkaline Plume: here the more technically correct ADZ will be used). On the basis of geochemical first principles, Savage (1998) presented a simple generic conceptual model of the evolution of the host rock[3] as a hypothetical 'plume' of alkaline cement leachates migrates away from the cementitious material (i.e. here, cementitious grout; see Figure 2-5).

Briefly summarised after (Alexander and Smellie 1998, Savage 2011), the model assumes that the leachates are pushed from the cement (following mixing of groundwaters with the cement pore waters) due to the flow of groundwater into the cement further upstream (see Neall (1994) and Lagerblad (2001) for a discussion of the initial expulsion of cement pore waters from a cement mass, followed by leaching of the cement phases by the incoming groundwaters). A zone of perturbed fluid composition (elevated pH, Na, K, Al and Si) where ion exchange reactions dominate, migrates ahead of a zone of mineral dissolution and growth. At the cement/host rock (or bentonite) interface (the proximal part of the plume), the alkaline leachates have not yet reacted with the host rock and so have a high pH and high concentrations of Na, K and Ca, reflecting the cement porewater chemistry. As the plume reacts with the host rock/bentonite (in this conceptualisation, the host rock is assumed to be aluminosilicate-bearing), the pH falls, as do the Na, K and Ca concentrations in the groundwater, while the concentrations of Al and Si rise fractionally. Beyond the distal edge of the plume, in the, as yet, undisturbed host rock/bentonite, the groundwater pH is near neutral, the Na, K and Ca concentrations are lower and the concentrations of both Al and Si are higher than in the plume waters.

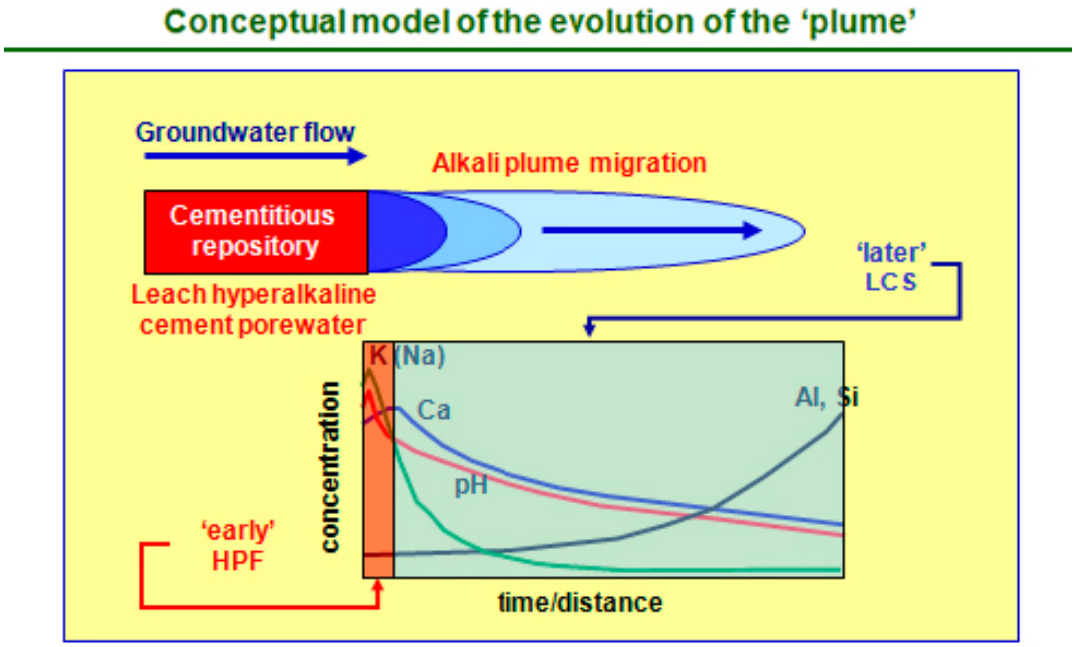

Figure 2-5. *Conceptual model of the alkaline plume (or ADZ) evolution (Pitty and Alexander 2011). The concentration profiles are applicable to both a host rock and to a bentonite EBS.*

[3] Note this model is equally applicable to interaction with bentonite.

This pattern has consequences for the secondary mineralogy: C-S-H phases will be found in the host rock/bentonite (through which the plume has migrated) in the proximal part of the plume, reflecting the fact that the leachate has not yet reacted with the host rock/bentonite and is equilibrated with the C-S-H phases which make up the cement. As the leachate moves downstream and interacts with the aluminosilicates in the host rock/bentonite (and the host rock/bentonite groundwater and porewater), the Al concentration increases, precipitating C-A-S-H phases. At the distal edge of the plume, the leachate has reacted with an even larger volume of host rock/bentonite (and the host rock/bentonite groundwater and porewater) and eventually precipitates minerals such as zeolites as the Al concentration in the groundwater becomes high enough and the pH low enough. In the presence of elevated Al levels in solution, zeolites will form preferentially due to the limited ability of C-A-S-H/C-S-H to incorporate Al in the mineralogical structure (Savage 1998).

If this evolutionary pattern could be observed from an imaginary fixed point in the host rock/bentonite (X in Figure 2-6), the theoretical sequence (assuming an infinite source of cement leachate and a constant fluid flow velocity) of events in a fracture will be (Alexander and Smellie 1998):

Figure 2-6a: Immediately following grout injection, the groundwater slowly saturates the grout cement.

Figure 2-6b: With saturation complete, alkaline plume evolution begins. The plume chemistry, not yet altered by sand/gravel or host rock/groundwater/porewater interaction, reflects the cement porewater composition.

Figure 2-6c: Following some reaction with the sand/gravel or host rock, the distal edge of the plume reaches the observation point, X. The leachate, having already reacted somewhat with the sand/gravel or host rock, has a lowered pH and Ca, Na and K concentrations. The Al and Si concentrations are still high (reflecting the host rock conditions) and so the leachate chemistry will lie in the zeolite stability field (cf. Figure 2-5). Initially, zeolites stable at low pH (high silica zeolites such as clinoptilolite, mordenite and dachiardite) will form, followed by zeolites stable at higher pH (low silica zeolites such as scolecite and phillipsite[4]).

Figure 2-6d: Middle of the plume reaches the observation point. By this point, the sand/gravel or rock upstream of the observation point has already been significantly reacted by the cement leachates and the leachate is thus less evolved than in Figure 2-6c. Consequently, the pH is higher and the Ca, Na and K concentrations higher than before. Additionally, a combination of the higher pH and some depletion in the host rock Al and Si reservoir due to previous reaction (Figure 2-6c), means lower Al and Si concentrations in the leachate. By this point, the leachate chemistry is lying in the C-A-S-H stability field (cf. Figure 2-5).

Figure 2-6e: The proximal part of the plume reaches the observation point. The bentonite or host rock upstream of the observation point has been extensively reacted by the passing plume and no longer has any significant buffer capacity remaining. Consequently, the cement leachate reaches the observation point having undergone little reaction and so the leachate chemistry effectively reflects that of the source cement porewater (high pH, high concentrations of Ca, Na and K, low concentrations of Al and Si; cf. Figure 2-5). By this point, the leachate chemistry is lying in the C-S-H stability field. Initially, low Ca/Si ratio phases (e.g. tobermorite) will form followed by high Ca/Si ratio phases (e.g. jennite, ettringite-thaumasite).

Clearly the precise position of the observation point, the site hydrogeology and geochemistry and the sand/gravel and host rock mineralogy will play a role in the precise phases observed (cf. Table 2-2a and b) as will the volume of bentonite or host rock matrix accessed by the leachate, but, in gross terms, the sequence at a given point will be as stated above.

If it is assumed that the plume continues to migrate, then, by analogy with the above argument, the zeolite zone produced by the distal part of the plume will later be over-run by the middle of the plume, inducing some re-dissolution of the zeolite phases and replacement by C-A-S-H phases. This mixed zeolite/C-A-S-H zone will be then over-run by the proximal part of the plume, inducing further re-dissolution of the zeolite/C-A-S-H phases and replacement by C-S-H phases. These complex mixtures have been observed in places at the advective-flow dominated fractured host rock site at Maqarin, Jordan (see Alexander 1992, Linklater 1998, Pitty and Alexander 2011, Smellie 1998 for details).

[4] Laboratory data (e.g. Chermak 1992, 1993) indicate that phillipsite is metastable.

Finally, it should be noted that 'reaction' in the fractures in any given host rock will include both the fracture surface minerals and any fault infill or gouge plus the accessible porosity in the rock matrix behind the fractures (as long as this is not sealed by reaction). In general, fractures and joints at Maqarin tend to seal competely (e.g. Figure 2-7) in years to decades, potentially leading to changes in the site hydrogeology and this is discussed further in Section 2.6 and Alexander and Neall (2007).

a) immediately following grout injection (in the case of SFR-1, x represents an observation point in the sand/gravel or host rock downstream of the repository)

b) saturation of the grout by groundwater followed by expulsion of grout pore water, plume evolution begins

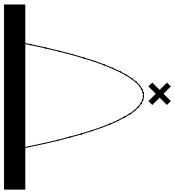

c) distal edge of plume reaches the observation point, initiation of zeolite formation

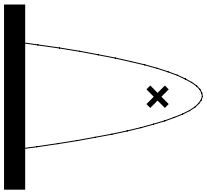

d) middle of plume reaches observation point (as the sand/gravel or rock buffer capacity is being consumed) CASH formation initiated

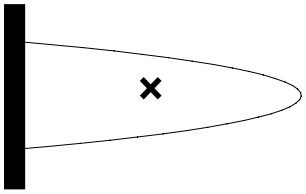

e) proximal part of the plume reaches the observation point (as the sand/gravel or rock buffer capacity is exhausted) C-S-H formation initiated

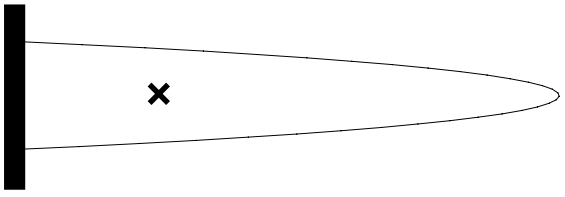

Figure 2-6. *Evolutionary pattern of the alkaline plume (from Alexander and Smellie 1998).*

Table 2-2a. Secondary minerals observed in the ACZ at the Maqarin site in Jordan (Milodowski et al. 1992, 1998a, b, 2011).

Mineralogy	General Formulae	Abundance
CARBONATES		
Calcite	$CaCO_3$	MAJOR
Aragonite	$CaCO_3$	MINOR to TRACE
Vaterite	$CaCO_3$	MINOR to TRACE
Strontianite	$SrCO_3$	MINOR to TRACE
Ankerite	$Ca(Mg,Fe)(CO_3)_2$	TRACE
Kutnahorite	$Ca_{0.75}(Mn,Mg)_{0.25}(CO_3)_2$	TRACE
COMPLEX CARBONATES		
Hydrotalcite	$MgAl_2(CO_3)(OH)_{16}.4H_2O$	MINOR to TRACE
SIMPLE OXIDES		
Hematite or ferric oxide	α-Fe_2O_3	MINOR to TRACE
Maghemite (?)	γ-Fe_2O_3	MINOR to TRACE
SIMPLE HYDROXIDES		
Brucite	$Mg(OH)_2$	MINOR to TRACE
Portlandite	$Ca(OH)_2$	MAJOR
Gibbsite	α-$AlOH_3$	MINOR to TRACE
Goethite	α-FeO.OH	MINOR to TRACE
Iron oxyhydroxide	undifferentiated	MINOR to TRACE
SULPHATES		
Gypsum	$CaSO_4.2H_2O$	MAJOR
Bassanite	$CaSO_4.0.52H_2O$	?
Anhydrite	$CaSO_4$	MINOR to TRACE
Barite	$BaSO_4$	TRACE
Celestite (celestine) [3]	$SrSO_4$ [3]	TRACE
Barytocelestite	$(Ba,Sr)SO_4$	TRACE
Calcian barytocelestite	$(Ba,Ca,Sr)SO_4$	TRACE
Hashemite	$BaCrO_4$ to $BaSO_4$ [complete solid-solution]	TRACE
Cd-sulphate phase	Undefined phase	TRACE
Pb-sulphate phase	Undefined phase	TRACE
Cu,Zn-sulphate phase	Undefined phase	TRACE
COMPLEX SULPHATES		
Ettringite [1]	$Ca_6Al_2(SO_4)_3(OH)_{12}.25H_2O$ [1]	MAJOR
Thaumasite [1]	$Ca_6Si_2(SO_4)(CO_3)_2(OH)_{12}.24H_2O$ [1]	MAJOR
Jourovskite	$Ca_3Mn(CO_3)(SO_4)(OH)_6.12H_20$	TRACE
SILICA MINERALS		
Quartz	SiO_2	MINOR
Silica gel	$SiO_2.nH_2O$	MINOR to TRACE
Opal-CT	SiO_2	NOT KNOWN
Opal-A	$SiO_2.nH_2O$	NOT KNOWN
APATITE-GROUP		
Hydroxyapatite	$Ca_{10}(PO_4)_6(OH)_2$	MAJOR to MINOR
Fluorapatite	$Ca_{10}(PO_4)_6F_2$	MAJOR to MINOR
Francolite	$Ca_{10-x-y}(Na,K)xMg_y(PO_4)_{6-z}(CO_3)_z(OH)_2F_{0.4z}F_2$	MAJOR to MINOR
Ellestadite	$Ca_{10}(SiO_4)_3(PO_4)_3O_{24}(Cl, F, OH)_2$	MAJOR to MINOR
Fluorellestadite [3]	$Ca_{10}(SiO_4)_3(PO_4)_3O_{24}(F)_2$ [3]	MAJOR to MINOR

Mineralogy	General Formulae	Abundance
C-S-H and C-A-S-H PHASES		
Afwillite	$Ca_3Si_2O_4(OH)_6$	MAJOR to TRACE
Tobermorite(s) [2]	$Ca_5Si_6O_{16}(OH)_2.2\text{-}8H_2O$ [2]	MAJOR
Jennite	$Ca_9H_2Si_6O_{18}(OH)_8.6H_2O$	MAJOR
Birunite	$Ca_{15}(CO_3)_{5.5}(SiO_3)_{8.5}SO_4.15H_2O$	MINOR to TRACE
C-S-H(I) hydrogel [4]	amorphous Ca:Si = 0.8–1.5 [4]	MAJOR
C-S-H(II) hydrogel [4]	amorphous Ca:Si = 1.5–2 [4]	MAJOR
C-S-H hydrogel [4]	amorphous, undefined/variable Ca:Si = <0.8 [4]	MAJOR
Tacharanite [5]	$Ca_{12}Al_2Si_{18}O_{15}(OH)_2.3H_2O$ [5]	MAJOR
C-A-S-H hydrogels	Highly variable compositions between tacharanite and zeolite compositions	MAJOR
ZEOLITE GROUP [7]		
Mordenite	$CaNa_2K_2Al_2Si_{10}O_{24}.7H_20$	MAJOR to TRACE
Dachiardite	$(CaNa_2K_2)_5Al_{10}Si_{38}O_{96}.25H_20$	MAJOR to TRACE
Henlandite	$(CaNa_2)Al_2Si_7O_{18}.6H_20$	MAJOR to TRACE
Epistilbite [7]	$Ca_3Al_6Si_{18}O_{48}.16H_20$	MAJOR to TRACE
Yugarawaralite	$Ca_2Al_4Si_{12}O_{32}.8H_20$	MAJOR to TRACE
Laumontite	$Ca_4Al_8Si_{16}O_{49}.16H_20$	MAJOR to TRACE
Wairakite	$Ca_4Al_{16}Si_{32}O_{96}.16H_20$	MAJOR to TRACE
Leonhardite	$Ca_4(Al_8Si_{16}O_{48}).14H_20$	MAJOR to TRACE
CLAY MINERALS		
Volkonskoite.	Cr-substituted smectite	MINOR to TRACE
OTHER PHASES		
Apophyllite [6]	$KCa_4Si_8O_{20}(OH,F).8H_2O$ [6]	MAJOR to TRACE
U-Ca-silicate	unidentified and undefined	TRACE
Ca-Cr-silicate hydrogel	unidentified and undefined	TRACE

Notes:

[1] A complex solid-solution is observed between ettringite and thaumasite mineralization;

[2] Tobermorites of variable hydration states are present (including 14Å tobermorite (sometimes formerly referred to as 'plombierite') with 8 H_2O; 11Å tobermorite with 4 H_2O; 9Å tobermorite with 2 H_2O).

[3] New species found during Phase IV of the Maqarin project.

[4] C-S-H hydrogels from Maqarin can host significant Al content.

[5] Includes non-crystalline C-A-S-H hydrogels with similar composition to tacharanite.

[6] Apophyllite analyses from Maqarin are significant deficiency in K^+ site occupancy (up to 25%) compared to ideal apophyllite stoichiometry, indicating probable major lattice substitution of K^+ by NH^{4+}.

[7] 'Zeolites' at Maqarin are tentatively inferred on the basis of micochemical composition (EPMA, EDXA and ATEM). Most appear to be amorphous C-A-S-H 'hydrogels' of zeolitic composition and only epistilbite has been confirmed by XRD as a crystalline zeolites.

Table 2-2b. Secondary minerals taken into account in modelling the Grimsel LCS experiment by one particular modelling group (Savage et al. 2011). Reactions are written as the dissolution of 1 mol of mineral and in terms of Al^{3+}, $SiO_2(aq)$, Na^+, K^+, Ca^{2+}, Mg^{2+}, HCO_3^-, SO_4^{2-}, H^+, Cl^-, F^- and H_2O.

Mineral	Composition	log *K*
Calcite	$CaCO_3$	2.0050
Portlandite	$Ca(OH)_2$	23.3400
Brucite	$Mg(OH)_2$	16.9760
C-S-H-1667	C-S-H ss, Ca/Si = 1.67, $1.00SiO_2 \cdot 1.67Ca(OH)_2 \cdot 1.00H_2O$	30.1640
C-S-H-14	C-S-H ss, Ca/Si = 1.4, $1.00SiO_2 \cdot 1.40Ca(OH)_2 \cdot 0.95H_2O$	23.9420
C-S-H-12	C-S-H ss, Ca/Si = 1.2, $1.00SiO_2 \cdot 1.20Ca(OH)_2 \cdot 0.91H_2O$	19.4580
C-S-H-10	C-S-H ss, Ca/Si = 1.0, $1.00SiO_2 \cdot 1.00Ca(OH)_2 \cdot 0.86H_2O$	15.0800
C-S-H-08	C-S-H ss, Ca/Si = 0.8, $2.27SiO_2 \cdot 1.82Ca(OH)_2 \cdot 1.82H_2O$	25.4330
C-S-H-06	C-S-H ss, Ca/Si = 0.6, $1.72SiO_2 \cdot 1.03Ca(OH)_2 \cdot 1.03H_2O$	13.7100
C-S-H-04	C-S-H ss, Ca/Si = 0.4, $1.39SiO_2 \cdot 0.56Ca(OH)_2 \cdot 0.56H_2O$	6.6928
C-S-H-02	C-S-H ss, Ca/Si = 0.2, $1.16SiO_2 \cdot 0.23Ca(OH)_2 \cdot 0.23H_2O$	2.0311
C-S-H-00	C-S-H ss, Ca/Si = 0.0, SiO_2	–1.2416
Analcime	Na-zeolite, $Na_{0.96}Al_{0.96}Si_{2.04}O_6 \cdot H_2O$	6.5548
Laumontite	Ca-zeolite, $CaAl_2Si_4O_{12} \cdot 4H_2O$	14.6980
Mesolite	Na-Ca-zeolite, $Na_{0.68}Ca_{0.66}Al_{1.99}Si_{3.01}O_{10} \cdot 2.65H_2O$	14.6450
Natrolite	Na-zeolite, $Na_2Al_2Si_3O_{10} \cdot 2H_2O$	19.5900
Scolecite	Ca-zeolite, $CaAl_2Si_3O_{10} \cdot 3H_2O$	17.0550
Stilbite	Na-Ca-zeolite, $Na_{0.14}K_{0.01}Ca_{1.02}Al_{2.18}Si_{6.82} \cdot 7.33H_2O$	1.4087
Gismondine	Ca-zeolite, $Ca_2Al_4Si_4O_{16} \cdot 9H_2O$	41.7170
Mordenite	Na-Ca-zeolite, $Ca_{0.29}Na_{0.36}Al_{0.94}Si_{5.06}O_{12} \cdot 3.47H_2O$	–5.4107
Wairakite	Ca-zeolite, $CaAl_2Si_4O_{12} \cdot 2H_2O$	19.4280
Prehnite	$Ca_2Al_2Si_3O_{10}(OH)_2$	34.7560
Foshagite	C-S-H phase, Ca/Si = 1.33, $Ca_4Si_3O_9(OH)_2 \cdot 0.5H_2O$	68.0480
Gyrolite	C-S-H phase, Ca/Si = 0.66, $Ca_2Si_3O_7(OH)_2 \cdot 1.5H_2O$	23.3530
Hillebrandite	C-S-H phase, Ca/Si = 2.0, $Ca_2SiO_3(OH)_2 \cdot 0.17H_2O$	38.0350
Okenite	C-S-H phase, Ca/Si = 0.5, $CaSi_2O_4(OH)_2 \cdot H_2O$	10.4640
Tobermorite-14A	C-S-H phase, Ca/Si = 0.83, $Ca_5Si_6O_{16}(OH)_2 \cdot 9.5H_2O$	65.1370

Figure 2-7. *Example of sub-bedding parallel fractures and joints (here sealed by secondary tobermorite) in the clay biomicrite host rock at Maqarin (Pitty and Alexander 2011).*

2.2.2 Potential impact on the host rock

The general indication is that clogging of fractures will occur when alkaline leachates migrate through a water-conducting feature and react with the fracture wall-rock, fracture infill material and accessible rock matrix. This is because the volume of the secondary minerals produced in the reaction is generally greater than that of the primary minerals (Milodowski et al. 1998a, b).

Alexander and Neall (2007) noted that a lack of information about potential fracture wall rock (and fracture fill minerals) pH buffering capacity meant it could not be ruled out that alkaline leachates from tunnel grouts would reach the SF deposition holes at Olkiluoto. This was supported by Montori et al. (2008) who noted in a modelling study that the Olkiluoto host rock did not have sufficient buffering capacity to significantly reduce the pH of the circulating solutions within the 200 m calculation domain in 10 ka. They further noted "In view of all the results, the possibility of sealing of the fracture by the high-pH solutions seems to be a very definite possibility."

If the assumption that there will be some degree of leaching from the cement grout is accepted (although note that this assumption is addressed further in Sections 2.4 and 2.6), it leads to the likelihood that some degree of flow volume clogging will occur in the host rock and this has clear implications for hydrogeological modelling of the site. However, minor movements could reactivate some of the fractures such that porosity would be created and circulation of alkaline water through the rock would be (perhaps repeatedly, as at Maqarin) re-initiated.

One important feature of reactivation of an existing fault network is that each seismic event only reactivates a part of all faults (see e.g. the discussion in McEwen and Andersson 2009). This general statement is also true for Maqarin: the full alteration/precipitation sequences described in Section 2.3.1 have rarely been seen in one single fracture. Some samples show multiple reactivations within one phase, while other samples record different stages of evolution of the alkaline plume. In this sense, the sequence of secondary phases observed at Maqarin, as given above, already is a simplification and interpretation of existing observations.

Maqarin, unlike the Forsmark SF repository, is a shallow, near-surface flow system, and, as such, the analogy between the sites cannot be taken too far. Nevertheless, a number of bounding alternative scenarios can be given for the assumed leaching of the cement grouts in the shallower (i.e. 200–370 m) zone of the deep SF repository:

Scenario 1. The rate of fracture sealing is high and of wide extent and the flow system within the ADZ breaks down. When tectonic reactivation occurs, the generated flow porosity is sealed within short timescales by infiltrating alkaline water. The rock body within the alkaline plume is a hydraulic barrier and groundwater flow will 'bend around' the ADZ, as observed locally at Maqarin. As long as sufficient alkali buffer capacity exists in the fault system, the growth of the ADZ will be very slow due to this effective self-sealing mechanism. Similar effects have been shown before and after major earthquakes when stress induced changes to the existing flow paths allow 'leakage' of groundwaters from new sources. Claesson et al. (2004) noted "...fluid source switching in response to fault sealing and unsealing, with the newly tapped aquifer containing chemically and isotopically distinct....water."

Comment: Likely scenario.

Scenario 2. Similar to 1, but reactivation is limited to a small number of shear-zones. If the boundary conditions of the SF repository hydrogeological system are assumed to be constant flux, all flow through the plume will be focussed into those few zones that remain open, resulting in higher fluxes through single structures or channels (as reported in the HPF experiment; see Section 2.4). If advection is faster than the rate of sealing, such structures may channel flow and lead to a relatively fast and very localised propagation of the plume where, as at Maqarin, advection will dominate over diffusion and the alkaline front will migrate a significant distance[5]. In the case that the site hydrogeological boundary conditions are constant gradient (because elevations of recharge and discharge areas are constant and remain unaffected by the ADZ), flux through individual fractures would be independent of the number of currently open (or reactivated) fractures in which advection may take place; i.e. the fractures would not be fast channels as in the case of constant-flux conditions.

Comment: Possible scenario, dependent on the hydrogeological environment around the grouted zone.

[5] Minimum of 500 m downstream at Maqarin (Pitty and Alexander 2011).

Scenario 3. Tectonic reactivation is very extensive, such that the rate and extent of fracture sealing are insufficient to keep up with the rate of seismic porosity generation. Under such conditions, the flow path geometry will not differ significantly from that outside the ADZ. One major difference is the presence of secondary alteration products, such as C-S-H gels, in the flow system. Due to the continued deformation and generation of new flow porosity within the faults, direct contact between alkaline leachates and unaltered wallrock as well as with the secondary phases precipitated during previous reactivation events will be present at all times. Further, the distal edge of the ADZ (cf. Figure 2-6) will physically migrate past any given point in the flow path, with the proximal part eventually over-running what was originally the distal edge.

Comment: Presently highly unlikely due to high tectonic activity required, but needs further consideration during glacial periods.

Scenario 4. Advection of alkaline water is fast and self-sealing due to interaction with the rock is relatively insignificant at these timescales (i.e. flow is faster even than Maqarin today). The alkaline plume grows at the rate of regional advection, i.e. it is not significantly influenced by reaction products sealing fractures.

Comment: Unlikely scenario. Advection rates predicted on the basis of hydrogeological modelling (see Table 6-8 to Table 6-10) result in typical travel times of a few hundred years between some grout bodies and the EBS, while, based on evidence from Maqarin and HPF, alkaline water/rock interactions are likely to proceed much faster.

Which scenario will occur in reality depends on the relative significance of sealing (or, more generally, leachate/rock interaction), tectonic reactivation of both fractures in the grout and in the sealed fractures in the ADZ and advective transport. The likely development of a highly impermeable zone due to fracture sealing leads to a deformation of the flow field around the ADZ which results in local changes in flow direction. Relatively high hydraulic gradients may develop across the sealed zone. If tectonic reactivation is efficient, flow paths across the sealed zone may develop, leading to episodic, fast and channelled advection following tectonic activity. Note that these factors may vary with time – according to some models, for example, deglaciation could be accompanied by seismic activity levels that might make scenario 3 feasible.

2.2.3 Potential impact on the bentonite

Impact of OPC cement leachates

Posiva (2012) noted that for repository relevant bentonite natural analogue studies, data are restricted and the information is ambiguous in many cases: nevertheless, some data of use do exist. For example, in the Jordan Natural Analogue Study, several sites across the country were examined to assess a range of mechanisms and processes of relevance to cementitious repository systems (see Kamei et al. 2010 for an overview). As noted in Section 2.2, the natural cements which are the source of the alkaline leachates, are produced by combustion of organic-rich limestones. At one site, Khushaym Matruk (Figure 2-2 and Figure 2-8) in central Jordan, it is believed that the cement leachates diffused down into the underlying clay-rich sediments (see Figure 2-9) and reacted with them. Techer et al. (2004) state that the clays have clearly reacted with the alkaline solutions, dissolving smectites and leaving zeolites as reaction products.

However, Pitty and Alexander (2011) modulate these conclusions, noting that "The observed transformations in the samples from the Khushaym Matruk site were mainly secondary recrystallisation in joints and mineralogical evolution in the clay-rich matrix near the contact with the ACZ. They appear to post-date the combustion processes and, consequently, they might be attributable to the circulation of alkaline solutions from leaching of the overlying ACZ (although other processes, such as weathering, cannot yet be ruled out). Zeolites have been found in the joint fillings and in foram tests in the matrix and the weight of evidence suggests that these phases have been produced by interaction with alkaline fluids. However, it is not yet possible to rule out if the matrix zeolites are a primary diagenetic feature of the sediments without further isotopic analysis." Unfortunately, no such additional studies have taken place on the Khushaym Matruk samples and so the existing results must be treated as ambiguous for the time being.

Figure 2-8. *Khushaym Matruk site in Jordan. The sampling area is at the base of the peak, left background.*

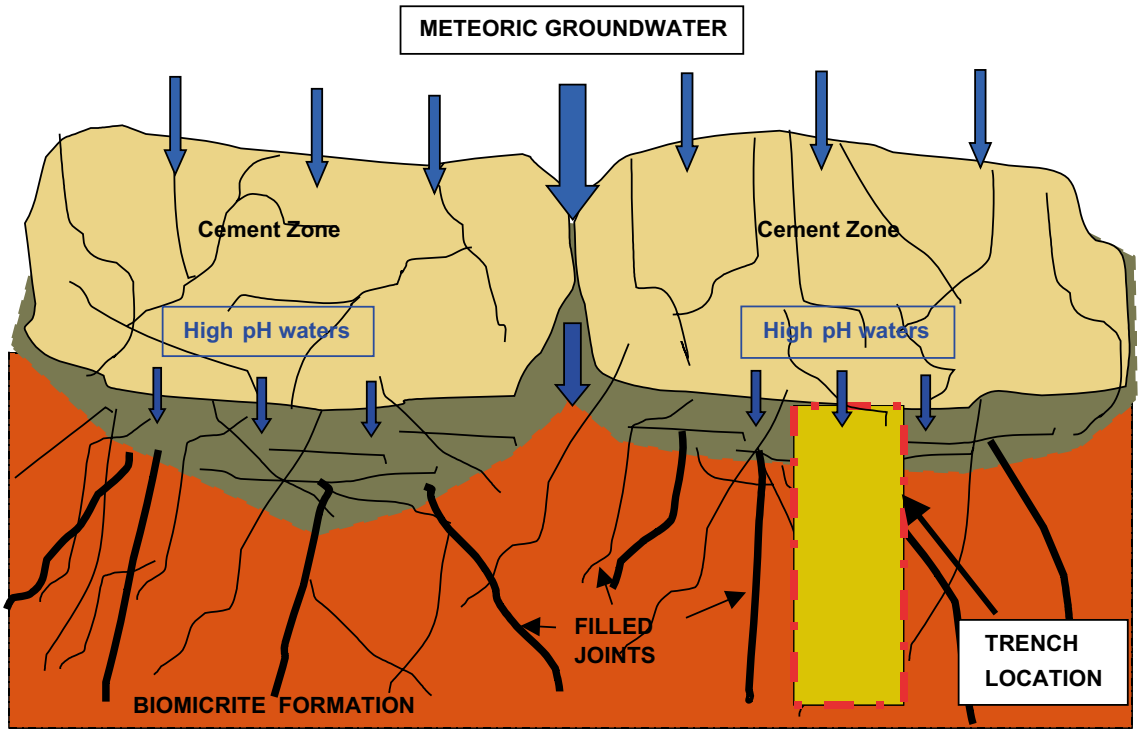

Figure 2-9. *Sampling at Khushaym Matruk was by trenching. The trench begins at the cement zone and moves away downslope into the underlying clay-rich sediments. The thermal aureole from the cements extends for the length of the trench (Pitty and Alexander 2011).*

Impact of low alkali cement leachates

SKB have been involved in the development of low alkali cements for some time and have also been involved in collaborative development work with various organisations such as Posiva and NUMO and in EU joint projects. Although there is currently no definite plan to employ low alkali grouts[6], SKB has nevertheless been involved in natural analogue studies of the potential impact of low alkali cements on bentonite (e.g. Alexander et al. 2012, Alexander and Milodowski 2011). These studies are nevertheless of interest to this project because there is every likelihood that any alkaline leachates released from the grouts will undergo some degree of buffering following reaction with the host rock before contacting the bentonite in the EBS and backfill (cf. discussion in Alexander and Neall (2007) and the modelling studies in Chapter 7).

SKB currently plans to use MX-80 bentonite in their SF repository and this has been shown to have a porewater pH of 8 in ambient groundwaters (Bradbury and Baeyens 2003), significantly less than that of any partially buffered alkali leachates at, for example, pH 11. Based on geochemical first principles, there will be reaction with bentonite, it will simply be less than at pH 13. Ahokas et al. (2006) noted that "According to Sellin et al. (2003), the dissolution rate for a number of silicates and aluminium silicates, e.g. quartz, kaolinite, increases by a factor of 10 if pH is increased from 11 to 13 and laboratory experiments referred to implied that bentonite is much more stable at pH 11 as compared to pH 13." The non-linearity of such pH dependency for silicate-containing minerals is very clear from the variation in silica solubility (see Figure 2-10) which increases dramatically above pH 9.5–10.

But Alexander and Neall (2007) noted this is certainly not the case for all aluminosilicates (e.g. Zevenberg et al. 1999) and montmorillonite dissolution rates are at a minimum at pH 8–8.5 (Huertas et al. 2001). Ramirez and Parnieix (2005), working with Callo-Oxfordian clay in NaOH (0.0001–1M) reported a smectite apparent activation energy of dissolution of around 21 $kJmol^{-1}$ [7]. Bauer and Berger (1998) found that, in 0.1–3M KOH at pH $11.5 \leq pH \leq 13.9$, the smectite apparent activation energy of dissolution was constant, at 52 ± 4 kJ mol^{-1}.

More recent work (Kuwahara 2008, Rozalen et al. 2009) on montmorillonite dissolution indicates that changes in dissolution rates with pH (Figure 2-11) are likely to be more gradual than shown for silica in Figure 2-10. As such, too much focus on pH 10–11 may be an over-simplification. As Alexander and Neall (2007) concluded, it appears that further natural analogue and laboratory work on the pH dependency of bentonite alteration in the pH range of 8 to 11 is still required[8].

Two new NA studies on bentonite interaction in low alkali cement leachates are currently ongoing in the Philippines and Cyprus (see Alexander et al. 2008a, b, Alexander and Milodowski 2011 respectively for details). These studies differ from Jordan insofar that the analogue cement leachates are not produced by a natural cement, but rather by the serpentinisation of ophiolites. The exact reactions involved are highly variable (see Alexander and Milodowski 2011 for details), but the alkaline groundwaters produced by reaction in the igneous layers of an ophiolite (Figure 2-12) are reasonable analogies of the low alkali cement leachates (see Table 2-3).

Bentonites are integral parts of ophiolites and the alkaline groundwaters (Figure 2-13) move upwards through the ophiolite until reaching the base of the overlying bentonites (Figure 2-14).

[6] Nevertheless, R&D projects such as the *Sealing of Tunnel at Great Depth* project in the Äspö URL continue to examine lower pH grouts such as silica sol and the *Low pH Programme* is looking into a variety of uses for low alkali cements (SKB 2011).

[7] Although note that low Ea values (around 20 $kJmol^{-1}$) are probably indicative of transport (diffusion) control in the experiments, instead of reaction control. Ea for diffusion in water is about 20 $kJmol^{-1}$.

[8] SKI (2005), noted that " (SKB) suggested that an upper limit of pH 11 would provide a margin, below which unfavourable interactions between bentonite and cement would be avoided. SKB did not provide any conclusive justification for this statement,... "

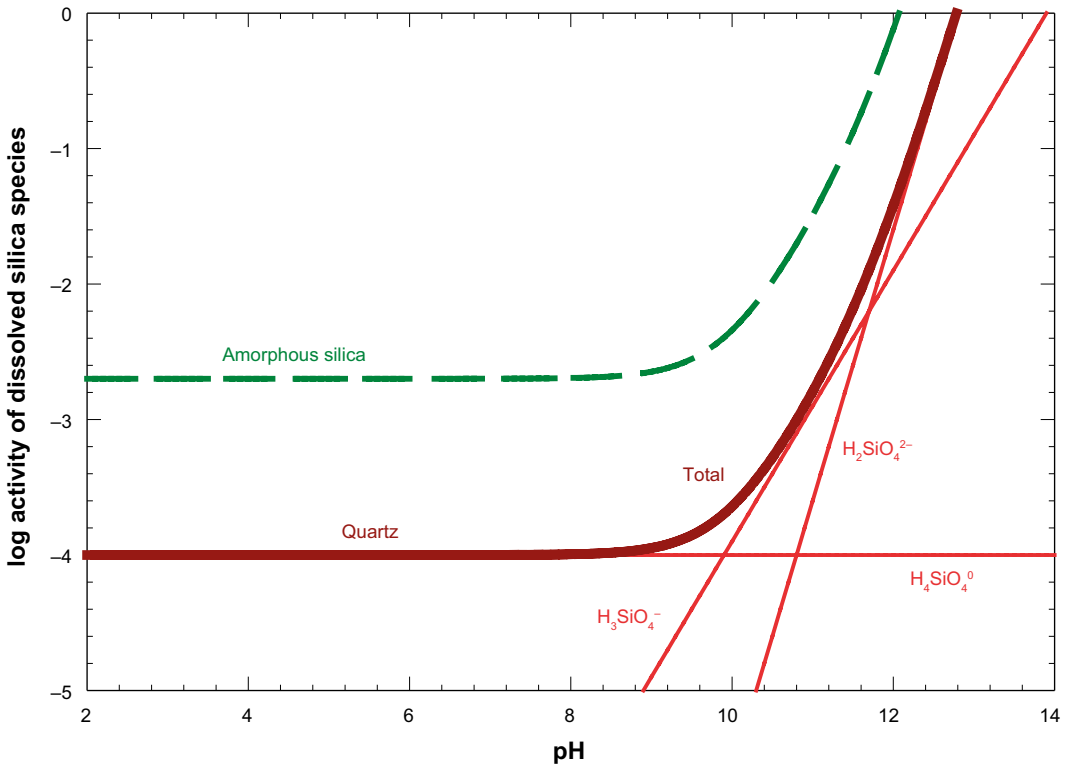

Figure 2-10. *pH dependence of silica solubility as an example of the pH dependence of aluminosilicate solubility (from Savage et al. 2010b). Note dramatic increase above pH 9.5–10.*

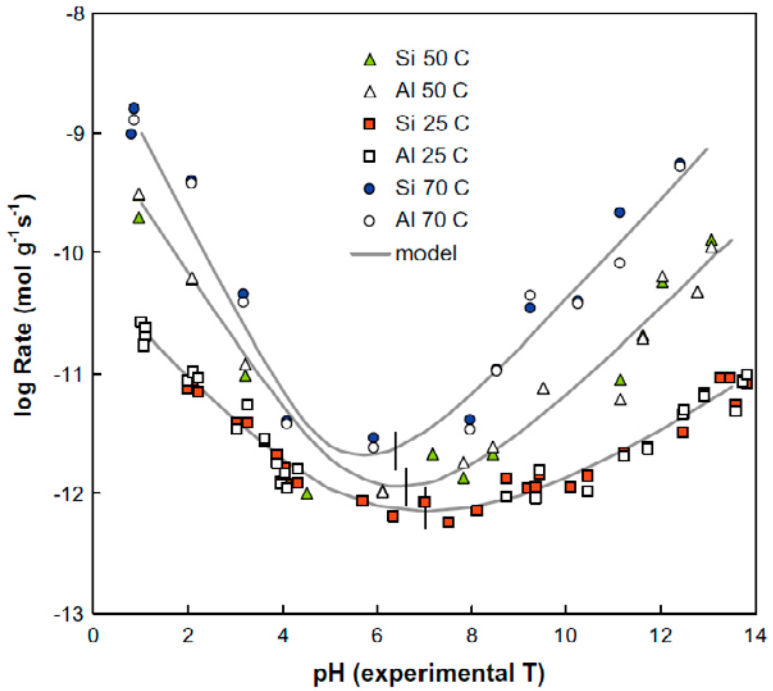

Figure 2-11. *pH and temperature dependence of montmorillonite dissolution (Rozalen et al. 2009).*

Table 2-3. Hydrochemistry of alkaline groundwaters: examples from around the world for comparison with the lower pH cement leachates. All data in ppm (Alexander et al. 2012).

Location	pH	Na	K	Ca	Mg	Cl
Cyprus[1]						
Cyprus 3a	11.5	385	15.1	1.0	0.3	420.0
Cyprus 3b	11.2	163.0	1.2	93.0	0.5	190.0
Worldwide[2]						
Greece	11.3	24.0	1.0	34.0	0.3	15.0
Bosnia	11.7	35.0	1.5	29.0	7.0	20.0
Oman	11.5	132	4.8	34.0	1.3	127.5
PNG	10.8	15.0	3.0	14.0	2.3	22.0
Western USA	11.5	19.0	1.0	40.0	0.3	63.0
Philippines[3]						
Manleluag 1	11.1	28.0	0.5	18.6	0.2	17.4
Manleluag 2	10.4	20.6	0.4	18.1	–	15.8
Poon Bato	10.9	18.4	0.9	33.1	0.05	20.9
Narra 1	10.8	158	0.9	3.1	0.0	95.0
Narra 3	10.3	157	0.9	2.4	0.1	80.0

[1] Neal and Shand (2002).

[2] Neal and Stanger (1983).

[3] Alexander et al. (2008b).

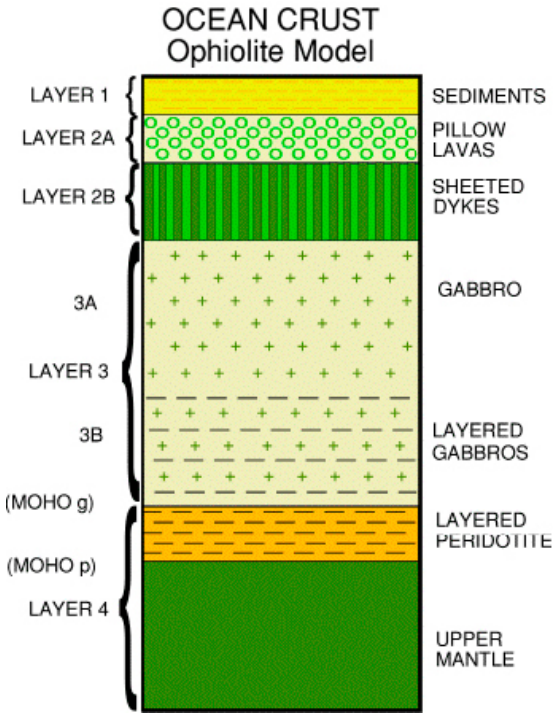

Figure 2-12. *Schematic lithographic section of an ophiolite. The 'sediments' at the top of the sequence include bentonites at the base.*

Figure 2-13. *Alkaline groundwater flowing from a fracture in the gabbro of the Zambales ophiolite, Philippines. The groundwater here has a pH of 11.1 and releases a mixture of hydrogen (up to 3,500 ppm) and methane (up to 5,000 ppm) bubbles (misty area in top corner of the pool).*

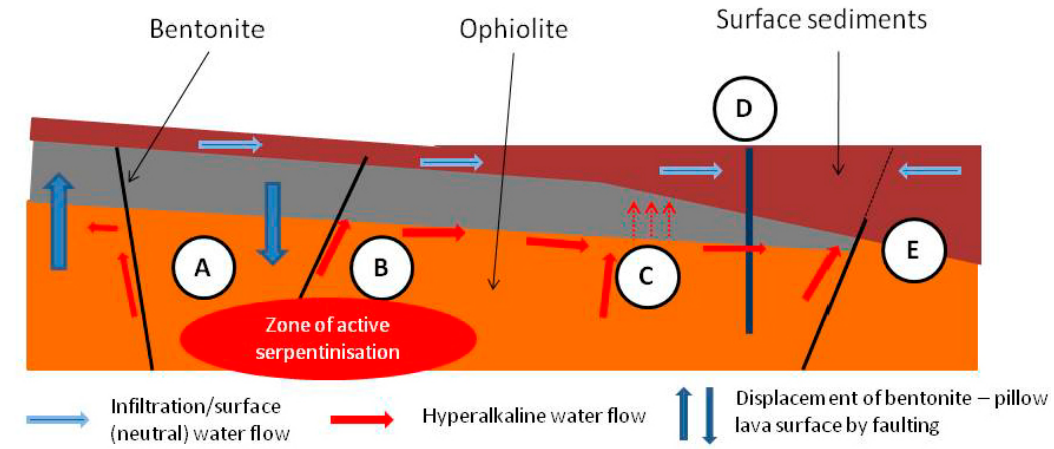

A – Active serpentisation producing hyperalkaline groundwater and H_2/CH_4 gas
B – High pH water under bentonite, neutral water above it
C – Potential interaction of high pH waters with base of bentonite (diffusion into it?)
D – Borehole through bentonite and into pillow lavas
E – Dispersed release of high pH waters into deep sediments?

Figure 2-14. *Conceptual model for alkaline groundwater/bentonite reaction (from Alexander et al. 2012).*

The preliminary results indicate that bentonite reaction would appear to be minimal and that the bentonite retains its swelling capacity and acts as a seal, effectively trapping the alkaline groundwaters below it. In Cyprus (Figure 2-15), the base of the bentonite shows a very small degree of reaction, with the smectites producing palygorskite as the reaction product (see Alexander et al. 2012 for details). This is consistent with observations from other natural alkaline systems such as soils (e.g. Singer 1979) and limited laboratory data (Moyce et al. 2014). These laboratory experiments indicate that palygorskite can develop relatively rapidly and in a closed system which is perhaps not unlike that present below the bentonite in Cyprus, suggesting a common reaction sequence which would be worth investigating further. Of importance is that less than a few percent of the bentonite has been reacted to palygorskite over a period of several hundred thousand years and that, otherwise, the bentonite appears to have retained its isolating properties regardless of the reaction. In the Philippines (Figure 2-16), no alkali reaction products have yet been reported, despite the confirmed presence of alkali groundwaters below the bentonite (e.g. Arcilla et al. 2009). Recent work from the open (and advective) system at Searles Lake (e.g. Savage et al. 2010b) reports different reaction products, but this may be a reflection of the very low solid/liquid ratio of this system. The repository environment would appear to be much better represented by the Cyprus and Philippine studies.

Figure 2-15. *Drilling through the bentonite at Parsata, Cyprus. Samples are recovered throughout the bentonite column (up to 40 m thick here) and at the base of the column, overlying the pillow lavas which are the source of the alkali groundwaters.*

Figure 2-16. *The Bigbiga study site, Luzon, Philippines. The pillow lava source rocks for the alkali groundwaters are exposed in the foreground (note groundwater seeping out onto the surface from fractures in the pillow lavas) with the lush green grass in the middle ground growing on the bentonite.*

2.3 URL studies on potential EBS and geosphere perturbations by cementitious alkaline leachates

2.3.1 Potential impact on the host rock

To date, little URL work has been focussed on examining the potential impact of alkali leachates on a fractured crystalline host rock. Of these, the HPF (Hyperalkaline Plume in Fractured Rock) experiment at the Grimsel Test Site was certainly the largest in terms of cost, effort and duration (see http://www.grimsel.com/gts-phase-v/hpf/hpf-introduction for details). Although the supporting laboratory experiments have been published in detail (see Section 2.5), only preliminary field data are available (Mäder et al. 2006). These indicate that sealing of fractures 'disrupts' the pre-existing flow conditions, with formation of secondary phases in the experimental shear zone inducing a decrease in fracture transmissivity and a focussing of flow in the remaining open porosity.

However, the data from HPF must be treated with caution as the pressure in the groundwater injection system was constantly increased to maintain constant flow conditions. In the case of a repository, the hydrogeologic system will probably be largely dominated by the relative elevations of the recharge and discharge regions, and these elevations can be assumed to remain largely constant over the timescales of interest[9]. This situation is best represented by constant-gradient conditions, which means that when permeability decreases (at constant gradient), flux will also decrease. In the case of the HPF supporting laboratory studies on a fractured rock core (see Mäder et al. 2004, 2006, Soler et al. 2006), a constant gradient was applied during infiltration of alkaline leachates and the production of secondary phases led to a decrease in hydraulic conductivity of 20-fold (over a 9 month period). This is discussed further in Section 2.5.

The LCS (Long-term Cement Studies: see http://www.grimsel.com/gts-phase-vi/lcs/lcs-introduction) is currently ongoing and takes a step further than HPF insofar that the approach has been to move towards more repository relevant boundary conditions. Instead of injecting alkaline fluids directly into a highly transmissive water conducting fracture as in HPF, cement grout has been injected into a much lower transmissivity system (see Figure 2-17). Following long-term leaching of the cement and presumed reaction of leachates with the host rock, the affected rock zone will be over-cored and mineralogical and physical changes will be defined in the laboratory. One zone was recently over-cored three years after the cement had been emplaced and the zone of contact between the cement and the host rock studied for signs of reaction. A preliminary evaluation showed that no reaction of the host rock could be observed, although the investigators noted that this may, in part, be due to limited grout penetration into the fracture (only "…a few millimetres.") and therefore the presence of a limited volume of cement for reaction. Although a cement grout formula was used and high pressures were employed, LCS is not a grout experiment, rather it has different basic aims (see http://www.grimsel.com/gts-phase-vi/lcs/lcs-aims for details). Therefore, the overall injection procedure did not follow standard grouting parameters and procedures (cf. discussion in Arenius et al. 2008). And, as such, the relevance of the above noted results to the scope of this report is probably limited and they should be treated with care.

Of perhaps more direct relevance to this project is the work that Posiva has been carrying out on various grout formulations at the ONKALO facility (e.g. Rautio 2005, Reiman et al. 2006) at Olkiluoto in Finland. When grout is used to seal fractures, the "…grout forms an adhesive bond, a mechanical lock, and a compression seal with the walls of the crack it fills. This prevents any water from bypassing the grout and migrating between it and the walls of the crack." (Bechtel/Parsons Brinckerhoff 2005), meaning that grouted systems should remain tight. However, Cama et al. (2012) in an experimental follow-on from a modelling study (Soler 2010) of grout/host rock reaction reported much less actual reaction between the grout and the ONKALO gneiss than expected, but the reaction time was only 19 days and the very low porosity (1%) made observation of any reacted phases very difficult. Interestingly, it has been noted that the LCS grout showed more intense groundwater/grout reaction at the grout/host rock interface than elsewhere in the grout, suggesting that the grout/host rock bond in this case was not as strong as normal. This may simply be a reflection of the fact that LCS is not a grouting experiment *per se* (see http://www.grimsel.com/gts-phase-vi/lcs/lcs-introduction for details), so the cases are not directly comparable.

[9] Obviously, this will not be the case in an area of significant uplift or erosion or at coastal sites: see McKinley and Alexander (2009) for discussion.

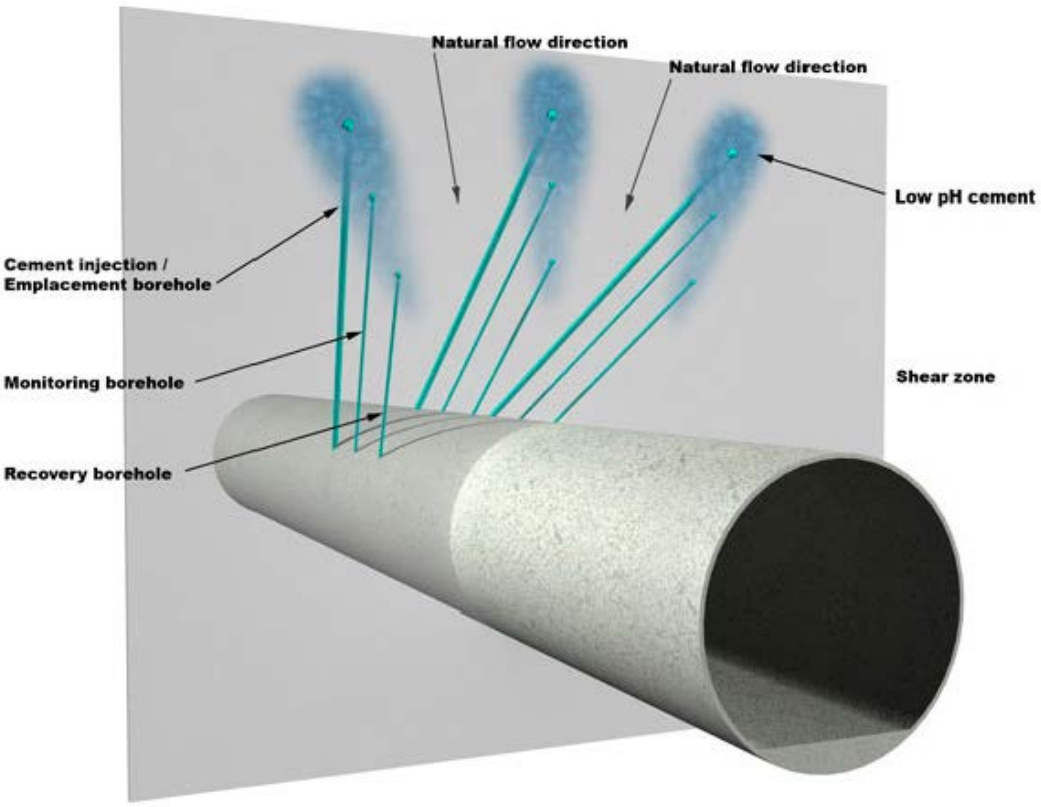

Figure 2-17. *Conceptual model of the LCS project. Solid cement sources will be emplaced within a lower transmissivity fracture in the Grimsel URL and any subsequent alkali leachate release will be observed via the monitoring boreholes. Finally, after a period of some years, the affected flow system will be over-cored an examined in detail in the laboratory. Image courtesy Nagra.*

When assessing the potential impact of grouts in the ONKALO facility on the Olkiluoto repository EBS, Vieno et al. (2003) quoted examples of low pH values observed in the vicinity of existing grouts in Olkiluoto and the Whiteshell URL as indications that grouts will not produce alkaline leachates. As these grouts had been in place for a relatively short time, it is to be expected that they will not be actively leaching to any significant degree, especially if they have done the job required of them (i.e. to block groundwater flow). In comparison, initial *in situ* pH values of >12 have been reported by Ahokas et al. (2006) for fresh low-alkali cement grout in borehole ONK-KR3, in agreement with the results of leaching experiments where even some low-alkali grouts have initial high pH leachates (e.g. Bodén and Sievänen 2006, NEA 2012). More recently, monitoring of the groundwater around recently grouted zones in ONKALO have shown groundwater pH levels of 8 for low-alkali grouts and 10–11 for OPC grouts. Nilsson et al. (2011) also reported that "….four samples from borehole KFR83 (*in SFR-1*) collected in 1987 showed high pH values and an unusual groundwater composition and were classified as unsuitable for modelling (Dataset II) due to possible contamination from cement, despite that this borehole is far from any known grouting location." Currently, SKB are collating examples of elevated pH in groundwater samples from all of their deep boreholes, including a heavily grouted zone at the Äspö URL. Until these sites can be further examined and a mechanistic understanding of the process obtained, it is recommended that a conservative approach be maintained and it is assumed that OPC grouts will produce alkaline leachates of some form (see also discussion below).

In a recent modelling study (Soler 2010, Soler et al. 2011a) it was assumed that groundwater flows around a grouted section of a fracture (Figure 2-18), rather than interacting fully with the grout. The grout (both OPC and low alkali types were considered) simultaneously hydrates and leaches, releasing alkaline leachates and solutes (mostly K, Ca, SO_4) into the flowing groundwater, potentially causing the formation of an ADZ.

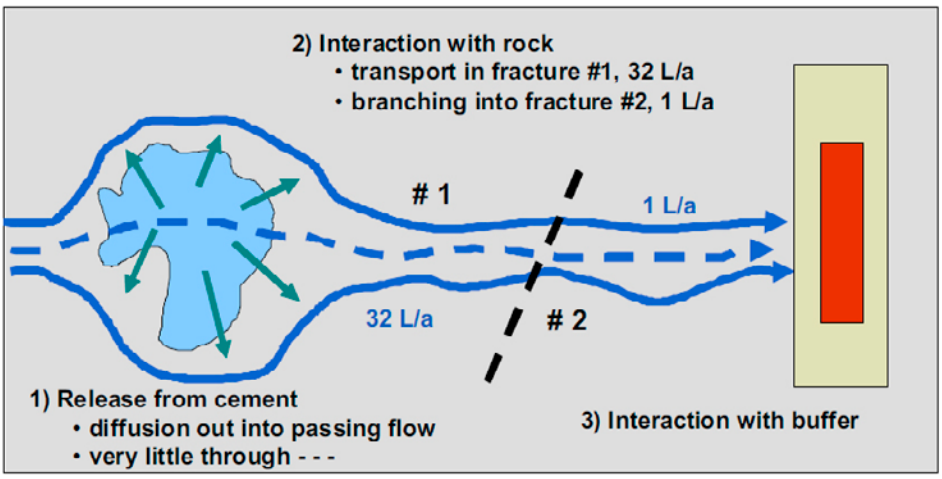

Figure 2-18. *Diagram showing the concept behind the calculations in Soler (2010). Only the processes on the left half of the diagram (flow of water around the grout and down the fracture) were included in the simulations.*

Here, Soler (2010) found higher pH values in the grout for the OPC case and these are explained by the composition of the grout and the evolution of porosity at the grout-water interface. The OPC grout has a lower silica fume content, which favours the presence of a C-S-H gel with a higher Ca/Si ratio, resulting in a higher pH in the grout. Also, there is effective sealing of porosity at the grout-water interface in the OPC case due to the precipitation of secondary ettringite and calcite. This sealing effect (secondary calcite) is less important in the low alkali grout case whereas the effective sealing in the OPC case causes a slower diffusive exchange between the grout and the open fracture. The modelled groundwater pH in the vicinity of the grouts is similar to that observed around two boreholes in ONKALO (Figure 2-19), leading Soler (2010) to note that "….results suggest that the main processes responsible for the evolution of pH are being captured." Nevertheless, model development continues and, more recently, Soler (2011) showed improved fit for pH monitoring data (for the low-alkali cement grout) when including Mg in the system.

Regardless of the precise nature of the grout/host rock contact, grouts, as with all concretes, degrade, so much so that the ASTM (American Society for Testing and Materials) have 8 standards to assess chemical reaction in grouts (including, for example, standard C1105-08a Standard Test Method for Length Change of Concrete Due to Alkali-Carbonate Rock Reaction) and 6 standards on concrete resistance to fluid penetration (see http://www.astm.org/Standard/index.shtml for additional examples).

Lagerblad (2001, 2005) pointed out that c/w ratios of < 0.4 are generally required to guarantee leach-resistance and, with a c/w of around 0.25 to 1.25 (e.g. Ahokas et al. 2006, Orantie and Kuosa 2008, Sievänen et al. 2006), it is to be expected that some of the grouts used in ONKALO and under consideration for Forsmark will be leachable, at least over the longer term.

Arenius et al. (2008) noted that the higher pH values observed in boreholes ONK-KR3 (low alkali cement grout) and ONK-KR4 (OPC grout) compared to the other drillholes (Figure 2-20) probably result from two reasons:

- these were the only two drillholes where grout was observed in the drill core,
- lower water flow rate from these holes allowed a longer time for cement-water interaction.

Interestingly, the flow rate has not increased during the monitoring interval, so the decrease in pH cannot be explained by the dilution effect of increased flow and is presumably due to limited availability of easily soluble phases. Boreholes ONK-KR1 and ONK-KR2 were also drilled near grouted zones and the absence of the initial high peak may have been due to a delay in initiation of monitoring or too great a distance from the grouted zone (certainly there was lack of visible grout in those drillholes (Arenius et al. 2008)). Nevertheless, there is clearly a lack of significant perturbation to the groundwater pH in these two boreholes although observation would have been more valuable if more information on the actual proximity of the grout were available. Posiva has also carried out numerous other tests on grout formulation etc (e.g. in a tunnel in Helsinki (Sievänen et al. 2005)), but it is not known if any follow-up measurements on the groundwater pH have been made at these sites.

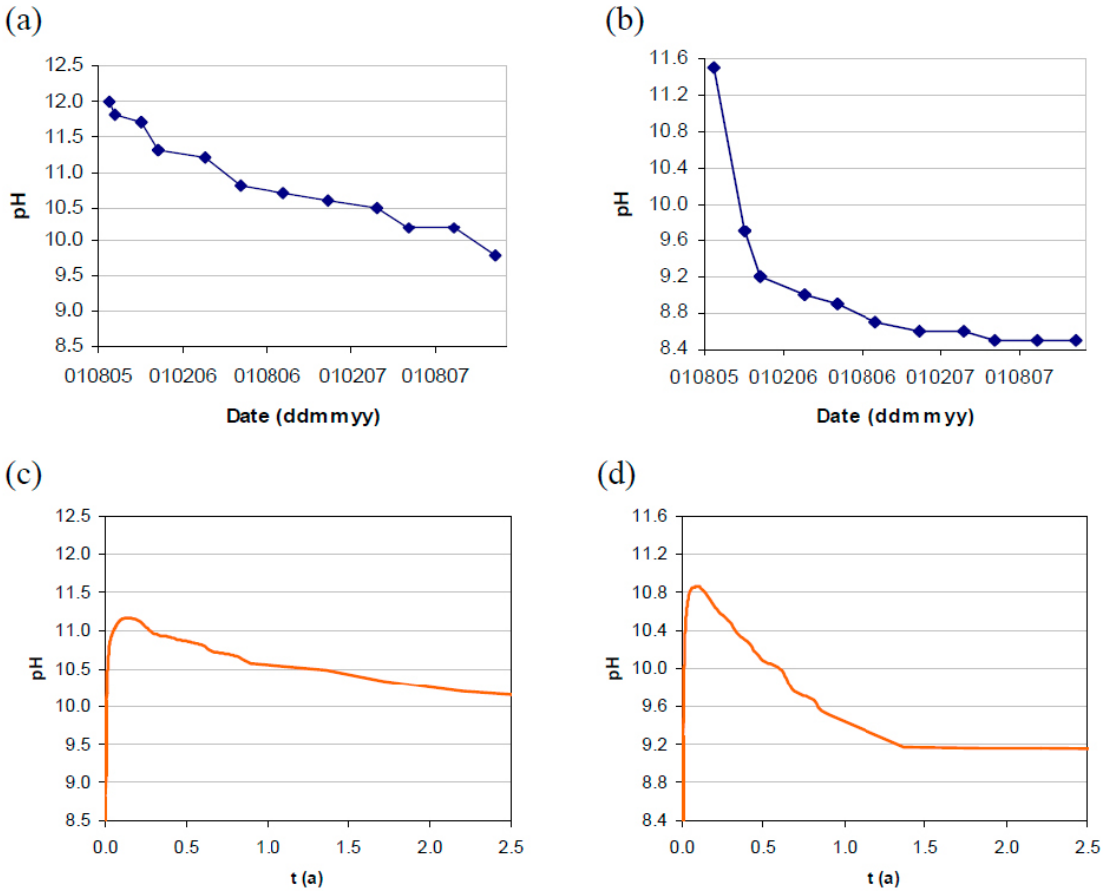

Figure 2-19. *Comparison of the groundwater pH variance with time in (a) borehole ONK-KR4 with OPC grout, (b) borehole ONK-KR3 with low alkali grout, (c) model output for OPC grout and (d) model output for low alkali grout (Soler 2010). Note that the pH and time scales are not the same for all graphs.*

Vieno et al. (2003) suggested that low leach rates were standard and that the observations from the Maqarin natural analogue site were anomalous because the "...groundwater percolates through a thick, more or less homogenous zone of cement minerals in a pistonlike flow pattern...", so explaining the observed high pH values. In fact, the natural cement (a pyrometamorphosed, kerogen-rich limestone) is actually a highly effective aquiclude across most of its terrain, with very rare (i.e. only two sites are known worldwide) flow through the cement in discrete fractures with transmissivities of 10^{-11} to 10^{-12} $m^2 s^{-1}$ (Degnan et al. 2011). Reaction in the cement is confined to a relatively thin zone immediately adjacent to the water-conducting fractures (Figure 2-21 and Figure 2-22) and, despite this, produces a leachate saturated in portlandite (with a maximum measured *in situ* pH of 12.9 where 'young' leachates were accessed, the highest ever reported for a natural groundwater).

Vieno et al. (2003) also suggested that any grout induced ADZ at ONKALO would be minimised by dilution with other groundwaters and, although dilution has not been directly assessed at the Maqarin site, data mining the existing extensive database could provide an indication of the applicability of this mechanism to other host rocks. It is of note, however, that "The results of the (HPF) field experiment point to a channelling effect which severely limits mixing of the injected high-pH solution with background Grimsel groundwater at late stages of the experiment." (Soler et al. 2006). In other words, it seems likely that dilution may also not be as robust a mechanism for minimising the effects of the alkaline plume, probably in part due to the changes to the flow system which occur during leachate/ fracture interaction.

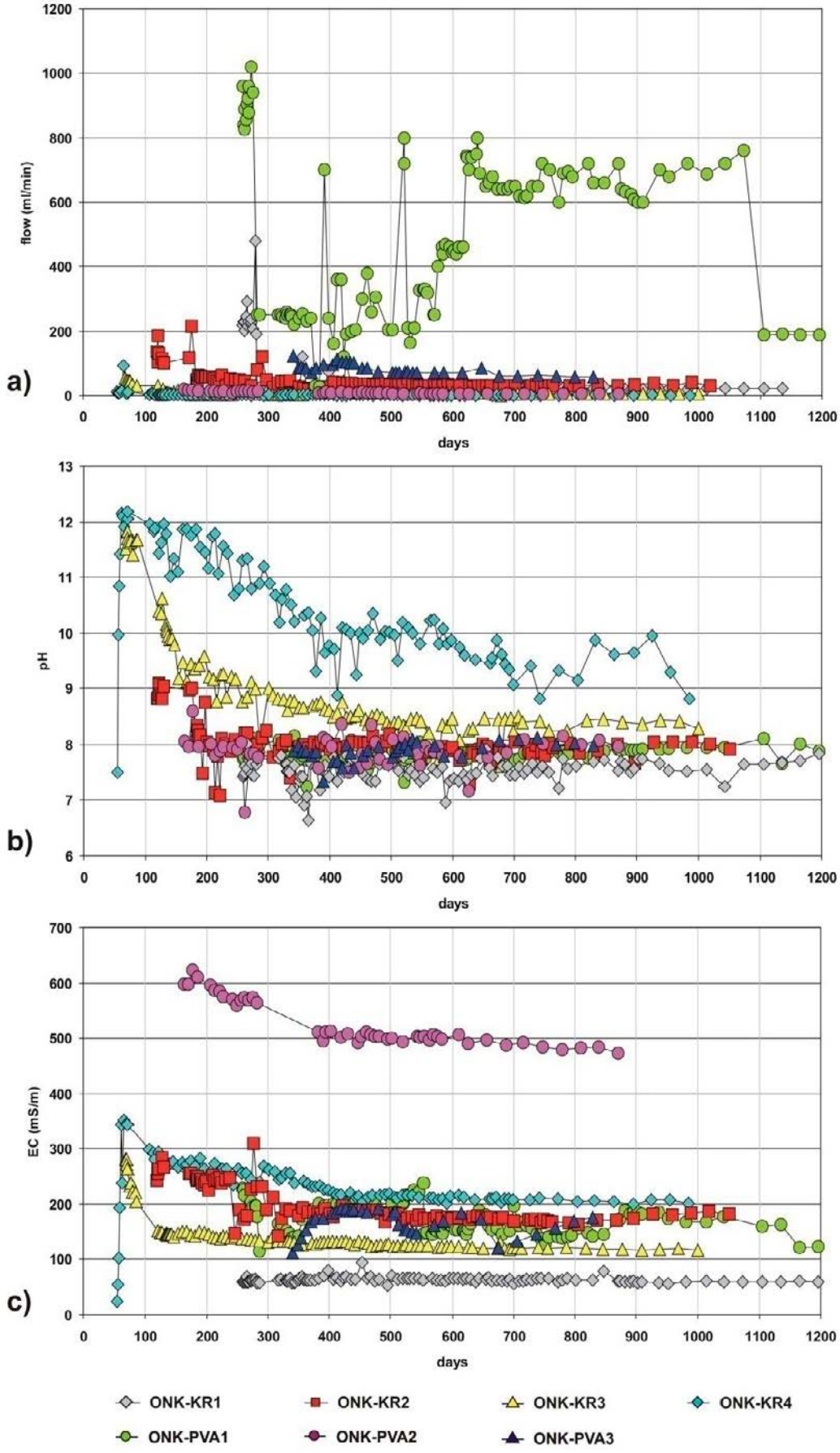

Figure 2-20. *Temporal variation of a) flow rate, b) pH and c) EC since the start of grouting in monitored drillholes at ONKALO. Days refer time after grouting or excavation of each drillhole (Arenius et al. 2008).*

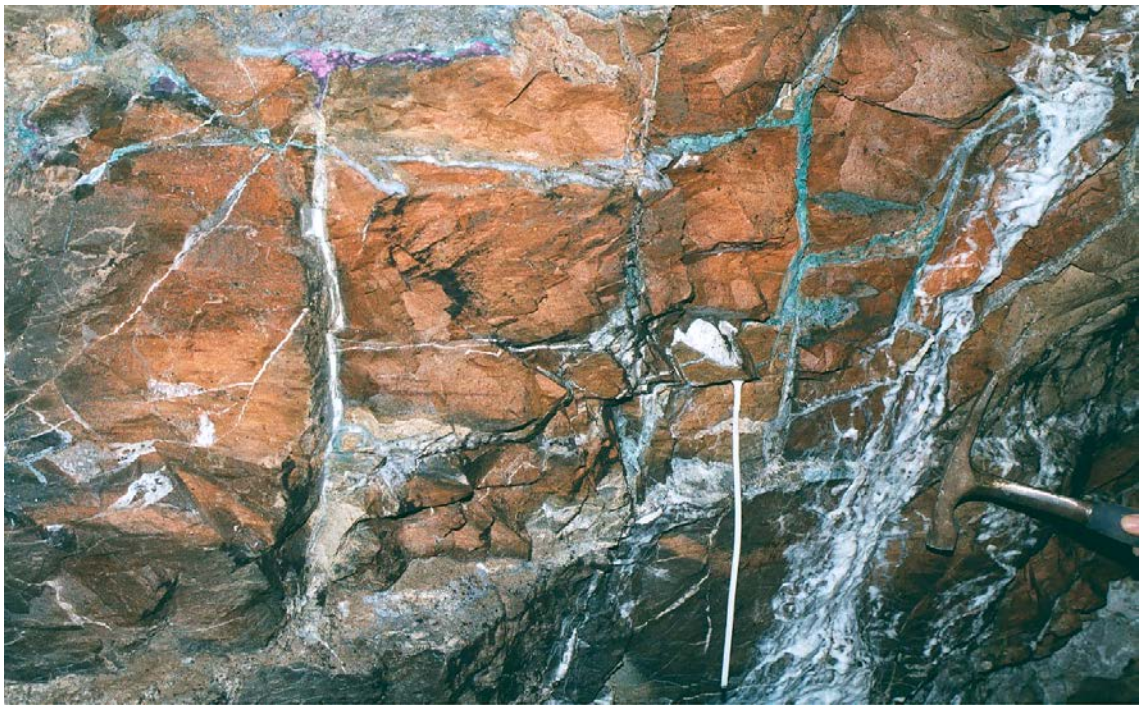

Figure 2-21. *Sealed fractures in the natural cement zone at the Maqarin site in Jordan (note field hammer at bottom right for scale). The zone of interaction in the cement is relatively narrow (Pitty and Alexander 2011).*

Figure 2-22. *Sealed fracture from the natural cement zone at the Daba site in central Jordan (site details in Pitty and Alexander (2011)). The knife is 8 cm long and the white material at the top of the sample is calcite fracture fill with the bleached zone in the black cement indicating the leached zone. Image courtesy H. Alexander Photogenics.*

2.3.2 Potential impact on the bentonite

There have been numerous URL experiments examining the *in situ* behaviour of bentonite and a non-exhaustive list includes:

ABM: The Alternative buffer materials (ABM: SKB (2011)) project is looking at a range of altenative (to SKB's current standard MX-80 bentonite) bentonites and includes an assessment of the impact of steel corrosion on the buffer behaviour.

CFM: The Colloid Formation and Migration (CFM: http://www.grimsel.com/gts-phase-vi/cfm-section/cfm-introduction) project is looking at the formation of bentonite colloids due to physical and chemical erosion and at any associated, colloid-facilitated radionuclide transport**.**

CRR: The Colloid and Radionuclide Retardation (CRR: http://www.grimsel.com/gts-phase-v/crr/crr-introduction) project investigated the migration behaviour of the radionuclides in the presence and absence of bentonite colloids by comparison of the eluted concentrations of the radionuclides and colloids from the flow field.

ECOCLAY-II: The Effects of Cement on Clay Barrier Performance – Phase II **(**ECOCLAY-II: (ECOCLAY 2005)) focussed on many aspects related to cement degradation, clay alteration and the performance assessment of the potential effects of an alkaline plume on clay properties.

ESDRED-module 1: The Engineering Studies and Demonstration of Repository Designs (ESDRED: http://www.esdred.info/module1.htm) project consists of six work modules and module 1 is looking into the design and construction of buffers for a horizontal disposal drift. The buffers include sand-bentonite mixes which are in contact with a variety of cementitious materials.

ESDRED-TEM: The Test and Evaluation of Monitoring Systems (TEM: http://www.grimsel.com/gts-phase-vi/tem/tem-introduction) is part of the EU ESDRED (http://www.esdred.info/) and MoDeRn (http://www.modern-fp7.eu/home/) projects. TEM aims to investigate the efficiency of an existing wireless magneto-inductive (MI) transmission technique and evaluate seismic tomography as a non-intrusive monitoring technique. The design includes shotcrete in contact with bentonite (Figure 2-23) in the GTS URL tunnel system.

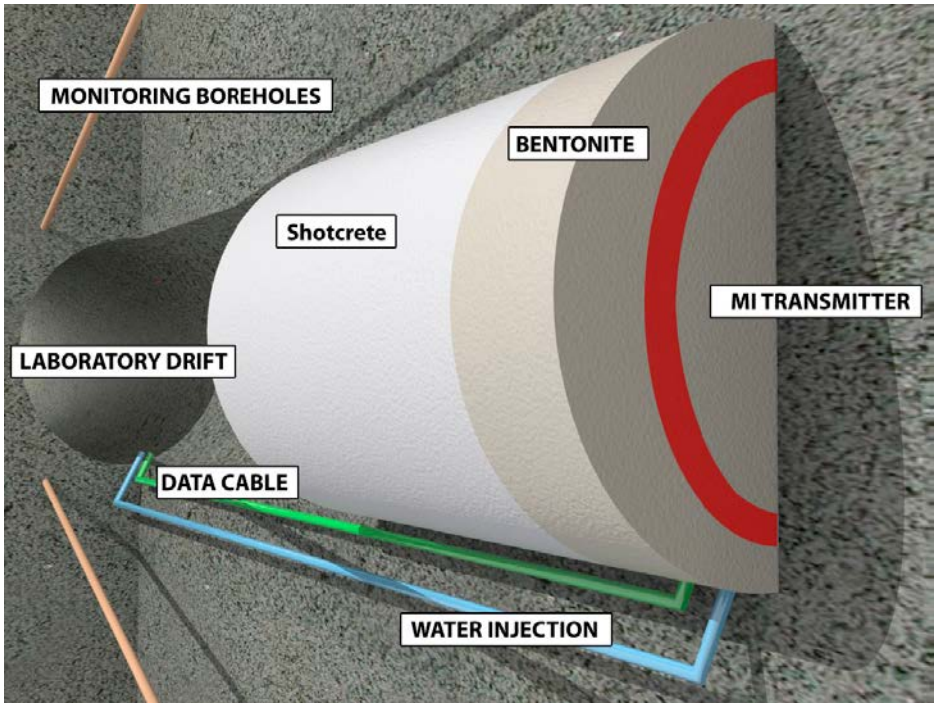

Figure 2-23. *The ESDRED-TEM project experimental layout. Image courtesy DMMultimedia.*

FEBEX I and II: The Full-scale Engineered Barriers Experiment (FEBEX; http://www.grimsel.com/gts-phase-v/febex/febex-i-introduction-) aimed to test the feasibility of manufacturing and assembling an EBS based on the Spanish SF disposal concept for a crystalline host rock (see Figure 2-24) and developing methodologies and models for assessment of the thermo-hydro-mechanical (THM) and thermo-hydro-geochemical (THG) behaviour of the EBS.

FEBEXe: The Full-scale Engineered Barriers Experiment extension (FEBEXe: http://www.grimsel.com/gts-phase-vi/febexe/febexe-introduction) is focussed on gaining a better understanding of bentonite resaturation, bentonite thermal conductivity and the impact of steel canister corrosion on the bentonite performance.

FORGE: The Laboratory Column Experiment (FORGE: http://www.grimsel.com/gts-phase-vi/forge/forge-introduction) is focussed on maximising the ability of repository tunnel plugs and seals (which include bentonite and sand-bentonite components) to increase the gas transport capacity of the backfilled tunnels without compromising the radionuclide retention capacity of the EBS.

GAST: The Gas Permeable Seal Test (GAST:) is examining the gas transport properties of the seals on repository tunnels and caverns. Both mortars and sand-bentonite barriers are under consideration (Figure 2-25).

GMT: The Gas Migration Test (GMT: http://www.grimsel.com/gts-phase-v/gmt/gmt-introduction) aimed to examine gas migration through the EBS, including the bentonite.

Lasgit: The Large-Scale Gas Injection Test (Lasgit: see Figure 2-26) is a full-scale *in situ* test designed to answer specific questions regarding the movement of gas through bentonite (SKB 2011).

Lot: The Long term test of buffer material (Lot) project is focussed on testing and validating models of the long-term behaviour of the bentonite buffer (SKB 2011), including buffer degradation processes (e.g. mineral redistribution and montmorillonite alteration) due to lomg-term heating.

Prototype Repository: The Prototype Repository aims to test and demonstrate appropriate parts of the Swedish repository design and construction processes (SKB 2011).

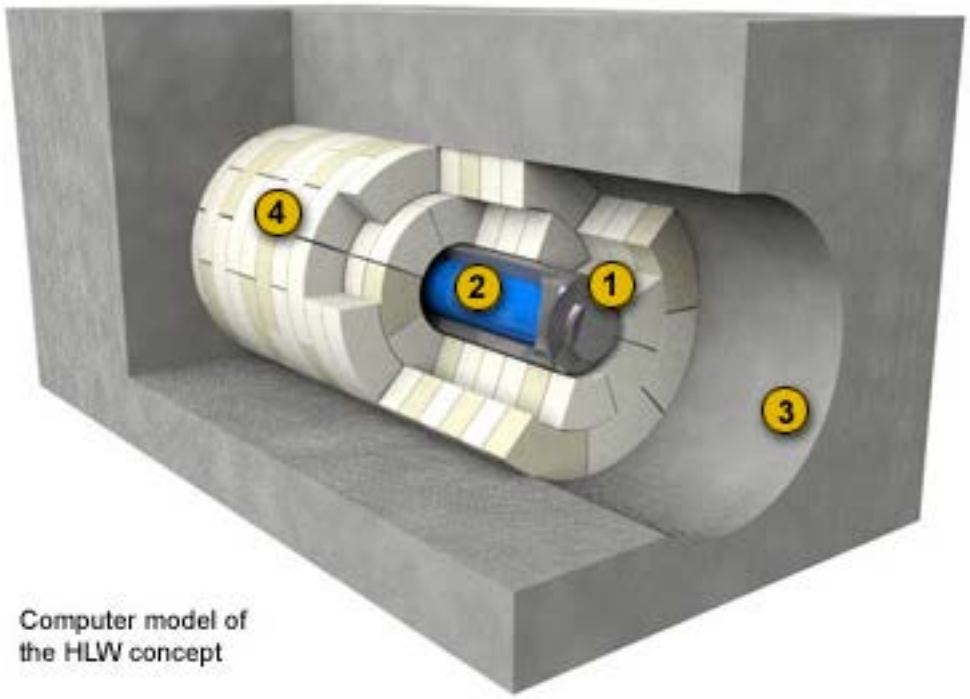

Figure 2-24. *Image of the FEBEX in situ experiment. Image courtesy Nagra.*

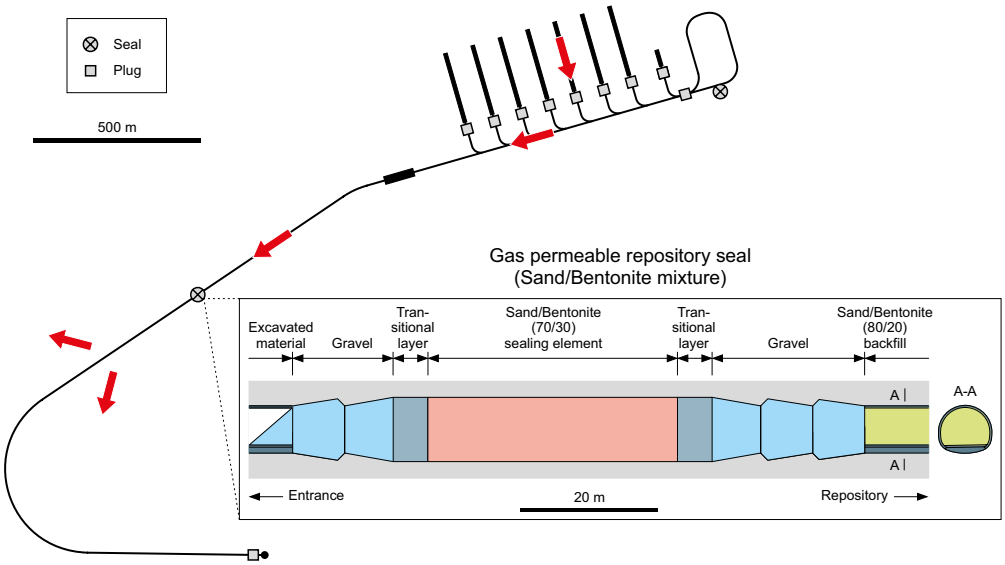

Figure 2-25. *Schematic diagram of the engineered gas transport system (EGTS) with detailed design drawing of repository seal (V4). Image courtesy Nagra.*

Figure 2-26. *The large scale gas injection test at the –420 m level in the Äspö URL (SKB 2011).*

This is clearly not an exhaustive list, but it is obvious that, outwith the ECOCLAY-II project, little has been done to examine the potential impact of cement leachates on bentonite. This is despite the fact that several of the above listed projects had bentonite and concrete in intimate contact and so some form of work could possibly have been initiated within the experiment (this is examined further in Section 2.6.3).

The overall conclusions of ECOCLAY-II were that, on the results of experiments carried out on compacted bentonite, "…indicate that the high pH front inducing mineral reactions on the smectite does not penetrate further than 5 cm, and the portlandite front with lower pH not further than 10–20 cm within a very long time span, up to 100,000 years." However, it was also noted that this penetration depth could be a significant part of the buffer for some designs and so this needs to be examined on a case-by-case basis. In the KBS-3H design, for example, the bentonite rings around the spent fuel container in the supercontainer are approximately 35 cm thick (Smith et al. 2008) whereas they are 31.5 cm thick in the KBS-3V design (SKB 2006) and are, as noted in Section 1.2, required to function for 1 Ma. As such, the ECOCLAY-II results are not encouraging, but it must be remembered that they are the product of short-term experiments and extrapolating them to repository timescales should be avoided.

2.4 Laboratory studies on potential EBS and geosphere perturbations by cementitious alkaline leachates

2.4.1 Potential impact on the host rock

Based on currently available experimental data (Table 2-4), it is not simple to predict the likely secondary phases which could be produced at Forsmark if cement leachates react with the host rock because there are a wide range of experimental variables present in the studies cited in the table. These include differences in host rock mineralogy, the cement leachate chemistry, rock-water ratios, closed vs open systems, temporal differences etc[10] and a lack of an agreed, standard experimental methodology has been criticised in previous laboratory studies of cementitious systems (e.g. Alexander and Möri 2003, Swanton et al. 2010). By comparison with the data available in Table 2-4, it seems that C-S-H, C-A-S-H and a wide range of zeolites would all be expected, but it is difficult to be more precise due to the primary mineral heterogeneity in the Forsmark host rock. For example, Sandström et al. (2008) reported a wide range of minerals in the Forsmark fracture material, noting "Chlorite (usually associated with corrensite) together with calcite are by far the most common fracture minerals. The relative abundance of additional fracture minerals is as follows;

laumontite > quartz, adularia, albite, clay minerals > prehnite, epidote > hematite and pyrite.

"Some minerals may be more common in specific intervals or at shallow depths (e.g. asphaltite, analcime and goethite). Other identified minerals (e.g. apophyllite, fluorite, galena) have only been found as minor occurrences. The most common clay minerals are corrensite > illite > mixed layer clays > smectite > kaolinite, vermiculite and other swelling clays. No carbonates other than calcite have been identified and no sulphate-minerals have been detected except for barite which only occurs in very small amounts (e.g. as inclusions in galena). Pyrite makes up more than 99% of the identified sulphides, but galena, chalcopyrite and sphalerite have also been identified. The confidence is high that all major fracture mineral phases within the Forsmark site have been identified."

An equally wide range of primary mineralogy has been reported for the rock matrix at Forsmark (Sandström and Stephens 2009), complicated by the fact that no fewer than 15 major rock types have been recognized for the site (Table 2-5). Although the modal volumes vary significantly between and, due to structural and other differences, within rock types, the following minerals are generally present:

quartz, K-feldspar, plagioclase (including sausseritised plagioclase), biotite, amphibole, muscovite, pyroxene, olivine, serpentine[11], chlorite, epidote, titanite, calcite, allanite and opaque phases.

Interestingly, Bateman et al. (2001a) reported the presence of C-S-H, C-A-S-H, C-K-S-H and C-K-(A)-S-H secondary phases on reacting crushed Äspö granodiorite in flow through experiments (Figure 2-27) with 'young' leachates. When this work was carried out, the Forsmark site had not yet been identified as a potential repository site and so Äspö granodiorite was a reasonable choice for a generic study. This is no longer the case and similar experiments should now be carried out on Forsmark fracture and rock matrix material.

[10] O. Karnland noted, for example, that batch experiments and tests on compacted bentonite show different release rates for silica and this may be explained by ion-equilibrium established between the hydroxide ions and the montmorillonite counter-ions in the pore fluid of compacted bentonite.

[11] Although only found in metamorphosed ultramafic rock (SKB code 101004, Table 2-5), this implies the presence of natural alkaline waters in the rock at some point in the past (cf. Moody 1976)

Table 2-4. Summary of some cement leachate/host rock and cement leachate/bentonite interaction experimental studies in the literature. For comparison, a range of NA studies are also included.

Reference	Rock type	Experimental set-up	Leachate	Phase alteration	Comments
Chermak (1992)	Opalinus Clay, Switzerland	Laboratory batch experiments at 150, 175 and 200°C for 40 days	0.1 and 0.01 M NaOH	Formation of analcime, followed by vermiculite and finally Na-rectorite	Closed system, temperatures not repository relevant
Chermak (1993)	Opalinus Clay, Switzerland	Laboratory batch experiments at 150, 175 and 200°C for 40 days	KOH	Phillipsite and then K-feldspar	Closed system, temperatures not repository relevant
Kawano and Tomita (1997)	Obsidian glass	Batch	0.001 to 0.5 N NaOH and KOH solutions at 150 and 200°C ~ for 1 to 30 days	As pH increased, smectite, phillipsite and rhodesite in NaOH and smectite, merlinoite and sanidine in KOH solutions	Closed system, temperatures not repository relevant Table 4 in paper lists numerous batch experiments starting with glass, tuffs, pumice et al. producing zeolitic reaction products
Milodowski et al. (1998a)	Basalt (incl. glass), Maqarin, Jordan	NA (porous media flow)	pH 12.9 groundwater (i.e. higher KOH/NaOH composition)	Ca-K-Na zeolite and amorphous zeolitic gel precursor with compositions intermediate to mordenite and dachiardite	No C-S-H/C-A-S-H minerals observed – may be due to significant buffering capacity of the mixed-lithology matrix around the basalt
Milodowski et al. (1998a, b, 2001)	Marl (clayey limestone), Maqarin, Jordan	NA (fracture flow)	pH 12.5 groundwater	brucite, hydrotalcite, C-S-H hydrogels, ettringite-thaumasite and poorly crystalline Mg-rich silicate (possibly akin to sepiolite or talc-like alteration products).	‘early’, weakly buffered groundwaters
Milodowski et al. (1998a, b, 2001), Cassagnabère et al. (2001)	Marl (clayey limestone), Maqarin, Jordan	NA (fracture flow)	pH 12.5 groundwater	‘early’ precipitate of high-Si zeolites such as mordenite or dachiardite, ‘later’ considerably more calcic and similar in composition to wairakite, laumontite and leonhardite	Only appear following buffering of the alkaline groundwaters
Milodowski et al. (1998a, b)	Marl (clayey limestone), Daba, Jordan	NA (fracture flow)	Unknown (fossil site) but, by analogy with other sites, near-neutral	smectitic clay followed by amorphous or opaline silica	
Rassineux et al. (2001)	Marl (clayey limestone), Kyushaym Matruk, Jordan	NA (diffusion front)	Unknown (fossil site) but, by analogy with other sites, portlandite buffered (ca pH 12.5)	Unaltered rock contains mixed layer illite/smectite (20:80). Increased reaction decreases smectite content to 60% near the cement. Locally, zeolites present.	More clay-rich marl than at Maqarin
Bateman et al. (2001a, b)	Borrowdale Volcanic Group, Cumbria, UK	Leachates injected through columns of crushed rock	1. ‘young’ (pH 13.5, high K, Na) 2. ‘evolved’ (pH 12.5, portlandite buffered)	one or more of C-S-H, C-A-S-H, C-K-S-H and C-K-(A)-S-H secondary phases	No evidence of zeolites

Reference	Rock type	Experimental set-up	Leachate	Phase alteration	Comments
Bateman et al. (2001a, b)	Aspö Granodiorite, Aspö URL, Sweden	Leachates injected through columns of crushed rock	1. 'young' (pH 13.5, high K, Na) 2. 'evolved' (pH 12.5, portlandite buffered)	1. one or more of C-S-H, C-A-S-H, C-K-S-H and C-K-(A)-S-H secondary phases	No evidence of zeolites
Bateman et al. (2001a, b)	Palfris Marl, Oberbauenstock, Switzerland	Leachates injected through columns of crushed rock	1. 'young' (pH 13.5, high K, Na) 2. 'evolved' (pH 12.5, portlandite buffered)	one or more of C-S-H, C-A-S-H, C-K-S-H and C-K-(A)-S-H secondary phases. Clays dissolve precipitating C-K-(A)-S-H.	No evidence of zeolites
Bateman et al. (2001a, b)	Opalinus Clay, Mont Terri URL, Switzerland	Leachates injected through columns of crushed rock	1. 'young' (pH 13.5, high K, Na) 2. 'evolved' (pH 12.5, portlandite buffered)	one or more of C-S-H, C-A-S-H, C-K-S-H and C-K-(A)-S-H secondary phases. Clays dissolve precipitating C-K-(A)-S-H.	No evidence of zeolites
Bateman et al. (2001a, b)	Bituminous Marl, Maqarin, Jordan	Leachates injected through columns of crushed rock	1. 'young' (pH 13.5, high K, Na) 2. 'evolved' (pH 12.5, portlandite buffered)	one or more of C-S-H, C-A-S-H, C-K-S-H and C-K-(A)-S-H secondary phases	
Bateman et al. (2001a, b)	Quartz	Leachates injected through columns of crushed mineral	1. 'young' (pH 13.5, high K, Na) 2. 'evolved' (pH 12.5, portlandite buffered)	Non-crystalline C-S-H gel	No evidence of zeolites
Savage et al. (2001a, b)	Analcime (minor component of bentonite)	Batch and fluidised bed experiments at 25, 50, 70 and 90°C	KOH solutions (i.e. 'young') buffered between pH 10 and 13	Analcime transformed to leucite by uptake of K at all pH values, but to a greater degree with higher pH. Leucite may then transform to K-feldspar	Modelling work in Savage et al. (2001b) suggests 60% of a 1 m thick bentonite layer could be converted to zeolites/sheet silicates in 1000a
Tajima et al. (2003)	Kunigel V1	Batch experiments at 50, 80 and 100°C	1. K/NaOH+$CaOH_2$ (pH 13) 2. $CaOH_2$ (pH 10.5–12.5) 3. 'low alkaline cement' (pH 11)	1. and 2. montmorillonite dissolved, C-S-H, C-A-S-H formed 3. Na-montmorillonite to Ca-montmorillonite	Increased pH and temp induced greater alteration to C-S-H, C-A-S-H. None observed with low-alkali cement leachate
Vuorinen et al. (2003, 2004, 2006)	MX-80 bentonite and Olkiluoto mica gneiss	Batch (continous agitation) up to 540 days and flow-through experiments up to 560 days	Fresh and saline alkaline waters (12.5–13.5)	Microcline, plagioclase, cordierite (+/– hornblende) leached, sericite/illite, epidote (saussurite) minor C-S-H precipitated	Crushed rock is not representative of the fracture minerals (i.e. calcite, pyrite, pyrrhotite, graphite and clays) likely to be encountered by the alkaline leachates in the host rock

Reference	Rock type	Experimental set-up	Leachate	Phase alteration	Comments
Karnland et al. (2004, 2007)	MX-80 bentonite	Diffusion cells	0.1, 0.3 or 1.0M NaOH,1M KOH, 0.02M $Ca(OH)_2$ (saturated), 1M NaCl and H_2O	Cristobalite/quartz and montmorillonite are dissolved (the latter incongruently)	Bentonite swelling pressure was strongly reduced by exposure to 0.3 (pH 13.3) and 1.0 M (pH 13.7) NaOH solutions. The reduction seems to be due to an instant osmotic effect, and to a continuous dissolution of silica minerals leading to mass loss.
Sato et al. (2004)	Na montmorillonite	Flow through cell	0.3M NaOHNaCl or 0.3M KOH-KCl, 30–70°C for 7–10 days	Observed solution chemistry to define dissolution rates	Derived rate law and kinetic parameters for smectite dissolution
Sato et al. (2004)	Na montmorillonite	*In situ* within AFM chamber	0.3M NaOH at 25°C for 1.5 hours and 2–8 days	Observed temporal changes in mineral particle size	Particle sizes measured by AFM during reaction. Kinetic parameters were derived
Sato et al. (2004)	Na montmorillonite	*In situ* within AFM chamber	1.0M NaOH – NaCl at 25°C for < 1 day	Observed temporal changes in mineral particle size	Particle sizes measured by AFM during reaction. Kinetic parameters were derived
Sato et al. (2004)	Na montmorillonite	Batch	0.3M NaOH at 50°C for 6 to 33 days	Initial and final mineral particle sizes	Particle sizes measured by AFM after reaction. Kinetic parameters were derived
Sato et al. (2004)	Na montmorillonite	Titration	Acid added to pH = 4, Alkali added to pH = 10 at 30 to 70°C for undefined time	pH observed as a function of time	Dissolution mechanisms studied
Yamaguchi et al. (2004)	Compacted sand and Namontmorillonite (Kunigel V1)	Batch	Na-Cl-OH water, 0.1, 0.3, 1 M NaOH at 50 to 170°C for 4 to 8 weeks	Observed the remaining mineralogy after reaction plus solution concentrations	Derived kinetic parameters
Yamaguchi et al. (2004)	Compacted sand and Namontmorillonite (Kunigel V1)	Flow through cell	0.5M and 10–5M NaOH at 10 to 90°C for 18 to 28 weeks	Observed mineral dissolution rates	Derived kinetic parameters
Wang et al. (2005, 2010)	Boom Clay, Belgium	Leachates injected through columns of Boom Clay	1. 'young' (pH 13.5, high K, Na) 2. 'evolved' (pH 12.5, portlandite buffered)	1. 'young' dissolved smectite, 2. 'evolved' released Si and Al to solution	1. 'young' increased hydraulic conductivity of the columns, 2. 'evolved' decreased it

Reference	Rock type	Experimental set-up	Leachate	Phase alteration	Comments
Mäder et al. (2006)	Grimsel Granodiorite, Grimsel URL, Switzerland	Leachates injected through fracture in intact rock	'young' (pH 13.5, high K, Na)	C-S-H phases	Transmissivity of fracture decreased over the 9 month experiment
Tajima et al. (2003)	Kunigel V1	Batch experiments at 50, 80 and 100°C	1. K/NaOH+$CaOH_2$ (pH 13) 2. $CaOH_2$ (pH 10.5–12.5) 3. 'low alkaline cement' (pH 11)	1. and 2. montmorillonite dissolved, C-S-H, C-A-S-H formed 3. Na-montmorillonite to Ca-montmorillonite	Increased pH and temp induced greater alteration to C-S-H, C-A-S-H. None observed with low-alkali cement leachate
Savage et al. (2010b)	Clays in Searles Lake (alkaline lake), California, USA	Modelling NA data (advective porous media flow)	Mildly alkaline (pH 9–10)	Fe-illite, analcime and K-feldspar	Palygorskite also abundant in the area (cf. comments in Alexander et al. (2012))
Alexander et al. (2012)	Natural bentonite, Parsata, Cyprus	NA (fracture flow and diffusion front)	Alkaline groundwaters (pH 11)	Palygorskite	Very limited reaction zone following 10^5 a reaction time
Moyce et al. (2014)	Borrowdale Volcanic Group, (metavolcanics), Sellafield, UK	Batch, undisturbed for 15 a	Initially 'young' (pH 13.5, high K, Na) and 'evolved' (pH 12.5, portlandite buffered). Now pH 10 after 15 years of reaction	palygorskite-like and sepiolite-like fibrous Mg-rich silicate	Possibly the missing link between short-term laboratory studies and NAs
Savage (2011)	Range of cement aggregates (granite to dolomite)	Samples from old concrete structures between 1 and 110 a	Reaction with rain, seawater and shallow groundwater	Range of secondary phases from alkali-silica gel to C-S-H phases to smectitic clays	Thin reaction zones around aggregates observed, but environments studied generally not repository relevant

Table 2-5. Rock types inside the Forsmark regional model volume from which data of mineralogical and geochemical composition are available (Sandström and Stephens 2009).

SKB code	SKB Rock name
101004	Metamorphosed ultramafic rock
101033	Metamorphosed diorite, quartz diorite or gabbro
101051	Metamorphosed, fine- to medium-grained granitoid
101051_700	Metamorphosed and oxidised, fine- to medium-grained granitoid
101054	Metamorphosed tonalite to granodiorite
101056	Metamorphosed granodiorite
101057	Metamorphosed, medium-grained granite to granodiorite
101057_101058_104	Metamorphosed and albitized granite
101057_700	Metamorphosed and oxidised, medium-grained granite to granodiorite
101057_706	Vuggy metamorphosed granite (quartz dissolution, high porosity)
101058	Metamorphosed, aplitic granite
101061	Pegmatite or pegmatitic granite
102017	Amphibolite
103076	Metamorphosed, felsic to intermediate volcanic rock
111058	Fine- to medium-grained granite

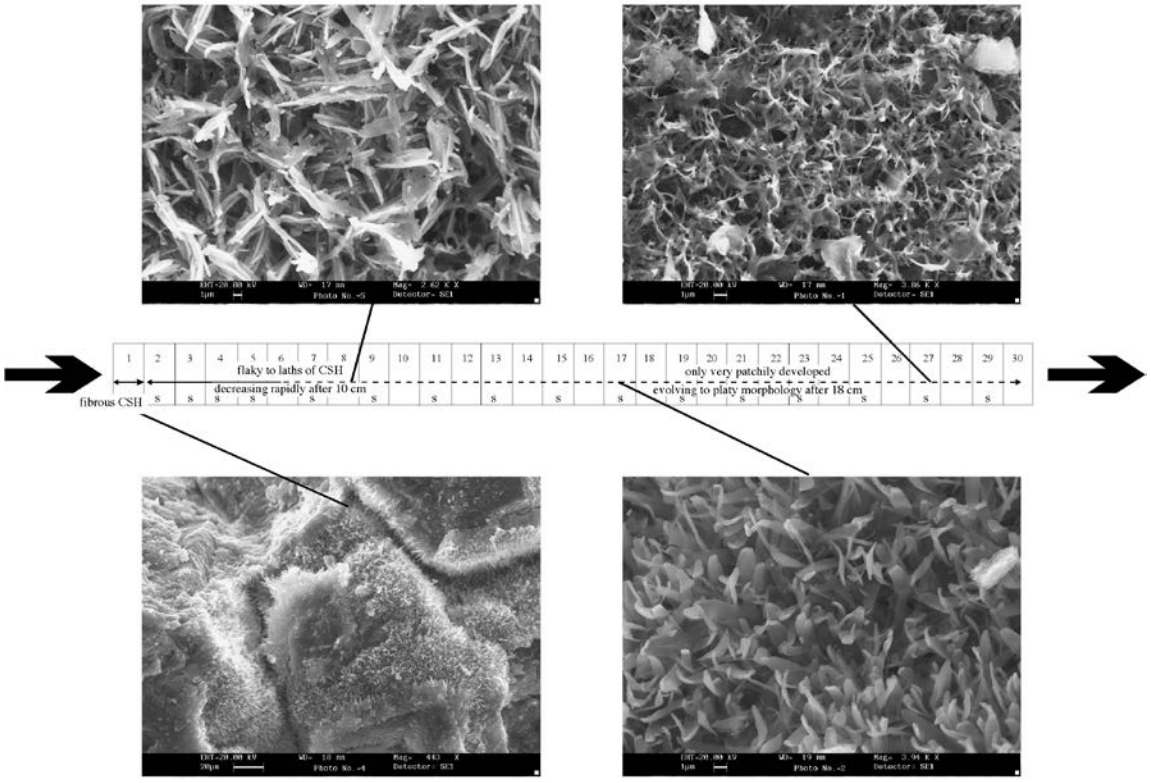

Figure 2-27. *Summary of reaction of primary minerals and precipitation of secondary phases following reaction of Äspö granite with 'young' alkali leachates (Bateman et al. 2001a).*

2.4.2 Potential impact on the EBS

SKB currently plan to use MX-80 bentonite in the Forsmark SF repository and this has been shown to have a porewater pH of 8 (Bradbury and Baeyens 2003), significantly less than that of low-alkali cement (pH 11 or less). Clearly, alkaline cement leachates with a pH of >13 ('young' leachates) and, later, pH 12.5 ('evolved' leachates) which come into contact with the bentonite will induce reaction which may alter the buffers properties. Soil engineers have known for many years that the treatment of clay soils with strongly alkaline calcium hydroxide solutions produces a highly cemented material with considerable strength and resistance to moisture. Diamond et al. (1963) reacted calcium hydroxide with montmorillonite as compacted solid mixtures at 60°C for 55 days. After the experiment, the initially plastic solid mixtures were extremely hard (hammer and chisel being needed for removal from container), due to formation of C-S-H gel and C-S-H-(I). Bérubé et al. (1990) produced pastes of metabentonite (mineralogical composition not determined, but probably nearer to illite than to smectite) with portlandite and cured them for 7 days at 80°C resulting in cementation due to the formation of C-A-S-H phases.

Bentonite and clay-rich host rock batch and flow-through cell experiments (see Table 2-4 for an overview) to examine the effects of alkaline leachates on bentonite generally indicate the presence of secondary zeolites (e.g. ECOCLAY 2005) and C-S-H gels (e.g. Vuorinen et al. 2003), concomitant with reduced surface area and pore size increase. For studies on mixed bentonite/quartz sand (e.g. buffer in Japan (JAEA 2007)) and bentonite/crushed host rock (e.g. backfill in Finland (Vuorinen et al. 2006)), alteration of the bentonite can be modified by the preliminary dissolution of more reactive phases first (i.e. cristobalite and microcline, respectively). This will obviously vary depending on the bentonite/rock ratio and the precise mineralogy of the crushed rock.

The presence of abundant Ca in the leachates means that the bentonite is exchanged to Ca-bentonite, even if it begins as a Na-bentonite (such as MX-80), and, in saline conditions, smectite has been seen to alter to Ca-montmorillonite. NaOH solutions (pH > 13) induce production of beidellite which significantly increases the CEC (ECOCLAY 2005, Vuorinen et al. 2006) and permanently decreases the swelling pressure, presumably due to the loss of Si.

Dissolution of montmorillonite increases Si porewater activity, leading to a decrease in swelling pressure, increased hydraulic conductivity and, eventually, fracturing of the bentonite due to cementation with secondary phases. Vieno et al. (2003) noted that the outstanding questions regarding this were:

- pH buffering capacity, alteration products, and the properties of the altered clay in highly compacted bentonite.
- The relative propagation rates of diffusing OH^- ions and the reaction front of the buffering and alteration processes in the highly compacted bentonite. Is it possible that, due to the kinetics of reactions, the plume of high pH could reach the canister surface and penetrate into a defective canister before the buffering reaction neutralise the high pH?
- The fate and effects of dissolving siliceous and aluminous reaction products in the long term. The potential of these species to re-precipitate and to cause cementation of the highly compacted bentonite in the phase when the pH eventually decreases again, should be investigated.

Both NaCl and NaOH solutions at concentrations of 0.3M and greater also significantly decrease the swelling pressure (Karnland et al. 2004, SKI 2005) while $Ca(OH)_2$ buffered leachates make no significant difference to the swelling pressure (ECOCLAY 2005). There also appears to be an unknown sink for Mg. Vuorinen et al. (2006) proposed uptake on C-S-H-gels, but comparison with experimental work on the Swiss Opalinus Clay (which is not unlike bentonite in its properties) by Adler (2001) and Adler et al. (2001) and on observations from the Maqarin site in Jordan (Milodowski et al. 1992, 1998a, b) suggests a Mg-hydroxide phase such as hydrotalcite or sepiolite, although Savage et al. (2010b) have also reported secondary Mg-montmorillonite at the Searles Lake site in the USA.

Ahokas et al. (2006) noted that, of the many studies of bentonite/alkaline leachate now available in the literature (cf. Table 2-4), few have looked at compacted bentonite (see e.g. Karnland et al. 2004). This is important as the initial low permeability of the compacted bentonite should minimise interaction with the alkaline leachates and subsequent chemical reaction appears to reduce this even more (Alexander et al. 2012, ECOCLAY 2005, Lehikoinen 2004). Different reasons have been given to explain some of the discrepancies between batch experiments and experiments with compacted bentonite.

For example, ion-equilibrium established between the hydroxide ions and the montmorillonite counter-ions in the pore fluid of compacted bentonite may have an effect, as previously demonstrated for NaCl by Karnland et al. (2003). The similarities in the osmotic response of OH^- and Cl^- solutions could explain this behaviour.

Additionally, neoformed minerals with lower density than the original montmorillonite leads to lower porosity in the clay, which is often claimed to reduce permeability. Generally, this effect is totally overshadowed by the loss of montmorillonite, which radically reduces the sealing properties. However, this is at odds with the data of Nakayama et al. (2004) which showed that the effective diffusivity of OH^- in a compacted bentonite/sand buffer was 10^{-10} to 10^{-11} m^2s^{-1}, roughly the same as Cl^-, I^- and tritiated water. Overall, however, the influence of compaction and high swelling pressure on smectite dissolution rates is currently not well understood (the above noted experiments are some of the very few conducted on compacted material to date) and should be the target of further experimental work (cf. comments in Neall and Johnson 2006). Alexander et al. (2012) also argued that the differences observed between 'standard' batch experiments and those which employ compacted bentonite could be explained by differences in open and closed systems, respectively. Certainly the recent laboratory experiments from the BIGRAD project (e.g. Moyce et al. 2014) indicate that palygorskite can develop relatively rapidly and in a closed system which is not unlike that present in the bentonite at the Parsata site in Cyprus (and, more importantly, similar to what is expected in a repository EBS), suggesting a common reaction sequence. Recent work from the open (and advective) system at Searles Lake (Savage et al. 2010b) reports different reaction products and claim smectite susceptibility to alter from pH 9 upwards, but the authors acknowledge that this is in a system which is far from the low flux, diffusion dominated system expected in a repository.

Overall, it remains difficult to provide an overarching conclusion to the likely impact of bentonite/cement leachate reaction based on current laboratory and natural analogue data. As with the cement leachate/host rock studies discussed in Section 2.4.1, the major problem remains the absence of an agreed, standard experimental methodology for the laboratory. Other factors include heterogeneity at the field scale (mineralogy, transport), and transport control vs. reaction control. Some laboratory experiments (e.g. dissolution experiments) require reaction control, but the field situation is under transport (diffusion) control. With respect to the natural analogue data, clearly it is preferred to examine the bentonite in an environment very similar to that expected in a repository (as is the case in Cyprus or the Philippines). But this should not rule out studying sites such as Searles Lake as the results can still add to the mechanistic understanding of bentonite reaction, it is simply that care must be taken to put the results in context.

2.5 Integrating the information from laboratory, URL, NA and modelling studies and assessing the relevance to Forsmark

2.5.1 Source term

Although at first glance the information from the Maqarin natural analogue site and the URL observations on grouts from the ONKALO and Whiteshell URLs appear to be at odds, this is probably not really the case. The lack of apparent reaction in the grouts can be explained in modelling terms quite easily – although some hard observational evidence to back this up would be appreciated (see Section 2.6.1) – and it perhaps should not really be a surprise. If the grout is doing its job properly, it should seal flow and itself efficiently. Similar information has been reported for other grouts, with Yamamoto et al. (2008) noting that 38 weeks of immersion in water in a laboratory made very little difference to the pH of the water in the reaction cells (Figure 2-28). Surprisingly, this is also the case in the natural cements in Jordan: it was noted above that they are widespread across the Middle East and that they generally act as a very good aquiclude. Across the massive range which this rock type stretches, only two active alkaline groundwaters have been found, with both springs within a few hundred metres of each other at Maqarin in northern Jordan (Figure 2-1).

These two alkaline groundwater sources have been produced by tectonics: the Eastern Springs straddles an anticline which has fractured the otherwise impervious rock and the Western Springs is suffering gravitational tectonics – i.e. the valley sides are so steep that fresh cement is regularly exposed for reaction by massive slumping of the valley walls (see discussion in Smellie 1998).

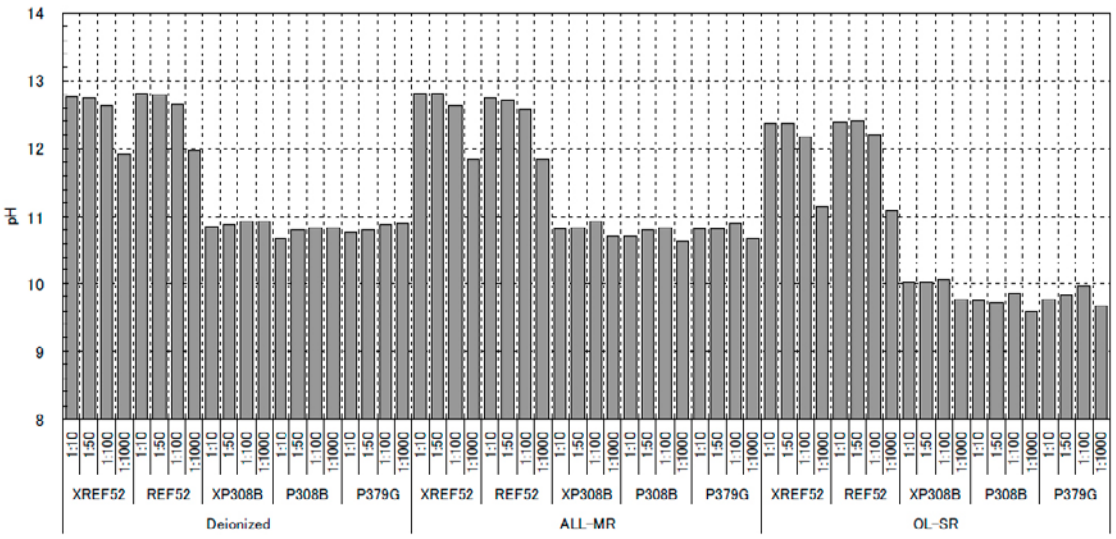

Figure 2-28. *38 weeks immersion of grouts in various groundwaters. Little change in pH was observed other than at higher water:solid ratios, possibly due to dilution of portlandite which is buffering the system (Yamamoto et al. 2008).*

As such, this is an anomalous site, but it is still directly relevant to the arguments here. The young grouts at both ONKALO and Whiteshell are analogous to the undisturbed natural cement and show, not surprisingly, little reaction. However, over the lifetime of the repository, it is unlikely that these grouts will not also be damaged by tectonics, so triggering cement leaching analogous to that seen in Maqarin. As the data from that site show, only a small, localised zone of the cement appears to react, so it is likely that significant tectonic activity would be necessary to disrupt the grouts significantly. But Swedenborg and Dahlström (2003) noted "...that cement grout acts basically as a 'lubricant' in a joint subjected to shear stress." and that grouted hard rock joints have a lower shear resistance than do ungrouted joints. This implies that, in the long-term, the grouts are likely to be heavily damaged by mechanical crushing, so opening up the already high porosity to further leaching.

Slunga (1990) noted "The Baltic Shield area is a seismicity area with few seismic events exceeding ML = 4" and Neall et al. (2007) provided a wide ranging summary of the current knowledge on earthquakes in Finland and noted that the (Olkiluoto) repository location "…is advantageous with respect to the stability of the geosphere". Overall, Forsmark is in a tectonically quiescent area, but tectonics cannot be fully ruled out due to:

- climate change, which is likely to increase sea-level by 10 m over the next 1000 years (e.g. SKB 2010b), so inducing marine transgression-related tectonics,
- concomitantly, post-glacial rebound is currently lifting the land mass by 6–7 mm/year (Ekman 1996), inducing 'relaxation' tectonics, even if this is unlikely to actually re-activate currently quiescent faults (Lambeck and Purcell 2003),
- postglacial earthquakes, in the immediate aftermath of future glaciations (La Pointe and Hermanson 2002),
- glacial jacking (Lönnqvist and Hökmark 2010).

The question is then to what degree could site tectonics disrupt the grouts enough (and often enough) to be a problem? For the Forsmark and Laxemar sites in Sweden, Fälth et al. (2010) noted that any risk of canister damage can be minimised with an appropriate repository layout. This, obviously, has no direct bearing on the grout behaviour, but it does suggest that the basic tectonic information is available to attempt an analysis of this sort. In parallel, further work on accessing and sampling older grouts would be advantageous as would be instrumenting and monitoring grouted tunnel sections in tectonically active areas to produce baseline information. Alexander and Neall (2007) proposed monitoring existing OPC and low alkali grouts in ONKALO to examine pH evolution with time (and compare with any new information from the LCS project on low alkali grouts). Currently, the data are ambiguous and the mechanism is neither well understood nor defined.

In summary, there is no clear-cut evidence to define the likely form of the leachate source term from a grout in the fractured Forsmark host rock. While evidence clearly exists for very little reaction in some grouts, this is from a very limited database indeed and needs to be statistically relevant before it can be assumed to be the norm. Even if it were the case, the potential impact of site tectonics must also be taken into account when assessing long-term impacts. As such, for the time being, assuming Maqarin-like reaction fronts and propagation of (even a limited) ADZ is the most conservative approach.

2.5.2 ADZ propagation

Information from the advective-transport NA system at Maqarin in Jordan allied with data from the URL experiments and laboratory column and batch experiments indicate that clogging of fractures (and porous media) will occur when alkaline leachates migrate through a water-conducting feature and react with the fracture infill material, fracture wall-rock and accessible rock matrix. In a recent review of the LCS project modelling studies, Savage et al. (2011) provide a comprehensive list of the various mechanisms that require to be included in any model of host rock reaction (although the authors also point out that the weighting of the mechanisms will vary depending on the leachate/rock system under study). It is also clear that sufficient uncertainty remains in many thermodynamic and kinetic datasets so that unique solutions remain only dimly seen.

In both the HPF experiments and column experiments, significant permeability reduction has been observed, despite only minor changes in mineralogy, suggesting that permeability may also be controlled by changes in the structure of the rock (pore geometries) rather than by only the bulk volumetric (porosity) – see also the discussion in Savage et al. (2011), Soler et al. (2011a) and Soler and Mäder (2010). As noted above, at Maqarin, the faults and joints seal completely and can remain sealed for geological timescales unless tectonically re-activated. This obviously has implications for any repository SA as it appears likely that the original repository hydrogeological environment could be significantly changed, both relatively quickly (cf. HPF where measurable differences were observed within a few years) and over large scales (cf. Maqarin where the alkaline plume extends for at least 500 m from the cement source[12]) where the site hydrogeology is appropriate.

The fracture transmissivities (T) at Maqarin are in the range 10^{-11} to 10^{-12} m^2s^{-1} (Degnan et al. 2011) whereas the mean value fracture transmissivities in fracture domains FFM01 and FFM02 (for example) at Forsmark are in the range $3 \cdot 10^{-9}$ to $1.5 \cdot 10^{-8}$ m^2s^{-1} regardless of depth as shown in Figure 2-29. Thus any alkaline leachates will move much faster through these particular systems at that depth. On approaching the repository horizon, the transmissivities are much lower (e.g. Follin et al. 2007) and so the extent of any ADZ would be expected to be more restricted.

Currently, it is difficult to predict the likely reaction of the Forsmark host rock to cement leachates due to a paucity of directly relevant data. It is likely that secondary phases will be produced, but the quantities will depend on the (likely) variable buffer capacity of the fracture minerals, fracture walls and rock matrix. In the HPF experiment, little buffering of the alkaline leachates was observed (Mäder et al. 2006, Soler et al. 2006, Soler and Mäder 2007, 2010), despite the existence of significant quantities of fault gouge in the experimental shear zone. The existing leachate/rock data for ONKALO (Vuorinen et al. 2006) indicate only weak buffering of the alkaline solutions, but these data should be treated with caution: the 75% mica gneiss, 20% pegmatitic granite and 5% tonalite is of little relevance to the host rock fracture mineral assemblage of calcite, pyrite, pyrrhotite, graphite and clays. The recent work of Cama et al. (2012) also show little reaction with the ONKALO mica gneiss rock matrix, but this does represent a very short reaction time of only 19 days and so is of limited value. Interestingly, Milodowski et al. (1998a) reported on the reaction of basalt boulders which had fallen into the ADZ at Maqarin (from the top of the valley) and noted the presence of significant quantities of Ca-K-Na zeolite and amorphous zeolitic gel precursors with compositions intermediate to mordenite and dachiardite. Admittedly, there were significant amounts of glass present in the primary basalt and it is possible that this reacted so thoroughly.

Overall, it is recommended that scoping laboratory experiments be carried out to better assess the true pH buffer capacity of the Forsmark flow systems (as Alexander and Neall (2007) recommended for ONKALO), preferably with an associated BPM (blind predictive modelling) exercise to increase confidence in the results of future coupled code modelling of the site (see discussion in Pate et al. (1994) on the BPM approach).

[12] Admittedly, this is a highly permeable, near-surface environment.

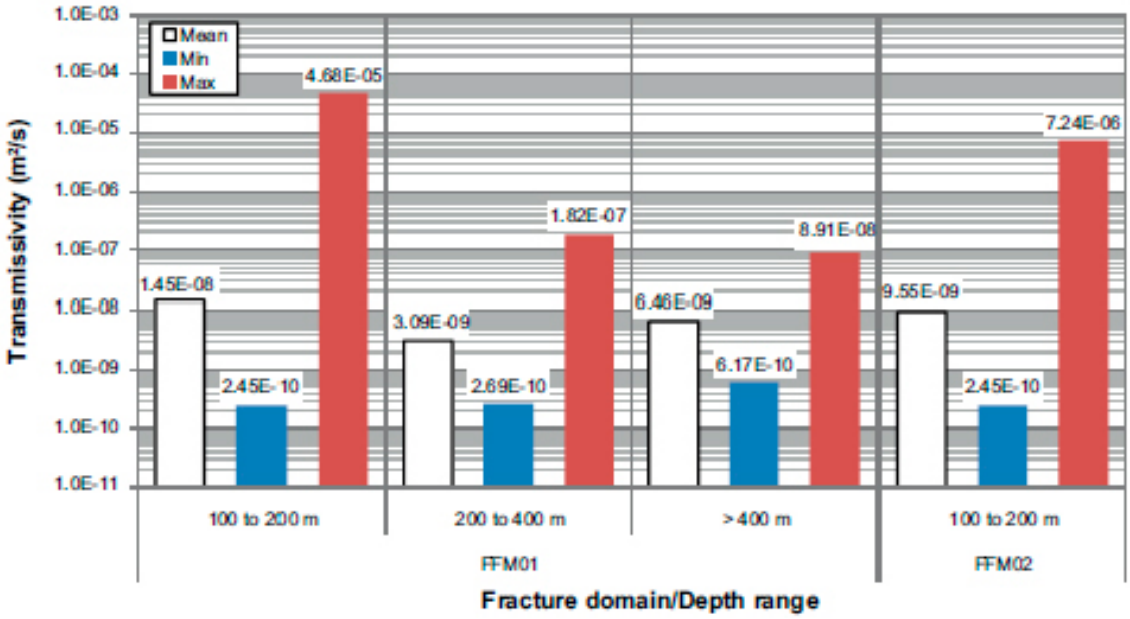

Figure 2-29. *Fracture transmissivities in different depth intervals in fracture domains FFM01 and FFM02 at Forsmark, compiled from Follin et al. (2007, Table 10-25).*

2.5.3 Potential perturbations to the EBS

The evidence presented above shows that, as with the data available for reaction of the Forsmark host rock, evidence of bentonite reaction depends as much on the experimental methodology employed as anything else. It is clear that experimental studies of compacted bentonite take longer, but they (along with similar and natural analogue studies) also have the great advantage of reflecting repository relevant conditions.

As noted elsewhere in this report, the current uncertainties on the likely alkali leachate source term, site hydrogeology and likely form of reaction between the leachates and the host rock, lead to the recommendation that a conservative approach to estimating the potential impact on the Forsmark EBS be taken for the moment (obviously, this should be updated as new information is collected on the site). Assuming OPC grouting in the upper 200 m of ramp and shafts, a maximum OPC volume of 3,600 m^3 will be employed at Forsmark. According to Orantie and Kuosa (2008), SKB's standard (high pH) grout mix UF-00-08-2 has a density of 1,602 kg m^{-3}, so 5,770 Mg[13] of grout are potentially available for reaction. Using the same parameters as Vieno et al. (2003)[14], means that about $3.1 \cdot 10^7$ moles of OH^- will be available, potentially exhausting the buffer capacity of around 62,000 Mg of pure bentonite (i.e. montmorillonite), or around 52% of the total bentonite buffer in the spent fuel deposition holes alone[15].

Obviously, this is very simplistic, ignoring as it does any interaction with the host rock surrounding the fractures through which it is transported, or any reaction with the sand/bentonite backfill never mind any dilution effects in the flow system etc but does support the recommendations made above that further work be carried out on the interaction of alkaline leachates with compacted bentonite. One critical area of focus would be to assess the mechanisms involved to determine what degree of degradation is necessary before particular barrier roles of the bentonite are compromised, something which will occur before full 'depletion' of the clay (cf. Metcalfe and Walker 2004).

[13] This assumes that all of the grout is OPC grout and ignores SKB's current move to consider low alkali cements.

[14] The authors assumed 5.4 moles of OH^- ions per kg of cement and that bentonite can neutralise about 0.5 moles of OH^- ions per kg of clay.

[15] Based on data from SKB (2010d): current assumption of 6,000 spent fuel deposition holes with maximum amount of buffer in a deposition hole of 22.3 Mg of which a maximum of 90% of this weight will be montmorillonite.

Karlsson et al. (1999) carried out similar mass balance calculations for the SLF 3–5 deep repository for long-lived waste and showed that the sand or gravel backfill has sufficient capacity to neutralise the cement leachates coming from the concrete structures present in the repository. The SFR-1 BMA and BTF vaults are so similar in terms of quantities of concrete and backfill of sand or gravel that SKB felt the conclusion from the SLF 3–5 study was applicable to SFR-1 as well. In other words, complete neutralisation in the gravel fill means that the pH in the surrounding rock does not exceed the pH in the groundwater. However, the original study was criticised by SKI (Benbow et al. 2002) on the basis the chosen reaction end product (C-S-H) and on over-estimating the available reaction surface area in the backfill. SKB (2008) noted that this could be addressed by using a fine-grained material as backfill if the spread of high pH from the repository to the surrounding rock needs to be limited, but this ignores clogging of the sand/gravel pore spaces by secondary reaction products (cf. Alexander 2012).

According to two recent studies of the degradation of the SFR-1 silo, only a small increase of the pH in the bentonite immediately adjacent to the concrete is obtained during the first thousand years (Cronstrand 2007, Gaucher et al. 2005). This, however, assumes that the bentonite functions perfectly (i.e. as a diffusive barrier) and this requires a high degree of quality control during original emplacement. It also assumes that groundwater contacting the outside of the bentonite has not previously been in contact with concrete elsewhere in the SFR-1, something which is not easy to prove following the more recent re-assessment of the site hydrogeology. In addition, the sand/bentonite base and cap to the silo contains only 10% bentonite, making the clay phase potentially vulnerable. Nevertheless, the approach is worth consideration for the Forsmark SF repository, but it will require arguments based on the quality of the EBS emplacement and these may not be acceptable.

2.6 What remains to be done? How can knowledge gaps of relevance to Forsmark be filled?

2.6.1 Grout long-term durability

Alexander and Neall (2007) noted that there was a lack of mechanistic understanding of grout durability in fractured rock and proposed that this be addressed to obtain a better idea of the likely degree of leachability of the cementitious material (and hence the likely source term). Little has been done since then and, in addition to the comments made above regarding the potential impact of tectonics on grouts, two other areas should be addressed, namely cement sealing and carbonation described below.

Cement sealing

In general, it is to be expected that any cementitious material present in the Forsmark SF repository will be degraded by the interaction with groundwaters in the longer term. However, it should be noted that many archaeological cements have survived for several millennia. For example, Malinowski and Garfinkel (1991) described the use of a lime-based concrete in the floors of a Neolithic (ca 7000 BC) construction in Galilee. Thomassin and Rassineux (1992) reviewed some of the literature on Gallo-Roman cement-based materials and noted that one of the most impressive examples is the 1.7 ka Roman mortar used in Hadrian's Wall in northern England which still contains substantial amounts of C-S-H compounds (Figure 2-30). The origin of the C-S-H compounds in Hadrian's Wall is thought to be from calcining of siliceous limestones to produce lime or by the inclusion in the mortars of larnite from metamorphosed cherts found locally in limestones (Jull and Lees 1990). The formation of the C-S-H compounds reduced the porosity and permeability of the cement which helped to ensure the wall's preservation, despite generally wet conditions (mean annual rainfall in the area from 1971–2000 of between 650 and 1,500 mm, depending on elevation: UK Met Office 2012).

The natural cements in the Maqarin area of Jordan are up to 2 Ma old (Alexander 1992) and, although usually heavily fractured into blocks (Figure 2-31), reaction is very much restricted to the outer edge of the blocks. This is possibly because the natural material is of low porosity and permeability (generally, the cements act as an aquiclude in Jordan and Syria) and the secondary reaction products naturally seal any flowing porosity.

Figure 2-30. *Section of Hadrian's Wall, northern England. The large stone blocks were held together with mortar (from Miller et al. 2000).*

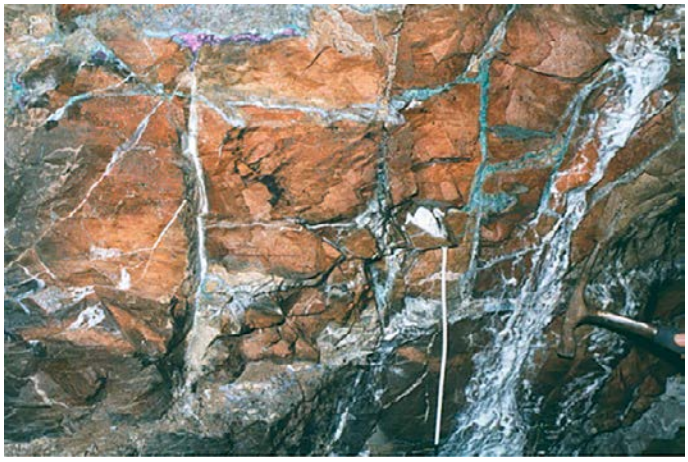

Figure 2-31. *Small aperture sealed fractures in the natural cements at the Maqarin site, Jordan (for scale, see hammer in bottom right corner). From Pitty and Alexander (2011).*

Milodowski et al. (1989) also reported the presence of unreacted natural cements from the Scawt Hill and Carneal Plug sites in Northern Ireland (Figure 2-32). These phases were produced during the thermal metamorphism of the host limestone and are estimated to be some 58 MA old. As with the cements in Jordan, these natural cements remained unchanged until accessed by groundwaters in the last 10–20 ka.

The detailed mechanisms behind the cement longevity at both these NA sites has never been assessed in any detail and would be well worth investigating to support any claims regarding the likely longevity of the grouts at Forsmark.

Another area possibly worth exploring is the longevity of grouts in existing tunnels elsewhere in the Fennoscandian Shield in the oldest tunnels possible. Not only would this allow a direct comparison with Forsmark grouts to improve understanding of the processes involved, but it could also increase confidence in the overall longevity of grouts under similar environments.

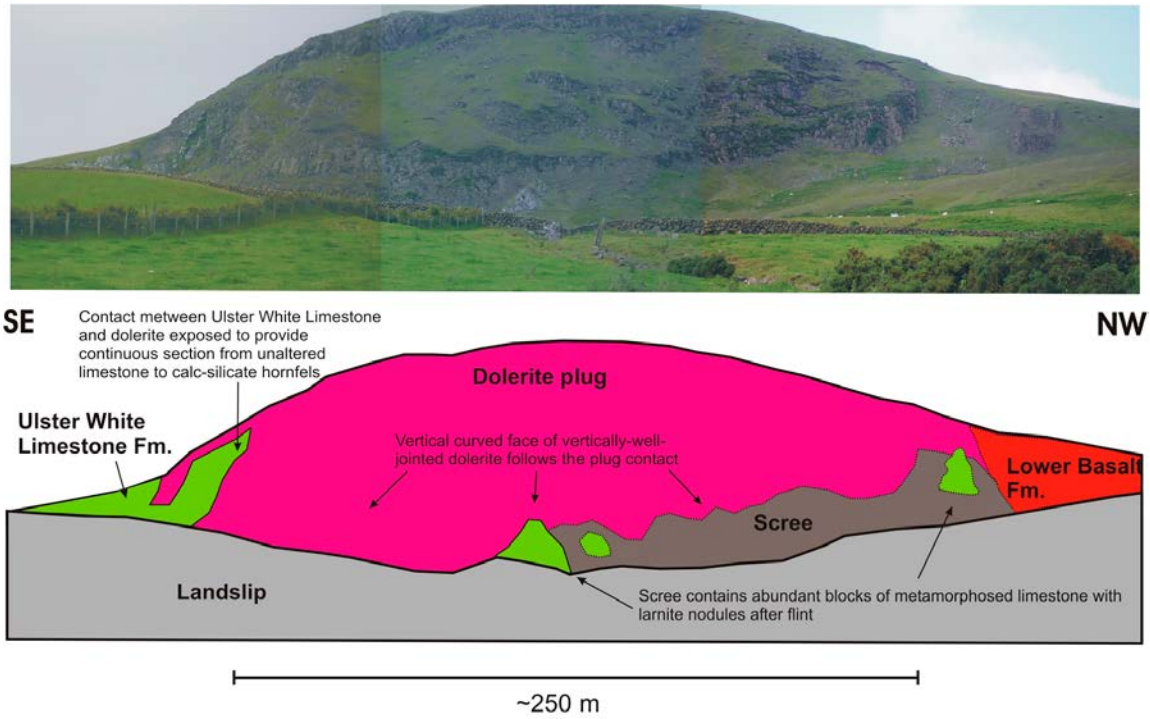

Figure 2-32. *The Scawt Hill site in Northern Ireland (top). The natural cements are in the contact zone between the Ulster White Limestone and the dolerite plug (bottom) (from Milodowski et al. 2009).*

Carbonation

One particular reaction may significantly reduce cement leaching, namely carbonation. This occurs when HCO_3^- and CO_2 in groundwater react with Ca^{2+} in the cement, producing calcium carbonate[16] in the cement porosity. In extreme cases, this can effectively seal the cement from further groundwater reaction, so reducing (or even halting) 'normal' leaching processes.

Normally, the reaction proceeds as groundwater HCO_3^- and CO_2 diffuse into the cement from the surface, so producing a reaction front characterised by a lower pH. At the front, groundwater HCO_3^-, CO_2 and cement Ca^{2+} will be at a minimum due to the low solubility of calcite and so free ions in the cement porewater will diffuse down the concentration gradient to the front. In saturated cements (e.g. in a water-conducting fracture), Ca^{2+} will diffuse much faster than HCO_3^-, so the front tends to be very near to the cement surface. In cements reacted in groundwaters with "High contents of Mg and/or HCO_3^- in the (ground)water leads to a more dense outer shell..." (Lagerblad 2005) of secondary precipitates on the cement which leads to more rapid sealing of the cement and reduced leaching.

To investigate carbonation processes more quantitatively in a (OPC) cementitious repository in a sedimentary host rock, Pfingsten (2001) modelled data from small cement discs using a 2-D coupled hydraulic and reactive transport code (2D-MCOTAC). Although the physical parameters modelled are of no direct relevance to grouts in Forsmark, the approach is of interest and could be applied to scope potential changes to the grouts from carbonation reactions. Indeed, Neall and Johnson (2006) noted that, although the carbonation mechanism can be viewed as mainly a favourable phenomenon in PA which could "....to a large degree mitigate the potential for high pH alteration of the buffer.", it has generally been neglected to date.

It would be worth conducting scoping calculations along the lines of Pfingsten (2001) to assess if carbonation could play a significant role in minimising alkaline leachate production from the grouts in Forsmark. Currently, no directly relevant NA studies of carbonation exist, but there is

[16] Where C-S-H phases are present, vaterite is the usual form of calcium carbonate while calcite forms with CH. In extreme cases, two separate fronts can form depending on the physical distribution of C-S-H and CH phases in the cement.

potential to study the process at Maqarin (see Figure 2-33). Based on $\delta^{13}C$ data, a period of CO_2 uptake has been identified at the site, but no more than a preliminary assessment was originally made due to changes in funding at the time. In addition, new work in support of carbon capture and sequestration (CCS), such as the NA work of Pearce (2006) or the ongoing NASCENT project (http://www.bgs.ac.uk/nascent/home.html), hold the potential to elucidate the likely impact of carbonation on cementitious systems.

Archaeological sites have also been examined, although rarely. For example, samples were collected from the Gallo-Roman amphitheatre in Béziers in France as an analogy to the long-term behaviour of a surface repository (Miller et al. 2006). Although the age of the cements is well known, the site has suffered from variable saturation and so it is difficult to draw firm conclusions on the high degree of carbonation observed. It is also generally difficult to access materials from archaeological sites now, with many falling under national or international protection. Hadrian's Wall, for example, is now an UNESCO World Heritage Site and cannot be disturbed. This is unfortunate as most archaeological cements would be appropriate analogues for low alkali cements and Holt (2008) rightly points out that "There is a lack of information on the long-term performance of these (*low alkali cement grouts*) materials, especially with regard to durability and ensuring a watertight repository structure for over 100 years."

2.6.2 Long-term reaction of the Forsmark host rock

Savage (2011) concluded the report on preliminary modelling efforts in the LCS project with the statement "The modelling exercises showed that there is an interest in keeping the numerical models as simple as possible and trying to obtain a reasonable fit with a minimum of processes, minerals and parameters. However, up-scaling processes and model parameterisation to the timescales appropriate to repository safety assessment are of considerable concern. Future modelling exercises of this type should focus on a suitable natural or industrial analogue that might aid assessing mineral–fluid reactions at these longer timescales." And this seems like an eminently sensible thing to do.

2.6.3 Long-term reaction of bentonite

An extensive amount of experimental data has been accumulated – particularly on the alteration of bentonite by high pH fluids. There is little direct evaluation of interaction between solid concrete and bentonite, because of the very slow rates of reaction involved, which make measurements impractical. Experiments may either be carried out on a representative bentonite or pure mineral components (the former being most realistic, but often difficult to carry out and interpret).

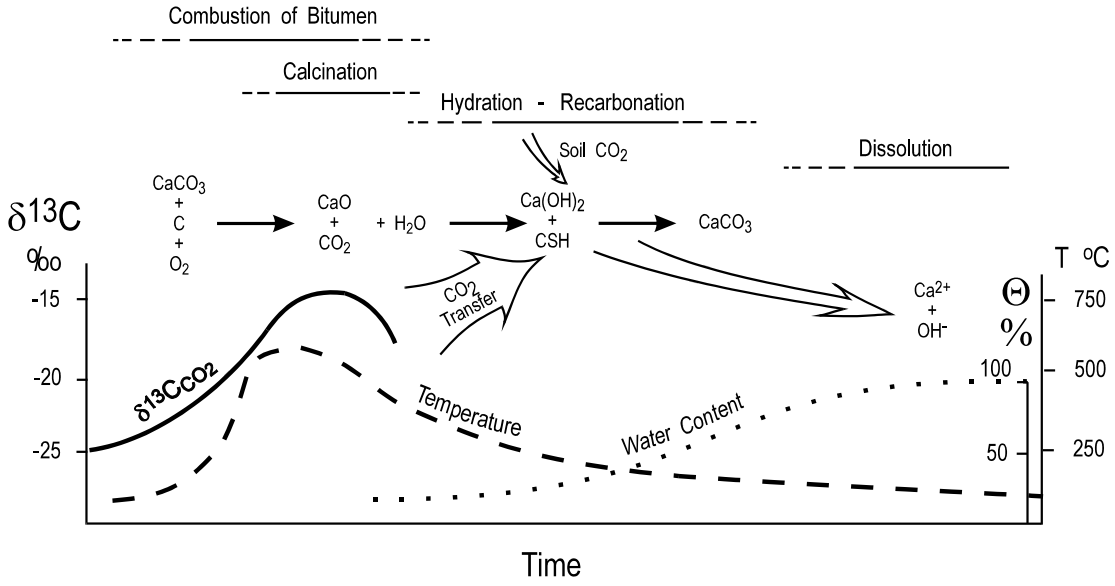

Figure 2-33. *Conceptual model showing sequence of thermal metamorphic and retrograde alteration reactions with changes in temperature and humidity in the reaction zone at Maqarin (from Clark et al. 1994).*

Basically, alteration experiments are of 2 types – batch and flow through. The former are more common, but less realistic, as the bentonite is usually dispersed to allow efficient contact between the solution and the solid phase. Except at extremely high pH (> around 13.5), reactions are slow at room temperature and hence either extremely long experimental times (years) or artificial acceleration by increasing the temperature is required. Both these approaches cause problems – it is extremely difficult to maintain such alkaline conditions in the laboratory, strictly controlled atmosphere conditions are required and material degradation in such fluids causes complications. High temperature measurements suffer from the problem that the kinetics of the overall reaction may change in an inherently unpredictable manner and the products of the alteration reaction may thus not be representative of those formed at lower temperatures (e.g. ettringite does not form above 60°C).

Flow through experiments may be carried out on compacted bentonite, although usually rather high sand content is needed to allow flow to occur. Alternatively, solute transport may occur by diffusion – here reaction is further slowed down by the kinetics of the solute transport process. Such studies are more realistic, but practically more complex and expensive to run (and, to date, only a few have been carried out because of this). In addition to the problems noted for batch experiments, flow through experiments may also suffer from clogging by reaction products – which may effectively stop progress of the reaction. Such cementation may actually occur in real systems but, here, the possible effect of reactivation must be considered – e.g. due to mechanical disturbances, gas pressurisation, etc – which are difficult, if not impossible, to recreate in the laboratory (particularly in a controlled atmosphere glove box).

The results of the ECOCLAY-II project, which indicated 10–20 cm of reaction of bentonite in alkali environments in 100 ka are not encouraging when compared to the planned thicknesses of the bentonite buffer in the KBS–3V and –3H designs (31.5 and 35 cm respectively). However, the ECOCLAY-II figures are based on short term laboratory and URL experiments and clearly need more relevant long-term support before these values can be extrapolated to the 1 Ma required here. It was pointed out in Section 2.3 that, other than the ECOCLAY work, there are effectively no URL data of relevance to the long-term behaviour of bentonite under alkaline conditions, despite the fact that many (if not most) of the experiments listed actually having bentonite in contact with cement and concrete. Would it then be worth piggy-backing a bentonite reaction study onto one of the existing (or planned) URL experiments? Yes, but only if:

- Repository relevant conditions could be guaranteed (e.g. saturated system with flow from the cement to the bentonite at repository relevant flow rates).
- If an appropriately long timespan can be expected. ECOCLAY-II lasted only 3 years and this is simply not long enough to have confidence that the data are actually of any relevance to a repository safety case. Some very simple (and cheap) ‘emplace and walk away’ type experiments could be set up in an URL such as Äspö immediately with a set of ten identical sets. One experimental set could be recovered for analysis every decade for the next century, providing information over a time period several orders of magnitude greater than most experiments.
- If the results can be coupled to appropriate natural analogue studies which address repository relevant temporal and spatial scales.

Currently, there is little natural analogue information available on the long-term reaction of bentonite in alkali solutions. Work is ongoing in the Philippines and Cyprus on lower pH (i.e. 10–12) environments and results to date are encouraging in that reaction appears to be minimal. Unfortunately there is little clay for reaction in the higher pH (i.e.12–13) environments at the Maqarin site in Jordan. However, as noted above, the Khushaym Matruk site in central Jordan would appear to be a suitable site, but the data provided to date are ambiguous and further study in this area could be profitable. With the background data now available for the site, it should now be possible to take appropriate samples to assess clay reaction over longer timescales than is possible in the laboratory.

2.7 Conclusions

This section has looked at the available data of relevance to this project from natural analogue and experimental studies (including URLs). It is clear that a significant body of data exists which can be utilised to both improve the coupled codes and to provide tests of code output. General code testing

in this form is ongoing elsewhere (e.g. in the LCS project; Savage et al. 2011) and it would be appropriate to consider such tests for the codes under development here. Additional points from this section worth further consideration include:

Durability of grout

Durability of OPC grouts in active faults needs to be addressed to obtain a better idea of the likely degree of leachability of the cementitious material (and hence the likely source term). There is some indication that potential tectonic disturbance of grouts could initiate leaching of alkaline porewaters from the grout, but this needs to be better defined, possibly in tectonically active, deep mines, for example. Ongoing study of grouted area in the Äspö rock laboratory is a good start, but any future study should include an comparison of the Äspö and Forsmark tectonic regimes to ensure that the environments are truly comparible.

Alteration of host rock mineralogy

A large body of data now exists in the literature (see Table 2-4, for example) and although some information has been assessed for model input (e.g. Savage 2011), this should be data-mined in an exhaustive fashion to provide information of direct relevance to the Forsmark site. In support of this, some limited experimental examination of alkaline leachate/flow system mineralogy interaction is necessary to fully assess the likely impact on the Forsmark host rock.

Host rock hydrogeology

Due to the likelihood of fracture blocking following reaction with the alkaline leachates from the cement grout, it cannot be assumed that the current flow regime is representative of future conditions. The modelling report from the HPF *in situ* experiment (Soler et al. 2006) makes it clear that current coupled codes cannot model the detailed changes with any great precision, not even at the small spatial and temporal scales of that experiment, so it is questionable if investing much effort in this area is currently appropriate.

Carbonation

Lagerblad (2001) noted that, where granulated blast furnace slag or pozzolan are used, cement porosity is larger, allowing easy access to easily soluble Ca^{2+} in CH and producing calcite in the connected porosity. It is not clear, however, if this means that low alkali cements will tend to seal more effectively than C-S-H-containing OPC, but this would appear to be worth further study. Neall and Johnson (2006) noted that, although the carbonation mechanism can be viewed as mainly a favourable phenomenon in PA which could "....to a large degree mitigate the potential for high pH alteration of the buffer.", it is generally neglected in PA. It would be worth conducting scoping calculations (cf. Pfingsten 2001) to assess if carbonation could play a significant role in minimising alkaline leachate production from grouts in Forsmark (although this would need to be coupled with the assessment of potential tectonic impact on grout durability).

Bentonite buffer

Savage (2006) made the point that alkaline leachate/bentonite interaction is a young science and "cutting edge" geochemistry so models and certainty in assessments could not be expected until the work became more mature. To help move towards more mature science, Alexander and Neall (2007) recommended that:

- although the codes themselves have improved markedly over the last couple of decades, the basic mineralogical thermodynamic databases are still very weak and are probably the limiting factor to any detailed modelling of leachate host rock/bentonite interaction. The basic lack of thermodynamic and kinetic data for the phases of interest could be tackled by a programme of fundamental laboratory research,
- to provide long-term supporting information, the site in Jordan where clay/leachate interaction has recently been reported be considered for a focussed NA study,
- further laboratory work on leachate interaction with compacted bentonite buffer be carried out (this could include a parallel study with saline alkaline leachates).

3 Description of relevant processes

3.1 Transport processes

The transport processes deemed to be of major importance for the evolution of the alkali disturbed zone (ADZ) are briefly described here. These processes are generally well understood and established within the scientific community, and are described in greater detail in e.g. the work performed within the RETROCK Concerted action (SKB 2004) as part of the European Atomic Energy Community's (Euratom) framework of the specific research and training programme.

3.1.1 Advective transport and dispersion along flow paths

Groundwater transport at the Forsmark site is dominated by advective flow in conductive channels in fractures and fracture zones in the rock. The magnitude of the flow is determined by the pressure head gradient, the groundwater density and the transmissivity of the fractures.

Two distinct flow modes can be observed in groundwater transport through channels in the rock. In a heterogeneous rock domain, comprising one or a few highly transmissive fractures and several less transmissive ones, the flow tend to be directed to those with high transmissivities (SKB 2004). For reactive-transport modelling in rock domains with such properties it is reasonable to model the individual paths carrying most of the flow. In a homogeneous rock domain, with randomly distributed fractures with similar transmissivities, the flow tends to be distributed evenly between the channels, with no specific preferential flow path. For reactive-transport modelling in such rock domains a continuous porous medium approach may be best suited. These two distinct flow modes may be considered as end-members of different flow patterns in fractured rocks. The relatively sparsely fractured granitic rock in Forsmark is highly heterogeneous, and the primary transport process is therefore advective flow through a fracture network with preferential flow paths. Dispersion of solutes arises as a consequence of the diversion of the flow in different flow channels with different hydraulic properties (SKB 2004). Intermixing of groundwaters originating from different flow channels with different properties and solute concentrations results in the dilution of the dissolved species. The effect of such mixing phenomena on the ADZ evolution is studied specifically by means of modelling in Sections 6.2.2 and 6.4.2 of this report. Dispersion may also arise due to other channelling effects e.g. in-plane flow channelling. In the SDM-Site bedrock transport properties report (Crawford 2008), these and other common and more exotic channelling phenomena are described in detail and how they may influence the flow properties at the Forsmark site.

In this report, the extent of advective transport and dispersion along flow channels is estimated by means of different hydrogeological models. The fractured rock is represented in these numerical models either as a discrete fracture network (DFN) or an equivalent continuous porous medium (ECPM). Both representations have equivalent hydraulic properties at a given scale. In a DFN model, flow is constrained to the fractures and dispersion is represented explicitly by flow separation at fracture intersections. In an ECPM model, alternative to an explicit representation through flow separation at fracture intersections, the dispersion process may be represented by an appropriate dispersion scheme, usually parameterised by a dispersion length that relates the amount of dispersion to the groundwater velocity. The dispersion length may have components longitudinal and transverse to the flow direction and the dispersion may also include a diffusion term.

3.1.2 Diffusive transport in rock matrix

Although the primary flow pathway in crystalline rock is considered to be through the fractures, there is also a process by which solutes can diffuse into and out of the rock matrix through a network of interconnected micro-pores adjoining the fractures. This diffusive transport mechanism is normally much slower than the advective transport in the fractures, but is important for the retention and release of solutes over long timescales, giving rise to e.g. retardation of the penetration of dilute or saline water to depth. A complete summary of the processes involved in matrix diffusion, both for laboratory and field conditions, and how these have been traditionally considered in previous models may be found in SKB (2004, Section 2.3). The rate of the diffusive transport of a solute is determined by its

concentration gradient and the properties of the rock matrix, primarily the effective diffusivity and porosity. In large-scale models it is sometimes convenient to include a maximum penetration depth for the solute that is appropriate for the timescales under consideration.

The reactive-transport models in this report involve dissolved reactive species interacting with the minerals in the rock matrix adjacent to the flow paths. The magnitude of the fracture surface in contact with the flowing water, A_Q, also referred to as the flow-wetted surface, has a dominating influence on the amounts of matrix minerals that can be accessed for reaction through matrix diffusion (SKB 2004). The extent of interaction with minerals on the fracture surface and in the matrix (provided that the porosity is connected and accessible to a sufficient depth) along a flow path is determined by the ratio between the flow-wetted surface and the advective water flow-rate in the fracture. This ratio, A_Q/Q_{flow}, is sometimes referred to as the flow related transport resistance or F-factor. For a single flow path of length L, averaged transmissivity T, and with a hydraulic pressure head gradient i, over the entire length, the total F-factor for that flow path can be expressed:

$$F = \frac{2L}{Ti} \quad \left(= \frac{2L}{v\delta} \right) \tag{3-1}$$

The product of the averaged flow path transmissivity and the hydraulic gradient equals that of the mean Darcy velocity and fracture aperture, $T\,i = v\,\delta$, so these two averaged entities are interchangeable in the equation. The above relations are utilised in the coupling between the hydrogeological models and the reactive-transport models in Chapter 8.

3.1.3 Summary of transport processes

Advective flow through the fractures in crystalline rock is the primary process for solute transport. Since rock matrix diffusion tends to retard the transport of solutes, those models that do not include this process when considering the transport of the alkaline water released from the grout can be considered to be conservative. That is, they will tend to predict the most pessimistic outcome for penetration of alkaline water to repository depth. However, consideration of rock matrix diffusion and reactions involving matrix minerals will potentially lead to more realistic results, although there will be a degree of uncertainty around the parameters chosen to represent this process.

3.2 Chemical processes

3.2.1 Chemical processes in the grouting

Introduction to OPC grouting

The construction of the access tunnel in Forsmark will lead to changes in the groundwater table level, inducing a hydraulic gradient that could produce groundwater inflow to the tunnel. To limit this possible disturbance, a considerable amount of grouting of the water conductive fractures will be needed during the construction phase. The estimated grout volume remaining in the rock volume after excavation (0–200 m depth) is between 900 and 3,600 m^3 (Brantberger and Janson 2009, Table 7-6). In this context, an important potential side effect is the chemical stability of the near-field environment. Indeed, when grouting is subjected to a groundwater flow, calcium leaching and the release of alkali compounds, which may be leached as hydroxides during the grout hydration process, may lead to the formation of an Alkali Disturbed Zone (ADZ), which in turn may affect the stability of the bentonite material used for the buffer and backfill (especially the montmorillonite dissolution and transformation processes). Potential long-term safety concerns include loss of bentonite swelling pressure, increase in hydraulic conductivity, and loss of plasticity and cracking of bentonite due to a cementation process (see Laine and Karttunen (2010) for a review on these issues).

The grout is a mixture of cement and water and may contain additives, such as superplasticizers (added for workability purposes), and partial replacements of cement by supplementary cementitious materials (SCM) such as fly ash or silica fume. The cement used for grouting is often milled to a fine particle size and is referred to as micro-cement. The characteristic features of a high-pH plume due to grout degradation will be highly dependent on the raw materials used for grout production (ordinary cement, low-pH cements with silica fume, non-cementitious materials as silica sol, etc). In addition,

the composition of the grout mix will determine to a great extent the mechanical and transport properties of the hardened grout material and hence the leaching kinetics and degradation rate in a more general sense (Heikola 2008, Holt 2008, Orantie and Kuosa 2008).

In this work, only Ordinary Portland Cement (OPC) grout is considered, in which the presence of additives and SCM is limited. The chemical composition of the hydrated grout and its porosity depend on a number of factors, such as the origin and manufacturer of the base materials, the water-to-cement ratio, or the volume fraction of additives and SCM. In practice, the grout composition will vary also depending on the hydraulic aperture of the fracture that needs to be sealed (see e.g. Arenius et al. 2008, Brantberger and Janson 2009), the tunnel depth or on the post grouting of leaking bolts (Arenius et al. 2008). Therefore, it is expected that the grout composition will not be homogeneous throughout the grouted fracture network. This aspect will have a direct impact on the nature and the rate of the leachates released from the grout as a whole.

One important issue that determines the initial state of the grout is the quality of the grouting process. As an example, the homogeneity of the grout mix depends on an effective mixing process of the fresh grout. Moreover, and although a lot of effort has been devoted to standardize future grouting techniques at Forsmark (Brantberger and Janson 2009, Emmelin et al. 2007), grouting processes such as the stop criterion or the drilling of the grouting fans depend upon the expertise of the grouting crew and the local conditions found in the rock mass (Fransson 2008). The effectiveness of the grouting technique is relevant for the long-term durability of the grout. This is due to the fact that the degradation rate depends among other factors upon the ratio between the surface of the grout exposed to groundwater flow and the total grout volume. If the grout were very sparsely distributed, the surface exposed to water flow would be large in relation to the volume. Thus, it is expected that this situation would lead to a faster grout degradation compared to a case in which the grout is more homogeneously distributed in fewer locations.

Precipitation/dissolution of cementitious materials and grout durability issues

The cement clinker (mainly C_3S, C_2S, C_3A, and C_4AF, cement chemistry notation) together with the initial gypsum (if available) is gradually dissolved when mixing cement with water. The precipitation of hydration products result in the solidification of the cement paste (setting of the grout). The usual cement hydrates that are present in an OPC system are listed in Table 3-1 (see e.g. Lothenbach et al. 2008). A small amount of unhydrated clinker will generally remain in the grout, depending on the effectiveness of the hydration process. The large water-to-cement ratio used in the grout mixes to ensure correct penetrability (typically higher than 0.8) yield a very porous structure (Galíndez and Molinero 2010, Grandia et al. 2010) with poor mechanical properties. Moreover, the resistance against groundwater flow is also much lower than for cement paste with typical water-to-cement ratios in the range 0.3–0.5. This is specially the case in OPC grouts, in which the addition of silica fume is limited, which yields hydraulic conductivity values larger than 10^{-11} m/s (see e.g. Holt 2008, Lagerblad and Trägårdh 1995). In previous studies by Posiva, the hydraulic conductivity has been set to a value as high as $5 \cdot 10^{-9}$ m/s in simulations at the geosphere level (Pastina and Hellä 2010). It should be noted that even though the total porosity may be higher than 50%, the connected capillary porosity is much lower (Grandia et al. 2010). As a result, the permeability of the grout is not reduced proportionally to the total porosity.

Table 3-1. Hydration products in Ordinary Portland cement mixes.

Hydration products in OPC
C-S-H phases (variable Ca/Si ratio)
portlandite
ettringite
hydrotalcite
calcite
monocarbonate
monosulphoaluminate
hydrogarnet*

* in the long term.

The hydration of cementitious materials has been studied using thermodynamic modelling in recent studies (Lothenbach et al. 2008, Lothenbach and Winnefeld 2006, Soler 2010, Soler et al. 2011b). This has allowed to quantify the phase assemblage of the cement hydrates as well as to model the evolution of the porewater composition in a realistic way, leading to a relatively good agreement with experimental observations obtained using advanced techniques. In an OPC system, the dominating phases are C-S-H (calcium silicate hydrates) and portlandite, which compose a large fraction of the total solid phase. Another type of approach, namely using the CEMHYD3D software package, has also been recently used for predicting the hydrated phase assemblage of a low-pH grout (Galíndez and Molinero 2010, Grandia et al. 2010).

The hydrated cement grout will be subject to important hydraulic pressure gradients and groundwater flow will contact the exposed surface of the grout. In the long-term, this will inevitably induce a gradual leaching of the cement hydrates. Calcium leaching is a very slow process by which part of the cement hydrates are dissolved when cement is in contact with water. First, the readily soluble alkalis in the cement porewater will be released to the groundwater, with no important effects on grout stability. Following this first stage, the calcium in solution will start to be leached, inducing a gradual dissolution of the portlandite to maintain equilibrium with the porewater. Ettringite and monosulphoaluminate (AFm phases) dissolution and C-S-H decalcification will follow if continued leaching conditions prevail (Adenot 1992). Figure 3-1 depicts a typical cross-section of a leached cement paste sample, showing different mineral zonation between degradation fronts (Adenot 1992). The degradation depth due to the leaching process, as well as the cumulative calcium leached quantity, are typically proportional to the square root of time (Le Bescop and Solet 2006, Nguyen et al. 2007). Severe portlandite dissolution and C-S-H decalcification can induce a substantial increase in porosity and permeability (Yokozeki et al. 2004) and a decrease in the mechanical properties such as compression strength and Young modulus (Le Bellégo et al. 2003, Nguyen et al. 2007).

The calcium leaching rate will obviously depend on the chemical composition of the groundwater in contact with the grout, which may in turn vary in time. In turn, the presence of certain aqueous species in the solution may accelerate the degradation of the grout by other coupled chemo-mechanical processes. This is the case with sulphate ions in solution (e.g. in the form of sodium or magnesium sulphate), which may lead to the formation of secondary expansive ettringite in the grout bulk (Santhanam et al. 2002). Ettringite precipitation is followed by a reduction in the total porosity. However, in the case of substantial expansions, the grout could be severely cracked, which could have a negative impact on the transport properties and degradation rate (Brown and Taylor 1999, Idiart et al. 2011). It is noted that even in the case of sulphate resistant cement (with a low C_3A initial content), there is evidence that the expansions due to sulphate attack may still occur in the long-term.

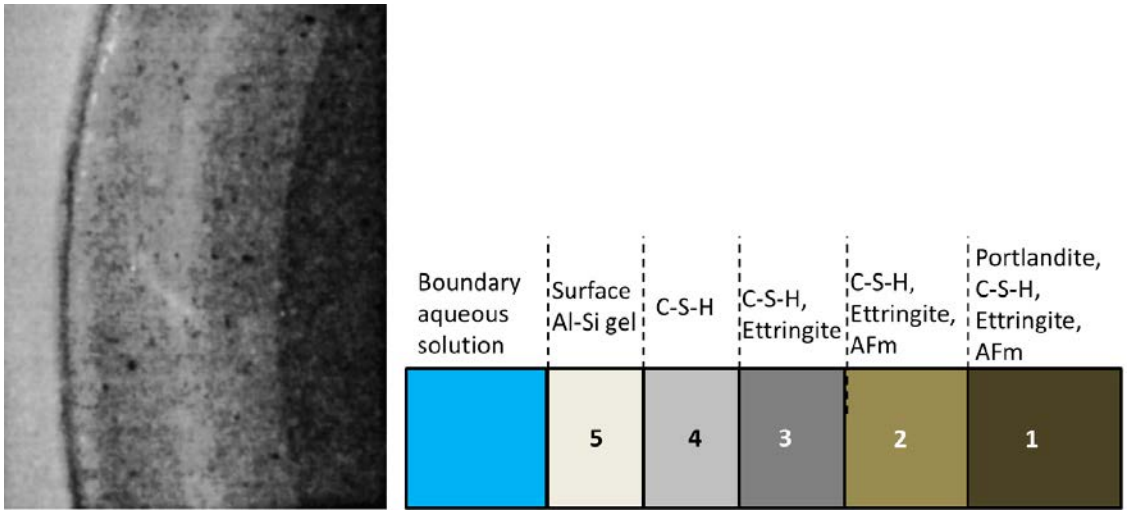

Figure 3-1. *Degradation fronts in a cement paste sample: (left) photo from Adenot (1992), and (right) illustration of the different degradation fronts.*

The presence of chlorides in solution in addition to sulphates may be beneficial for the durability of the grout, as sulphate attack is mitigated to some extent, due to the precipitation of Friedel's salt, a reduced amount of sulphate products, and a reduced expansivity of the secondary ettringite (Lee et al. 2008).

The presence of carbonates in the groundwater could lead to the precipitation of calcite in the grout surface exposed to flow (Lagerblad and Trägårdh 1995). This could result in a reduction of the porosity of the grout due to the higher molar volumes of the reaction product (i.e. calcite) with respect to the reactants (Galíndez and Molinero 2010, Grandia et al. 2010). These reactants consist mainly of portlandite, but also other cement hydrates may dissolve (Thiery et al. 2007). Since calcite precipitation does not entail expansion of the cement paste, the reduction in porosity will decrease the permeability of the grout. Therefore, in this case the long-term performance of the grout is enhanced provided that no other deleterious reactions occur.

To complicate things, in the presence of sulphates and chlorides simultaneously with a carbonate source, the degradation of the grout could be enhanced when compared to conventional external sulphate attack. In this case, thaumasite precipitation may occur in cementitious alkaline systems (Hobbs 2003). In addition, low temperatures (4–15°C) close to the conditions at Forsmark site would favour the stability of thaumasite. Compared to ettringite, the alumina is replaced by silicon and the carbonate partly substitutes the sulphate in thaumasite. Therefore, the formation of thaumasite requires a source of calcium silicate (mainly C-S-H phases), sulphate, carbonate and humidity (Schmidt 2010 and references therein). As it forms, the concrete or mortar converts to a friable material which disintegrates rather easily. There are several possible sources of carbonate that can lead to thaumasite precipitation in cementitious systems, among which there is the carbonate in groundwater (Romer et al. 2003). It has been suggested that the thaumasite form of sulphate attack is magnified by the presence of chlorides (Torres et al. 2003). It is noted that thaumasite precipitation does not involve aluminium. Therefore, while the use of sulphate-resisting Portland cement limits the degradation process of conventional sulphate attack (to some extent), it does not represent an effective measure against thaumasite formation.

OPC leachate water composition

The OPC leachate composition is intimately related to the grout porewater composition. As a consequence of the hydration process of the cementitious grout, the porewater composition evolves in time due to the clinker gradual dissolution and the precipitation of cement hydrates, such as amorphous C-S-H phases, portlandite, ettringite, or monosulphoaluminate (Lothenbach et al. 2008). In an OPC system, the pH of the porewater evolves with the hydration process, and if no leaching occurs the pH will rise to a value higher than 13.0. However, when the system is allowed to interact with external groundwater with a very different composition, the grout will release OPC leachates. The composition of the leachates will depend to a large extent on the gradients between the species concentrations in the groundwater and in the grout porewater.

Regarding the leaching process, there is a consensus in that the degradation of OPC can be regarded as a three-stage process (Miller et al. 2000, Wang et al. 2010, and references therein). First, the leachates released from cement are rich in alkalis (i.e. Na and K) with a pH > 13.0. These alkalis are readily released to the groundwater and the rate limiting is the transport through the grout porous network. Since there is in principle no source of alkalis in the solid phase, it is expected that the pH of the porewater will rapidly drop to a value below 13.0. Thereafter, in a second stage, the high concentration of Ca due to the dissolution of portlandite buffers the pH to a value of around 12.5. Finally, in the last stage, when portlandite has been depleted, chemistry is controlled by the solubility of the (amorphous) C-S-H phases, with a pH that ranges from 12.5 to around 10. Figure 3-2 depicts a pH evolution curve that considers these aspects (adapted from Miller et al. 2000). The dependence between the pH of pore water and the Ca-Si ratio of the C-S-H has been studied by a number of researchers. A large set of experimental data has been gathered in Grandia et al. (2010) and is shown in Figure 3-3. The decrease of the pH from 12.5 to 10 in Figure 3-2 depends upon the relation between pH and Ca-Si ratio in the C-S-H, with Ca-Si ratios in the range 0.75 to 1.25, approximately.

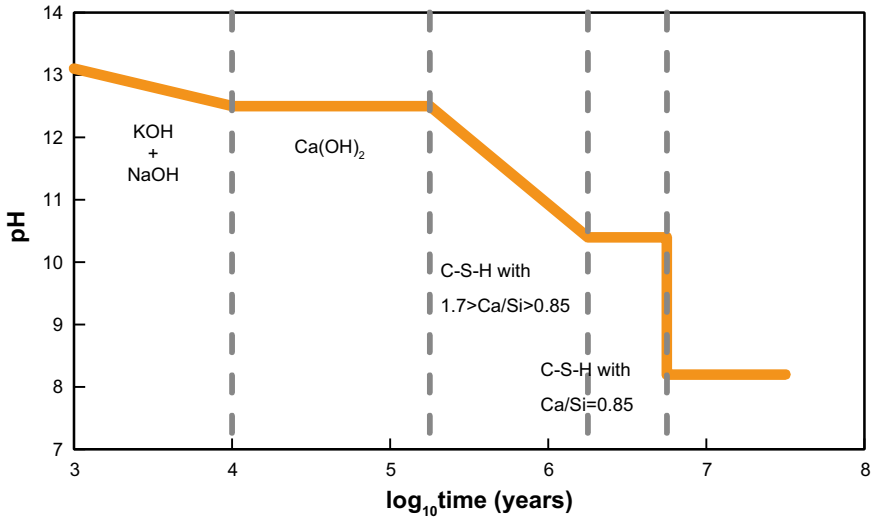

Figure 3-2. *Estimation of pH evolution of Ordinary Portland Cement pore fluid (adapted from Miller et al. 2000). C-S-H: calcium-silicate hydrate. Ca/Si: calcium/silica ratio.*

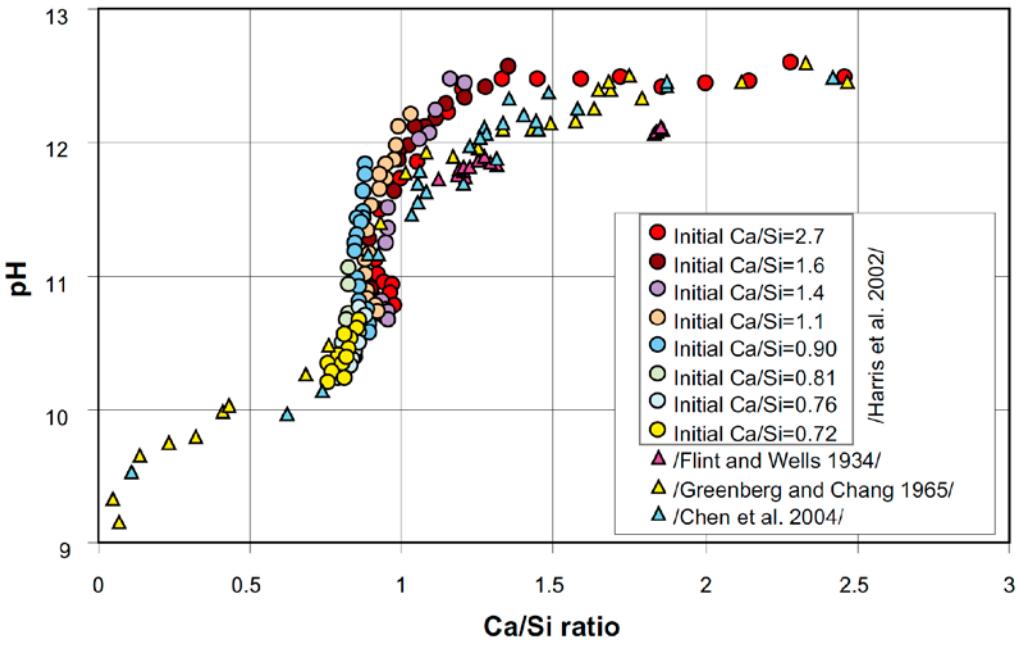

Figure 3-3. *Evolution of the C-S-H composition vs. pH reported from experiments in the literature (extracted from Grandia et al. 2010).*

Given the relatively low availability of alkalis in cement porewater, it seems reasonable to assume that the pH of the OPC leachates will be rapidly governed by the dissolution of portlandite, thus fixing the pH to a value between 12.3 and 12.6 (see e.g. Moranville et al. 2004). This procedure has been followed by a number of authors in previous studies on the development and effects of a alkaline plume (Lichtner and Eikenberg 1994, Savage et al. 2002, Steefel and Lichtner 1994, 1998, Watson et al. 2009). In some of these studies an additional scenario corresponding to an early age porewater composition (considering the effect of alkalis) has also been considered, although it is recognized that pH will be governed by portlandite dissolution in the mid- and long-term (see also Savage et al. 2011).

In order to calculate the composition of the cement porewater after leaching of the alkalis, a given reference water is typically equilibrated with portlandite (Savage et al. 2002, Watson et al. 2009) and optionally with additional cement hydrates such C-S-H, ettringite, brucite, etc (Lichtner and Eikenberg 1994, Steefel and Lichtner 1994, 1998). However, the pH will still be governed by portlandite in the latter case. The composition of the water prior to equilibration depends on each particular problem, but it is generally assumed that it is a reference groundwater composition. More recent studies use more sophisticated models to simulate the simultaneous hydration and leaching of the grout, leading to a more realistic evolution of the leachate composition in time (Soler 2010, Soler et al. 2011b). However, these studies were focused on low-pH cement, which has not been considered in this work. Moreover, in the present study it was decided not to simulate realistically the high-pH pulse duration. Instead, scoping calculations are performed under a very aggressive scenario in which portlandite dissolution controls the pH of the OPC leachates throughout the simulations. In this way, the pH is fixed as a boundary condition to a value of around 12.4.

Other aspects influencing grout durability

Other aspects that may compromise the long-term performance of the grout are related to the potential mechanical changes that the bedrock may undergo. These could be a result of natural events, such as glaciations (glacial offloading) or tectonic events, or events during construction and operation of the repository (Alexander and Neall 2007), which could lead to an alteration of the fracture system in terms of an increase of fracture apertures and changes in fracture connectivity (see also Chapter 2). These processes could affect existent grouted fractures. For instance, in the case of a grouted fracture that is subject to an increase of the fracture aperture, the grout will not serve as a barrier for groundwater flow anymore. Thus, the transmissivity of that fracture will be increased. In this case, also the durability of the grout will be severely compromised, since the surface exposed to groundwater flow will be significantly increased.

During the glaciation period, the porewater in the grout will be subject to very low temperatures, with the consequent expansion due to ice formation. In the event of freezing/thawing cycles of the porewater in the grout, internal pressures (loading-unloading) will develop which may induce micro-cracking of the grout (Zuber and Marchand 2000). As a consequence, a reduction of the grout resistance against groundwater flow would be expected.

3.2.2 pH buffering reactions along flow paths

The geochemistry of alkaline solutions is characterized by the strong dependence of speciation on pH for many components that affects mineral solubilities and aqueous complexation. Some of the key aspects of alkaline geochemistry have been summarized in Mäder and Ekberg (2006). In the following, some basic concepts of the geochemical behaviour of a system under highly alkaline conditions, as the one considered in this work, are outlined.

Dissolution of primary minerals

Under highly alkaline conditions, the dominant aqueous species of the principle components can differ significantly from the aqueous species found under near neutral pH conditions. These changes will have a large impact on the dissolution/precipitation processes of most of the silicates found e.g. in the Forsmark site.

In a pure aqueous hydroxide system the highest pH that may be attained is limited by the solubility of the corresponding solid hydroxide: the upper pH limits for the pure Mg-OH and Ca-OH systems at 25°C is 10.2 (limited by brucite) and 12.5 (limited by portlandite), respectively. Higher pH values can be reached only if an additional K-OH or Na-OH components are available (Mäder and Ekberg 2006).

The dissolution of silicates is known to consume protons (i.e. acid buffering) at conditions near neutral pH. However, under highly alkaline conditions, the behaviour is reversed, and the dissolution yields consumption of hydroxides (pH buffering capacity). For example, at a pH between 10 and 11.5 K-feldspar dissolution will consume OH^- due to the change in the predominant aqueous species with silica relative to near neutral pH conditions (Mäder and Ekberg 2006). Therefore, the dissolution of K-feldspar will buffer high-pH water towards a pH value of around 10.

Under highly alkaline conditions (pH above 10–12) the dissolution of silicates and most oxides will buffer the solution towards a lower pH value. This is the case of quartz and plagioclase (e.g. albite) which are known to react quite readily at high-pH conditions.

The dissolution/precipitation kinetic rates (denoted as r_i, in mol/m^3 of rock/s) for the different kinetically constrained minerals ($i = 1 \ldots N_K$, where N_K is the number of minerals under kinetics) used in this work have the simplified form given by the following expression (e.g. Palandri and Kharaka 2004):

$$r_i = \pm SA_i \left(k_{25}^{nu} + k_{25}^{H+} a_{H+}^{n_H} + k_{25}^{OH-} a_{OH-}^{n_{OH}} \right)_i \left(\Omega_i - 1 \right) \quad (3\text{-}2)$$

in which SA_i (m^2/m^3 of rock) is the reactive surface area of mineral i, k_{25}^j (mol/m^2/s) is the reaction rate constant for the different mechanisms (j = nu in pure water at neutral pH, $j = H^+$ for the acid mechanism, and $j = OH^-$ for the base mechanism) that are specific for each mineral, a_j is the activity of species j, n_j is a power constant, and Ω_i is the saturation ratio for mineral i. Positive r_i values are for precipitation and negative values denote dissolution.

The kinetic rate laws for the dissolution of silicates usually display a sharp increase with increasing pH (see Brantley et al. 2008, Palandri and Kharaka 2004, and references therein).

In the cases where the porosity changes due to chemical reactions do not significantly affect the transport of solutes, the high-pH plume through the fractures will reach a steady state situation in which the pH profile along the fracture does not vary with time anymore (provided that an unlimited source of primary minerals is considered). The shape of the pH profile will be determined by the combination of the advective-dispersive transport conditions and the dissolution reaction rates of the primary minerals. Under steady state conditions, the dissolution/precipitation rates will not vary with time and therefore a continuous dissolution or precipitation will keep the pH at a constant level. This situation will also be accompanied by a constant rate of precipitation of secondary minerals.

Precipitation of secondary minerals

The fast dissolution rates for primary minerals may lead to a transient situation of oversaturation in the associated pore solution with respect to silica, alumina, calcium and magnesium. This situation can trigger an important precipitation of cement hydrates such as C-S-H and C-A-S-H phases or brucite. The actual degree of supersaturation will depend on the flow regime, the specific surface areas of the minerals involved, and the travel time (Mäder and Ekberg 2006). Therefore, precipitation of these phases will generally be a function of space and time.

The precipitation of secondary minerals also plays an important role in the pH buffering capacity of a system. For instance, the precipitation of brucite at high pH is accompanied by a consumption of OH^-.C-S-H and C-A-S-H phases also control to a large extent the concentration of silica, calcium and aluminium in solution. Moreover, C-S-H phases are stable over a fairly wide range of pH (from 10 to over 13), and may coexist with zeolites in the range of pH 10–11 (Mäder and Ekberg 2006). The precipitation of secondary minerals is generally controlled (and limited) by primary mineral dissolution. Therefore, these have been traditionally considered under local equilibrium (Montori et al. 2008, Savage et al. 2011, Soler and Mäder 2007, Steefel and Lichtner 1994).

In order to assess the pH buffering capacity of the fracture system against an alkaline plume, it is necessary to quantify the extent of the interaction between the grout leachates and the minerals in the fracture surfaces and partially filling the fracture (fault infill or gouge). The dissolution of primary minerals and the precipitation of secondary minerals in the fracture near the grouted zones as a result of this interaction could buffer the pH to some extent. The mineral phases that could potentially precipitate in this scenario are the following (Alexander 2010, Lichtner and Eikenberg 1994, Montori et al. 2008, Savage et al. 2011, Soler et al. 2011b, Soler and Mäder 2007):

- brucite,
- amorphous and/or crystalline C-S-H,
- amorphous and/or crystalline C-A-S-H phases,
- other cement hydrates (ettringite, monosulphoaluminate, etc),
- calcite,
- zeolites,
- saponites.

The precipitation of secondary minerals could eventually lead to a gradual sealing of the fracture and porosity reduction of fracture infillings (Alexander 2010, Montori et al. 2008, Soler 2010). The hydraulic conductivity may be then significantly reduced, as already determined experimentally in Soler and Mäder (2010). This reduction is beneficial, because the transport of the alkaline plume could be retarded or even completely stopped. The role of Mg-bearing phases like brucite, and saponite-Mg in the sealing of porosity has been pointed out as important in previous modelling studies (Montori et al. 2008, Steefel and Lichtner 1994), although no experimental or natural analogues studies exist (to the authors' knowledge) to support this. The porosity clogging occurred faster in the cases where Mg-bearing phases were considered as secondary minerals, compared to the simulations in which these phases were disregarded (Montori et al. 2008).

It has previously been stated that the interaction between alkaline solutions and the host rock will generally modify the hydraulic conductivity of almost any fracture, significantly altering transport processes through the fracture network (Alexander 2010). However, it is noted that even if reliable modelling tools were available to predict such effects on fracture transmissivity, the impact of fracture reactivation due to mechanical changes in the bedrock could overcome the sealing of fractures by secondary minerals. Moreover, the interaction between the cement leachates and the grout with the fracture minerals is not expected to occur homogeneously in space (within the fracture plane), but in a heterogeneous manner. This is not possible to simulate in a model that considers transport through a fracture in a 1D fashion, as in the present work. With this in mind, the complete sealing of a grouted fracture by precipitation of secondary phases appears as a strong assumption. Therefore, it is thought that considering a conservative scenario in which fracture sealing is not modelled may be more appropriate at this point.

Interaction of grout and cement leachates with the rock matrix

Cement leachates – rock matrix interaction

The interaction of the cement leachates with the rock matrix has been studied by a number of authors (Soler et al. 2011b, Steefel and Lichtner 1994, 1998). The cement leachates can diffuse through the rock matrix porosity and react with the minerals present. In this way, the rock matrix could represent an additional source of pH buffering capacity while at the same time retarding the transport of the high-pH plume.

Steefel and Lichtner (1994) studied the solute diffusion from an alkaline fluid-filled fracture into a marl rock matrix. In their calculations, the pH drop within the rock matrix was primarily due to the dissolution of dolomite and consequent precipitation of brucite (accompanied by calcite precipitation). In addition, the model also predicted the precipitation of katoite (crystalline hydrogarnet phase) and foshagite (crystalline C-S-H phase), and to a lesser extent of sepiolite, gibbsite, and some zeolites. As a consequence of the diffusion of fluid into the rock matrix, the matrix porosity was predicted to be filled by calcite within the first 10 to 500 years, except adjacent to the fracture, where a slight increase in porosity was predicted.

Calcite precipitation has also been identified as the responsible for porosity reduction in the rock matrix adjacent to the fracture in a recent modelling study by Soler et al. (2011b). This reaction was also accompanied in this case by some precipitation of saponites and zeolites deeper into the rock matrix.

Grout – rock matrix interaction

The grout is not only exposed to the interaction with groundwater flow. In fact, most of the outer surface of the grout is in contact with the fracture walls. Thus, the grout-rock interaction should also need to be addressed. The interaction of grout (during hydration and beyond) with fracture minerals and the rock matrix has been recently assessed with numerical modelling in Soler (2010) and Soler et al. (2011b). Model predictions suggest that the grout-rock interaction is limited by a fast (few days) precipitation of cement minerals (C-S-H, C-A-S-H, and ettringite) in the vicinity of the cement-rock interface, preventing further reactions by sealing of the matrix.

However, recent experiments have not confirmed the simulation results (Cama et al. 2012). In fact, after 19 days there were no signs of mineral precipitation in these experiments. This discrepancy has been attributed in part to the large reactive surface areas considered in the model, as opposed to what is expected in a low porosity bulk rock, where most mineral surfaces may not be directly in contact with water (Cama et al. 2012), thus greatly reducing the reactivity of the rock.

3.2.3 Summary of chemical processes

In this section, the diverse chemical processes that are involved in the development and during the transport through the fracture network of an alkali disturbed zone (ADZ) have been discussed. The coupling with mechanical and hydraulic processes has also been addressed.

First, some considerations regarding the initial state and the evolution in time of the grout have been introduced. Different issues as the construction techniques, the geochemical processes during hydration, and the chemo-mechanical processes that will determine to a large extent the durability of the grout have been briefly presented. The aim of this introduction has been to show the complexity of the processes that determine the evolution of the grout, which is considered in this work as the source term for the ADZ. As will be presented in the following sections, the source term has been conceptualized in this work as an alkaline solution in equilibrium with portlandite and with a constant composition in time. This simplification is based on the discussion regarding OPC leachate water composition and may be regarded as a worst case scenario, in which the availability of the high-pH leachates is constant in time. It has been considered that for the purpose of the scoping simulations intended in this work this assumption is reasonable and conservative.

Section 3.2.2 discussed the geochemical processes that are expected to occur during the transport of the alkaline plume through the fracture network and its associated rock matrix available for diffusion of solutes. All these processes have been included in the conceptualisation of the problem in the reactive transport modelling presented in Chapter 7, except for the grout-rock matrix interaction processes. The presence of grout is not considered explicitly in the conceptual model, but a constant OPC leachate composition is used as boundary condition.

It may be stated that the degree of confidence is acceptable regarding the precipitation of secondary minerals as a result of the alkaline plume – fractured rock interaction. With a good level of approximation, secondary minerals are usually assumed to precipitate under equilibrium, since it occurs fast compared to transport processes and primary mineral dissolution. However, for the primary minerals, it should be noted that experimental data on silicate dissolution reaction rates for alkaline conditions (pH > 10–11) are scarce. Therefore, the extrapolation of the pH dependency functions of the reaction rates can only be considered as an approximation (Mäder and Ekberg 2006, Pfingsten et al. 2006).

Moreover, a larger uncertainty exists in the determination of the reactive surface area for the different minerals in the fracture infill and the rock matrix (Luttge 2011, Rowe and Brantley 1993, Savage et al. 2011, Soler et al. 2011b). This is in part due to the inherent difficulties in the available experimental procedures to directly measure surface areas (e.g. BET surface area) that can then be extrapolated (or upscaled) to field conditions (see e.g. Steefel et al. 2005). On the other hand, the calculation of surface area based on geometric considerations is also limited by the usual assumptions considered to simplify the system topology. The determination of the reaction rates and surface areas has been already pointed out as a source of uncertainty in previous studies of the diffusion of a alkaline plume in a marl rock matrix (Savage et al. 2011, Steefel and Lichtner 1994). In that study, the sensitivity of the model to reactive surface area was assessed, leading to substantial differences in the pH buffering capacity of the rock matrix.

4 Conceptualisation

In this section, the problem of OPC leachate ingress along flow paths in the rock is conceptualised based on the various processes and observations/natural analogues in previous sections. The section is divided into two main domains; a hydrogeological conceptualisation which form the basis for the modelled flow field and flowpath calculations in subsequent sections; and a conceptualisation of the mechanistic understanding of the reactive transport processes.

4.1 Hydrogeological conceptualisation

The models described here are based on those used for SR-Site, as described in Joyce et al. (2010), Svensson and Follin (2010) and Vidstrand et al. (2010) and adopt the same basic conceptualisation. The site at Forsmark consists of fractured crystalline bedrock overlain with Quaternary deposits. This is represented conceptually by a division in to three hydraulic domains:

- HCD (Hydraulic Conductor Domain) representing deformation zones,
- HRD (Hydraulic Rock mass Domain) representing the less fractured bedrock in between the deformation zones, and
- HSD (Hydraulic Soil Domain) representing the regolith (Quaternary deposits).

A representation of these domains is shown in Figure 4-1. The HRD and HCD fractures are characterised based on site borehole data and include a depth dependent fracture intensity and transmissivity profile. Both fracture intensity and transmissivity decrease with depth. In particular, there is a dominant horizontal flow in the upper 200 m of bedrock arising from the sheet joints, which form a shallow bedrock aquifer.

The HCD is represented by a series of deterministic fractures, one per deformation zone. Each was given a geometry, a thickness and a set of depth dependent transmissivities based on the site data. Transmissivity values were also conditioned around borehole measurement locations. Porosity values were calculated as a function of transmissivity and thickness. In the hydrogeological base case, a deterministic set of properties were used plus ten realisations of stochastic properties. In this study only deterministic properties were used for the deformation zones. Figure 4-2 shows representations of deformation zones with deterministic and stochastic properties. The sheet joints are also represented by a set of deterministic fractures whose properties were obtained by interpolation of site data.

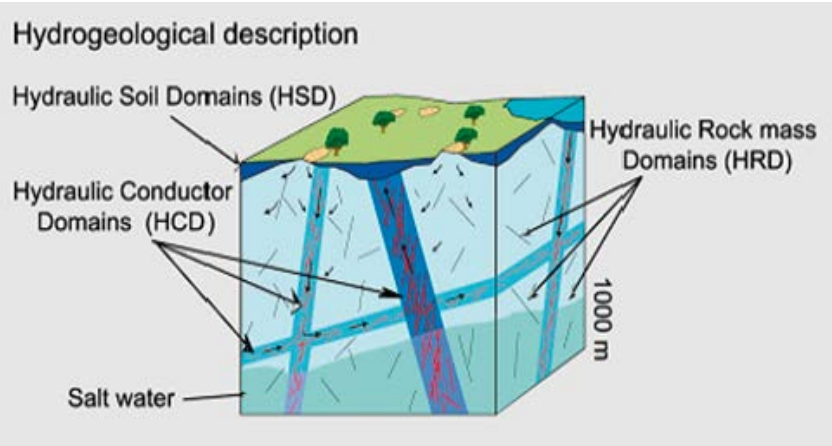

Figure 4-1. *Schematic showing the division of the crystalline bedrock and the regolith (Quaternary deposits) into three hydraulic domains, HCD, HRD and HSD. (Rhén et al. 2003, Figure 3-2).*

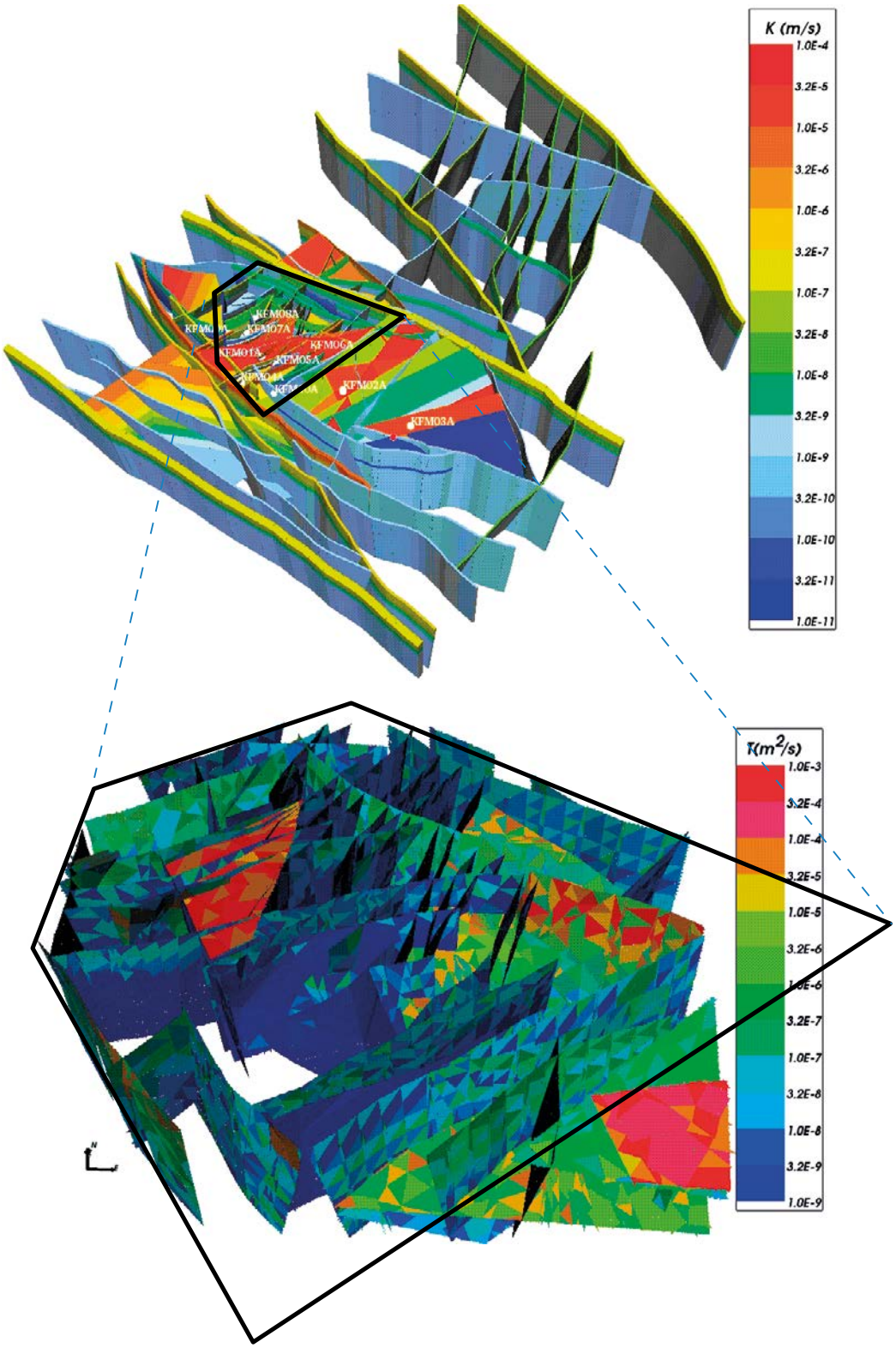

Figure 4-2. *Top: The resulting homogeneous (deterministic) property model of the deformation zones. Here, the regional scale deformation zones are coloured to indicate the hydraulic conductivity within the zones and drawn as volumes to show their assigned hydraulic width. Bottom: Example visualisation of a stochastic realisation of the deformation zones that occur inside the local model domain. (Adapted from Follin 2008, Figures 6-1 and 6-2).*

Within the candidate area, the HRD is divided into six fracture domains, FFM01 to FFM06 (Figure 4-3), each of which has five fracture sets (NS, NE, NW, EW and HZ) and three depth zones (above –200 m, –200 m to –400 m and below –400 m elevation). These represent a grouping of the fractures according to location and characteristic properties. Outside the candidate area a lack of borehole data led to the adoption of a continuous porous medium (CPM) concept for the SR-Site hydrogeological base case model. However, subsequent data from investigations at SFR (Öhman and Follin 2010) allowed an initial fracture characterisation of the surrounding bedrock, leading to the extended spatial variability case described in Joyce et al. (2010). This case forms the basis of the hydrogeological models described in this report as it provides an extended fractured region. This extended region may be important when considering the discrete flows through fractured rock that provide the recharge to the repository.

The HSD has been conceptualised into a layered structure of varying thickness to which has been assigned properties representing the Quaternary deposits, as shown in Figure 4-4. Each layer is described in Table 4-1. The numerical implementations of the HSD are presented in Joyce et al. (2010), Svensson and Follin (2010) and Vidstrand et al. (2010).

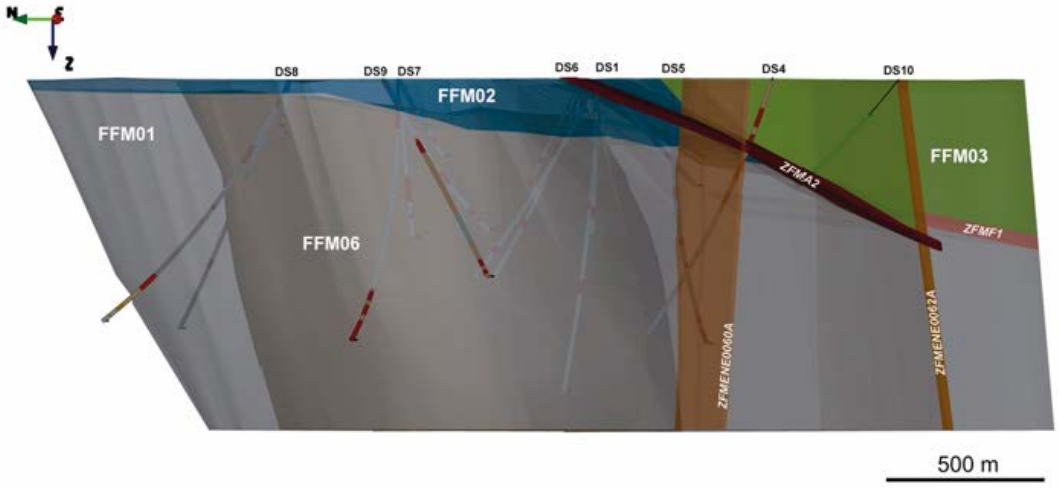

Figure 4-3. *Three-dimensional view of the fracture domain model, viewed towards ENE. Fracture domains FFM01, FFM02, FFM03 and FFM06 are coloured grey, dark grey, blue and green, respectively. The gently dipping and sub-horizontal zones A2 and F1 as well as the steeply dipping deformation zones ENE0060A and ENE0062A are also shown (Follin 2008, Figure 3-10).*

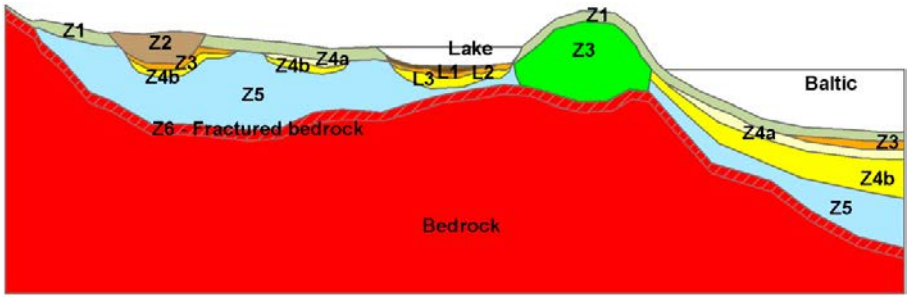

Figure 4-4. *Conceptual model for the layering of Quaternary deposits at Forsmark. The different layers are explained in Table 4-1. (Hedenström et al. 2008, Figure 3-1).*

Table 4-1. Names and definitions of Quaternary deposits (Hedenström et al. 2008, Table 2-4).

Layer	Description and comments
L1	Layer consisting of different kinds of gyttja/mud/clay or peat. Interpolated from input data, thickness will therefore vary.
L2	Layer consisting of sand and gravel. Interpolated from input data, thickness will therefore vary.
L3	Layer consisting of different clays (glacial and postglacial). Interpolated from input data, thickness will therefore vary.
Z1	Surface affected layer present all over the model, except where peat is found and under lakes with lenses. Thickness is 0.10 m on bedrock outcrops, 0.60 m elsewhere. If total regolith thickness is less than 0.60 m, Z1 will have the same thickness as the total, i.e. in those areas only Z1 will exist.
Z2	Surface layer consisting of peat. Zero thickness in the sea. Always overlies by Z3.
Z3	Middle layer of sediments. Only found where surface layers are other than till, clay or peat.
Z4a	Middle layer consisting of postglacial clay. Always overlies by Z4b.
Z4b	Middle layer of glacial clay.
Z5	Corresponds to a layer of till. The bottom of layer Z5 corresponds to the bedrock surface.
Z6	Upper part of the bedrock. Fractured rock. Constant thickness of 0.5 m. Calculated as an offset from Z5.

The hydrogeological conditions at Forsmark are also affected by a number of transient changes, such as climate conditions and sea level changes. Following a period of glaciation, the site is expected to be submerged. During this period, head gradients will be low and there will be a period of density driven flow when glacial water will be replaced by infiltrating sea water. Due to post-glacial land rise, the site will emerge from the sea and the infiltrating sea water will be replaced by meteoric water. As the land continues to rise, groundwater will tend discharge to a retreating shoreline. The duration of the temperate period is uncertain and will be affected by factors such as global warming (SKB 2010b). Permafrost will precede the next glacial period, causing changes to the hydraulic properties of the upper bedrock and soil layers. During the glacial period, advancing and retreating ice sheets will cause large head changes and give rise to infiltration of glacial melt water, replacing the meteoric water.

This report examines the effect of introducing alkaline water released from injected grout in the upper portion of the ramp and shafts in the central area of the repository. It is assumed that the grout has a penetration distance of 5 m into the rock around the ramp and shafts. It is also assumed that the alkaline water released by the grout is produced indefinitely and does not vary in composition over time. Therefore the source of alkaline water is considered to be the same during the open repository, temperate and glacial situations. Two depths of grouting are considered, one to a depth of 200 m and one to a depth of 370 m. An alternative repository sealing case is also considered where the bentonite backfill in the upper 370 m of the ramp and shafts is replaced by coarsely crushed rock, with a grouting depth of 370 m. A summary of the cases considered is given in Table 4-2.

4.2 Conceptualisation of the reactive-transport problem in the fracture – rock matrix system

Transport in fractured bedrock involves a number of different physic-chemical processes (SKB 2004) that take place in a complex (and spatially variable) geometry of the fracture and the adjacent rock matrix (Winberg et al. 2003). The problem of reactive transport through fractured porous media can be conceptualised in a number of ways (see e.g. the review by MacQuarrie and Mayer 2005).

Table 4-2. Case summary.

Case	Ramp/shaft backfill	Grout depth (m)
200 m grouting	SR-Site	200
370 m grouting	SR-Site	370
370 m sealing	Coarsely crushed rock above –370 m	370

One well-known approach is the one-dimensional dual porosity approach, in which the fracture rock is conceptualised as being composed of two continua coexisting at all points of interest, the fracture and the matrix (e.g. Lipson et al. 2007). Another approach is the discrete fracture models, in which the fracture and the rock matrix are explicitly discretised either in a 2D or a 3D framework (Sidborn et al. 2010, Steefel and Lichtner 1998, Xu and Pruess 2001). Finally, equivalent continuum models have also been proposed for a fractured porous rock, characterized by equal fracture and matrix solute concentrations (MacQuarrie and Mayer 2005). In this approach the solute transport properties of the equivalent continuum are obtained by weighted averaging of fracture and matrix properties such as porosity, tortuosity and mineral surface areas.

In this work, the problem of the alkali disturbed zone (ADZ) is simulated using a two-dimensional framework, considering a fracture and the associated rock matrix The geometry has been assumed symmetric with respect to the fracture mid-thickness, and therefore the model only considers half of the fracture aperture and a rock matrix with no flow conditions at the matrix final depth. This corresponds either to the assumption of equidistant fracture spacing, or to a case in which the rock matrix available for diffusion is limited to a certain depth, which is probably a conservative assumption in the case of the Forsmark site.

There is an inherent numerical complexity of modelling reactive transport through a fracture with matrix diffusion which is mainly due to two aspects. On one hand, the domain discretisation presents very different length scales between the fracture length (typically with a length in the tens to hundreds of meters range) and the rock matrix, with a width that is much smaller than the fracture length. On the other hand, the solute transport along the fracture length is usually advective-dispersive, while the very low porosity of the rock matrix limits solute transport to diffusion only. Moreover, molecular diffusion and chemical reactions in the rock matrix may limit the geochemically altered zone to a narrow region adjacent to the fracture surface (see e.g. Steefel and Lichtner 1998). Therefore, the transport in the direction perpendicular to the fracture plane is much slower than along the fracture. As a result, the discretisation of the geometry needs to be much more refined in the direction perpendicular to the fracture plane. To simultaneously capture both reactive transport processes at the field-scale may thus require a disproportioned number of grid cells (MacQuarrie and Mayer 2005). This situation generally leads to models in which the grid elements are distorted, which may induce numerical instabilities.

In addition to this, the complexity of the geochemical setup considered in this work also has an influence on the convergence of the numerical simulation: large concentration and pH gradients, pH-dependent kinetic mineral reactions mixed with precipitation of minerals at equilibrium, and large number of minerals and aqueous complexes. In an attempt to decrease the uncertainty in the thermodynamic and kinetic data, it was decided to perform all the simulations at 25°C because most of the available data have been produced at this temperature (although a more realistic value should be around 15°C).

In this work, the fracture has been conceptualized as a porous medium with fracture infill materials occupying half of the porosity. In turn, the rock matrix has been idealized as a homogeneous porous medium with a very low porosity such that advective transport is negligible, and only diffusion is relevant. The matrix depth available for molecular diffusion is assumed finite, as will be outlined in Section 7.2.

The interaction between the groundwater flowing in the fractures and the stagnant water in the pores of the adjacent rock matrix is typically assessed by the flow related transport resistance or F-factor, which is defined as the ratio between the flow-wetted surface (surface of the fracture in contact with the flowing water) and the flow-rate in the flow channel (see Equation 3-1, Section 3.1). Different F-factors have been considered in this work, assuming a fixed length and varying the velocity of the flow.

The source of the ADZ has been conceptualized conservatively with an alkaline solution in equilibrium with portlandite, with a fixed pH of 12.4, and a constant composition, following the discussion of the chemical processes presented in Section 3.2.

5 Data

5.1 Transport related parameters in the rock matrix

The transport properties of the rock matrix are taken from the SR-site hydrogeological modelling (Joyce et al. 2010, Svensson and Follin 2010, Vidstrand et al. 2010). A dual porosity model is used in some of the models described here, with different properties for the fractures and the rock matrix. In other models described here an effective porosity is used, which represents a combination of the fracture and matrix porosities (see further Chapter 6 for more detailed descriptions of the models used). The DFN models reported here only use the fracture porosity, implemented in terms of a transport aperture for discrete fractures. The fracture porosity in ECPM models is obtained by upscaling the DFN for the extended spatial variability case, developed in SR-Site, as described in Joyce et al. (2010). Other properties for the rock matrix are as specified for the SR-Site hydrogeological base case.

5.2 Hydraulic properties of the rock

The hydraulic properties of the rock are the same as those used for SR-Site (Joyce et al. 2010, Svensson and Follin 2010, Vidstrand et al. 2010) for the extended spatial variability case. These properties are based on a DFN for the bedrock that uses a semi-correlated fracture size to transmissivity relationship where the FFMs are defined (Equation 5-1), where T is transmissivity, r is fracture radius, a and b are the factor and exponent respectively of the power-law relationship between r and the mean of $\log_{10}(T)$, σ is the standard deviation of $\log_{10}(T)$ and $N(0,1)$ denotes a normally distributed random deviate with a mean equal to zero and a standard deviation of 1. The parameters for FFM01 and FFM06 are reproduced in Table 5-1. Outside the region defined by the FFMs, preliminary data from investigations at SFR (Öhman and Follin 2010) allowed an initial fracture characterisation, with a correlated fracture size to transmissivity relationship (Equation 5-2), using the parameters given in Table 5-2. This reduced the uncertainties in the physical properties of the bedrock outside the FFM region and allowed an extended DFN region to be used and an ECPM representation to be used everywhere outside the DFN region. This provides a better representation of the discrete flow pathways in fractured rock.

$$T = 10^{\log(ar^b)+\sigma N(0,1)} \tag{5-1}$$

$$T = ar^b \tag{5-2}$$

The transient evolution of the site is affected by land rise and the Baltic Sea salinity evolution. The SR-Site data for these processes are used, as reproduced in Figure 5-1 and Figure 5-2 respectively.

Table 5-1. Hydrogeological DFN parameters for the semi-correlated transmissivity model of FFM01 and FFM06 with depth dependency: above –200m, –200 m to –400 m and below –400 m RHB 70. (Follin 2008, Appendix C).

Fracture domain (m RHB 70)	Fracture set name	Orientation set pole: (trend, plunge) conc.	Size model, power law (r_0, k_r) (m, –)	Intensity, (P_{32}), valid size interval: (r_0, 564 m) (m^2/m^3)	Parameter values for the transmissivity model shown in Equation 5-1 T (m^2s^{-1})
FFM01 and FFM06 above –200	NS	(292, 1) 17.8	(0.038, 2.50)	0.073	(a,b,σ) = (6.3 ·10^{-9}, 1.3, 1.0)
	NE	(326, 2) 14.3	(0.038, 2.70)	0.319	
	NW	(60, 6) 12.9	(0.038, 3.10)	0.107	
	EW	(15, 2) 14.0	(0.038, 3.10)	0.088	
	HZ	(5, 86) 15.2	(0.038, 2.38)	0.543	
FFM01 and FFM06 –200 to –400	NS	As above	As above	0.142	(a,b,σ) = (1.3 ·10^{-9}, 0.5, 1.0)
	NE	As above	As above	0.345	
	NW	As above	As above	0.133	
	EW	As above	As above	0.081	
	HZ	As above	As above	0.316	
FFM01 and FFM06 below –400	NS	As above	As above	0.094	(a,b,σ) = (5.3 ·10^{-11}, 0.5, 1.0)
	NE	As above	As above	0.163	
	NW	As above	As above	0.098	
	EW	As above	As above	0.039	
	HZ	As above	As above	0.141	

Table 5-2. Hydrogeological DFN parameters for a correlated transmissivity model of the fractures within the former CPM area, based on data from SFR investigations (Öhman and Follin 2010) with depth dependency.

Fracture domain (m RHB 70)	Fracture set name	Orientation set pole: (trend, plunge) conc.	Size model, power law (r_0, k_r) (m, –)	Intensity, (P_{32}), valid size interval: (r_0, 564 m) (m^2/m^3)	Parameter values for the transmissivity model shown in Eq. 5-2 (a, b) T (m^2s^{-1})
Shallow > –60	EW	(2.7, 7.4) 12.6	(0.038, 3.45)	2.598	($6.00\cdot10^{-9}$, 1.29)
	NW	(232.7, 11.9) 13.2	(0.038, 3.10)	1.154	($8.00\cdot10^{-9}$, 1.13)
	NE	(128.3, 8.2) 11.7	(0.038, 3.45)	1.339	($1.00\cdot10^{-8}$, 1.25)
	Hz	(115.9, 84.5) 27.6	(0.038, 2.60)	1.062	($1.41\cdot10^{-7}$, 1.43)
	Gd	(232.2, 85.1) 6.5	(0.038, 2.79)	1.871	($2.11\cdot10^{-8}$, 1.09)
Repository –60 to –245	EW	(5.0, 12.7) 8.5	(0.038, 3.45)	1.407	($6.00\cdot10^{-9}$, 1.29)
	NW	(234.0, 6.0) 12.3	(0.038, 2.95)	0.856	($8.00\cdot10^{-9}$, 1.13)
	NE	(128.2, 5.5) 11.5	(0.038, 3.45)	1.033	($1.00\cdot10^{-8}$, 1.25)
	Hz	(137.0, 84.3) 42.9	(0.038, 2.55)	0.850	($2.06\cdot10^{-9}$, 1.85)
	Gd	(354.2, 85.4) 7.1	(0.038, 2.72)	1.208	($4.00\cdot10^{-9}$, 1.05)
Below ZFM871 < –245	EW	(2.5, 19.6) 9.7	(0.038, 3.45)	0.918	($6.00\cdot10^{-9}$, 1.29)
	NW	(233.3, 7.0) 14.9	(0.038, 3.10)	0.867	($8.00\cdot10^{-9}$, 1.13)
	NE	(304.7, 0.1) 11.2	(0.038, 3.45)	1.023	($1.00\cdot10^{-8}$, 1.25)
	Hz	(127.7, 80.9) 27.9	(0.038, 2.75)	0.596	($1.34\cdot10^{-9}$, 1.32)
	Gd	(269.8, 84.5) 6.6	(0.038, 2.70)	1.287	($9.80\cdot10^{-10}$, 0.93)

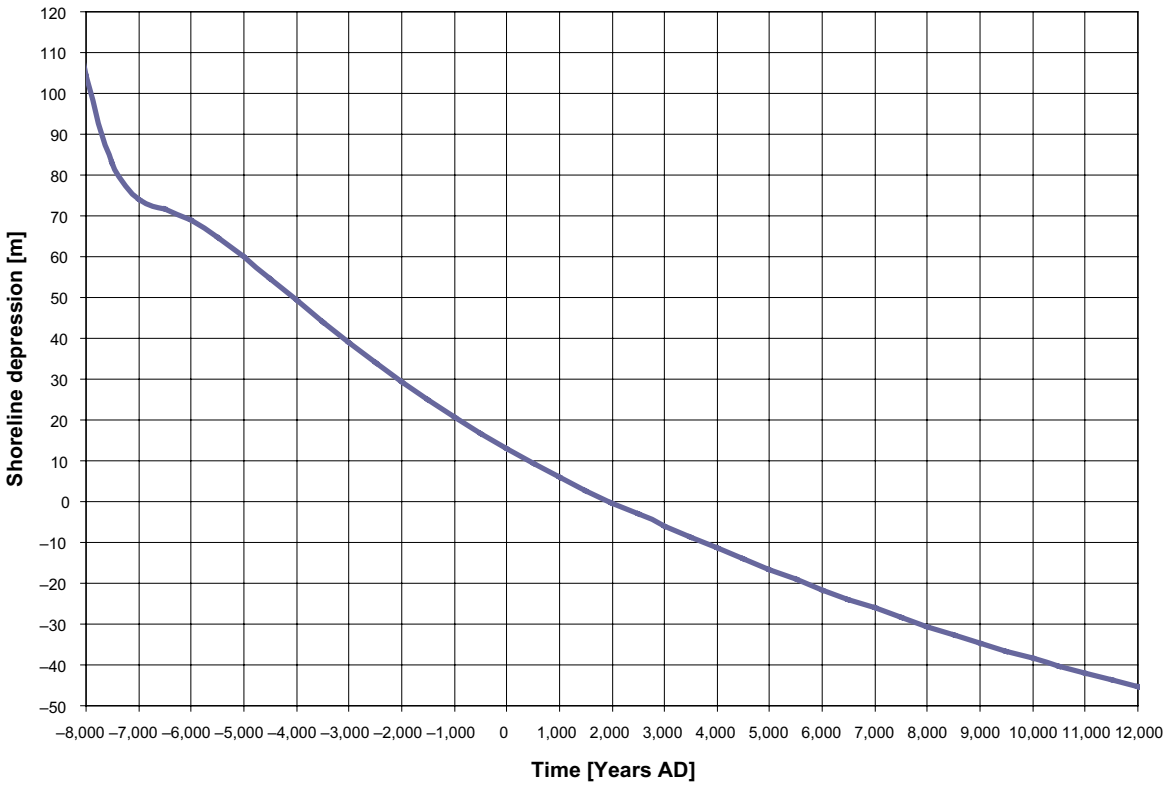

Figure 5-1. *Evolution of the shoreline (SKB 2010b).*

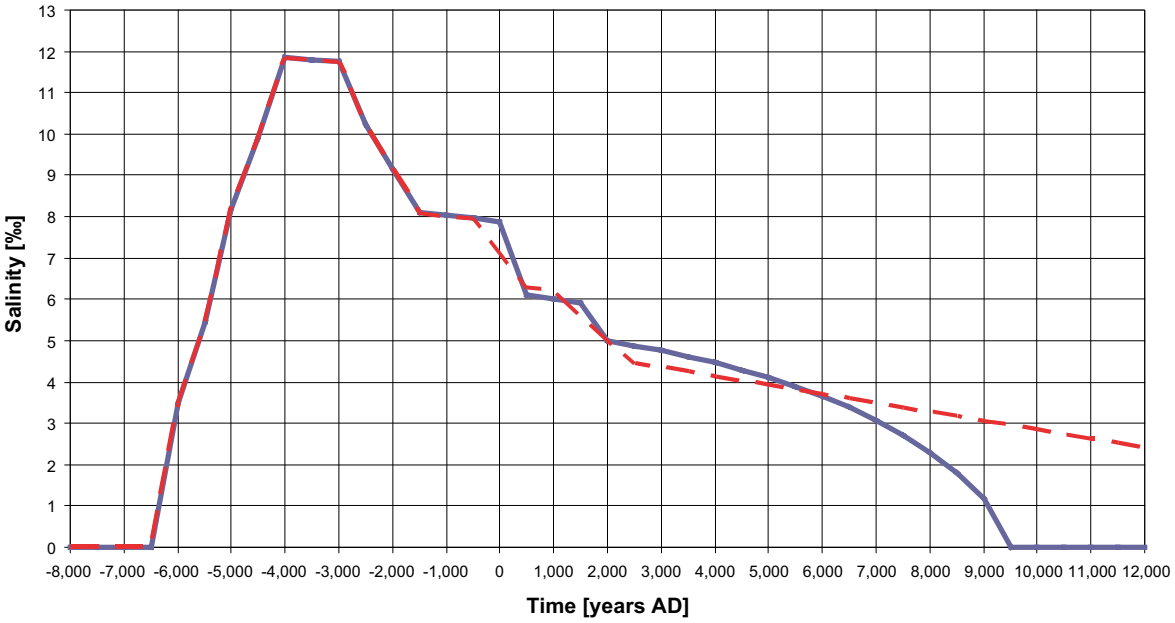

Figure 5-2. *Evolution of the salinity of the Baltic Sea. The curve used in this report is shown as a solid blue line (SKB 2010c) and the final SR-Site curve is shown as a dashed red line (Lindborg 2010).*

5.3 Hydraulic properties in the repository structures

The hydraulic properties of the repository structures used for the hydrogeological modelling are taken from SR-Site, as summarised in Table 5-3. The top sealing properties (representing eroded and permafrost damaged backfill) are used for the ramp and shafts above an elevation of –200 m for the 200 m grouting and 370 m grouting cases. The 370 m sealing cases uses coarsely crushed rock properties between –370 m and –50 m elevation and top sealing properties above –50 m. Grout properties apply to the rock within 5 m of a grouted repository structure.

Table 5-3. Properties of the repository structures (adapted from Joyce et al. 2010, Table 4-2).

Structure	Height (m)	Width (m)	Backfill hydraulic conductivity (m/s)	Backfill porosity (–)
Main tunnel	6	10	$1.0 \cdot 10^{-10}$	0.45
Transport tunnel	6	7	$1.0 \cdot 10^{-10}$	0.45
Deposition tunnel	6	4	$1.0 \cdot 10^{-10}$	0.45
Deposition hole	8	1.5	$1.0 \cdot 10^{-12}$	0.41
Central area tunnel	6	7	$1.0 \cdot 10^{-5}$	0.45
Ramp	6	5.2	$1.0 \cdot 10^{-10}$	0.45
Elevator shaft	4.34	4.34	$1.0 \cdot 10^{-10}$	0.45
Skip shaft	3.96	3.96	$1.0 \cdot 10^{-10}$	0.45
Air intake shaft	3.32	3.32	$1.0 \cdot 10^{-10}$	0.45
Air exhaust shaft	2.81	2.81	$1.0 \cdot 10^{-10}$	0.45
Deposition area air exhaust shaft	3.07	3.07	$1.0 \cdot 10^{-10}$	0.45
Top sealing	N/A	N/A	$1.0 \cdot 10^{-1}$	N/A
Coarsely crushed rock	N/A	N/A	$1.0 \cdot 10^{-5}$	0.45
EDZ	0.3	N/A	$3.3 \cdot 10^{-8}$	$1.0 \cdot 10^{-4}$
Grout	N/A	N/A	$1.0 \cdot 10^{-8}$	$5.0 \cdot 10^{-5}$

5.4 Chemical properties of the OPC leachate

As discussed in Section 3.2, the composition of an OPC grout contains important amounts of portlandite and C-S-H phases. The pH of the porewater of an aged grout will be governed by the dissolution of portlandite, which buffers the pH to a value around 12.4. This situation corresponds to a case in which the grout has leached all the readily soluble alkalis, but that has still not been severely degraded in terms of calcium leaching. The amount of portlandite present after complete hydration will generally depend on the addition of supplementary cementitious materials, such as silica fume. The larger the replacement of cement by silica fume, the lower the portlandite volume fraction of the grout. In this work, it has been assumed that the silica fume content is very low, so that portlandite dissolution can be considered the main pH buffer throughout the simulation period. Therefore the OPC leachate composition has been assumed to remain constant in time. This is of course a conservative assumption, leading to a very aggressive scenario. In reality, it is expected that a high-pH pulse will develop instead, and after severe calcium leaching the pH of the grout porewater will decrease substantially. This time dependent evolution of the chemical properties of the OPC and the resulting leachate composition is difficult to assess in a cautious manner. In order not to underestimate the boundary pH, a pessimistic approach is therefore chosen in this report. A boundary pH decreasing with time would furthermore increase the model complexity and complicate the interpretation of the results.

To calculate the composition of the OPC grout leachate, it is assumed that the groundwater in the fracture network first interacts with an aged grout. The assumed composition of the groundwater corresponds to the Altered Meteoric water used in the SR-Site model (Salas et al. 2010, Table 4-2). This groundwater is equilibrated with calcite and portlandite (as in Savage et al. 2002, Watson et al. 2009) and charge-balanced with pH in order to obtain a simplified OPC leachate composition with a pH of around 12.4. The mineral saturation indices are shown in Table 5-4. This simplified composition has been considered sufficient for the present scoping calculations[17].

5.5 Chemical properties in the fracture—rock matrix

The mineralogy of the fracture has been set to qualitatively comply with the observations in Sandström et al. (2008). The primary minerals considered in the simulations and the assumed mineral volume fractions are gathered in Table 5-5. Mineral abundances vary significantly within different fractures in Forsmark, and other minerals may be locally more abundant. However, at this stage a more detailed study of the effect of fracture mineral heterogeneity was not pursued. Calcite is the only carbonate mineral and occurs abundantly (Sandström et al. 2008). Chlorite also occurs abundantly and has been identified by XRD as clinochlore (Sandström et al. 2008) although large variations in FeO/MgO ratios have been observed. Therefore clinochlore has been selected as representative for chlorite in this work.

Corrensite has been identified as the most abundant clay mineral in Forsmark (followed by illite) mostly in chlorite samples as ingrowths of corrensite. Since corrensite is a chlorite-like clay mineral with layers of chlorite and smectite, and in order to limit the number of primary minerals in the system (so that it is easier to interpret the results), it has not been included in the simulations. Instead, illite has been selected as the only clay mineral (it is the second most abundant clay mineral). Other minor clays like kaolinite or smectites have also been left out of the analysis. Albite has been included as it is also commonly found in fracture fillings and has an important role at high pH where the dissolution rate is relatively high. Quartz has been identified in many of the analysed samples in Sandström et al. (2008) and has an important role in the precipitation of secondary minerals at high pH. K-feldspar has been included as is also usually found as the low temperature adularia variety (the kinetic data for K-feldspar is available). Note that mineral abundances are qualitative since there is no quantitative data available. Laumontite (zeolite), although present in the fracture infill, has not been considered as a primary mineral because it is stabilised for pH > 8 (Savage et al. 2010a), and therefore its dissolution is expected to be negligible.

[17] The possibility of using real OPC leachates composition was investigated. However, only porewater compositions corresponding to an early stage (pH > 13) were found. It is thought that this high pH value is too aggressive for representing real conditions because the volume ratio of grout porewater with respect to groundwater in the fractures will be very small.

Table 5-4. Boundary OPC water composition considered in the simulations.

Property	
Temperature	25°C
pH	12.407

Primary Species	Total Concentration (mol/kg water)	Mineral	log (SI)
AlO^{2-}	$7.72 \cdot 10^{-8}$	Clinochlore-14A	21.029
$SiO_{2\,(aq)}$	$1.26 \cdot 10^{-4}$	Saponite-Ca	14.766
Na^{+}	$1.19 \cdot 10^{-2}$	Saponite-Mg	14.454
K^{+}	$1.43 \cdot 10^{-4}$	Tobermorite-11A	6.204
Ca^{2+}	$1.49 \cdot 10^{-2}$	Brucite	4.137
Mg^{2+}	$3.09 \cdot 10^{-4}$	Foshagite	3.820
HCO_3^{-}	$8.35 \cdot 10^{-6}$	CSH0.80	2.365
SO_4^{2-}	$8.86 \cdot 10^{-4}$	Gyrolite	1.720
Cl^{-}	$6.78 \cdot 10^{-3}$	Hillebrandite	1.465
Fe^{2+}	$1.79 \cdot 10^{-6}$	CSH1.60	1.452
F^{-}	$8.43 \cdot 10^{-5}$	CSH1.40	1.460
Br^{-}	$7.17 \cdot 10^{-6}$	CSH1.20	1.226
Li^{+}	$2.02 \cdot 10^{-6}$	CSH1.00	0.699
Sr^{2+}	$4.34 \cdot 10^{-6}$	Portlandite	0.000
		Calcite	0.000
		Okenite	–1.480
		Prehnite	–1.725
		Quartz	–2.827
		Mesolite	–5.789
		Analcime	–6.944
		Scolecite	–7.227
		K-Feldspar	–8.463
		Albite	–9.576
		Gismondine	–10.764
		Natrolite	–11.663
		Illite	–15.177
		Mordenite	–15.979
		Stilbite	–16.001
		Wairakite	–16.254
		Gismondine	–10.764

Table 5-5. Assumed mineralogical composition of the fracture (vol %).

Mineral	Composition	vol %
Calcite	$CaCO_3$	15
Quartz	SiO_2	10
K-feldspar	$KAlSi_3O_8$	5
Illite	$K_{0.6}Mg_{0.25}Al_{2.3}Si_{3.5}O_{10}(OH)_2$	5
Clinochlore-14A	$Mg_5Al_2Si_3O_{10}(OH)_8$	10
Albite	$NaAlSi_3O_8$	5
Porosity		50
Total		100

Primary minerals are kinetically constrained (except for calcite) and allowed to dissolve and/or precipitate. The kinetic rates are dependent on the pH of the solution. Table 5-6 gathers the input data taken from recent compilations and studies of kinetic data (Brantley et al. 2008, Palandri and Kharaka 2004, Soler 2010) and used in the kinetic expression given by:

$$R_m = A_m \sum_{i=1}^{3} k_{m,i} a_{i,m}^{n} \left(\frac{IAP_m}{K_{eq,m}} - 1 \right) \qquad 5\text{-}3$$

in which R_m (mol/m^3 rock/s) is the reaction rate for mineral m, A_m (m^2/m^3 rock) is the mineral surface area, $k_{m,i}$ (mol/m^2/s) is the reaction rate constant for mineral m and corresponding to the mechanism i (i = 1 for acid, i = 2, for neutral, i = 3 for basic), $a_{i,m}{}^{n}$ represents the effect of the different mechanisms affecting the reaction rate (a is the activity of species H^+ and OH^- for i = 1 and 3, respectively), n is a power constant, and IAP_m and $K_{eq,m}$ are respectively the ion activity product of the solution with respect to mineral m, and the equilibrium constant for the mineral reaction m. Negative values indicate dissolution, while positive values correspond to precipitation.

Mineral surface areas are assumed values, based on the geometric approximation proposed by Soler (2010). A surface area of 3,000 m^2/m$^3_{min}$ would correspond to the case of mineral spherical grains with a radius of 1 mm, as stated in Soler (2010). In order to test the sensitivity of this crucial parameter (see Section 3.2.3 for a discussion on the uncertainty of mineral surface areas), different cases have been simulated, only differing in the surface area of the primary minerals (3, 30, 300, 1,000, 3,000 m^2/m$^3_{min}$). It is noted that in the present work, surface areas are fixed values, and are not updated due to changes in mineral volume fractions and porosity (this option is currently not implemented in the PFLOTRAN code, which has been used for the reactive transport simulations). This may however be justified by the large uncertainty in the determination of the surface area parameter.

Table 5-6. Rate parameters for the primary minerals in the fractured bedrock.

Mineral	Mechanism	log *k* (mol/m^2/s)	a_i^{ni} terms	Reference
Albite	Acid	–9.87	$a_{H^+}^{0.457}$	Palandri and Kharaka (2004)
	Neutral	–12.04	–	
	Base	–16.98	$a_{H^+}^{-0.572}$	
Clinochlore	Acid	–11.11	–	
	Neutral	–12.52	–	
	Base	–14.6	$a_{H^+}^{-0.2}$	Soler (2010)
Illite	Acid	–11.85	$a_{H^+}^{0.37}$	Palandri and Kharaka (2004), assumed same as muscovite in Soler (2010)
	Neutral	–13.55	–	
	Base	–14.55	$a_{H^+}^{-0.22}$	
K-feldspar	Acid	–10.06	$a_{H^+}^{0.5}$	Palandri and Kharaka (2004)
	Neutral	–12.41	–	
	Base	–21.2	$a_{H^+}^{-0.823}$	
Quartz	Acid	–11.36	$a_{H^+}^{0.309}$	Brantley et al. (2008), same as in Soler (2010)
	Base	–9.22	$a_{OH^-}^{0.411}$	

The secondary minerals considered in the simulations are similar to those used in the recent simulations of cement-rock laboratory experiments performed by different recognized research teams (the minerals proposed by IDAEA CSIC team from Spain have finally been chosen) and published in Savage et al. (2011, Table 9) and Soler and Mäder (2010, Table 2). These are gathered in Table 5-7. The exceptions are laumontite (Ca-zeolite) as well the amorphous C-S-H phases with Ca/Si < 0.8, which have not been included in the simulations. The main reason for excluding laumontite was to avoid instant precipitation in the initial fracture-rock matrix system (it was shown in preliminary calculations that the initial solution in the fracture was supersaturated with respect to laumontite, but also that it was not precipitating as a secondary mineral).

The thermodynamic database used in the simulations is the Hanford database (for more details see Hammond and Lichtner 2010, Lichtner and Hammond 2012, Section 7.1.1), with the exception of the C-S-H with Ca/Si ratio of 0.8, which is missing in this database and has been therefore extracted from the THERMODEMM database (Blanc et al. 2007). Fast kinetics has been assumed for the secondary minerals and for calcite, to resemble local equilibrium conditions (a rate constant of $1 \cdot 10^{-5}$ mol/m^2/s together with a surface area of 1,000 m^2/m^3 have been used).

The composition of the rock matrix has been extracted from Sandström and Stephens (2009, Table 3-7). Although other rock compositions are reported in that work, most of these contain primarily quartz, K-feldspar, and plagioclase (albite has been considered here because it is also present in the fracture fillings and to limit the number of minerals in the system), and to a lesser extent biotite and other minerals (around 5%). Moreover, the choice of rock type 101057 (metagranite) is based on the estimated volume fraction in the Forsmark target volume for the repository (73.6% in the target volume RFM029 (Crawford 2008)). Only the minerals that are present in large quantities have been included in the simulations and are depicted in Table 5-8. Biotite has been excluded due to the low volume fraction together with the much slower dissolution rate when compared to albite and quartz. The remaining solid volume fraction (8.1%) has been considered as non-reactive in the present study.

Table 5-7. Secondary minerals considered in the simulations.

Mineral	Description
calcite	–
portlandite	Cement hydrate
brucite	–
C-S-H-1.60	Amorphous C-S-H (Ca/Si = 1.6)
C-S-H-1.40	Amorphous C-S-H (Ca/Si = 1.4)
C-S-H-1.20	Amorphous C-S-H (Ca/Si = 1.2)
C-S-H-0.80	Amorphous C-S-H (Ca/Si = 0.8)
hillebrandite	Crystalline C-S-H (Ca/Si = 2.0)
foshagite	Crystalline C-S-H (Ca/Si = 1.33)
tobermorite-14A	Crystalline C-S-H (Ca/Si = 0.83)
gyrolite	Crystalline C-S-H (Ca/Si = 0.66)
okenite	Crystalline C-S-H (Ca/Si = 0.5)
saponite-Ca	–
saponite-Mg	–
analcime	Na-zeolite
mesolite	Na-Ca-zeolite
natrolite	Na-zeolite
scolecite	Ca-zeolite
stilbite	Na-Ca-zeolite
gismondine	Ca-zeolite
mordenite	Na-Ca-zeolite
wairakite	Ca-zeolite

Table 5-8. Mineralogical composition of the rock matrix (101057 – metagranite).

Mineral	Composition	vol %
Quartz	SiO_2	34.6
K-feldspar	$KAlSi_3O_8$	23.4
Albite	$NaAlSi_3O_8$	33.8
Porosity		0.1

The composition of the initial rock matrix and fracture porewater has been assumed to be identical in an attempt to avoid initial disequilibrium between fracture and matrix (as in Soler 2010). This composition corresponds to the Old Meteoric water as used in the SR-Site model (Salas et al. 2010, Table 4-2). The initial matrix/fracture water has been equilibrated with calcite and quartz and the pH has been fixed to 8.50. Moreover, the Al and Mg content were assigned a very low value to avoid supersaturation with respect to all the secondary minerals (as in Soler 2010). The composition of the initial water used in all the reactive transport simulations is depicted in Table 5-9. The resulting solution is in equilibrium with respect to calcite and quartz and undersaturated with respect to the other primary minerals in the fracture and the rock matrix, and also with respect to the secondary minerals considered in the simulations. The thermodynamic data of these secondary minerals is gathered in Table 5-10. The secondary species considered in the simulations are depicted in Table 5-11. Some secondary species identified as relevant for the present analysis were missing in the Hanford database and have therefore been extracted from the default TOUGHREACT database (specified in Table 5-11).

Table 5-9. Initial solution composition used in all reactive transport simulations.

Property	
Temperature	**25°C**
pH	**8.5**

Primary species	Total Concentration (mol/kg water)	Mineral	log (SI)
AlO^{2-}	$1.00 \cdot 10^{-9}$	Albite	–2.911
$SiO_{2\,(aq)}$	$1.10 \cdot 10^{-4}$	Analcime	–2.921
Na^+	$1.19 \cdot 10^{-2}$	Brucite	–8.529
K^+	$1.43 \cdot 10^{-4}$	Calcite	0.000
Ca^{2+}	$2.47 \cdot 10^{-4}$	Clinochlore-14A	–29.736
Mg^{2+}	$1.00 \cdot 10^{-9}$	CSH0.80	–2.321
HCO_3^-	$1.81 \cdot 10^{-3}$	CSH1.00	–5.866
SO_4^{2-}	$8.85 \cdot 10^{-4}$	CSH1.20	–7.218
Cl^-	$8.86 \cdot 10^{-3}$	CSH1.40	–8.862
Fe^{2+}	$8.74 \cdot 10^{-9}$	CSH1.60	–10.749
F^-	$8.43 \cdot 10^{-5}$	Foshagite	–25.269
Br^-	$7.16 \cdot 10^{-6}$	Gismondine	–10.074
Li^+	$2.02 \cdot 10^{-6}$	Gyrolite	–8.583
Sr^{2+}	$4.34 \cdot 10^{-6}$	Hillebrandite	–14.494
		Illite	–6.064
		K-Feldspar	–1.792
		Mesolite	–1.996
		Mordenite	–3.865
		Natrolite	–6.815
		Okenite	–5.218
		Portlandite	–9.393
		Prehnite	–7.946
		Quartz	0.000
		Saponite-Ca	–13.731
		Saponite-Mg	–14.583
		Scolecite	–4.054
		Stilbite	–2.386
		Tobermorite-11A	–23.796
		Wairakite	–10.253

Table 5-10. Thermodynamic data of the secondary minerals considered in the simulations with PFLOTRAN.

Secondary Minerals	Log K_{25C}	Stoichiometric Coefficients																
		Ca^{++}	Mg^{++}	Sr^{++}	Fe^{++}	Na^{+}	K^{+}	Li^{+}	F^{-}	HCO_3^{-}	Al^{+++}	$SiO_2(aq)$	$H_3SiO_4^{-}$	SO_4^{-}	H^{+}	OH^{-}	Cl^{-}	$O_2(aq)$	H_2O
Portlandite	22.5552	1	0	0	0	0	0	0	0	0	0	0	0	0	–2	0	0	0	2
Brucite	16.298	0	1	0	0	0	0	0	0	0	0	0	0	0	–2	0	0	0	2
Gyrolite	22.9099	2	0	0	0	0	0	0	0	0	0	3	0	0	–4	0	0	0	4.5
CSH1.60	–12.9323	1.6	0	0	0	0	0	0	0	0	0	0	1	0	0	2.2	0	0	–1
CSH1.40	–11.8533	1.8	0	0	0	0	0	0	0	0	0	0	1	0	0	1.8	0	0	–1
CSH1.20	–10.5324	1.2	0	0	0	0	0	0	0	0	0	0	1	0	0	1.4	0	0	–1
CSH1.00	–8.9185	1	0	0	0	0	0	0	0	0	0	0	1	0	0	1	0	0	–1
CSH0.80	–9.4975	0.8	0	0	0	0	0	0	0	0	0	0	1	0	0	0.6	0	0	–0.26
Tobermorite–11A	65.6121	5	0	0	0	0	0	0	0	0	0	6	0	0	–10	0	0	0	10.5
Foshagite	65.921	4	0	0	0	0	0	0	0	0	0	3	0	0	–8	0	0	0	5.5
Hillebrandite	36.819	2	0	0	0	0	0	0	0	0	0	1	0	0	–4	0	0	0	3.17
Okenite	10.3816	1	0	0	0	0	0	0	0	0	0	2	0	0	–2	0	0	0	3
Analcime	6.1396	0	0	0	0	0.96	0	0	0	0	0.96	2.04	0	0	–3.84	0	0	0	2.92
Gismondine	41.717	2	0	0	0	0	0	0	0	0	4	4	0	0	–16	0	0	0	17
Saponite–Mg	26.2523	0	3.16	0	0	0	0	0	0	0	0.33	3.67	0	0	–7.32	0	0	0	4.66
Saponite–Ca	26.29	0.165	3	0	0	0	0	0	0	0	0.33	3.67	0	0	–7.32	0	0	0	4.66
Prehnite	32.9305	2	0	0	0	0	0	0	0	0	2	3	0	0	–10	0	0	0	6
Mesolite	13.6191	0.675	0	0	0	0.676	0	0	0	0	1.99	3.01	0	0	–7.96	0	0	0	6.627
Natrolite	18.5204	0	0	0	0	2	0	0	0	0	2	3	0	0	–8	0	0	0	6
Scolecite	15.8767	1	0	0	0	0	0	0	0	0	2	3	0	0	–8	0	0	0	7
Stilbite	1.0545	1.019	0	0	0	0.136	0.006	0	0	0	2.18	6.82	0	0	–8.72	0	0	0	11.69
Mordenite	–5.1969	0.2895	0	0	0	0.361	0	0	0	0	0.94	5.06	0	0	–3.76	0	0	0	5.384
Wairakite	18.0762	1	0	0	0	0	0	0	0	0	2	4	0	0	–8	0	0	0	6

Table 5-11. Equilibrium constants (log K_{25C}) of secondary species considered in the simulations (with reactions written as the destruction of 1 mole of species). These secondary species are written in the thermodynamic database in terms of: H^+, Ca^{2+}, Al^{3+}, $SiO_2(aq)$, Mg^{2+}, Na^+, K^+, HCO_3^-, SO_4^{2-}, Cl^-, Fe^{2+}, F^-, Br^-, Li^+, Sr^{2+}, H_2O.

Species	Log $K_{25°C}$	Species	Log $K_{25°C}$
CO_3^-	10.3288	KSO_4^-	–0.8796
AlO_2^-	22.8833	LiCl(aq)	1.5115
CaCl+	0.6956	LiOH(aq)	13.64
$CaCl_2(aq)$	0.6436	$LiSO_4^-$	–0.77
$CaCO_3(aq)$	7.0017	$MgCl^+$	0.1349
CaF^{+-}	0.6817	$MgCO_3(aq)$	7.3499
$CaHCO_3^+$	–1.0467	MgF^+	–1.3524
$CaHSiO_3^+$	8.5689*	$MgHCO_3^+$	–1.0357
$CaOH^+$	12.8341	$MgHSiO_3$	+8.3184*
$CaSO_4(aq)$	–2.1111	$MgOH^+$	11.7851
$CO_2(aq)$	–6.3447	$MgSO_4(aq)$	–2.4117
FeCl+	0.1605	NaBr(aq)	1.3568
$FeCO_3(aq)$	5.5988	NaCl(aq)	0.777
FeF+	–1.36	$NaCO_3^-$	9.8144
$FeHCO_3^+$	–2.72	NaF	0.9976
FeOH+	9.5	$NaHCO_3(aq)$	–0.1541
$FeSO_4(aq)$	–2.2	$NaHSiO_3(aq)$	8.304
$H_3SiO_4^-$	9.9525	NaOH(aq)	14.7948
$HAlO_2(aq)$	16.4329	$NaSO_4^-$	–0.82
HF(aq)	–3.1681	OH^-	13.9951
HF_2^-	–2.5509	$SrCl^+$	0.2485
$HFeO_2^-$	29.2024*	$SrCO_3(aq)$	7.4635
$HSiO_3^-$	9.9525	SrF^+	–0.1393
HSO_4^-	–1.9791	$SrHCO_3^+$	–1.18
KBr(aq)	1.7372	$SrOH^+$	13.29
KCl(aq)	1.4946	$SrSO_4(aq)$	–2.3
KOH(aq)	14.46		

* from ToughReact database.

6 Hydrogeological modelling

6.1 Open-repository period

In this section the model set-up and flow path calculation results are shown for the flow situation just before and during the open repository phase. This model uses the hydrogeological code DarcyTools (Svensson et al. 2010) and is based on the SR-Site model presented in Svensson and Follin (2010). Some deviations and modifications have however been introduced; the more important are:

- As compared to the base-case used in the SR-Site hydrogeological modelling, the DFN from the SR-Site extended spatial variability case is used in this report, underlying the ECPM representation. See further Section 4.1.
- No salinity fields are included in the present work. The conclusion from the SR-Site work was that the salinity field has a very weak influence on inflow rates and hence flow paths. Considering that an open repository generates a head difference of 500 m, with reference to the surrounding rock, it is easily shown that pressure gradients due to a salinity field are orders of magnitude smaller.

The simulations reported in this section were carried out as follows:

- First natural, or undisturbed, steady state flow and pressure fields were established. Zero flux vertical boundary conditions were used in order to let the water table adjust to the boundary condition.
- Secondly the open repository simulations were carried out with a restart from the undisturbed case. In this simulation the vertical pressure distribution at vertical boundaries were frozen to the distribution found for undisturbed conditions. It is thus assumed that the open repository does not affect the vertical boundaries. In the SR-Site work it was shown that the drawdown of the groundwater table does not reach the domain boundaries. This shows that the assumption is acceptable.
- Finally particle tracking was performed in a steady flow field.
- It may seem natural to place particles in the grouted volumes and track these forward in time. This case will also be shown below. However, an alternative is to use backward particle tracking from points where there is a simulated inflow to the open repository. It is then tested if the particle has its origin in, or passes, the grouted volumes. This alternative is favoured as a good illustration of flow paths is obtained.

Descriptions of the simulated open-repository cases are compiled in Table 6-1.

If backward particle tracking from inflow points is used the grouted volumes need to be defined in order to determine if a particle passes any of these volumes. In the code DarcyTools a method called “Distgen” is used. This method collects all cells that have a cell centre a certain distance from an object. Here all cell centres closer than 10 m to the ramp are considered as grouted. The cells that represent grouted volumes are shown in Figure 6-1. In this report two proposed levels of OPC grouting are considered –200 m and –370 m (Figure 1-1). Here OPC grouting down to –370 m is first considered and if this case does not show any critical flow paths, the 200 m case does not need to be investigated.

Table 6-1. Open-repository simulation cases.

Case	Description
A	This is the main case discussed. Particles are backward tracked from inflow points with an inflow larger than 0.1 l/min (6,792 points). This case is used for visualization. Repository is grouted with grouting level II, according to Svensson and Follin (2010). Grouting level II implies that the penetration depth is about 4 m and that all conductivities larger than 10^{-8} m/s are reduced to this value.
B	Same as A but all inflow points with an inflow larger than 0.01 l/min are used as starting position. 67,369 particles are simulated. The inflow covered by these points is 1,293 l/min or 98% of the total inflow.
C	Forward simulation. 18,616 particles are released close to the ramp.
D	Same as A but for ungrouted repository.

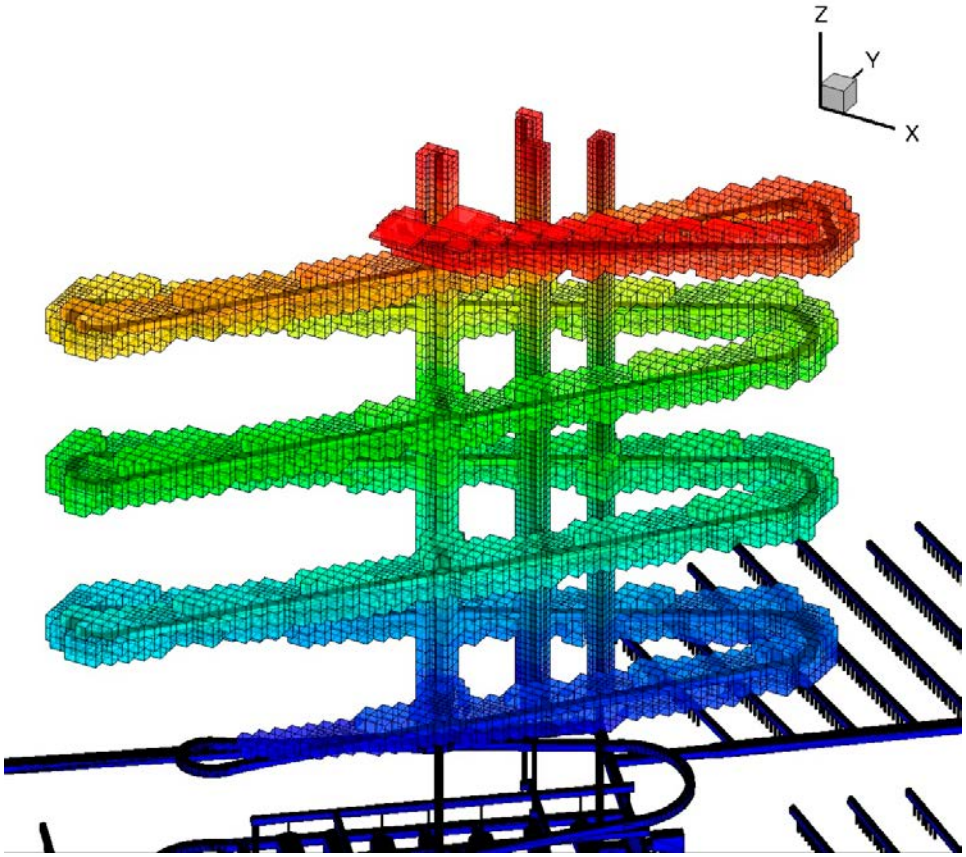

Figure 6-1. *The OPC grouted volumes shown as computational cells. Colour only indicates vertical coordinate. The volumes are shown as transparent and the ramp in the volumes can hence be seen. The same basic repository outline as shown in Figure 1-1 is used.*

Figure 6-2 shows the starting positions for the 6,792 backward tracked particles used for Cases A and D.

Particle tracks for Case A are shown in Figure 6-3, Figure 6-4, and Figure 6-5. Tracks together with permeability field are shown in Figure 6-4 and tracks together with lakes are shown in Figure 6-5. It is found that the tracks are not strongly correlated to the permeability field at 465 mbsl. However, close to ground they tend to end up in lakes and then follow the streams. Both these statements are only based on visual inspections of the results.

The forward simulation of particles released close to the ramp is illustrated in Figure 6-6. As expected, the particles will move directly to the open ramp. This is easily concluded from a visual inspection of the results.

For an ungrouted repository the total inflow will increase from 31 l/s (grouting level II) to 110 l/s. The particle tracks (see Figure 6-7) will however be very similar to Case A (Figure 6-3).

The most important case is Case B, where 67,369 particles were backward tracked from inflow points. This case is however not visualized, as too many trajectories would result. Also the ungrouted repository was tested with all inflow points (60,080) larger than 0.01 l/min. None of these two cases resulted in any critical flow paths, even though the particles were backward tracked for 100 years. For these cases, the grouted volumes (Figure 6-1) were defined as ending volumes for the backward particle tracking. Hence, any particle reaching the grouted volumes is recorded as “arrived”. For the two cases no particles got in contact with the grouted volumes.

For all open-repository cases investigated, no single flow path from the OPC grouted volumes to the deposition holes was found. This is a promising result, although it may be noted that flow paths may be present under different conditions from those modelled.

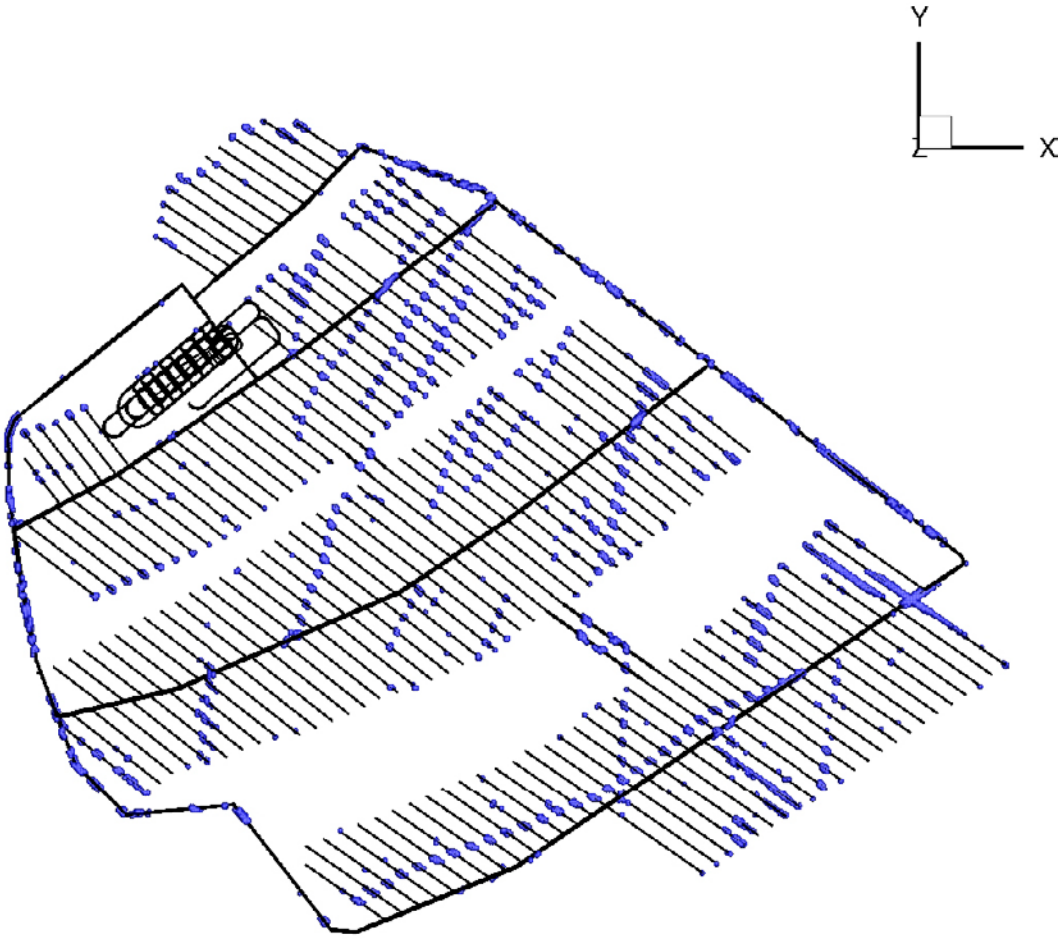

Figure 6-2. *Release locations for the 6,792 particles in Cases A and D. Trajectories start from 500 randomly chosen points. Repository depth is 465 mbsl.*

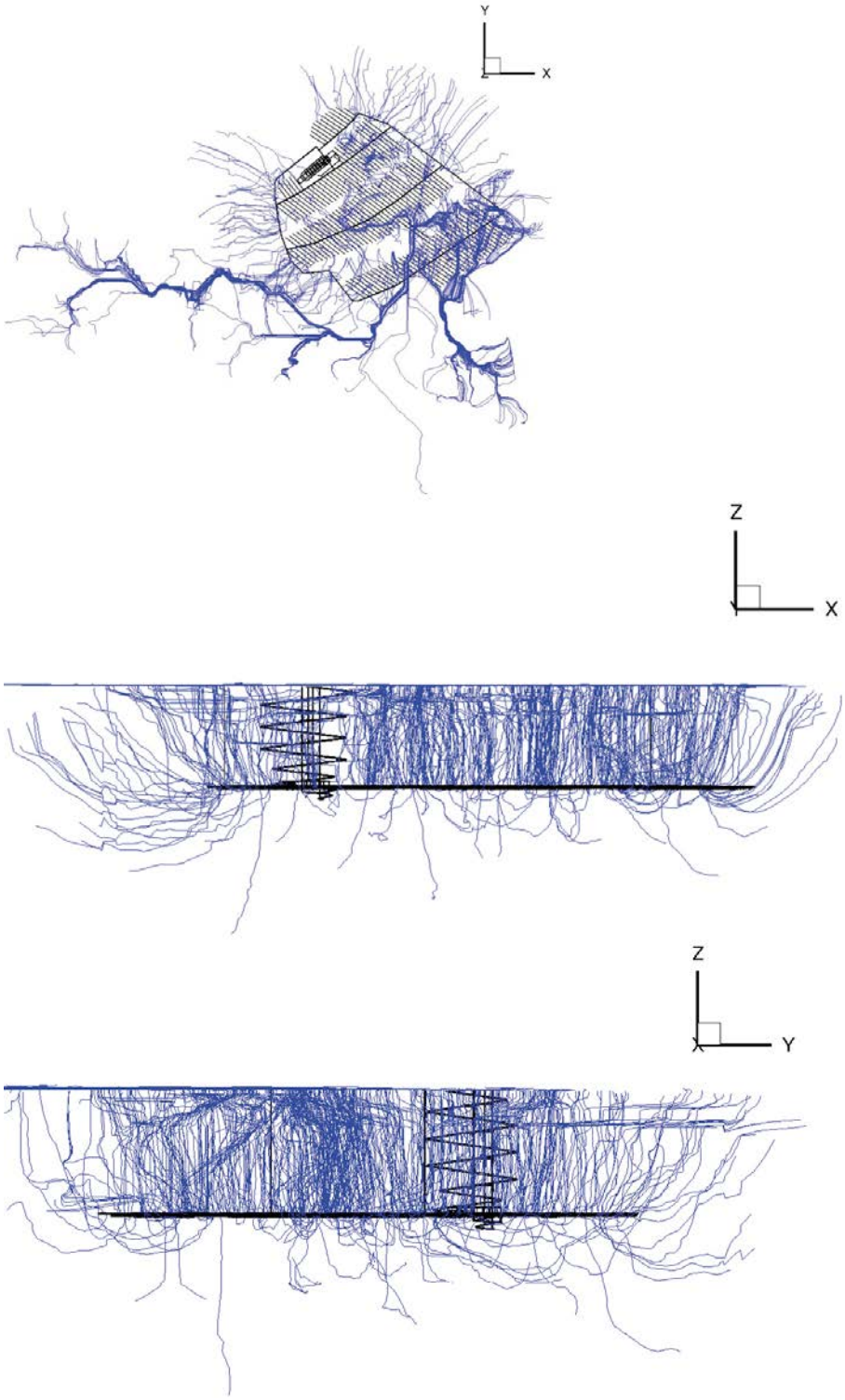

Figure 6-3. *Backward particle tracking trajectories for Case A. The particles were tracked for 1,000 days.*

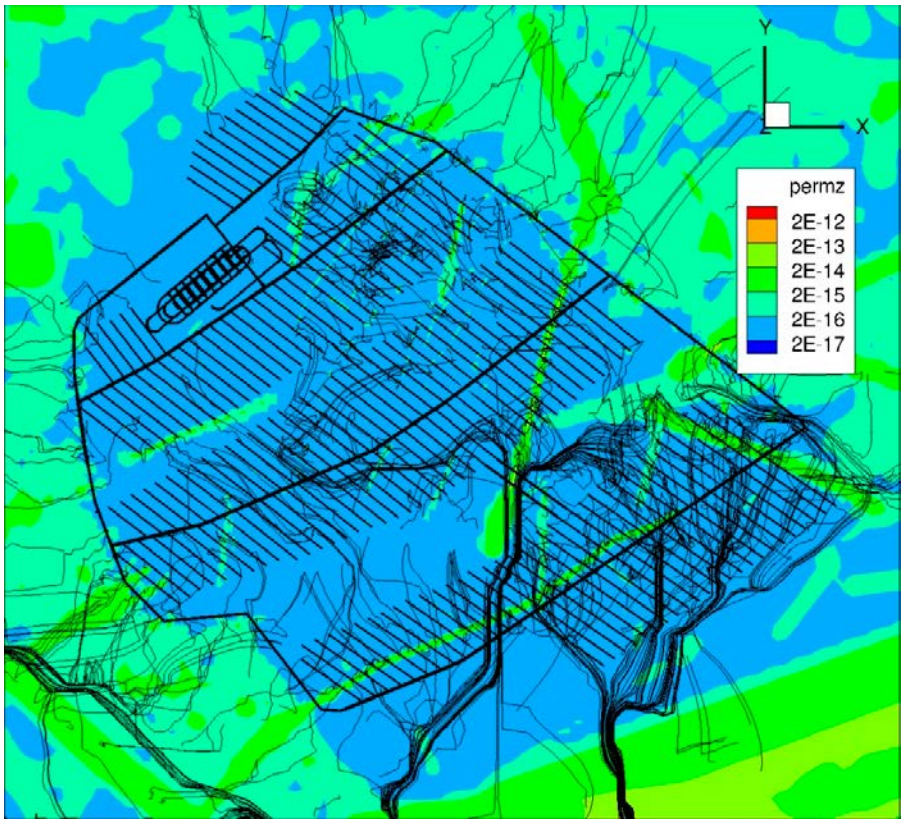

Figure 6-4. *Backward particle tracking trajectories for Case A, shown with the permeability (unit m^2) field at –465 m.*

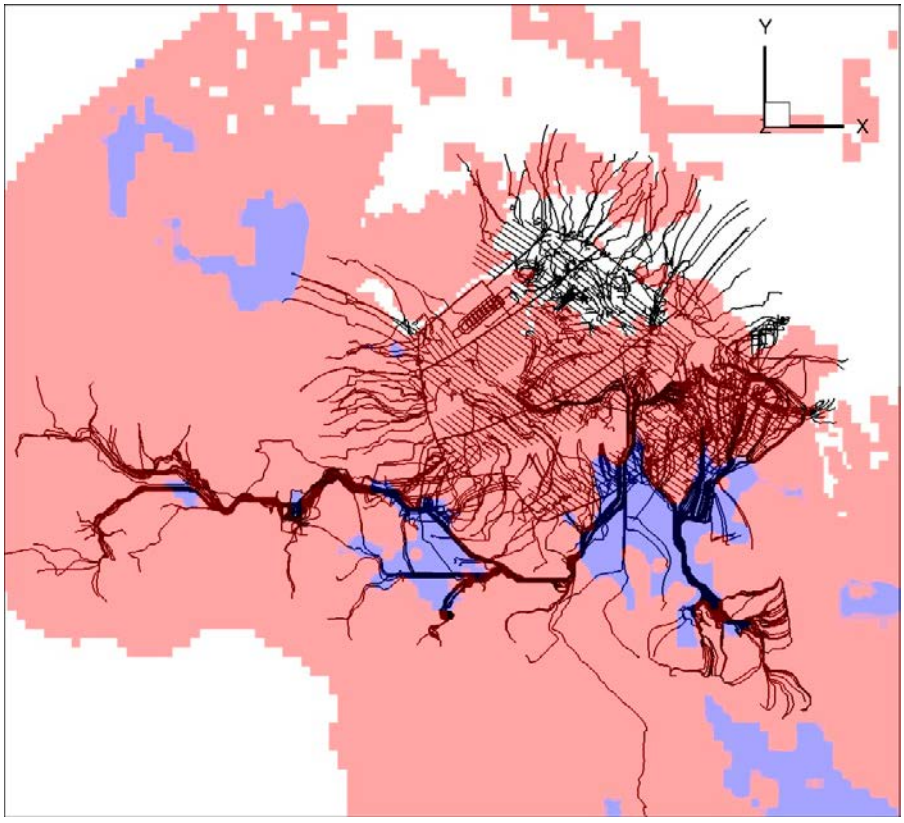

Figure 6-5. *Backward particle tracking trajectories for Case A, shown with simulated lakes (blue colour). The simulation of lakes and streams is explained in Svensson and Follin (2010).*

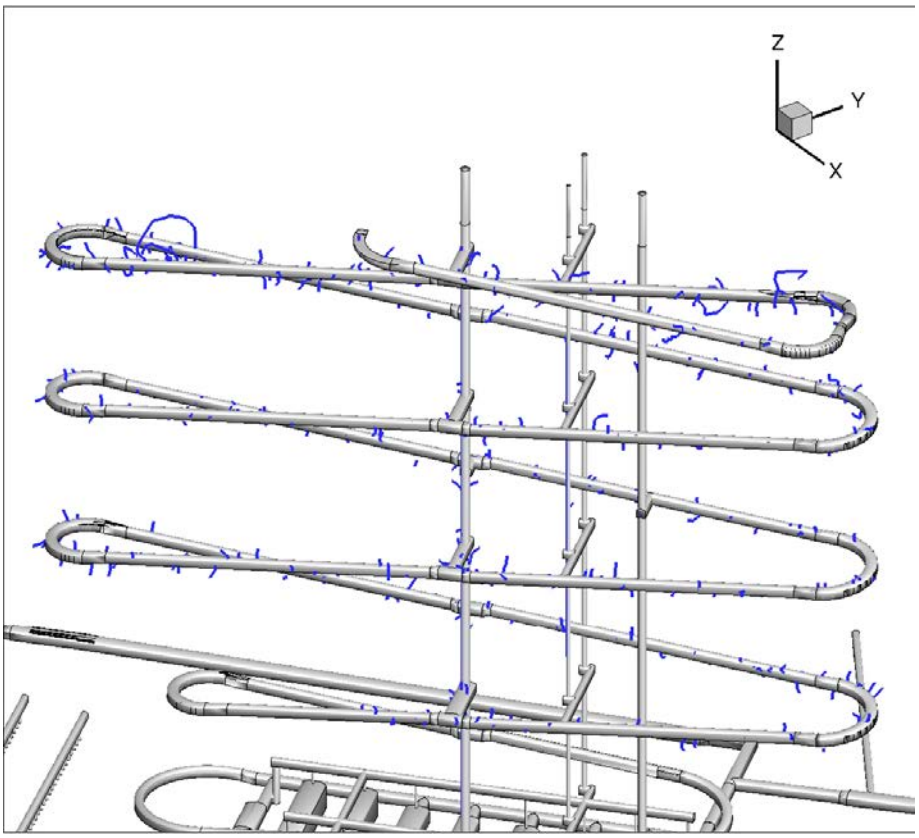

Figure 6-6. *Forward modelling of particles released close to the ramp, Case C. All trajectories are going from the release point to the ramp. This is easily verified by a visual inspection of the results.*

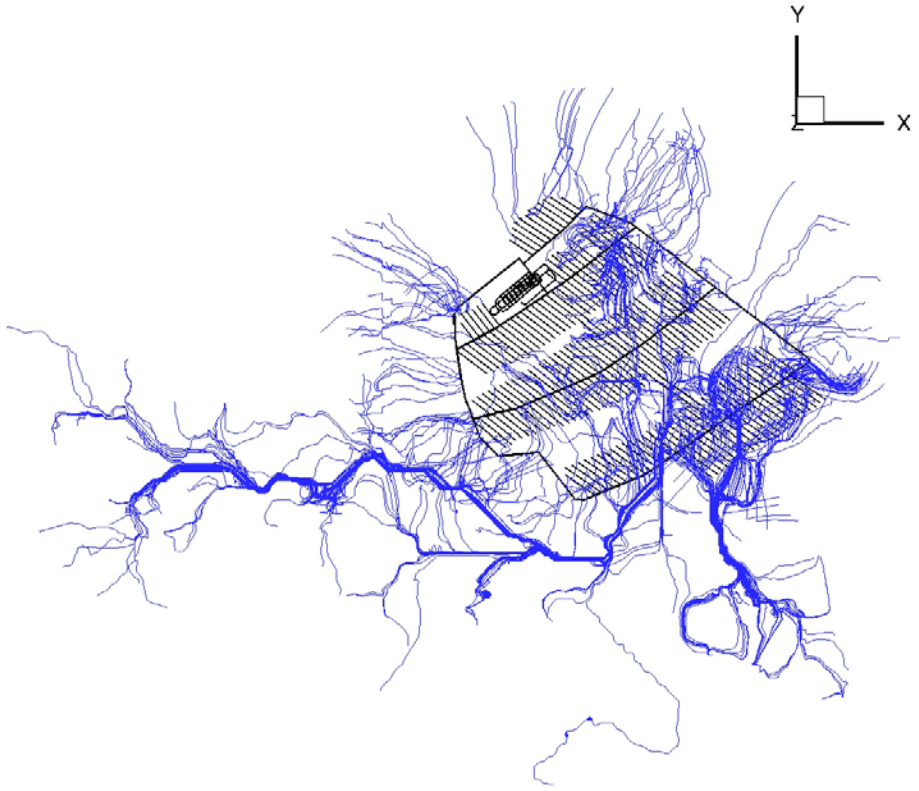

Figure 6-7. *Backward particle tracking trajectories for an ungrouted repository, Case D. Particles tracked for 1,000 days.*

6.2 Temperate period

The modelling reported in this section relates to the transport of alkaline water released from OPC grout during a period when temperate climate conditions are present. The time period 8000 BC to 1000 AD represents the submerged conditions in the past, which are assumed to repeat following future periglacial and glacial conditions. The time period 2000 AD to 12,000 AD represents the interval following the closure, backfilling and saturation of the repository until the next permafrost or glacial period.

The models are adapted from those employed for SR-Site (Joyce et al. 2010). As with SR-Site, three scales are used to model processes occurring at different levels of detail using the ConnectFlow software (Serco 2011). The three scales communicate data and share properties to ensure that they have a consistent hydraulic representation, as shown in Figure 6-8. The hydraulic properties used in the models are described in Chapter 5. The extended spatial variability case from SR-Site is chosen as the case studied here since it has the largest discrete fracture network (DFN) region around the repository and so can represent the detailed constrained flows within the fractures over a larger volume. Only a single realisation of the hydraulic rock mass domain (HRD) is considered and the fractures used are those generated during the SR-Site modelling. The hydraulic conductor domain (HCD) has the same depth-dependent deterministic properties as SR-Site.

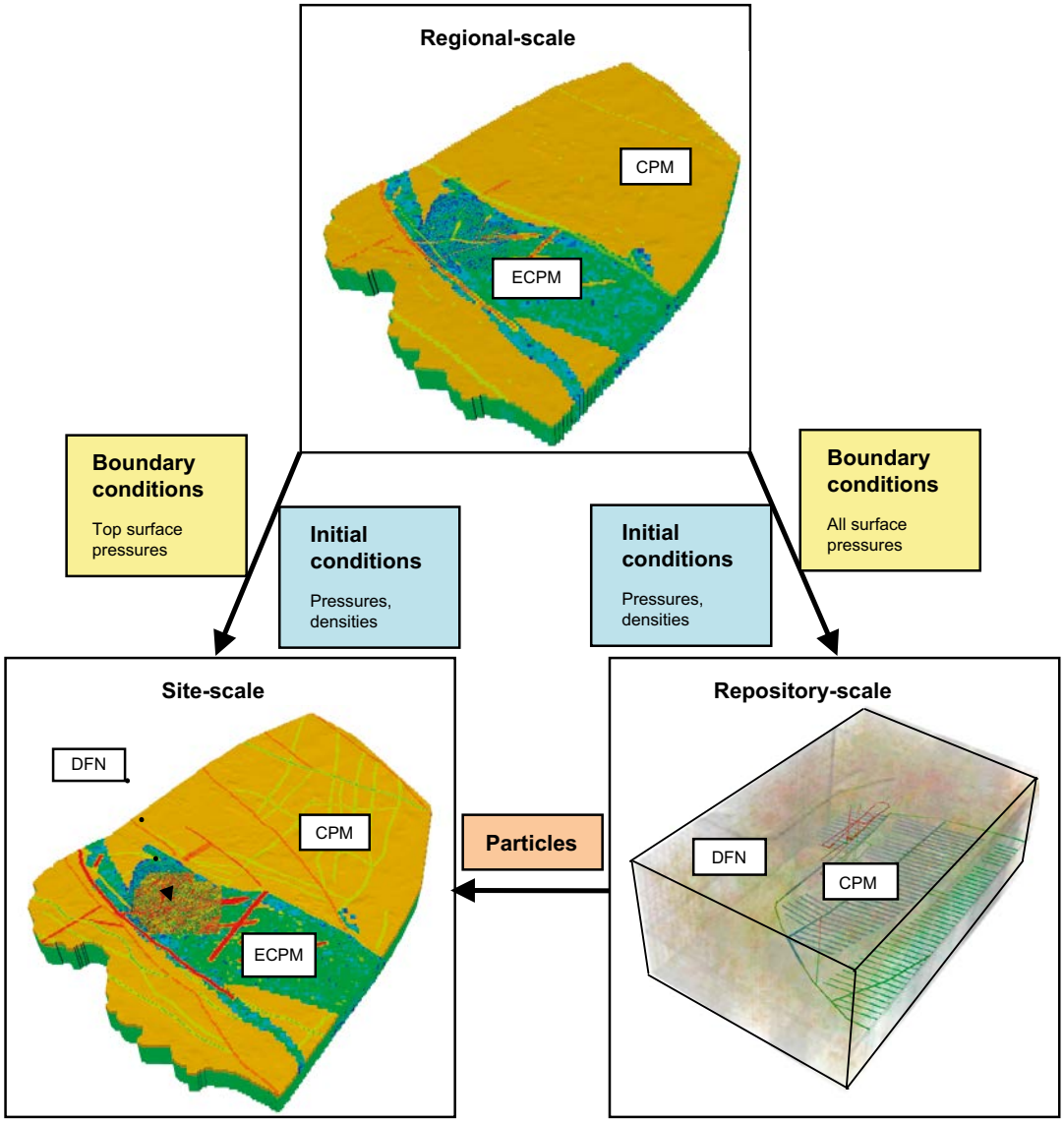

Figure 6-8. *Illustration of the concepts of model scales, embedding, and the transfer of data between scales (Joyce et al. 2010, Figure 3-9).*

The repository-scale model has the highest level of detail of the three scales around the repository structures, particularly the deposition holes, deposition tunnels and main tunnels, each of which is modelled as a continuous porous medium (CPM) that matches the geometry and properties of those structures. Other repository structures, such as transport tunnels, ramps, shafts and the central area are modelled as fractures with hydraulic properties and geometries equivalent to those of the corresponding structures. An excavation damaged zone (EDZ) around the repository structures is represented as a series of fractures running parallel to and below each structure. The surrounding bedrock is represented by a DFN to model the HRD and HCD. There is no representation of the hydraulic soil domain (HSD).

The site-scale model has an intermediate level of detail around the repository. It uses a DFN representation of the HRD and HCD in the local area around the repository and uses fractures with appropriate properties to represent all of the repository structures and associated EDZ. However, the DFN region is embedded within an equivalent continuous porous medium (ECPM) representation of the regional HRD and HCD. The HSD is represented in a simplified form as four layers of CPM, each of a constant 1 m thickness, over the whole top surface of the model.

The regional-scale model is at the largest scale and represents transient processes that are primarily influenced by the bulk properties of the rock, such as the evolution of groundwater composition with time, including diffusion into the rock matrix. At this scale the HRD and HCD are only represented as an ECPM, with the HSD represented in the same way as for the site-scale model.

A simplified approach was taken to represent the grouting by modifying the hydraulic properties of the grouted parts of the ramp and shafts. Where the grout was applied, the hydraulic properties of the grout were used if they gave a lower hydraulic conductivity to the ramp or shafts. This simulated the effect of the grout reducing the flow in to the ramp and shafts from the fractures. The simplification is conservative in that the flows in the surrounding fractures are higher than if they were grouted. However, it would also potentially reduce the flow up and down the ramp and shafts, although modelling experience from SR-Site (Joyce et al. 2010) has shown that there is no significant recharge to the repository through the lower part of the ramp and shafts. Therefore it is expected that recharge pathways from the grouted region will be primarily through the fracture network.

6.2.1 DFN recharge pathways

The flow pathways from the grouted regions of the ramp and shafts to the deposition holes are important in determining if alkaline water released from the grout can penetrate to the canister locations. Within fractured rock, these recharge pathways will predominantly be constrained to the discrete geometries of the fractures. Therefore, it is appropriate to employ the DFN representations used in the repository-scale and site-scale models when modelling these processes.

To determine the recharge pathways, for the repository deposition holes, backward particle tracking is used to calculate a path from each deposition hole to the ground surface in the reverse flow direction. The calculations are carried out stochastically, with path direction decisions at each fracture intersection made according to a flow weighted random process. The effect is to calculate possible recharge flow pathways from the ground surface to each deposition hole. Note that only one possible recharge pathway is calculated for each release point and so some recharge pathways will not be considered. The Q1 (release from a fracture intersecting a deposition hole), Q2 (release from the EDZ above a deposition hole) and Q3 (release from the tunnel over a deposition hole) release types from SR-Site are considered, thus giving up to three potential flow pathways to each deposition hole. Since some deposition holes are not intersected by fractures, due to the sparsity of the fracture network, the Q1 pathway is not always present.

The backward particle tracking calculations must be carried out in a steady state flow field. Therefore variable density, steady state groundwater flow calculations are carried out at a number of representative time slices for the repository-scale and site-scale models using pressures and densities imported from the SR-Site regional-scale model, as described in Joyce et al. (2010). This gives rise to a pressure field and associated advective flow velocities which are consistent with the imported pressure boundary conditions and groundwater densities. The time slices chosen were 3000 BC to represent the time when the site is submerged during the post-glacial period, 2000 AD to represent the current conditions and 9000 AD to represent the end of the temperate period when the receding shoreline is remote from the repository site.

The particles are initially released at the Q1, Q2 and Q3 locations for each deposition hole within the repository-scale model. To be computationally feasible, this model is divided into three blocks, as described in Joyce et al. (2010) and shown in Figure 6-9. The particles are backward tracked within each block until they reach the boundaries of the model. The particles are then continued within the site-scale model until they reach the top surface of the model. This process is equivalent to that used for the forward particle tracking reported in Joyce et al. (2010). There are 6,916 deposition hole locations and three release types, so 20,748 particles are released in total.

Performance measures are calculated for each particle that is released. These are path length in the rock, L_r, travel time in the rock, t_r, and flow-related transport resistance in the rock, F_r. The same method for calculating the performance measures as SR-Site is used, but only the portion of the backwards path from the release location to where it first intersects the grout is considered. A path is considered to intersect the grouted region if it comes within 5 m of a grouted repository structure. Paths are included even if they fail the starting criteria for SR-Site (there is an available starting fracture for Q1 and there is sufficient flow for Q1, Q2 and Q3) or if they get stuck in the repository-scale model. Such paths can continue in the site-scale model by a flux-weighted selection of a nearby fracture. This approach is conservative in that even recharge pathways that come close to a deposition hole are considered. Paths that do not intersect the grout are discarded.

The recharge pathways from the surface to deposition hole locations vary with release time. Figure 6-10 and Figure 6-11 show the recharge locations and discharge locations respectively for flow to and from the deposition holes in the repository. The discharge locations were obtained by forward particle tracking from the deposition hole positions to the ground surface in the repository-scale and site-scale models. At 3000 BC the recharge is from the southwest and northeast and the discharge is directly above the site. At this time the site is submerged under the sea and the head gradients are low, so flow is primarily density driven and diffuse. At 2000 AD and 9000 AD recharge is from the southwest and south and discharge is primarily along the shoreline to the north and northeast. At 2000 AD the shoreline is close to the site, but at 9000 AD it is further to the northeast.

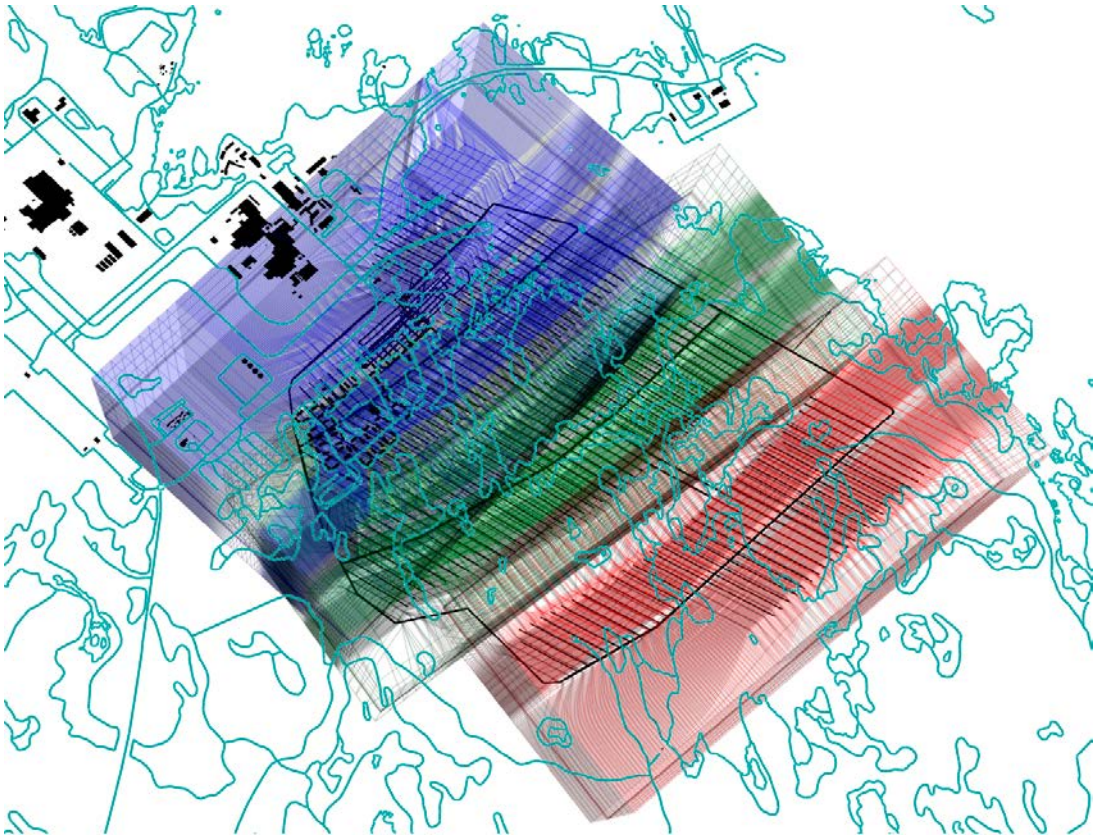

Figure 6-9. *Repository-scale blocks (Joyce et al. 2010, Figure 4-12). Block 1 is coloured blue, block 2 is green and block 3 is red.*

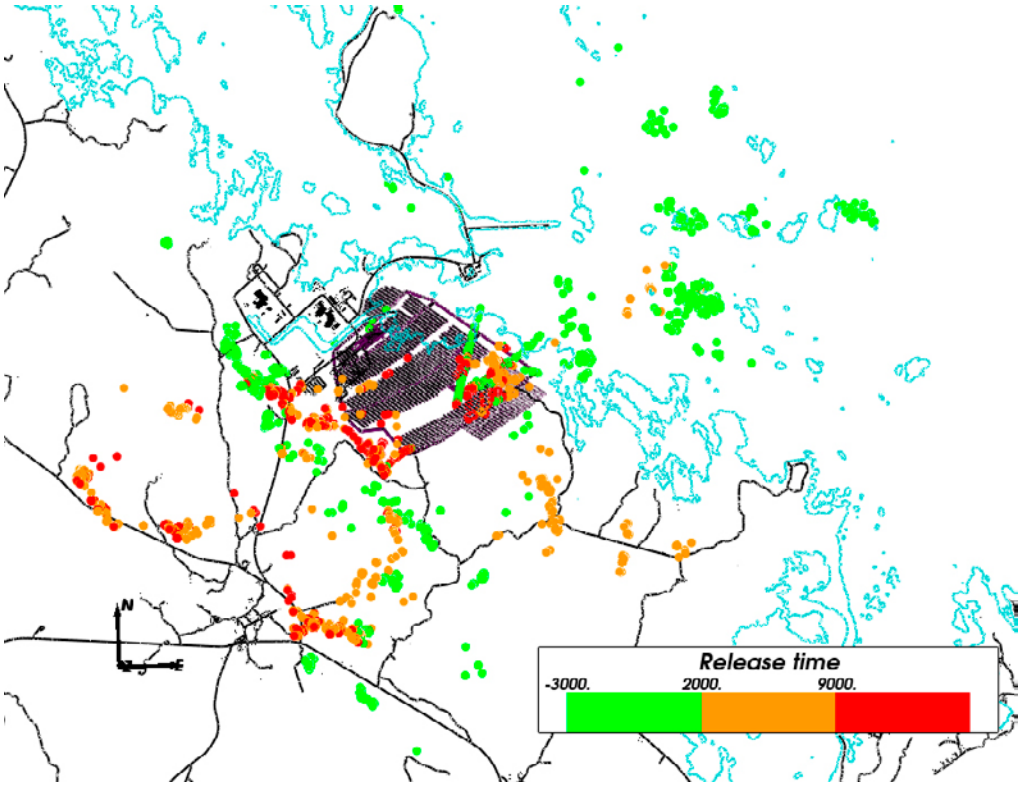

Figure 6-10. *Recharge locations on the top surface for flow pathways to deposition holes for each release time (in years AD), including those that do not intersect the grout. The shoreline at 2000 AD is shown in blue and buildings and roads are shown in black.*

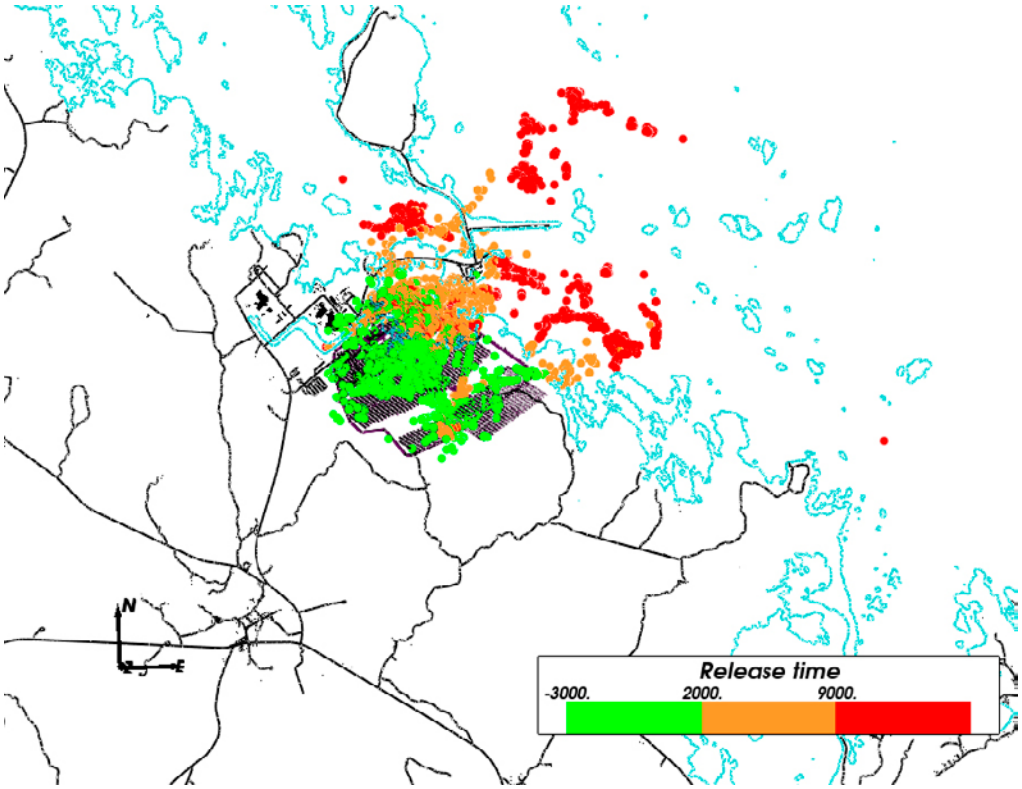

Figure 6-11. *Discharge locations on the top surface for flow pathways from deposition hole locations for each release time (in years AD), including those that do not intersect the grout. The shoreline at 2000 AD is shown in blue and buildings and roads are shown in black.*

Table 6-2 shows the number of recharge pathways to the deposition holes that pass through a grouted region for each case and release time. The recharge pathways for some of these cases are illustrated in Figure 6-12 to Figure 6-14. In all cases the percentage of recharge pathways passing through the grouted regions is small. However, at 3000 BC, where there is more vertical recharge down to the repository, the number of recharge paths intersecting the grout is significantly higher than for the other release times. At 9000 AD the more horizontal flows, caused by the receding shoreline, lead to very little recharge via the grouted regions to deposition holes. At 2000 AD there is an intermediate situation where some recharge flow to the deposition holes passes through the grout. Figure 6-12 to Figure 6-14 show the recharge pathways for each release time for the case with grouting to a depth of 200 m. The paths are very similar for the other two cases. These figures clearly show the differences in the number of recharge pathways that pass through the grout for each release time. However, most of the pathways follow the same route from the ramp and shafts to the repository section to the north of the ramp. This route essentially follows three fractures in a "Z" configuration. At 3000 BC there are additional routes through some horizontal fractures connected to the ramp and shafts to a vertical fracture connected to the repository section to the east of the ramp. Clearly these routes rely on a particular configuration of the HRD fractures and so the results may be sensitive to the realisation considered. However, due to time constraints, additional realisations were not within the scope of this study.

All of the intersections of the recharge pathways with the grouted region are above -200 m elevation, except for a few deeper intersections for the 370 m sealing case. This is because the fracture intensity and flow is highest in the upper 200 m of the bedrock. In particular, the sheet joints carry flow to the upper parts of the ramp and shafts. Intersections below –200 m occur in the 370 m sealing case due to the higher hydraulic conductivity in the ramp and shafts below –200 m and Figure 6-15 contains one such pathway at 2000 AD.

The number of recharge pathways to the deposition holes that intersect the grout for a less pessimistic case are shown in Table 6-3. In this case recharge pathways have been excluded if they do not meet the SR-Site starting criteria (due to an absence of fractures or insufficient flow) and if they do not meet the FPC (Full Perimeter Criteria) and EFPC (Extended Full Perimeter Criteria) as described in Joyce et al. (2010). Here, there is the same pattern of behaviour between cases and release times, but the number of pathways intersecting the grout is approximately halved. Nearly all of the change comes from applying the starting criteria rather than FPC and EFPC.

There is some uncertainty and variability in the penetration depth of the grout into the fractures. So, 20 m is considered as an alternative to the 5 m grout radius already used so that the sensitivity of the results to this uncertainty can be assessed. The number of recharge pathways that intersect the grout in this case are shown in Table 6-4. These results are very similar to the case with a 5 m grouting radius. The lack of sensitivity to the grouting radius is probably due to the very low intensity of recharge pathways in the region of the repository ramp.

Table 6-2. The number and percentage of recharge pathways to deposition hole locations that pass through a grouted region, out of a total of 20,748 particles released for the Q1, Q2 and Q3 release types, for each case and particle release time. The grouting radius is 5 m.

Case	Release time	Count	Percentage
200 m grouting	3000 BC	160	0.77
	2000 AD	92	0.44
	9000 AD	2	0.01
370 m grouting	3000 BC	160	0.77
	2000 AD	92	0.44
	9000 AD	2	0.01
370 m sealing	3000 BC	153	0.74
	2000 AD	88	0.42
	9000 AD	2	0.01

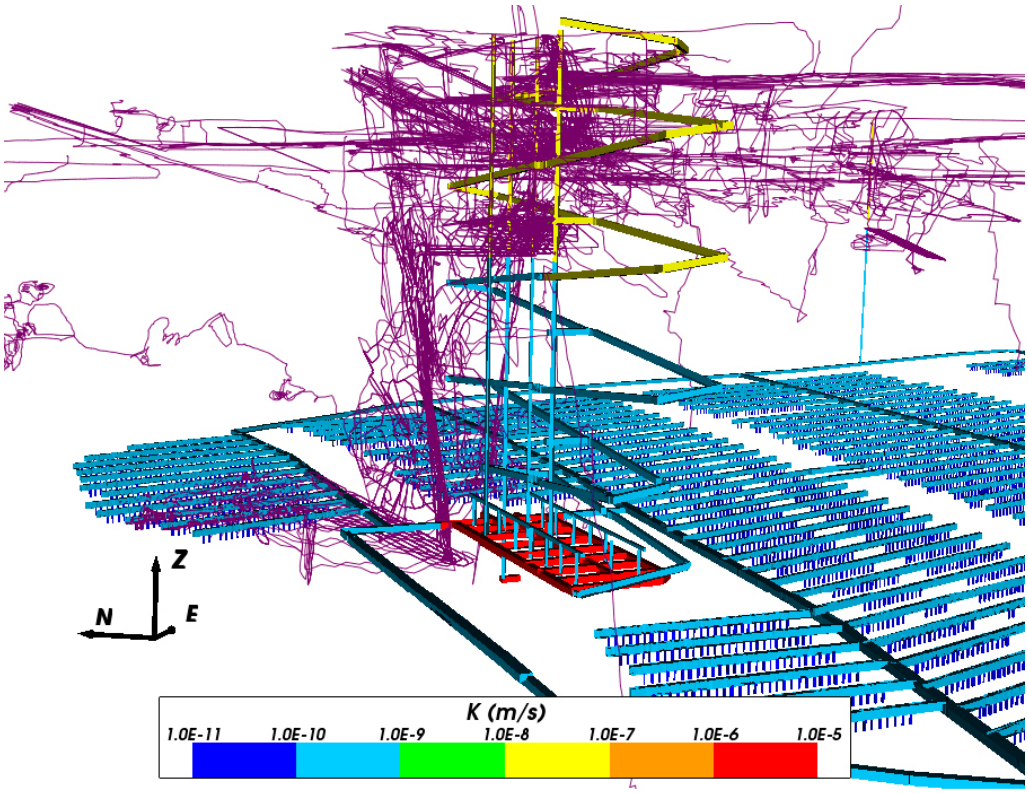

Figure 6-12. *Recharge pathways (purple) to deposition holes that pass through a grouted region at 3000 BC. Grouting depth is 200 m. SR-Site properties are used in the ramp and shafts. Repository structures are coloured by hydraulic conductivity.*

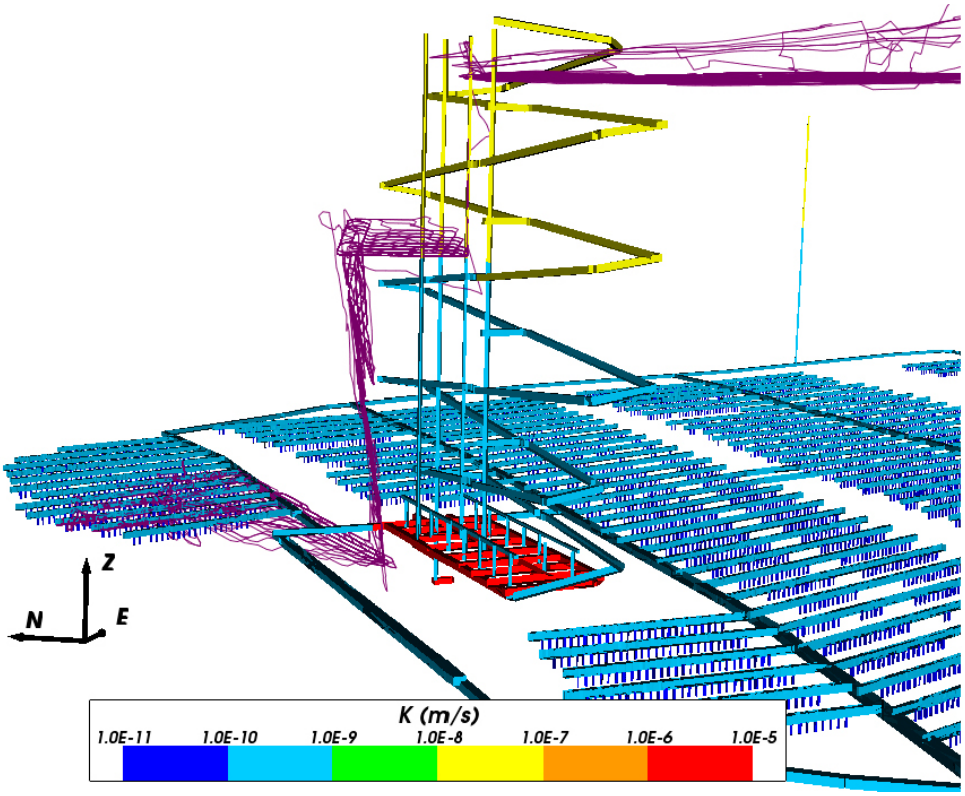

Figure 6-13. *Recharge pathways (purple) to deposition holes that pass through a grouted region at 2000 AD. Grouting depth is 200 m. SR-Site properties are used in the ramp and shafts. Repository structures are coloured by hydraulic conductivity.*

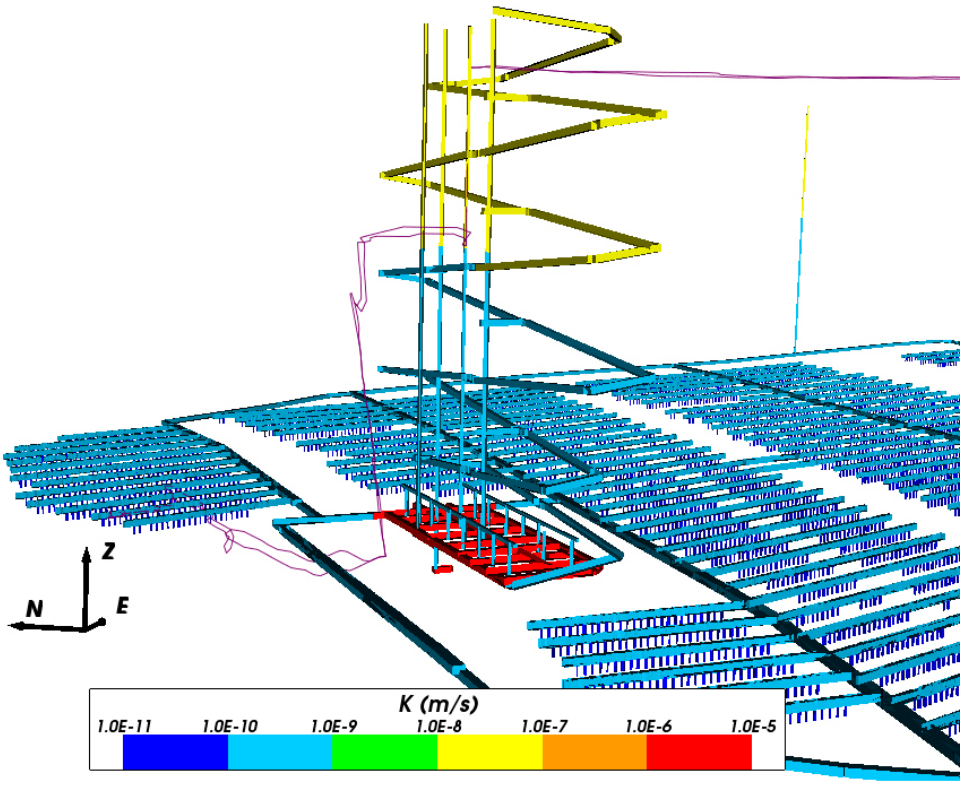

Figure 6-14. *Recharge pathways (purple) to deposition holes that pass through a grouted region at 9000 AD. Grouting depth is 200 m. SR-Site properties are used in the ramp and shafts. Repository structures are coloured by hydraulic conductivity.*

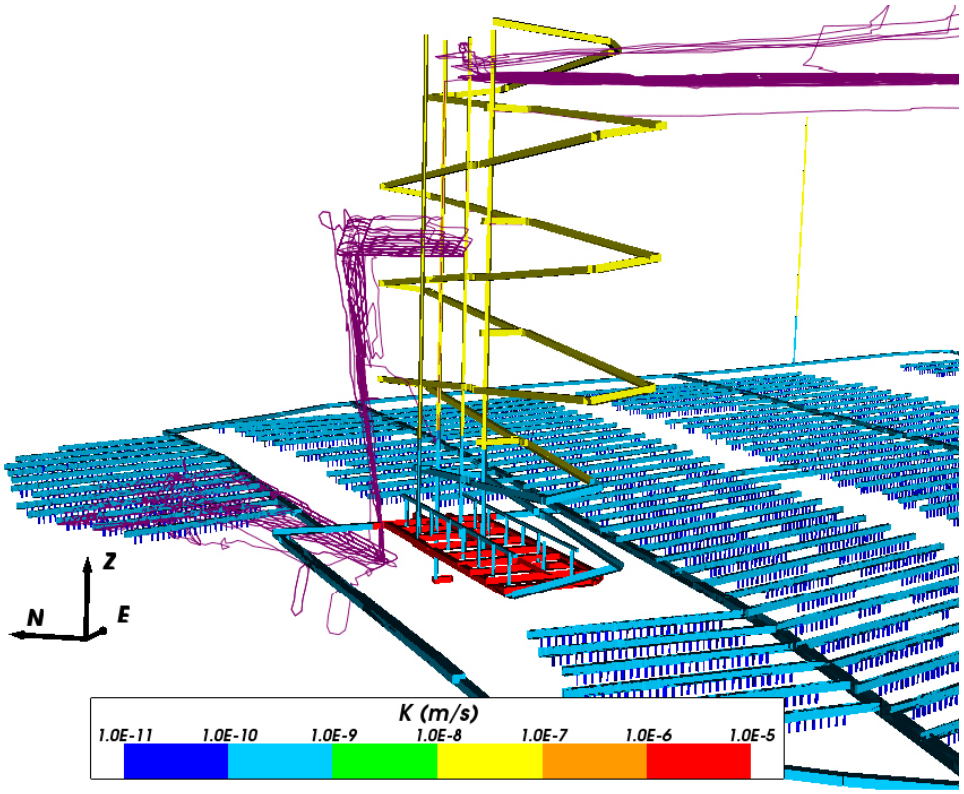

Figure 6-15. *Recharge pathways (purple) to deposition holes that pass through a grouted region at 2000 AD. Grouting depth is 370 m. Alternative repository sealing properties are used in the ramp and shafts. Repository structures are coloured by hydraulic conductivity.*

Table 6-3. The number and percentage of recharge pathways to deposition hole locations that pass through a grouted region, out of a total of 20,748 particles released for the Q1, Q2 and Q3 release types, for each case and particle release time. Particles are excluded if there is insufficient flow at the start location or if they do not meet the FPC and EFPC criteria. The grouting radius is 5 m.

Case	Release time	Count	Percentage
200 m grouting	3000 BC	79	0.38
	2000 AD	50	0.24
	9000 AD	1	0.00
370 m grouting	3000 BC	79	0.38
	2000 AD	50	0.24
	9000 AD	1	0.00
370 m sealing	3000 BC	76	0.37
	2000 AD	33	0.16
	9000 AD	1	0.00

Table 6-4. The number and percentage of recharge pathways to deposition hole locations that pass through a grouted region, out of a total of 20,748 particles released for the Q1, Q2 and Q3 release types, for each case and particle release time. The grouting radius is 20 m.

Case	Release time	Count	Percentage
200 m grouting	3000 BC	163	0.79
	2000 AD	92	0.44
	9000 AD	2	0.01
370 m grouting	3000 BC	165	0.80
	2000 AD	93	0.45
	9000 AD	2	0.01
370 m sealing	3000 BC	155	0.75
	2000 AD	88	0.42
	9000 AD	2	0.01

Table 6-5, Table 6-8 and Table 6-11 give performance measure statistics for the portion of the recharge pathways in the rock between the grouted region and the deposition holes. There appears to be little variation in the mean log values and the standard deviation of the log values for different cases and release times. This is probably a reflection of the limited number of routes used from the grout to the deposition holes. There is more variation in minimum values, as might be expected since this value will be more sensitive to the differences between individual pathways. In particular, the minimum F_r values show significant variation between release times, although little variation between cases. Note that the 9000 AD results are based on very few recharge pathways intersecting the grout, so it is difficult to draw too many conclusions from the performance measure statistics for this release time.

Table 6-6, Table 6-9 and Table 6-12 show the corresponding performance measure statistics for the less pessimistic case with the additional pathway rejection criteria described above. All of the performance measure statistics increase in value although the difference is not great, especially in the mean values.

Table 6-7, Table 6-10 and Table 6-13 show the performance measure statistics when a 20 m grouting radius is used. The values generally descrease, but the change is very minor. Again, the lack of sensitivity to the grouting radius is due to the small number of recharge pathways near to the ramp.

Figure 6-16 to Figure 6-18 show the deposition hole locations that are at the end of recharge pathways that pass through a grouted region, coloured by F_r. All of these deposition hole locations are close to the ramp, primarily lying to the north. For 3000 BC there is an additional group of deposition hole locations to the east. There does not appear to be a strong correlation between location and F_r value, but the deposition holes with the lowest F_r values are to the east of the ramp at 3000 BC.

Table 6-5. Statistics for path length in the rock, L_r, of recharge pathways between the grouted region and the deposition holes for each case and particle release time. The grouting radius is 5 m.

Case	Release time	Min L_r (m)	Mean $\log_{10}(L_r)$ (m)	SD $\log_{10}(L_r)$ (m)
200 m grouting	3000 BC	$6.050 \cdot 10^{2}$	3.044	$2.491 \cdot 10^{-1}$
	2000 AD	$6.131 \cdot 10^{2}$	2.986	$1.971 \cdot 10^{-1}$
	9000 AD	$9.114 \cdot 10^{2}$	2.976	$2.294 \cdot 10^{-2}$
370 m grouting	3000 BC	$6.050 \cdot 10^{2}$	3.043	$2.490 \cdot 10^{-1}$
	2000 AD	$6.131 \cdot 10^{2}$	2.985	$1.977 \cdot 10^{-1}$
	9000 AD	$9{,}114 \cdot 10^{2}$	2.976	$2.294 \cdot 10^{-2}$
370 m sealing	3000 BC	$6.339 \cdot 10^{2}$	3.034	$2.350 \cdot 10^{-1}$
	2000 AD	$5.455 \cdot 10^{2}$	2.978	$1.845 \cdot 10^{-1}$
	9000 AD	$9.882 \cdot 10^{2}$	3.071	$1.078 \cdot 10^{-1}$

Table 6-6. Statistics for path length in the rock, L_r, of recharge pathways between the grouted region and the deposition holes for each case and particle release time. Particles are excluded if there is insufficient flow at the start location or if they do not meet the FPC and EFPC criteria. The grouting radius is 5 m.

Case	Release time	Min L_r (m)	Mean $\log_{10}(L_r)$ (m)	SD $\log_{10}(L_r)$ (m)
200 m grouting	3000 BC	$6.407 \cdot 10^{2}$	3.049	$2.418 \cdot 10^{-1}$
	2000 AD	$6.544 \cdot 10^{2}$	3.032	$1.931 \cdot 10^{-1}$
	9000 AD	$9.821 \cdot 10^{2}$	2.992	N/A
370 m grouting	3000 BC	$6.407 \cdot 10^{2}$	3.048	$2.416 \cdot 10^{-1}$
	2000 AD	$6.539 \cdot 10^{2}$	3.030	$1.947 \cdot 10^{-1}$
	9000 AD	$9.821 \cdot 10^{2}$	2.992	N/A
370 m sealing	3000 BC	$6.339 \cdot 10^{2}$	3.027	$2.295 \cdot 10^{-1}$
	2000 AD	$5.455 \cdot 10^{2}$	3.007	$2.102 \cdot 10^{-1}$
	9000 AD	$1.404 \cdot 10^{3}$	3.147	N/A

Table 6-7. Statistics for path length in the rock, L_r, of recharge pathways between the grouted region and the deposition holes for each case and particle release time. The grouting radius is 20 m.

Case	Release time	Min L_r (m)	Mean $\log_{10}(L_r)$ (m)	SD $\log_{10}(L_r)$ (m)
200 m grouting	3000 BC	$5.504 \cdot 10^{2}$	3.018	$2.310 \cdot 10^{-1}$
	2000 AD	$5.950 \cdot 10^{2}$	2.964	$2.040 \cdot 10^{-1}$
	9000 AD	$8.298 \cdot 10^{2}$	2.952	$4.639 \cdot 10^{-2}$
370 m grouting	3000 BC	$5.079 \cdot 10^{2}$	3.009	$2.330 \cdot 10^{-1}$
	2000 AD	$5.950 \cdot 10^{2}$	2.962	$2.037 \cdot 10^{-1}$
	9000 AD	$8.298 \cdot 10^{2}$	2.952	$4.639 \cdot 10^{-2}$
370 m sealing	3000 BC	$5.268 \cdot 10^{2}$	3.005	$2.355 \cdot 10^{-1}$
	2000 AD	$4.520 \cdot 10^{2}$	2.956	$1.911 \cdot 10^{-1}$
	9000 AD	$9.151 \cdot 10^{2}$	3.052	$1.279 \cdot 10^{-1}$

Table 6-8. Statistics for travel time in the rock, t_r, of recharge pathways between the grouted region and the deposition holes for each case and particle release time. The grouting radius is 5 m.

Case	Release time	Min t_r (y)	Mean $\log_{10}(t_r)$ (y)	SD $\log_{10}(t_r)$ (y)
200 m grouting	3000 BC	$9.935 \cdot 10^{1}$	2.619	$5.316 \cdot 10^{-1}$
	2000 AD	$1.091 \cdot 10^{2}$	2.587	$5.567 \cdot 10^{-1}$
	9000 AD	$4.952 \cdot 10^{2}$	2.916	$3.134 \cdot 10^{-1}$
370 m grouting	3000 BC	$9.935 \cdot 10^{1}$	2.619	$5.316 \cdot 10^{-1}$
	2000 AD	$1.091 \cdot 10^{2}$	2.586	$5.570 \cdot 10^{-1}$
	9000 AD	$4.952 \cdot 10^{2}$	2.916	$3.134 \cdot 10^{-1}$
370 m sealing	3000 BC	$6.398 \cdot 10^{1}$	2.675	$5.445 \cdot 10^{-1}$
	2000 AD	$1.067 \cdot 10^{2}$	2.570	$4.934 \cdot 10^{-1}$
	9000 AD	$3.333 \cdot 10^{2}$	2.830	$4.341 \cdot 10^{-1}$

Table 6-9. Statistics for travel time in the rock, t_r, of recharge pathways between the grouted region and the deposition holes for each case and particle release time. Particles are excluded if there is insufficient flow at the start location or if they do not meet the FPC and EFPC criteria. The grouting radius is 5 m.

Case	Release time	Min t_r (y)	Mean $\log_{10}(t_r)$ (y)	SD $\log_{10}(t_r)$ (y)
200 m grouting	3000 BC	$1.221 \cdot 10^{2}$	2.790	$5.832 \cdot 10^{-1}$
	2000 AD	$1.215 \cdot 10^{2}$	2.725	$5.363 \cdot 10^{-1}$
	9000 AD	$1.374 \cdot 10^{3}$	3.138	N/A
370 m grouting	3000 BC	$1.221 \cdot 10^{2}$	2.790	$5.831 \cdot 10^{-1}$
	2000 AD	$1.215 \cdot 10^{2}$	2.724	$5.370 \cdot 10^{-1}$
	9000 AD	$1.374 \cdot 10^{3}$	3.138	N/A
370 m sealing	3000 BC	$1.238 \cdot 10^{2}$	2.733	$5.361 \cdot 10^{-1}$
	2000 AD	$1.215 \cdot 10^{2}$	2.755	$4.964 \cdot 10^{-1}$
	9000 AD	$1.370 \cdot 10^{3}$	3.137	N/A

Table 6-10. Statistics for travel time in the rock, t_r, of recharge pathways between the grouted region and the deposition holes for each case and particle release time. The grouting radius is 20 m.

Case	Release time	Min t_r (y)	Mean $\log_{10}(t_r)$ (y)	SD $\log_{10}(t_r)$ (y)
200 m grouting	3000 BC	$9.921 \cdot 10^{1}$	2.616	$5.310 \cdot 10^{-1}$
	2000 AD	$1.090 \cdot 10^{2}$	2.586	$5.568 \cdot 10^{-1}$
	9000 AD	$4.951 \cdot 10^{2}$	2.916	$3.135 \cdot 10^{-1}$
370 m grouting	3000 BC	$9.921 \cdot 10^{1}$	2.612	$5.304 \cdot 10^{-1}$
	2000 AD	$1.090 \cdot 10^{2}$	2.584	$5.543 \cdot 10^{-1}$
	9000 AD	$4.951 \cdot 10^{2}$	2.916	$3.135 \cdot 10^{-1}$
370 m sealing	3000 BC	$6.393 \cdot 10^{1}$	2.669	$5.447 \cdot 10^{-1}$
	2000 AD	$1.065 \cdot 10^{2}$	2.570	$4.936 \cdot 10^{-1}$
	9000 AD	$3.332 \cdot 10^{2}$	2.830	$4.342 \cdot 10^{-1}$

Table 6-11. Statistics for flow-related transport resistance in the rock, F_r, of recharge pathways between the grouted region and the deposition holes for each case and particle release time. The grouting radius is 5 m.

Case	Release time	Min F_r (y/m)	Mean $\log_{10}(F_r)$ (y/m)	SD $\log_{10}(F_r)$ (y/m)
200 m grouting	3000 BC	$9.164 \cdot 10^{4}$	7.629	$9.269 \cdot 10^{-1}$
	2000 AD	$4.721 \cdot 10^{6}$	7.766	$9.301 \cdot 10^{-1}$
	9000 AD	$5.083 \cdot 10^{7}$	8.042	$4.756 \cdot 10^{-1}$
370 m grouting	3000 BC	$9.164 \cdot 10^{4}$	7.629	$9.269 \cdot 10^{-1}$
	2000 AD	$4.721 \cdot 10^{6}$	7.766	$9.302 \cdot 10^{-1}$
	9000 AD	$5.083 \cdot 10^{7}$	8.042	$4.756 \cdot 10^{-1}$
370 m sealing	3000 BC	$2.218 \cdot 10^{5}$	7.750	$9.455 \cdot 10^{-1}$
	2000 AD	$4.734 \cdot 10^{6}$	7.776	$9.145 \cdot 10^{-1}$
	9000 AD	$1.294 \cdot 10^{7}$	7.695	$8.249 \cdot 10^{-1}$

Table 6-12. Statistics for flow-related transport resistance in the rock, F_r, of recharge pathways between the grouted region and the deposition holes for each case and particle release time. Particles are excluded if there is insufficient flow at the start location or if they do not meet the FPC and EFPC criteria. The grouting radius is 5 m.

Case	Release time	Min F_r (y/m)	Mean $\log_{10}(F_r)$ (y/m)	SD $\log_{10}(F_r)$ (y/m)
200 m grouting	3000 BC	$5.496 \cdot 10^{6}$	7.947	$8.933 \cdot 10^{-1}$
	2000 AD	$6.806 \cdot 10^{6}$	8.067	$8.661 \cdot 10^{-1}$
	9000 AD	$2.392 \cdot 10^{8}$	8.379	N/A
370 m grouting	3000 BC	$5.496 \cdot 10^{6}$	7.947	$8.933 \cdot 10^{-1}$
	2000 AD	$6.806 \cdot 10^{6}$	8.067	$8.664 \cdot 10^{-1}$
	9000 AD	$2.392 \cdot 10^{8}$	8.379	N/A
370 m sealing	3000 BC	$1.570 \cdot 10^{6}$	7.922	$8.722 \cdot 10^{-1}$
	2000 AD	$6.386 \cdot 10^{6}$	8.203	$8.068 \cdot 10^{-1}$
	9000 AD	$1.899 \cdot 10^{8}$	8.279	N/A

Table 6-13. Statistics for flow-related transport resistance in the rock, F_r, of recharge pathways between the grouted region and the deposition holes for each case and particle release time. The grouting radius is 20 m.

Case	Release time	Min F_r (y/m)	Mean $\log_{10}(F_r)$ (y/m)	SD $\log_{10}(F_r)$ (y/m)
200 m grouting	3000 BC	$9.159 \cdot 10^{4}$	7.615	$9.356 \cdot 10^{-1}$
	2000 AD	$4.721 \cdot 10^{6}$	7.766	$9.301 \cdot 10^{-1}$
	9000 AD	$5.083 \cdot 10^{7}$	8.042	$4.756 \cdot 10^{-1}$
370 m grouting	3000 BC	$9.159 \cdot 10^{4}$	7.611	$9.312 \cdot 10^{-1}$
	2000 AD	$4.721 \cdot 10^{6}$	7.764	$9.255 \cdot 10^{-1}$
	9000 AD	$5.083 \cdot 10^{7}$	8.042	$4.756 \cdot 10^{-1}$
370 m sealing	3000 BC	$2.218 \cdot 10^{5}$	7.736	$9.574 \cdot 10^{-1}$
	2000 AD	$4.734 \cdot 10^{6}$	7.776	$9.145 \cdot 10^{-1}$
	9000 AD	$1.294 \cdot 10^{7}$	7.695	$8.249 \cdot 10^{-1}$

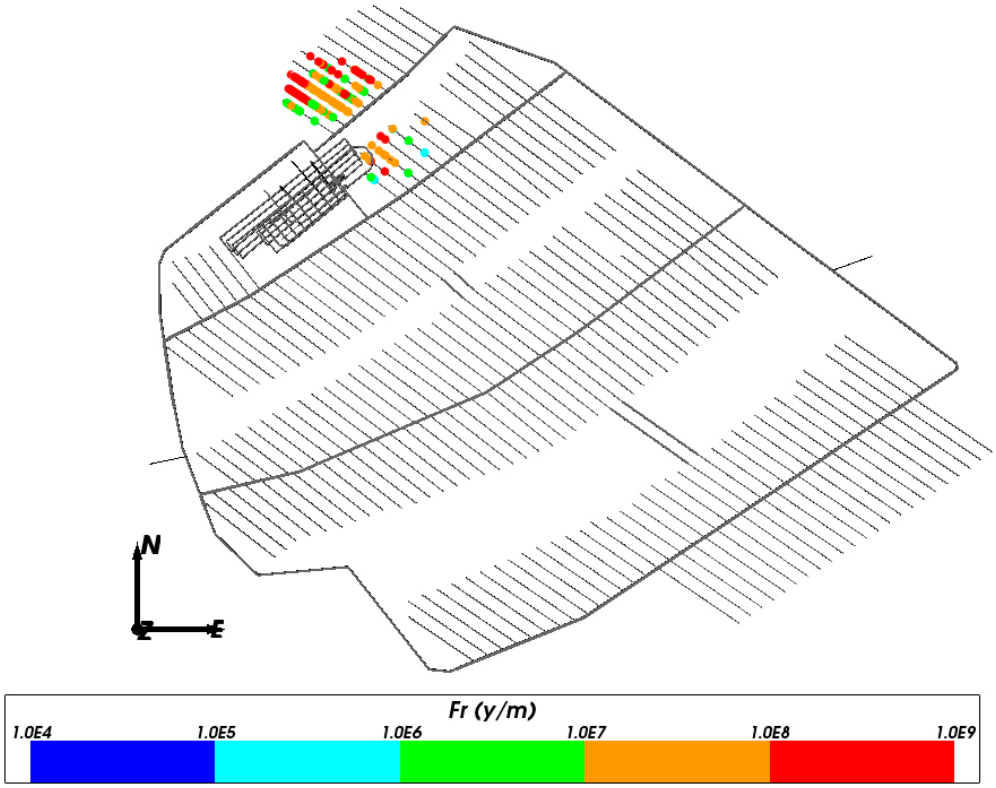

Figure 6-16. *Deposition hole locations, coloured by F_p at the end of recharge pathways that pass through a grouted region at 3000 BC. Grouting depth is 200 m. SR-Site properties are used in the ramp and shafts. Repository structures are coloured black.*

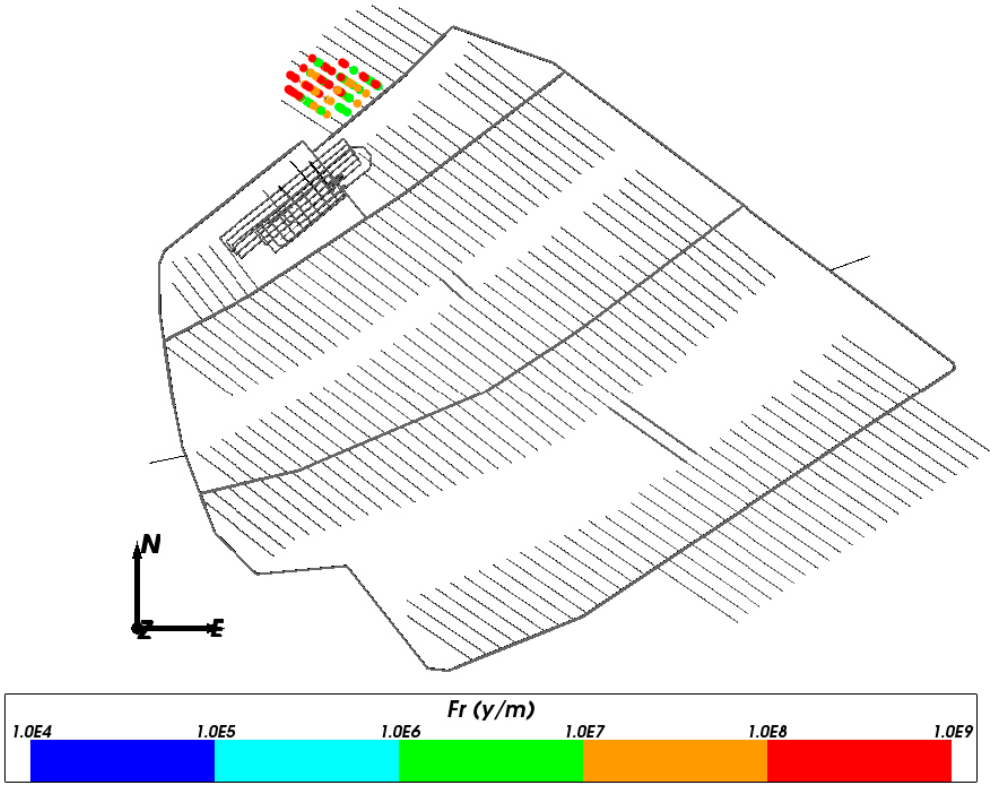

Figure 6-17. *Deposition hole locations, coloured by F_p at the end of recharge pathways that pass through a grouted region at 2000 AD. Grouting depth is 200 m. SR-Site properties are used in the ramp and shafts. Repository structures are coloured black.*

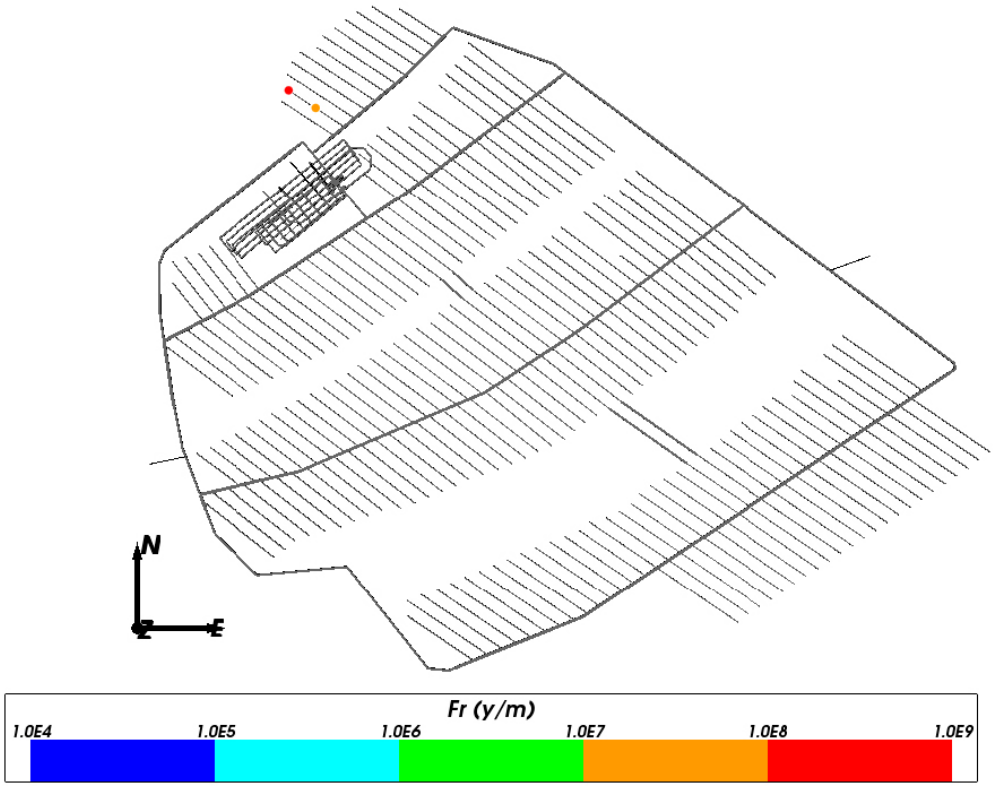

Figure 6-18. *Deposition hole locations, coloured by F_r at the end of recharge pathways that pass through a grouted region at 9000 AD. Grouting depth is 200 m. SR-Site properties are used in the ramp and shafts. Repository structures are coloured black.*

6.2.2 ECPM transient evolution of alkaline water

To consider the transient evolution of the alkaline water under temperate conditions an ECPM regional model is used. This model is equivalent to the SR-Site regional-scale model for the extended spatial variability case, but the more refined local region with 20 m elements has been extended to provide more detailed modelling of the alkaline plume evolution in the repository area. Additionally, repository structures have been added using the implicit fracture zone (IFZ) method, as described in Joyce et al. (2010). The hydraulic properties of the rock are updated by the repository IFZs to include the grout, but it is not possible to distinguish between the 370 m grouting and 370 m sealing cases at this scale, so the 370 m sealing case is not considered. As with SR-Site, a transient evolution of boundary conditions is used to reflect land rise and changes in the salinity of infiltrating water over time. The processes of advection, density dependent flow, dispersion and diffusion in the fractured rock and rock matrix diffusion are included, using the same parameters as for SR-Site. There are no chemical reactions included so there is a conservative assumuption that there are no pH buffering reactions between the grout leachate and the host rock. The initial conditions are taken from the SR-Site extended spatial variability case at 2000 AD, but with the addition of an extra reference water as a tracer to represent the alkaline water released by the grout. The system is then allowed to evolve over 10,000 years.

The location of the alkaline water plume relative to the repository structures after 3000 years of evolution are shown in Figure 6-19 and Figure 6-20 for the 200 m grouting case and 370 m grouting case respectively. In both cases, the plume follows the main advective flow direction towards the shoreline to the north and northeast. Even with the unrealistic assumption of no pH buffering reactions between the grout leachate and the host rock, there is no appreciable penetration of alkaline water to the deposition hole locations in these models. This is also shown by Figure 6-21 and Figure 6-22, which represent the fraction of alkaline water at the centre of each deposition hole. For a 200 m grouting depth, no hole has an alkaline water fraction greater than $1.0 \cdot 10^{-4}$ and for a 370 m grouting depth, no hole has an alkaline water fraction greater than $2.0 \cdot 10^{-3}$, which is insufficient to have any effect on pH. However, only bulk flows at a fairly large scale are considered and so some of the discrete flow pathways seen in the DFN models would not be represented.

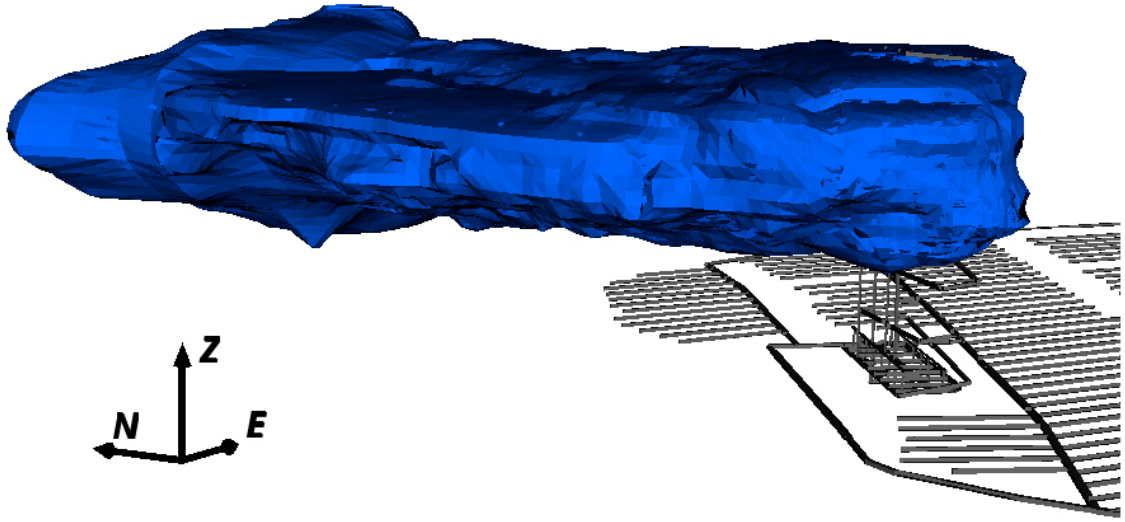

Figure 6-19. *The extent of the alkaline water plume at 12,000 AD. Grouting depth is 200 m. The plume is coloured by alkaline water fraction, with fractions less than 0.1 removed. Repository structures are coloured grey.*

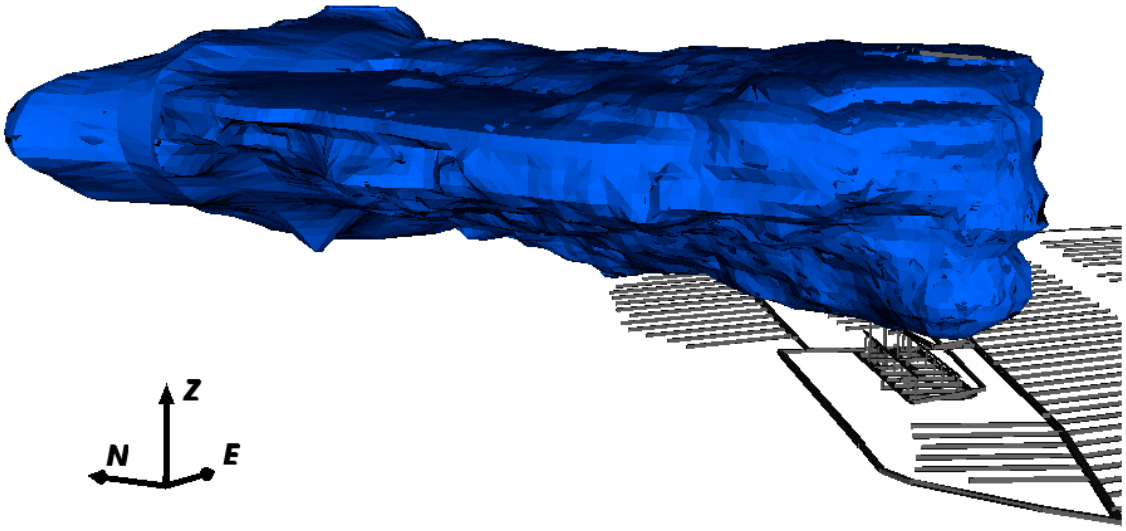

Figure 6-20. *The extent of the alkaline water plume at 12,000 AD. Grouting depth is 370 m. The plume is coloured by alkaline water fraction, with fractions less than 0.1 removed. Repository structures are coloured grey.*

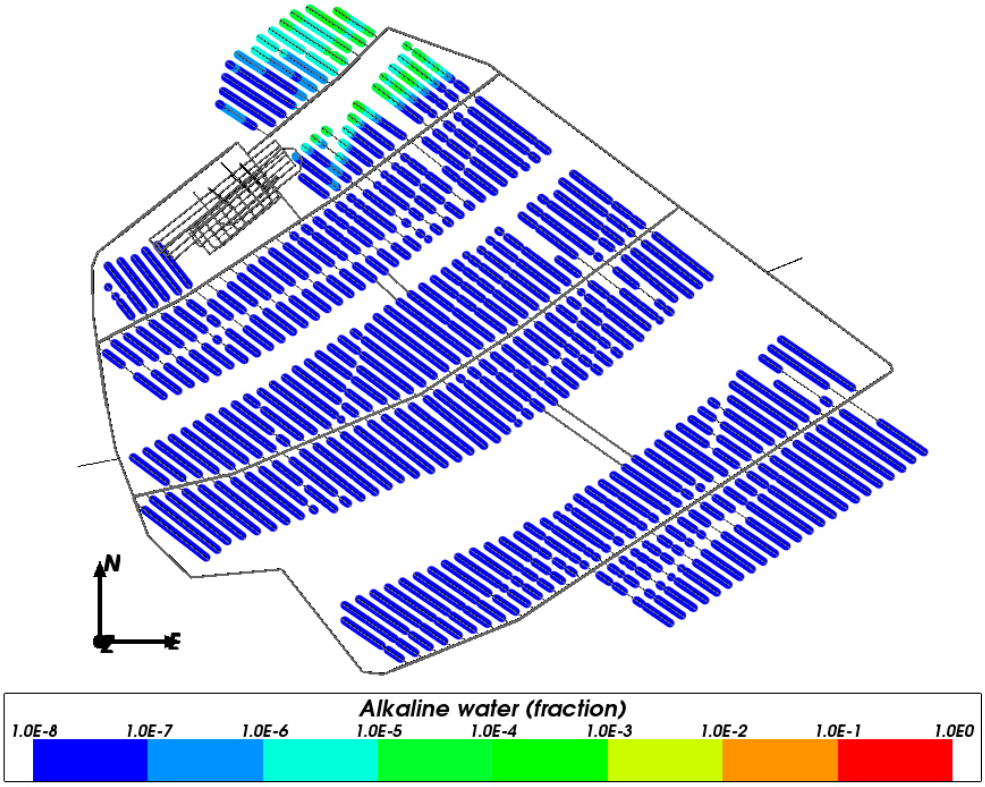

Figure 6-21. *Deposition hole locations coloured by the fraction of alkaline water at 12,000 AD. Grouting depth is 200 m. Repository structures are coloured grey.*

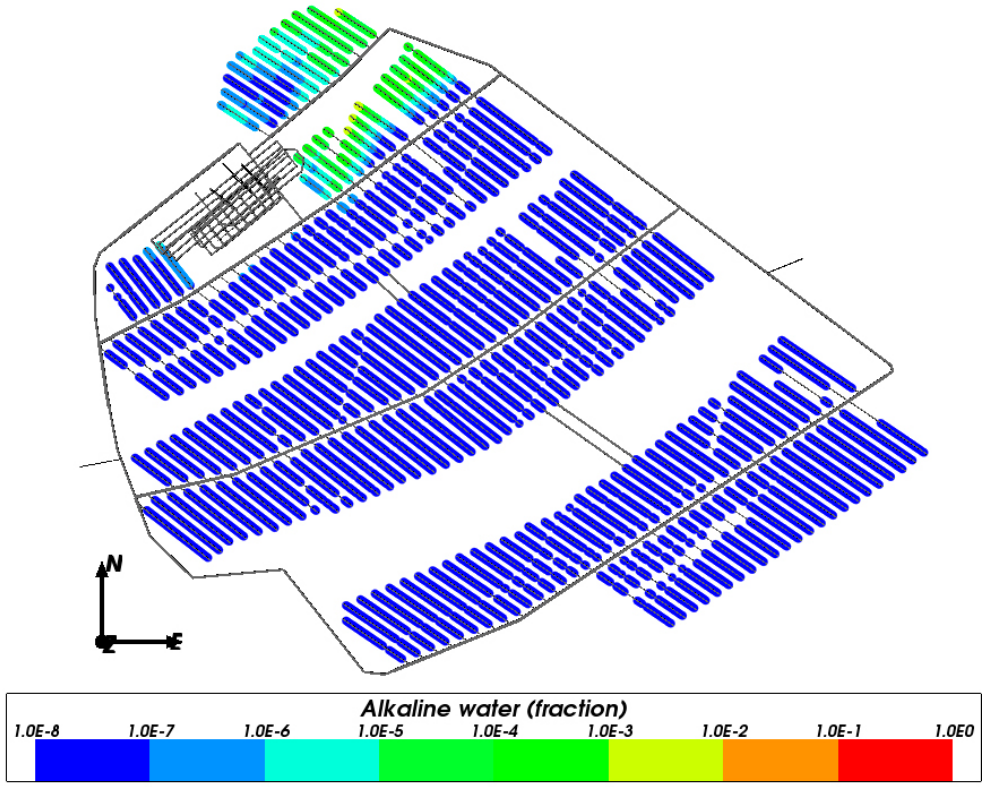

Figure 6-22. *Deposition hole locations coloured by the fraction of alkaline water at 12,000 AD. Grouting depth is 370 m. Repository structures are coloured grey.*

6.3 Permafrost period

6.3.1 ECPM recharge pathways

The modelling reported in this section relates to the transport of alkaline water released from OPC grout during a period when periglacial climate conditions are present. In short this means that negative ground temperature occurs and that permafrost is apparent within the modelled site.

The model set-up and flow path calculation results are shown for the flow situation just before and during the first permafrost event that will affect the Forsmark site in about 8,000 years' time. This model uses the hydrogeological code DarcyTools (Svensson et al. 2010) and is based on a developed set-up of the SR-Site model presented in Svensson and Follin (2010).

The primary developments of the SR-Site model set-up that have been introduced are:

- As compared to the base-case used in the SR-Site hydrogeological modelling, the DFN from the SR-Site extended spatial variability case is used in this report, underlying the ECPM representation. See further Section 4.1. This DFN is assessed in all parts of the regional SDM model domain.
- As compared to the SR-Site model by Svensson and Follin (2010), a grid refinement of the surface and the tunnel walls has been assessed.
- Present and future lakes have been incorporated and specifically modelled as heat boundary conditions.
- The solution is a coupled hydraulic-chemical-thermal model.

The hydraulic properties used in the models are described in Chapter 5. Same as in Sections 6.1 and 6.2, the extended spatial variability case from SR-Site is chosen as the case studied here since it has the largest discrete fracture network (DFN) region around the repository and so can represent the detailed constrained flows within the fractures over a larger volume. Only a single realisation of the hydraulic rock mass domain (HRD) is considered and the fractures used are those generated during the SR-Site modelling. The hydraulic conductor domain (HCD) has the same depth-dependent deterministic properties as within SR-Site.

The repository and the ground surface has the highest level of detail with a grid resolution of 2 metres around the repository structures, particularly the deposition holes, deposition tunnels and main tunnels, each of which is modelled as a continuous porous medium that matches the geometry and properties of those structures. Any excavation damaged zone (EDZ) around the repository structures is not represented.

The simulations reported were carried out as follows:

- The model is initialized at 8,000 BC with a homogeneous water elevation covering the entire domain, a homogeneous ground surface temperature of 4 degrees Centigrade, and a depth profile of salinity as specified in Svensson and Follin (2010) with one specific relationship for some of the fracture domains and one other for the surrounding rock.
- First the model simulates 10,000 years and is stopped at present day (2,000 AD). Only a visual inspection of the results is conducted. The results seem in alignment with similar results established within SR-Site.
- The second step simulates upcoming 6,000 years up to 8,000 AD which is chosen to represent the time just before the first permafrost period.
- The third step takes additional 2,000 years and stops at the peak of the first permafrost period, with a ground surface temperature just below –1 degree Centigrade.
- The fourth step is in large the same as the third step. However, added on the northwest boundary is a hydrostatic pressure profile taken from the SR-Site simulations as a representative case for an ice sheet approaching on top of the permafrost. The case is simulated for 200 years in order to reach a pseudo-steady state solution.
- Particle tracking were conducted in a steady flow field. Results of the final situation after the second, third, and fourth steps are presented herein.
- Case A represents the results after the second step above described.
- Case B represents the results after the third step above described.

- Case C represents the results after the fourth step above described.
- The release locations of particles are taken from the simulation done for the open-repository period in Section 6.1. The release locations (Figure 6-2) are taken as the positions with an inflow larger than 0.1 l/min within the Repository design. The case of higher inflow is deemed more significant since the natural flow conditions during permafrost conditions and also present day are significantly slower than during the open repository. Hence only the most conductive parts are believed important for the questions herein asked.

The shore line elevation and salinity at the different times specified as top-boundary conditions for the model are shown in Figure 5-1 and Figure 5-2 (dashed red line) respectively. The assumed ground temperature evolution over time is an additional top-boundary condition and is shown in Figure 6-23.

Some remarks worth noting regarding the model set-up in this section are:

- The assessed shore line elevation curve (Figure 5-1), salinity development (dashed red line in Figure 5-2) and temperature development (Figure 6-23) are all simplifications of the more complex curves reported in SKB (2010b). The temperature series are further used in the wrong setting. The assessed series are intended for use of reconstruction of the historical climate and not forward prediction. The series assessed are compiled by the last and first part of the 120 kyear time series used in SR-Site. The forward predicting time series would have longer periods of lower temperature around present day.
- The extensions of present and future lakes along with the time they are lakes are also simplified. The extension is always assumed as the outer boundary given by the lake delivery. This data set is also under the process of being up-dated. The timings are roughly captured from the so called "Pandora table" reported in Brydsten and Strömgren (2010).
- It may seem natural to place particles in the grouted volumes and track these forward in time. This case however is not put forward. Instead, an alternative is to use backward particle tracking from points where there is a simulated inflow to the open repository. It is then tested if the particle has its origin in, or passes, the grouted volumes. This alternative is favoured as a good illustration of how flow paths are obtained.
- It should be kept in mind that a future glaciation is at least 50–60 kyears into the future for the modelled site. In Case C, the ice-sheet is assumed to advance over the permafrost conditions that may prevail in about 8,000 years.

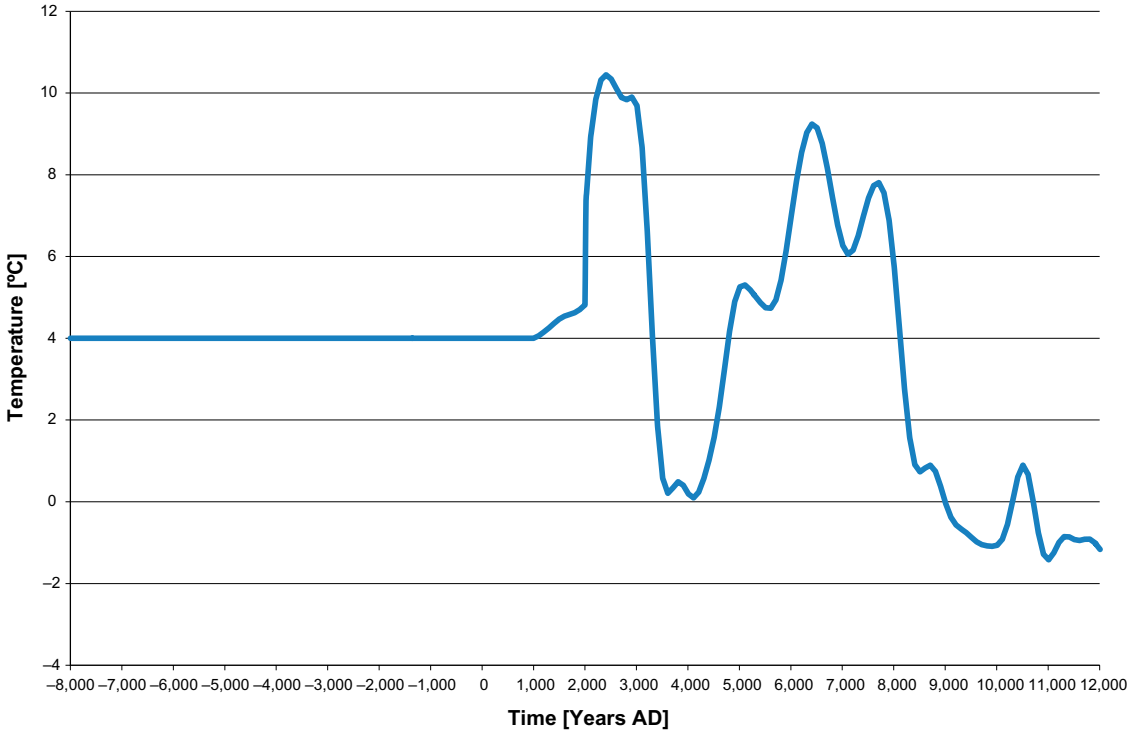

Figure 6-23. *Evolution of the ground temperature.*

Particle trajectories corresponding to the release locations in Figure 6-2 for Case A are shown in Figure 6-24 and for Case B in Figure 6-25. The trajectories within the repository volume are found primary beneath the –370 m elevation. The eastern ventilation shaft is at no simulated situation found to be in a recharge area for the deposition holes. This is naturally to be expected since both Case A and B have their recharge area up-stream towards the west. The western shaft is during the time just before the first permafrost (Case A) found to be surrounded by trajectories recharging the deposition holes. However, in this set-up no recharge is found to pass through the near-field of the western ventilation shaft (Figure 6-26). However, one should bear in mind that this simulation represents one statistical realisation of the fracture network. Hence since many of the trajectories are found on elevations between –370 and –200 m it could not be ruled out that pathways released from a grouted volume around this ventilation shaft could reach the deposition holes' volume.

The main shaft area also have trajectories passing through the volume, however in this case it is during the permafrost conditions, ie. Case B (Figure 6-27). Again however no trajectories are found in this volume at an elevation above –200 m (Figure 6-28).

Figure 6-29 shows the repository design and remaining trajectories when all parts of the flow trajectories below –370 metres elevation have been removed for case C. It is seen that none of the remaining trajectories passes through the main shaft region. In fact due to the proximity of discharge locations in close by taliks the glacial flow system is primary a discharge area and the majority of backtracked particles comes from deeper sections of the flow domain. As the ice-sheet margin approach the site, the flow situation taken in Section 6.4 will be approached and may be a better representation of the hydrogeological properties of the site.

It should be noted that the first permafrost period modelled here is weak, and neither the freezing process in the ground nor changes in the hydraulic properties are significant. The effect on hydraulic properties might be more prominent if the permafrost case would be significantly colder and the future lake situation a little different. One talik that could have a significant impact sits close on top of the main shaft. Although it is not likely that this talik would significantly contribute to the recharge, the assessed models domains are too small to rule out such possibilities.

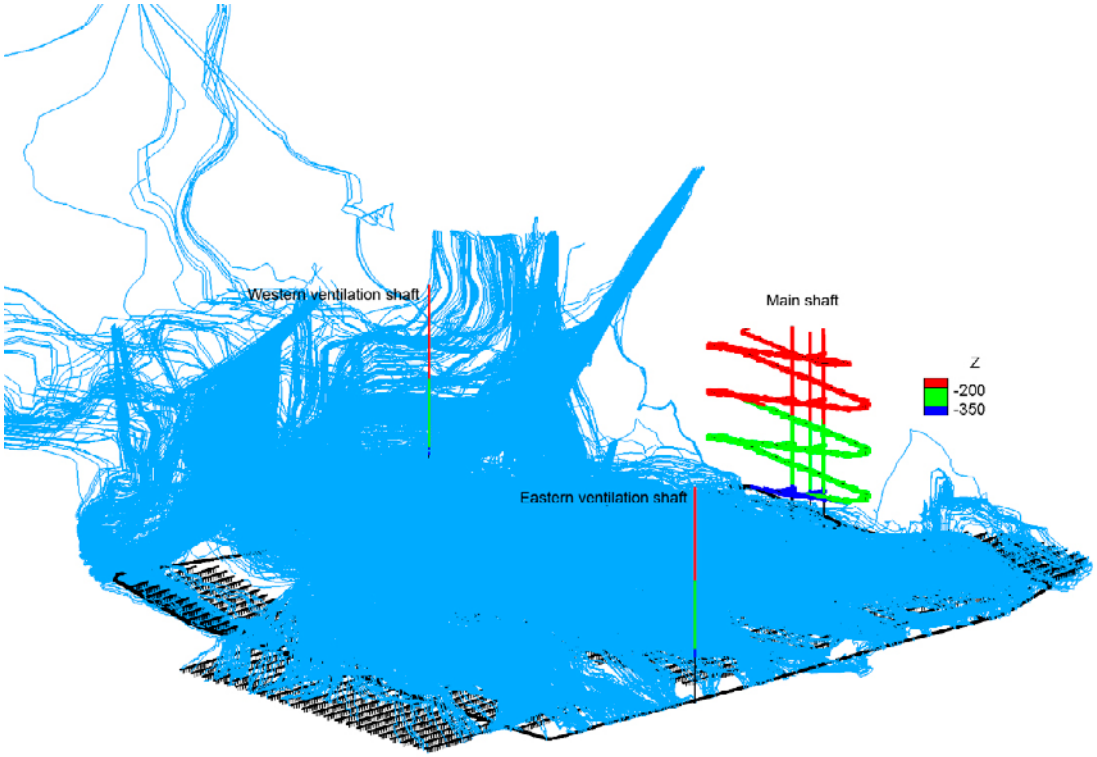

Figure 6-24. *Backward particle tracking trajectories for Case A. The particles were tracked for 10,000 days.*

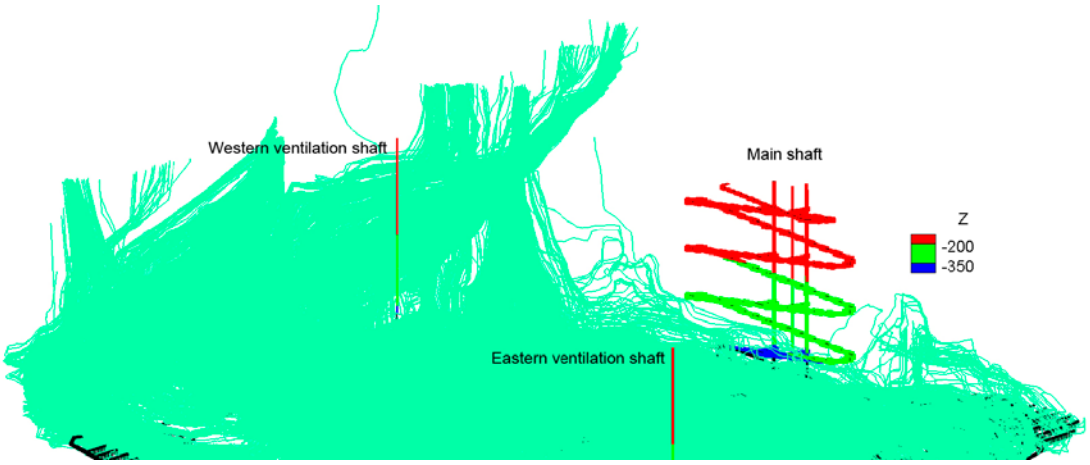

Figure 6-25. *Backward particle tracking trajectories for Case B. The particles were tracked for 10,000 days.*

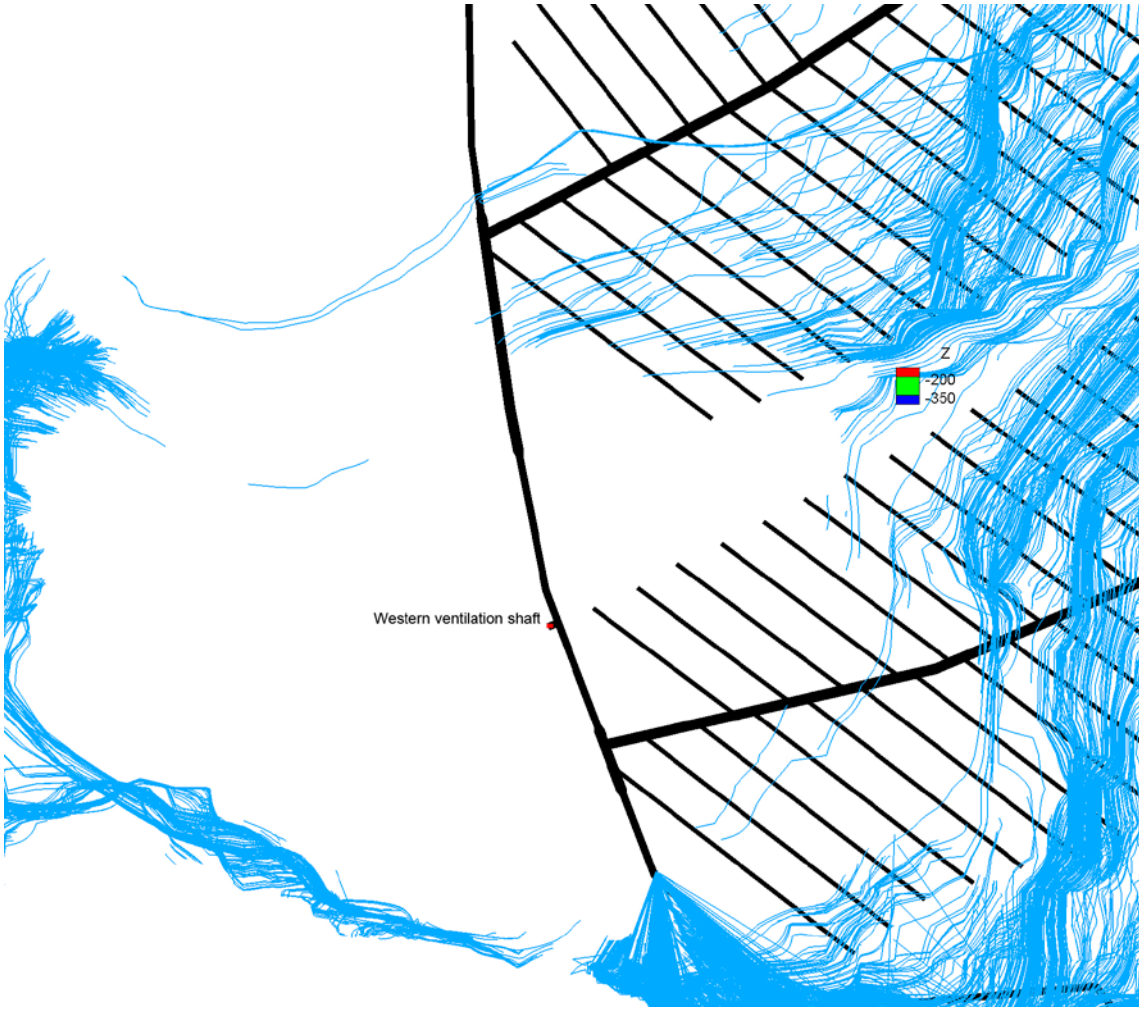

Figure 6-26. *Backward particle tracking trajectories for Case A. Focused around the western ventilation shaft (indicated by the red dot). Only trajectory parts above elevation –370 m are shown.*

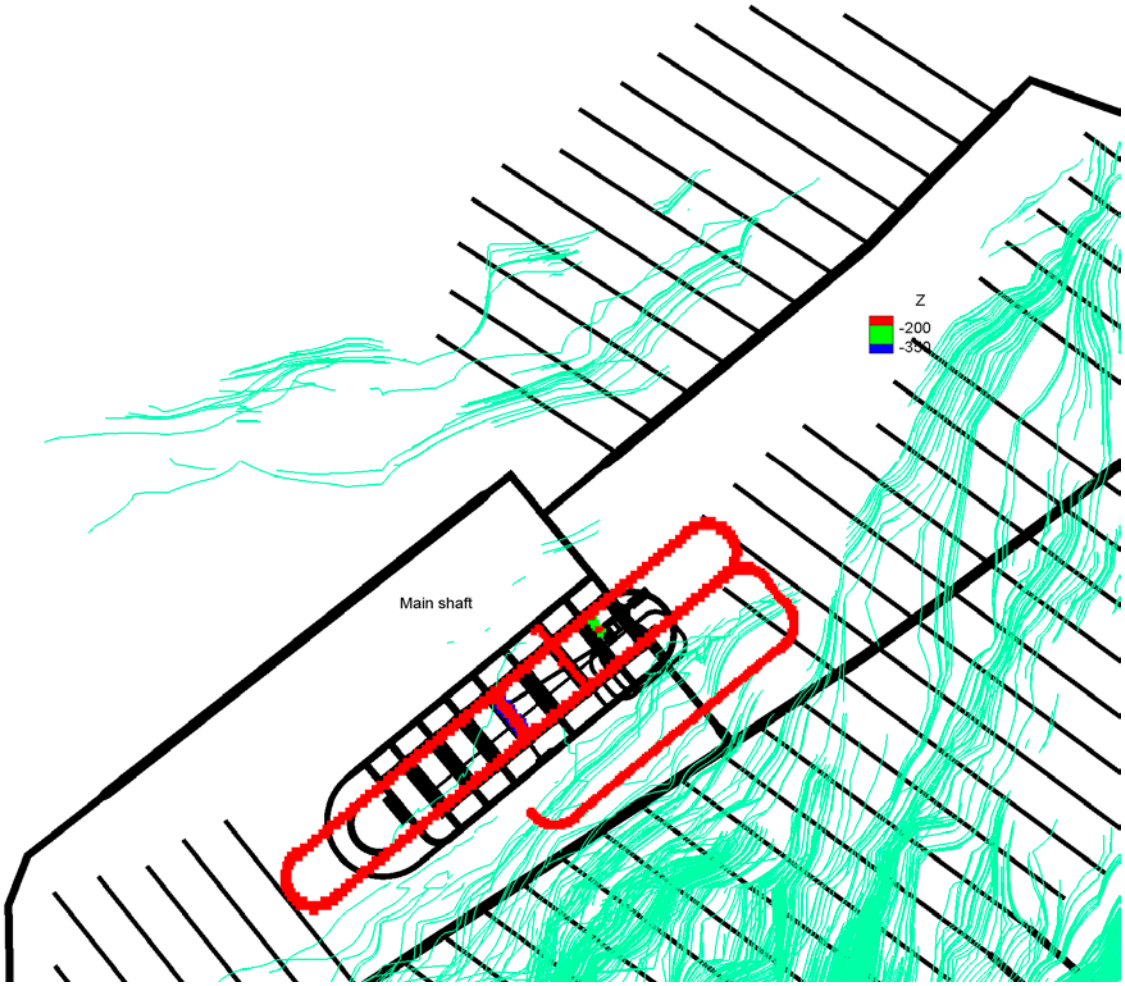

Figure 6-27. *Backward particle tracking trajectories for Case B. Focused around the main shaft. Only trajectory parts above elevation –370 m are shown.*

Figure 6-28. *Backward particle tracking trajectories for Case B. Focused around the main shaft. Only trajectory parts above elevation –200 m are shown.*

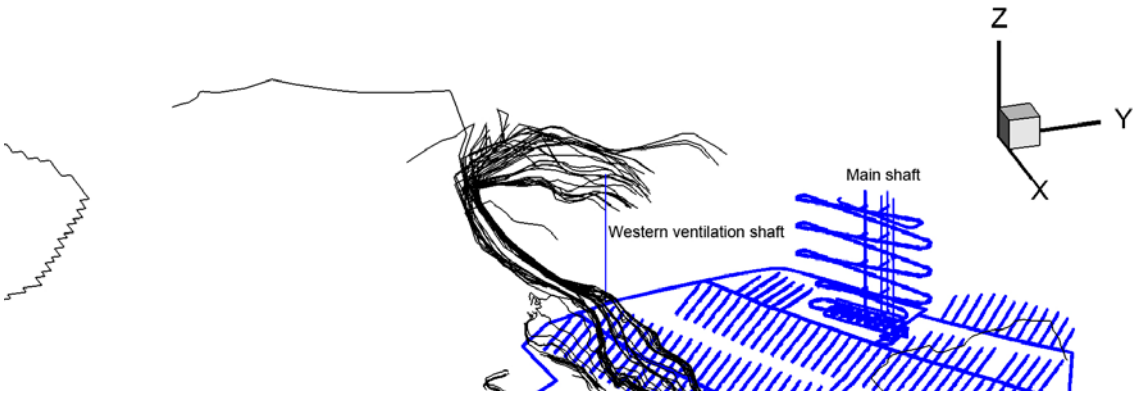

Figure 6-29. *Backward particle tracking trajectories for Case C. Only trajectory parts above elevation –370 m are shown.*

6.4 Glacial period

6.4.1 DFN recharge pathways

The methodology for calculating DFN recharge pathways for the temperate period, as described in Section 6.2.1, can be applied to glacial conditions. Instead of importing pressure boundary conditions and density values from a temperate period regional model, they are imported from an SR-Site glacial model (Vidstrand et al. 2010). A steady state pressure and velocity field is then calculated that is consistent with the pressure boundary conditions and density values. This is used for carrying out backward particle tracking calculations to determine recharge pathways in the same way as for the temperate climate situation. Glacial ice front location II was chosen for these calculations as the ice front is directly over the repository site and hence is likely to have the biggest impact on the results.

Figure 6-30 and Figure 6-31 show the recharge and discharge locations of flow pathways that reach deposition holes under glacial ice front location II conditions. In contrast to the temperate climate period, the flow is from the northwest to the southeast. The flow is driven by the glacial pressure imposed on the top surface of the northwest half of the model.

Table 6-14 shows the number of recharge pathways that pass through a grouted region and reach a deposition hole location. The count is similar to that at 2000 AD for the 200 m grouting case. However, the count is significantly higher for the 370 m grouting and 370 m sealing cases. This is because under glacial ice front location II conditions a significant number of the recharge pathway intersections with the grout are below –200 m elevation. This is clearly visible in the differences between Figure 6-32 showing recharge pathways with a grouting depth of 200 m and Figure 6-33 with a grouting depth of 370 m. These figures also show that the recharge via the grouted region is to deposition holes in the central and south eastern sections of the repository rather than to the sections closest to the ramp.

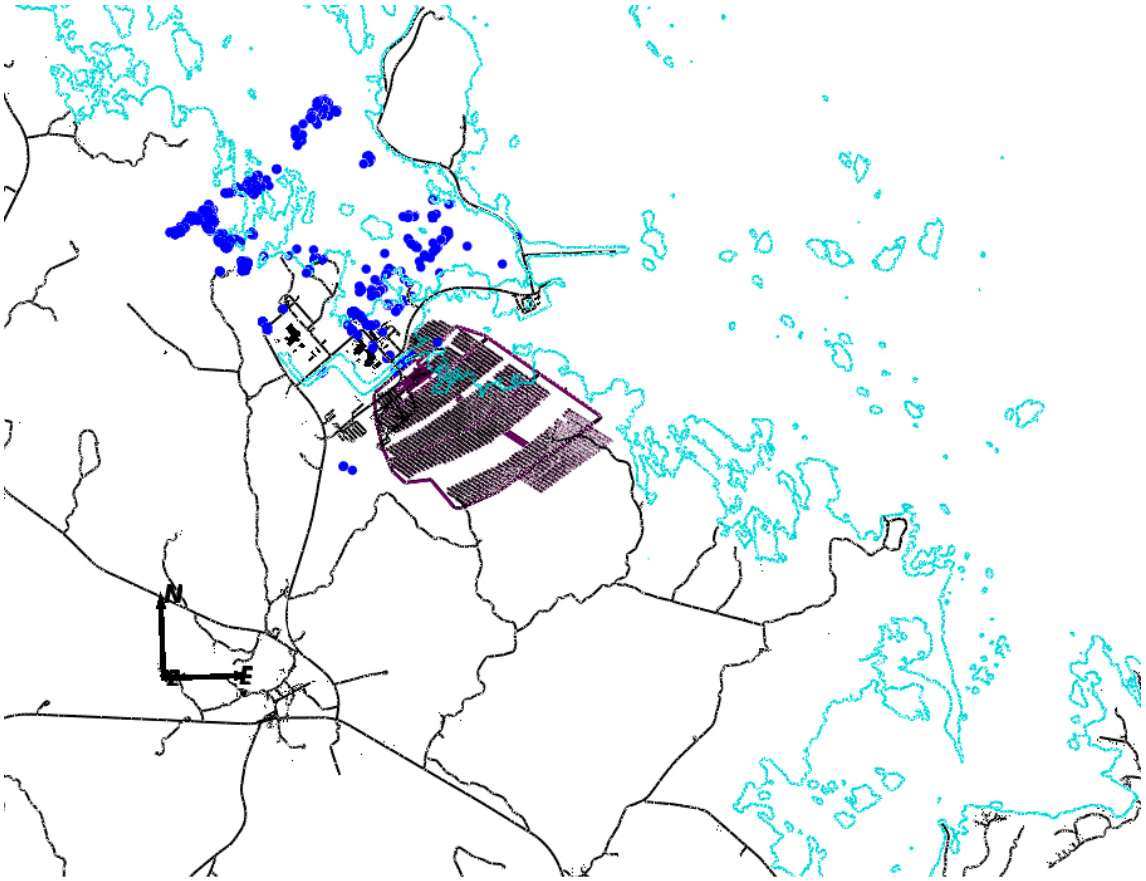

Figure 6-30. *Recharge locations on the top surface for flow pathways to deposition holes for glacial ice front location II, including those that do not intersect the grout. The shoreline at 2000 AD is shown in blue and buildings and roads are shown in black.*

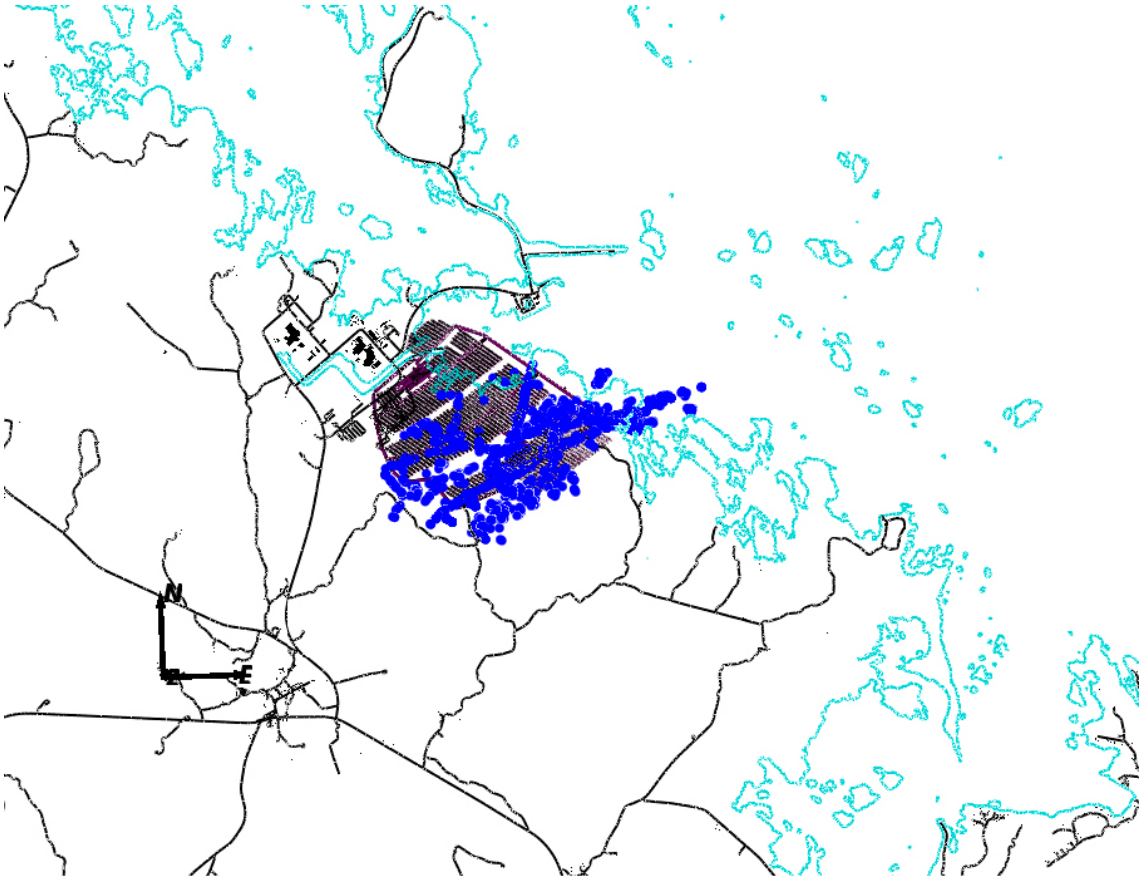

Figure 6-31. *Discharge locations on the top surface for flow pathways from deposition holes for glacial ice front location II, including those that do not intersect the grout. The shoreline at 2000 AD is shown in blue and buildings and roads are shown in black.*

Table 6-14. The number and percentage of recharge pathways to deposition hole locations that pass through a grouted region, out of a total of 20,748 particles released for the Q1, Q2 and Q3 release types, for each case under glacial ice front location II conditions. The grouting radius is 5 m.

Case	Release time	Count	Percentage
200 m grouting	Glacial II	96	0.46
370 m grouting	Glacial II	192	0.93
370 m sealing	Glacial II	205	0.99

The number of recharge pathways to the deposition holes for a less pessimistic case is shown in Table 6-15. In this case, recharge pathways have been excluded if they do not meet the SR Site starting criteria (due to an absence of fractures or insufficient flow) and if they do not meet the FPC (Full Perimeter Criteria) and EFPC (Extended Full Perimeter Criteria) as described in Joyce et al. (2010). As for the temperate climate period, the counts are approximately halved.

There is some uncertainty and variability in the penetration depth of the grout into the fractures. So, 20 m is considered as an alternative to the 5 m grout radius already considered so that the sensitivity of the results to this uncertainty can be assessed. The numbers of recharge pathways that intersect the grout in this case are shown in Table 6-16. The counts increase significantly, particularly for the 370 m grouting depths. The increased sensitivity to the grouting radius compared to the temperate period is probably due to the higher intensity of recharge pathways in the region of the repository ramp, particularly below –370 m elevation.

Table 6-15. The number and percentage of recharge pathways to deposition hole locations that pass through a grouted region, out of a total of 20,748 particles released for the Q1, Q2 and Q3 release types, for each case under glacial ice front location II conditions. Particles are excluded if there is insufficient flow at the start location or if they do not meet the FPC and EFPC criteria. The grouting radius is 5 m.

Case	Release time	Count	Percentage
200 m grouting	Glacial II	51	0.25
370 m grouting	Glacial II	113	0.54
370 m sealing	Glacial II	106	0.51

Table 6-16. The number and percentage of recharge pathways to deposition hole locations that pass through a grouted region, out of a total of 20,748 particles released for the Q1, Q2 and Q3 release types, for each case under glacial ice front location II conditions. The grouting radius is 20 m.

Case	Release time	Count	Percentage
200 m grouting	Glacial II	139	0.67
370 m grouting	Glacial II	345	1.66
370 m sealing	Glacial II	345	1.66

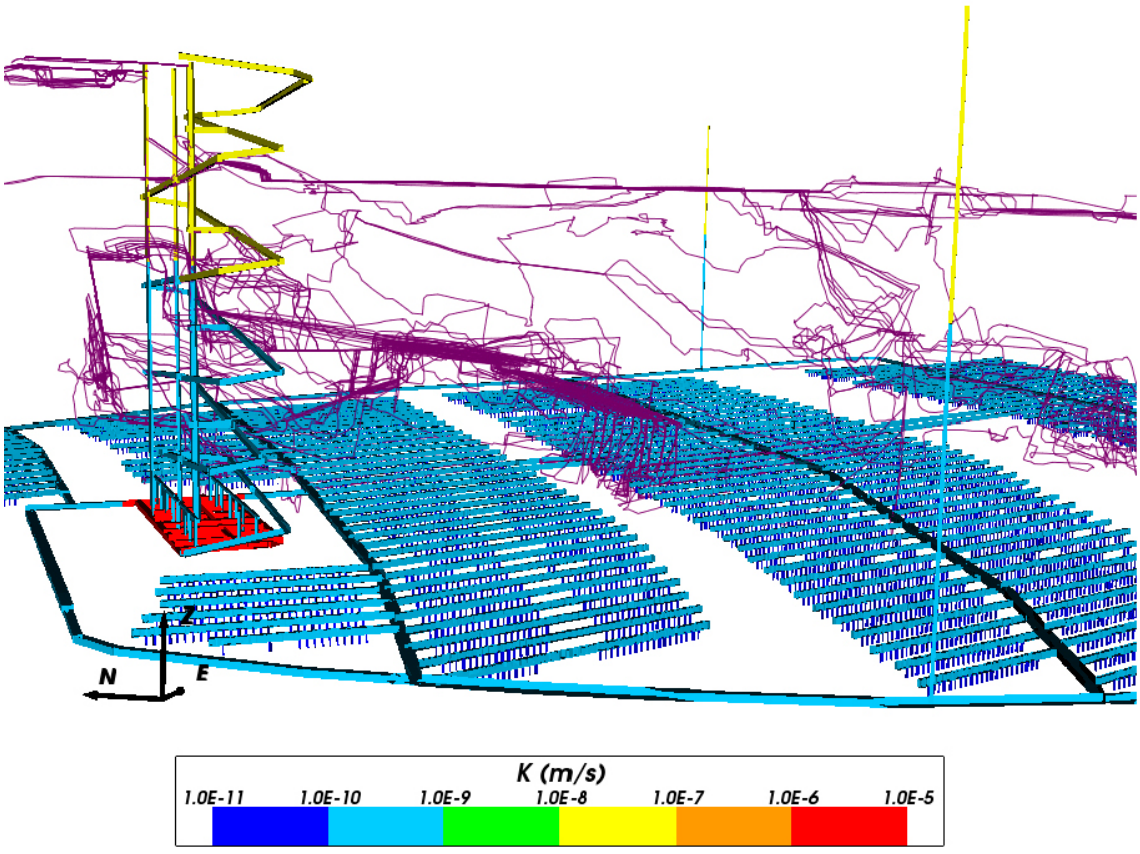

Figure 6-32. *Recharge pathways (purple) to deposition holes that pass through a grouted region for ice front location II. Grouting depth is 200 m. SR-Site properties are used in the ramp and shafts. Repository structures are coloured by hydraulic conductivity.*

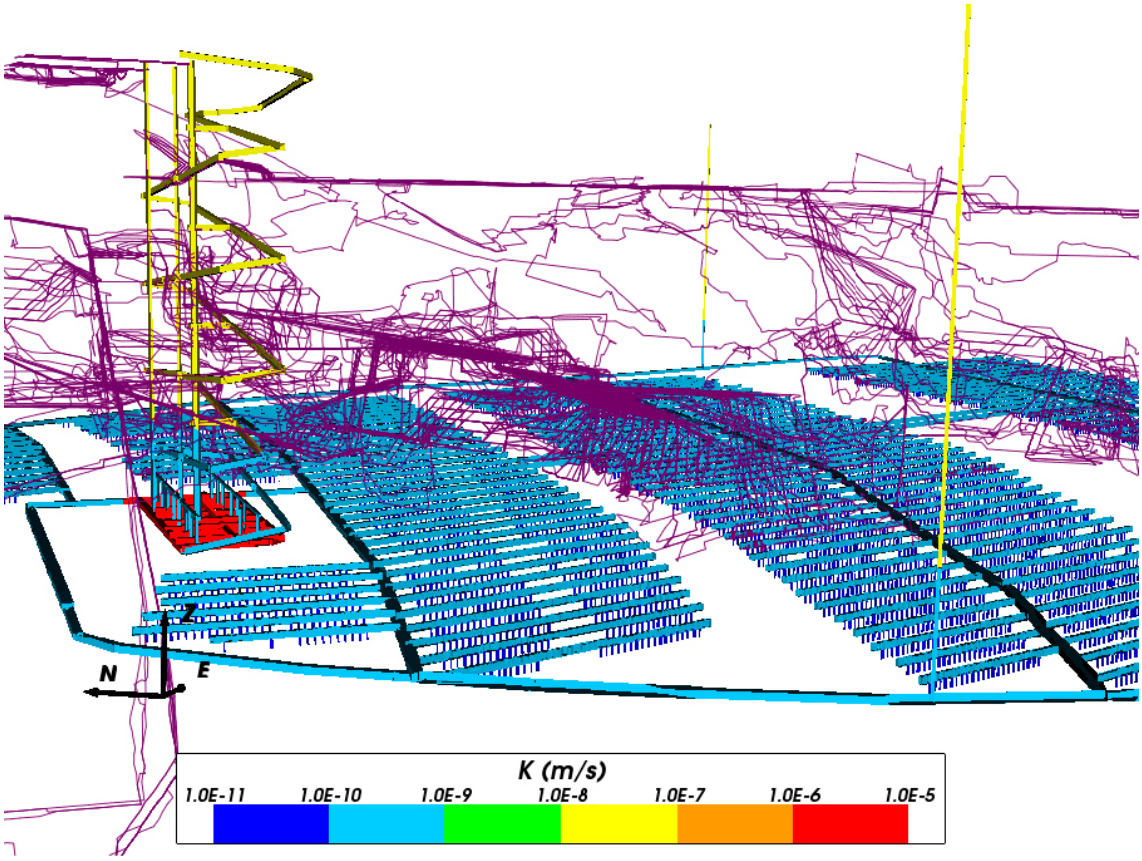

Figure 6-33. *Recharge pathways (purple) to deposition holes that pass through a grouted region for glacial ice front location II. Grouting depth is 370 m. Alternative repository sealing properties are used in the ramp and shafts. Repository structures are coloured by hydraulic conductivity.*

Table 6-17, Table 6-20 and Table 6-23 give performance measure statistics for the portion of the recharge pathways in the rock between the grout region and the deposition holes. There is little variation in the mean log values and the standard deviation of the log values between cases. However, the minimum values for the 370 m sealing case are somewhat lower than the other two cases. The F_r and t_r values are lower than for the temperate climate situation for all cases due to the higher flow velocities, caused by the greater head gradient, under glacial ice front location II conditions.

Table 6-18, Table 6-21 and Table 6-24 show the corresponding performance measure statistics for the less pessimistic case with the additional pathway rejection criteria described above. All of the statistics are similar to the pessimistic case.

Table 6-19, Table 6-22 and Table 6-25 show the performance measure statistics when a 20 m grouting radius is used. The minimum values generally descrease and the mean values generally increase but the changes are minor. The performance measure statistics seem to be less sensitive than the counts of recharge pathways intersecting the grout are to the grout radius.

Table 6-17. Statistics for path length in the rock, L_r, of recharge pathways between the grouted region and the deposition holes for each case under glacial ice front location II conditions. The grouting radius is 5 m.

Case	Release time	Min L_r (m)	Mean $\log_{10}(L_r)$ (m)	SD $\log_{10}(L_r)$ (m)
200 m grouting	Glacial II	$8.686 \cdot 10^{2}$	3.192	$2.539 \cdot 10^{-1}$
370 m grouting	Glacial II	$3.554 \cdot 10^{2}$	3.115	$2.156 \cdot 10^{-1}$
370 m sealing	Glacial II	$4.245 \cdot 10^{2}$	3.121	$2.247 \cdot 10^{-1}$

Table 6-18. Statistics for path length in the rock, L_r, of recharge pathways between the grouted region and the deposition holes for each case under glacial ice front location II conditions. Particles are excluded if there is insufficient flow at the start location or if they do not meet the FPC and EFPC criteria. The grouting radius is 5 m.

Case	Release time	Min L_r (m)	Mean $\log_{10}(L_r)$ (m)	SD $\log_{10}(L_r)$ (m)
200 m grouting	Glacial II	$8.958 \cdot 10^{2}$	3.170	$2.358 \cdot 10^{-1}$
370 m grouting	Glacial II	$3.554 \cdot 10^{2}$	3.097	$1.968 \cdot 10^{-1}$
370 m sealing	Glacial II	$4.353 \cdot 10^{2}$	3.111	$2.601 \cdot 10^{-1}$

Table 6-19. Statistics for path length in the rock, L_r, of recharge pathways between the grouted region and the deposition holes for each case under glacial ice front location II conditions. The grouting radius is 20 m.

Case	Release time	Min L_r (m)	Mean $\log_{10}(L_r)$ (m)	SD $\log_{10}(L_r)$ (m)
200 m grouting	Glacial II	$8.530 \cdot 10^{2}$	3.261	$2.832 \cdot 10^{-1}$
370 m grouting	Glacial II	$3.358 \cdot 10^{2}$	3.118	$2.361 \cdot 10^{-1}$
370 m sealing	Glacial II	$3.737 \cdot 10^{2}$	3.129	$2.329 \cdot 10^{-1}$

Table 6-20. Statistics for travel time in the rock, t_r, of recharge pathways between the grouted region and the deposition holes for each case under glacial ice front location II conditions. The grouting radius is 5 m.

Case	Release time	Min t_r (y)	Mean $\log_{10}(t_r)$ (y)	SD $\log_{10}(t_r)$ (y)
200 m grouting	Glacial II	$8.173 \cdot 10^{-1}$	1.009	$8.614 \cdot 10^{-1}$
370 m grouting	Glacial II	$7.158 \cdot 10^{-1}$	$9.106 \cdot 10^{-1}$	$7.368 \cdot 10^{-1}$
370 m sealing	Glacial II	$7.178 \cdot 10^{-1}$	$9.491 \cdot 10^{-1}$	$8.024 \cdot 10^{-1}$

Table 6-21. Statistics for travel time in the rock, t_r, of recharge pathways between the grouted region and the deposition holes for each case under glacial ice front location II conditions. Particles are excluded if there is insufficient flow at the start location or if they do not meet the FPC and EFPC criteria. The grouting radius is 5 m.

Case	Release time	Min t_r (y)	Mean $\log_{10}(t_r)$ (y)	SD $\log_{10}(t_r)$ (y)
200 m grouting	Glacial II	1.070	1.029	$7.915 \cdot 10^{-1}$
370 m grouting	Glacial II	$7.158 \cdot 10^{-1}$	$9.471 \cdot 10^{-1}$	$6.561 \cdot 10^{-1}$
370 m sealing	Glacial II	$9.222 \cdot 10^{-1}$	1.025	$8.757 \cdot 10^{-1}$

Table 6-22. Statistics for travel time in the rock, t_r, of recharge pathways between the grouted region and the deposition holes for each case under glacial ice front location II conditions. The grouting radius is 20 m.

Case	Release time	Min t_r (y)	Mean $\log_{10}(t_r)$ (y)	SD $\log_{10}(t_r)$ (y)
200 m grouting	Glacial II	$8.162 \cdot 10^{-1}$	1.252	$9.254 \cdot 10^{-1}$
370 m grouting	Glacial II	$4.083 \cdot 10^{-1}$	$9.772 \cdot 10^{-1}$	$7.767 \cdot 10^{-1}$
370 m sealing	Glacial II	$7.167 \cdot 10^{-1}$	$9.719 \cdot 10^{-1}$	$7.577 \cdot 10^{-1}$

Table 6-23. Statistics for flow-related transport resistance in the rock, F_r, of recharge pathways between the grouted region and the deposition holes for each case under glacial ice front location II conditions. The grouting radius is 5 m.

Case	Release time	Min F_r (y/m)	Mean $\log_{10}(F_r)$ (y/m)	SD $\log_{10}(F_r)$ (y/m)
200 m grouting	Glacial II	$1.035 \cdot 10^{4}$	5.515	1.228
370 m grouting	Glacial II	$6.622 \cdot 10^{3}$	5.310	1.111
370 m sealing	Glacial II	$4.571 \cdot 10^{3}$	5.376	1.231

Table 6-24. Statistics for flow-related transport resistance in the rock, F_r, of recharge pathways between the grouted region and the deposition holes for each case under glacial ice front location II conditions. Particles are excluded if there is insufficient flow at the start location or if they do not meet the FPC and EFPC criteria. The grouting radius is 5 m.

Case	Release time	Min F_r (y/m)	Mean $\log_{10}(F_r)$ (y/m)	SD $\log_{10}(F_r)$ (y/m)
200 m grouting	Glacial II	$1.309 \cdot 10^4$	5.588	1.177
370 m grouting	Glacial II	$6.622 \cdot 10^3$	5.316	1.067
370 m sealing	Glacial II	$1.272 \cdot 10^4$	5.481	1.349

Table 6-25. Statistics for flow-related transport resistance in the rock, F_r, of recharge pathways between the grouted region and the deposition holes for each case under glacial ice front location II conditions. The grouting radius is 20 m.

Case	Release time	Min F_r (y/m)	Mean $\log_{10}(F_r)$ (y/m)	SD $\log_{10}(F_r)$ (y/m)
200 m grouting	Glacial II	$1.035 \cdot 10^4$	5.843	1.270
370 m grouting	Glacial II	$6.590 \cdot 10^3$	5.397	1.153
370 m sealing	Glacial II	$4.570 \cdot 10^3$	5.382	1.160

Figure 6-34 and Figure 6-35 show the deposition hole locations that are at the end of recharge pathways that pass through a grouted region, coloured by F_r. These confirm that the deposition holes affected by recharge through grouted regions are mostly those in the middle and south eastern sections of the repository. As expected, the deposition holes associated with the lowest F_r values tend to be those closest to the ramp.

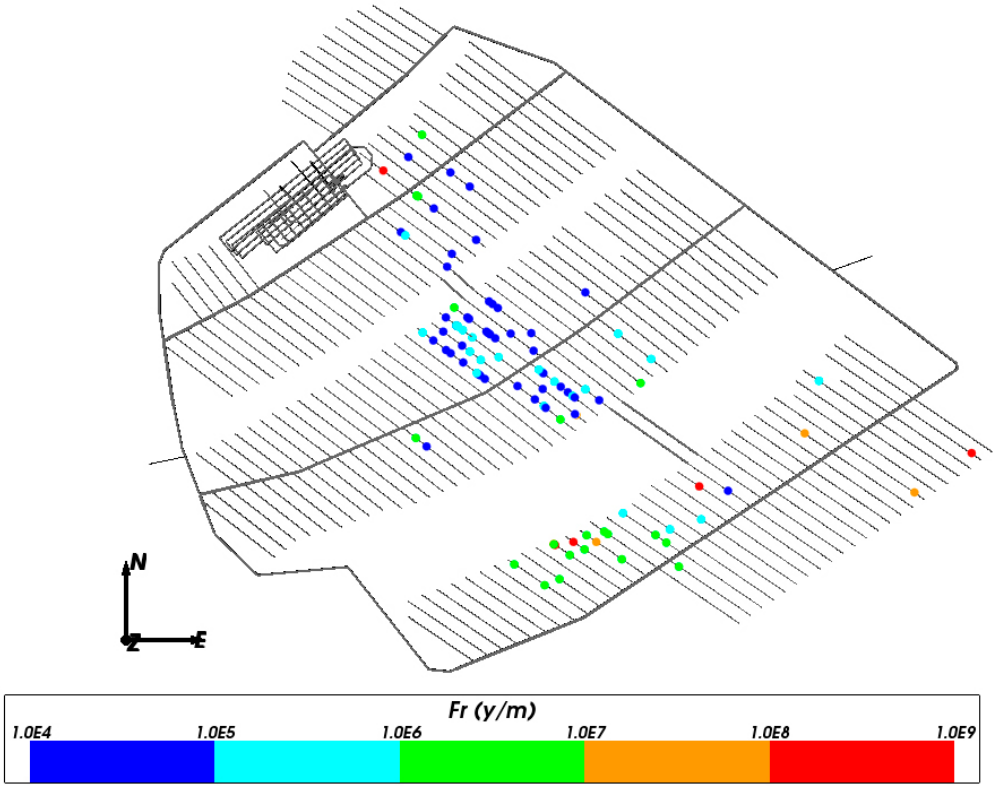

Figure 6-34. *Deposition hole locations, coloured by F_r, at the end of recharge pathways that pass through a grouted region under glacial ice front location II conditions. Grouting depth is 200 m. SR-Site properties are used in the ramp and shafts. Repository structures are coloured black.*

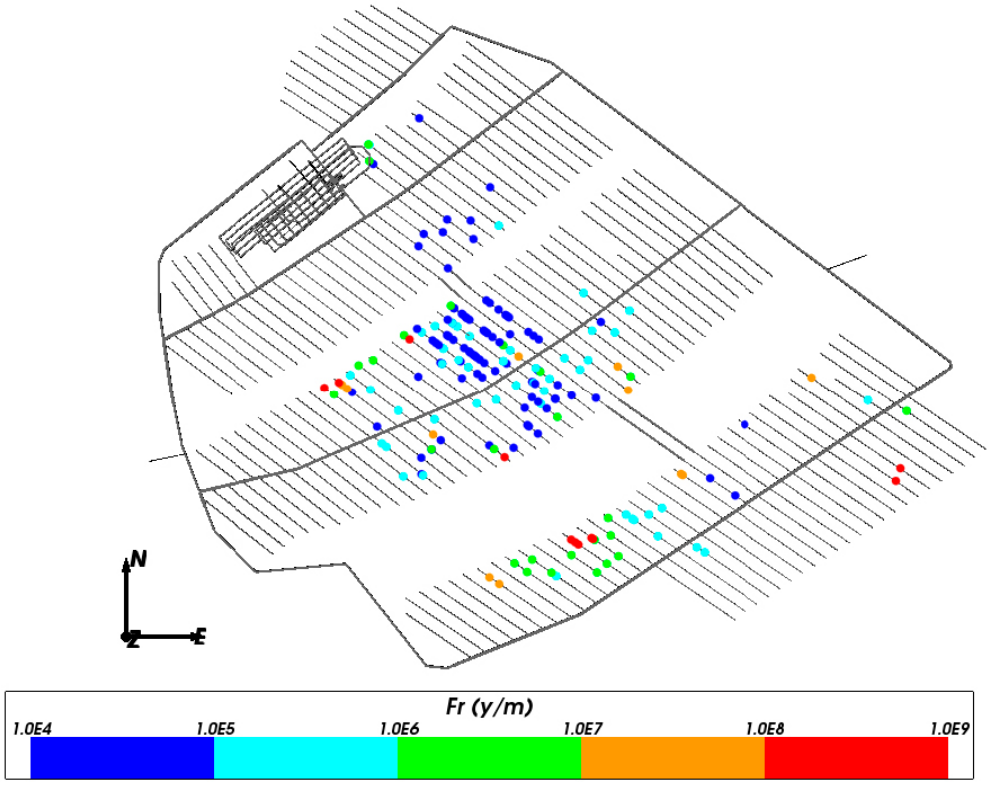

Figure 6-35. *Deposition hole locations, coloured by F„ at the end of recharge pathways that pass through a grouted region under glacial ice front location II conditions. Grouting depth is 370 m. Alternative repository sealing properties are used in the ramp and shafts. Repository structures are coloured black.*

6.4.2 ECPM transient evolution of alkaline water

The transient evolution of the alkaline water under glacial ice front location II conditions using an ECPM regional model are calculated using a similar methodology to that described in Section 6.2.2. However, the pressure and density boundary conditions on the top, bottom and sides of the model are fixed to those imported from the SR-Site glacial model (Vidstrand et al. 2010), i.e. there is no change due to land rise or changes in the salinity of infiltrating water. Thus the pessimistic assumption is that the ice front is over the repository for the whole 10,000 years. Two reference waters (glacial and deep saline) are mixed to represent the imported salinities. Again, an extra reference water is added to represent the alkaline water released from the grout. The processes of advection, dispersion and diffusion in the fractured rock and rock matrix diffusion are included, using the same parameters as for SR-Site. There are no chemical reactions included, so there is a conservative assumuption that there are no pH buffering reactions between the grout leachate and the host rock. The initial condition starts the alkaline water at the ramp and shaft location, rather than the position reached at the end of the temperate period as an illustration of the processes involved. The system is then allowed to evolve over 10,000 years.

The location of the alkaline water plume relative to the repository structures after 10,000 years of evolution are shown in Figure 6-36 and Figure 6-37 for the 200 m grouting case and 370 m grouting case respectively. In both cases, the plume follows the main advective flow direction towards the southeast. There is some penetration of alkaline water to the deposition hole locations in these models, particularly for the 370 m grouting depth. This is also shown by Figure 6-38 and Figure 6-39, which represent the fraction of alkaline water at the centre of each deposition hole. For a 200 m grouting depth the maximum alkaline water fraction in any deposition hole is 0.11 (corresponding to a pH of around 9.2 based on simple non-reactive mixing of waters) and for a 370 m grouting depth the maximum alkaline water fraction in any hole is 0.36 (corresponding to a pH of around 9.4 based on simple non-reactive mixing of waters). The highest alkaline water fractions are closest to the ramp. These results suggest a certain amount of alkaline water could penetrate to some deposition hole locations under glacial ice front location II conditions with a 370 m grouting depth, although not enough to significantly raise pH levels. The quantities for a 200 m grouting depth are lower and limited to fewer locations.

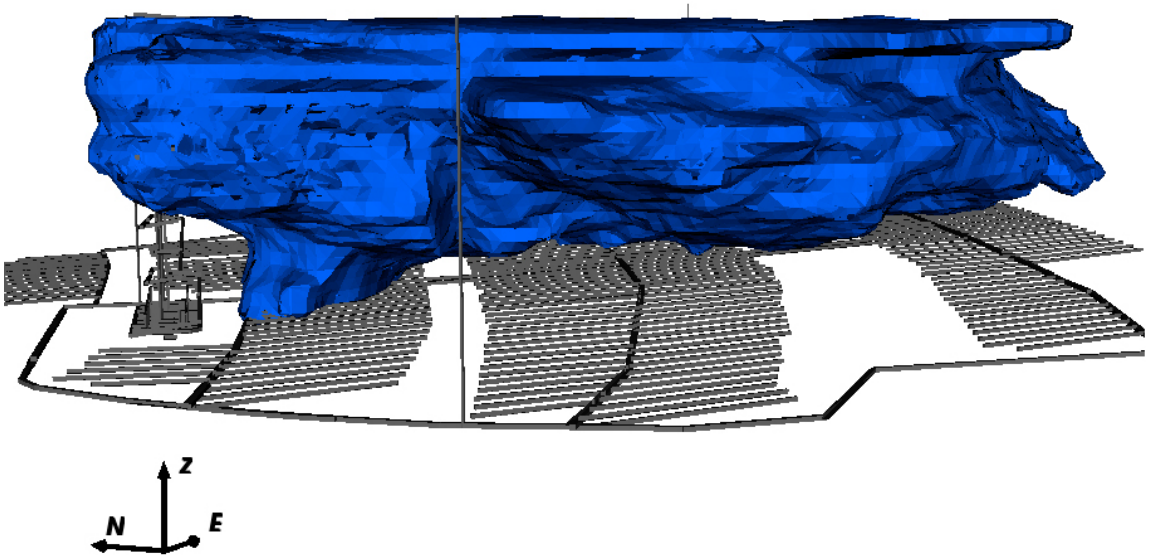

Figure 6-36. *The extent of the alkaline water plume after 10,000 years under glacial ice front location II conditions. Grouting depth is 200 m. The plume is coloured blue, with fractions less than 0.1 removed. Repository structures are coloured grey.*

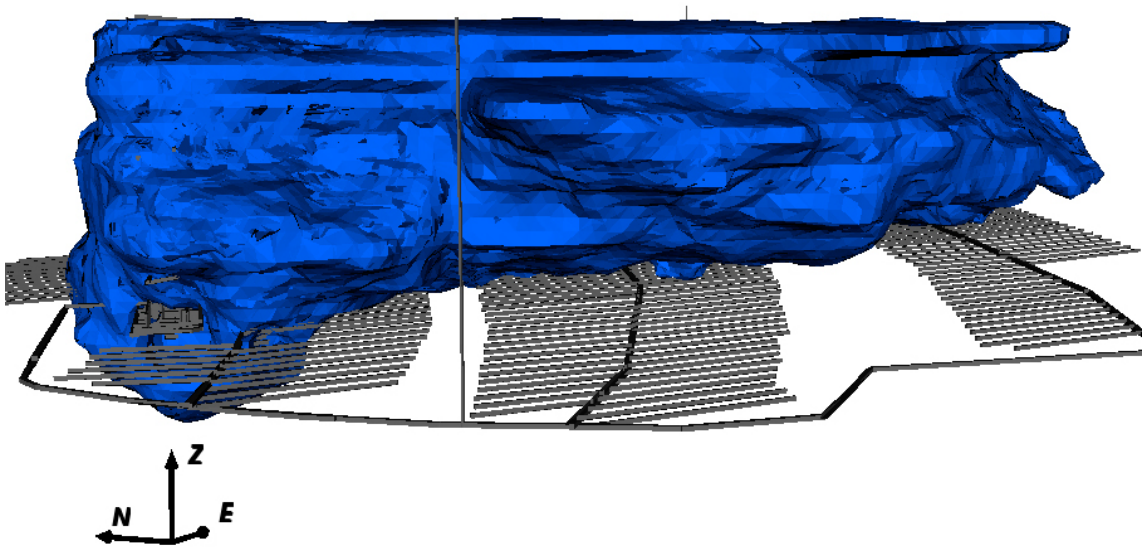

Figure 6-37. *The extent of the alkaline water plume after 10,000 years under glacial ice front location II conditions. Grouting depth is 370 m. The plume is coloured blue, with fractions less than 0.1 removed. Repository structures are coloured grey.*

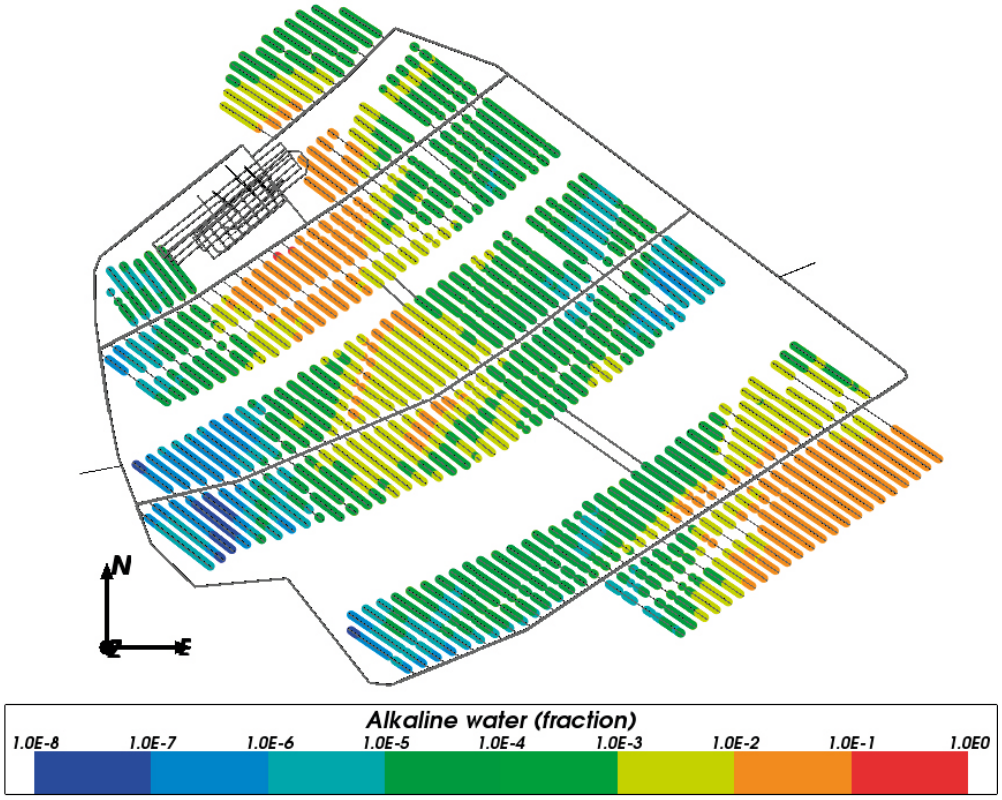

Figure 6-38. *Deposition hole locations coloured by the fraction of alkaline water after 10,000 years under glacial ice front location II conditions. Grouting depth is 200 m. Repository structures are coloured grey.*

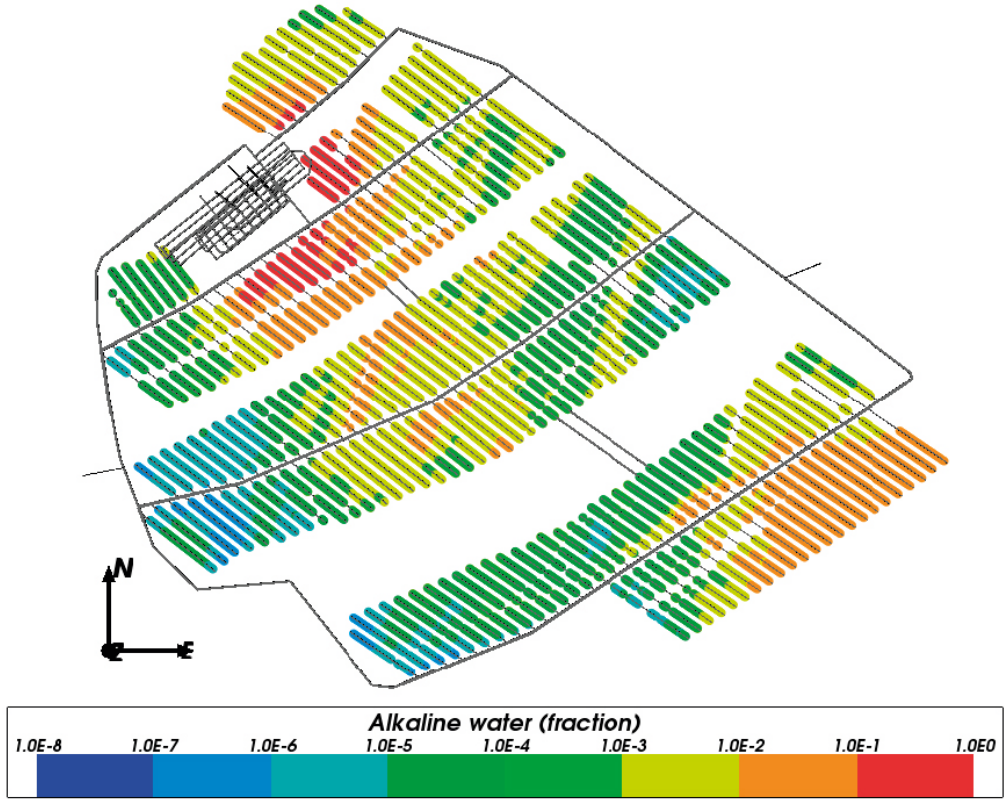

Figure 6-39. *Deposition hole locations coloured by the fraction of alkaline water after 10,000 years under glacial ice front location II conditions. Grouting depth is 370 m. Repository structures are coloured grey.*

6.5 Summary of hydrogeological modelling

No recharge pathways to deposition holes in the repository that intersected grouted rock volumes were found for the open-repository and periglacial permafrost periods.

Backward particle tracking calculations in DFN models show that very few recharge pathways to deposition holes pass through grouted regions. The number of such pathways varies with release time, with the highest number for 3000 BC and the fewest for 9000 AD. The 2000 AD and glacial ice front location II conditions give an intermediate number of intersections with grouted regions. The depth of grouting and the physical properties of the backfill in the ramp and shafts seem to have little effect on the results during temperate conditions. This is because most of the flow circulates in the upper 200 m of the bedrock and flow is predominantly upwards or horizontal. However, under glacial ice front location II conditions the recharge pathways also pass through the lower parts of the ramp and shafts and so the grouting level and the ramp and shaft backfill does have an effect on the results. Additionally, under glacial ice front location II conditions the deposition holes receiving recharge via the grouted regions are in the central and south eastern parts of the repository, due to downward and southeasterly components to the flow, whereas under temperate conditions they are in the northern part of the repository, close to the ramp.

Under temperate conditions only a few routes are used to carry flow from the grouted region to deposition holes and these depend on a particular configuration of the HRD fractures. Therefore the results have some sensitivity to the realisation of the fractures chosen, although only one realisation was considered here. Also, the nature of the backward particle tracking method is such that it only gives one possible recharge pathway for each start point and does not find all possible recharge pathways. Thus some deposition holes may receive recharge via a grouted region that were not identified and some deposition holes that were identified may only receive a small portion of their recharge via a grouted region. One way to partly address this would be to release more particles per deposition hole, although this was not done for this study.

Considering a less pessimistic case where some of the recharge pathways are rejected according to SR-Site starting critieria, FPC and EFPC, the number of intersections with the grout is reduced significantly. However, there is no significant effect on the performance measure statistics. This suggests that the excluded paths did not have atypical performance measure values.

Since there is some uncertainty and variability in the grout penetration depth, a grouting radius of 20 m was used as an alternative to the 5 m grouting radius in order to quantify the sensitivity of the results to this parameter. The number of recharge pathways intersecting the grout and the performance measure statistics were largely unaffected by the change of grouting radius for the temperate climate period. This is probably due to the low intensity of recharge pathways in the region of the ramp. Under glacial ice front location II climate conditions, there is much more sensitivity in the number of recharge pathways intersecting the grout to the grouting radius. However, there does not appear to be much sensitivity in the performance measure statistics to the grouting radius.

ECPM regional-scale modelling of the transient evolution of the alkaline water for 10,000 years shows that it is transported in the direction of the main advective flow towards the shoreline to the north and northeast under temperate conditions and towards the southeast under glacial conditions. There is no appreciable penetration of alkaline water to deposition hole locations for the two grouting depths considered under temperate conditions. Under glacial ice front location II conditions there is a certain amount of penetration of alkaline water to some deposition hole locations close to the ramp for the 370 m grouting case, although not enough to significantly raise pH levels. With a 200 m grouting depth the fraction of alkaline water at deposition hole locations is lower and limited to fewer locations. However, glacial ice front location II conditions for 10,000 years are highly pessimistic as the ice front is likely to be located over the repository for much shorter periods.

7 Reactive-transport modelling

The following sections summarize the results obtained with the reactive transport modelling of the alkali disturbed zone (ADZ) induced by an OPC leachate in the fractured bedrock at the Forsmark site. All of the simulations presented in this chapter considered a very conservative scenario in which:

- the composition of the OPC boundary solution is constant in time, and the pH of this solution is kept fixed at a value of 12.4 (forced equilibrium with portlandite),
- the potential dilution of the ADZ with the surrounding groundwater in the fracture is not considered (see Figure 7-1),
- the interaction of the grout (i.e the source term) with the fracture walls and the rock matrix is not considered.

Therefore, the results should be regarded as highly pessimistic cases and, from a safety assessment viewpoint, highly conservative. First, a brief overview of the numerical tools used in this work is presented. Thereafter, the verification of the transport in the fracture and in the rock matrix with the use of analytical solutions and multiple numerical codes is shown. The results of the reactive transport modelling are summarized next. Different cases have been considered, in which the main variables studied have been the reactive surface area of the fracture and rock matrix minerals, the velocity of the flow, the matrix depth available for diffusion, and the feedback between permeability and diffusivity with porosity changes induced by dissolution/precipitation of minerals. Section 7.5 summarizes the main findings of the reactive transport modelling.

7.1 Numerical codes used

Three reactive transport codes have been used in this work to benchmark some of the capabilities and the results obtained with the different codes. However, most of the reactive transport simulations presented in this report have been performed with the code PFLOTRAN. This is mainly due to the high-performance features that have allowed calculating a large number of simulations. In general, the three codes have been largely validated over the last years in different scientific fields (see the work in e.g. Hammond and Lichtner 2010, Piqué et al. 2010, Sena et al. 2010, Sidborn et al. 2010), and the test cases presented in the corresponding manuals (Lichtner 2001, Parkhurst et al. 2010, Pruess et al. 1999, Xu et al. 2008). Therefore, their use in this project is considered to be well-supported.

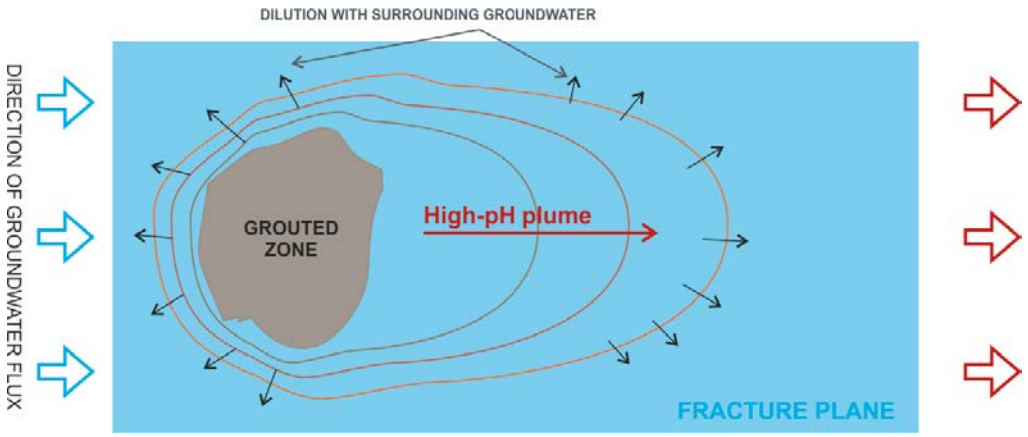

Figure 7-1. *Schematic representation of groundwater flux through a grouted fracture, showing the dilution of the Alkali Disturbed Zone (ADZ) with the surrounding groundwater.*

7.1.1 PFLOTRAN

PFLOTRAN (Hammond and Lichtner 2010, Lichtner and Hammond 2012) is a 3D parallel multiphase flow and multicomponent reactive transport code for geochemical analysis that originated from the serial FLOTRAN code developed at Los Alamos National Laboratory (Lichtner 2001). The code is composed of flow and transport modules (PFLOW and PTRAN, respectively), with the option of running the modules in coupled or decoupled mode (Hammond et al. 2007). PFLOW-generated fluid flow velocities or fluxes are utilized by PTRAN to compute solute transport. More details may be found at http://ees.lanl.gov/source/orgs/ees/pflotran/. Some of the main characteristics are listed in the following:

- The code has been fully parallelized based on domain decomposition and makes use of the PETSc library (Balay et al. 1997), meaning that large-scale simulations may be performed over a large number of processors. The PETc framework enables the use of numerous features from PETc including nonlinear solvers, linear solvers, or sparse matrix data structures.
- Within PTRAN, transport and geochemical reactions can be solved fully coupled (implicit Backward Euler, as in this work) or with operator splitting (Saaltink et al. 2001).
- The domain is discretised spatially using the integrated finite volume approach, with fully-implicit backward-Euler time differencing.
- Aqueous complexation is modelled under local equilibrium.
- Mineral precipitation/dissolution is modelled under kinetics assumptions.
- The Debye-Hückel model is used to calculate activities.
- The thermodynamic database used in this work is the Hanford database (Hammond and Lichtner 2010, Lichtner and Hammond 2012). It is equivalent to the EQ3/6 database (data0.com.V8.R6 in Wolery 1992), with some minor modifications. Reactions included in the database consist of aqueous complexation, mineral precipitation and dissolution, gaseous reactions, and surface complexation. Ion exchange reactions and their selectivity coefficients are entered directly from the input file.

7.1.2 TOUGHREACT

The code TOUGHREACT (version v1.2) allows simulating thermo-hydro-geochemical processes (Xu et al. 2008). This code results from coupling the calculation of geochemical reactions to the THOUGH2 v2 code, which solves multiphase, non-isothermal fluid flow, heat flow and multi-component transport.

The main characteristics of the software are the following (for more details see Pruess et al. 1999, Xu et al. 2008):

- Space discretisation (1D to 3D) is based on the Integral Finite Difference (IFD) Method, which for regular grids is equivalent to the Finite Difference Method (Pruess et al. 1999).
- In the IFD, space discretisation is made directly from the integral form of the conservation equations without converting them into partial differential equations (Pruess et al. 1999).
- Time is fully implicitly discretised as a first-order backward finite difference.
- The coupling between fluid flow, mass transport and geochemical reactions is made using the operator splitting approach (Sequential Non-Iterative Approach in this work, see Saaltink et al. 2001).
- Aqueous complexation is modelled under local equilibrium.
- Mineral precipitation/dissolution can be modelled under equilibrium and/or kinetics assumptions (Xu et al. 2008).
- The extended Debye-Hückel model is used to calculate activities, with parameters derived by Helgeson et al. (1981). The activities of pure mineral phases are assumed to be unity and the activity of water is calculated according to Helgeson et al. (1981).
- Advection and diffusion processes are considered (the diffusion coefficients are assumed to be the same for all species, although different diffusivities for each material in the model can be specified).

The multiphase reactive transport formulation used by TOUGHREACT can be found in the freely available user guide (Pruess et al. 1999). In this work, the Equation Of State (EOS) module used is the EOS number 1 (see TOUGH2 manual, Pruess et al. 1999).

7.1.3 PHAST

The transport through the fracture and the rock matrix has been analysed with the reactive transport code PHAST v.2.2.0 (Parkhurst et al. 2010), which simulates multi-component reactive transport in 3D saturated groundwater flow systems. The code is a groundwater flow and solute transport simulator with capabilities to model a wide range of geochemical reactions.

The main characteristics of the software are the following (more details can be found in Parkhurst et al. 2010):

- It is based on 3D finite difference method.
- Variable weighting for spatial discretisation is available: default option is upstream weighting (used in this work).
- Variable weighting also for temporal discretisation is available: default option is fully implicit (used in this work).
- Flow and transport calculations are based on a modified version of the finite difference code HST3D (Kipp 1997).
- Geochemical reactions are solved with the geochemical code PHREEQC (Parkhurst and Appelo 1999), which is embedded in PHAST.
- Reactive transport calculations are split into a transport step and a chemical-reaction step, method referred to as operator splitting: PHAST implements a sequential non-iterative approach (SNIA), i.e. at each time step no iterations between the solute transport and the chemical reactions are performed.
- Activities of water and aqueous species are calculated as the mol fraction of water, and with the B-dot model, respectively. See Appendix A7 and Helgeson (1969) for a description of the B-dot model.
- Independent tortuosity coefficients can be assigned to each domain in the model, to consider different diffusion coefficients.

7.2 Implementation of the conceptual model

The main assumptions that have been considered in the implementation of the model are the following:

- All the simulations have been carried out in pseudo two-dimensional grids (with only 1 grid cell in the third dimension), and conceptualizing the fracture as a straight line (Figure 7-2).
- Groundwater flow is under water saturated and isothermal conditions.
- The temperature considered is 25°C to minimize the uncertainty in the thermodynamic and kinetic data.
- The rock matrix is assumed homogeneous and with a negligible hydraulic conductivity, so that only diffusive transport is relevant.
- The fracture has been considered homogeneous along the thickness (aperture) and along its length, with an assumed fracture porosity (equal to 0.5) and an assumed volume fraction of the infill minerals identified to be present in the fracture in Sandström et al. (2008), as shown in Table 5-5 of Section 5.5.
- The length of the fracture in all cases is 100 m, so that different F-factors have been accounted for by changing the velocity of the fluid flow. Note that the length has been fixed to avoid having different meshes and because the region of maximum perturbation of the system (pH > 12) is always much less than 100 m. Therefore, the fracture length should not be compared with the path lengths in Table 6-5.
- Advective-dispersive flow is assumed along the fracture, with an assumed longitudinal dispersivity of 0.6 m.

The numerical discretisation considered in the simulations is as follows: in the direction parallel to flow in the fracture (X-direction), the cell size is 0.5 m. In the direction normal to the flow in the fracture (Y-direction) the discretisation is variable, with a unique grid cell for the fracture half-thickness (0.05 mm, as in Sidborn et al. 2010), and gradually increasing in the rock matrix from 0.05 mm up to

0.01 and 0.05 m for the cases with matrix depth of 0.1 m and 0.4 m, respectively. The total number of elements in the domain is 4,000 and 7,200 for the two cases, respectively. In addition, the simulations that only consider a fracture with no rock matrix have 200 elements.

The simulations have been carried out with an AMD Quad CPU Workstation (4x AMD Opteron 6234 Interlagos 2.4 GHz 12-Core, i.e. 48 cores in total). Typical computation times using the parallelized version of PFLOTRAN ranges from some minutes for the case of a fracture without rock matrix to 2 to 4 days for the cases considering rock matrix.

For the reactive transport modelling, a rock matrix with 0.1 m depth has been considered for the reference case, which corresponds either to a fracture spacing of 0.2 m, or to a matrix thickness available for molecular diffusion. Chemical reactions are also considered in the matrix. Additionally, two cases considering the absence of the rock matrix and a rock matrix of 0.4 m have also been simulated to gain insight into the sensitivity of the pH buffering capacity of the fractured bedrock to this parameter[18]. The values of the porosity and the effective diffusion coefficient of the matrix have been assumed similarly as in Sidborn et al. (2010). A discussion of the rock matrix porosity and diffusivity values can be found in Sidborn et al. (2010, Sections 5.1.1 and 5.1.2 respectively). The diffusivity value is conservative since it is based on formation factors in non-fractured and unaltered matrix rock deep in the matrix. The F-factors assumed in the reactive transport simulations result from the hydrogeological modelling in Chapter 6. Two cases have been considered (for the case of no OPC grout in the exhaust air shafts in the deposition area)[19]:

- the *minimum* F-factor for a release time of 2000 AD (rounded to $4 \cdot 10^6$ y/m), and
- an F-factor representative for the glacial period (rounded to $4.0 \cdot 10^5$ y/m, see Table 6-23).

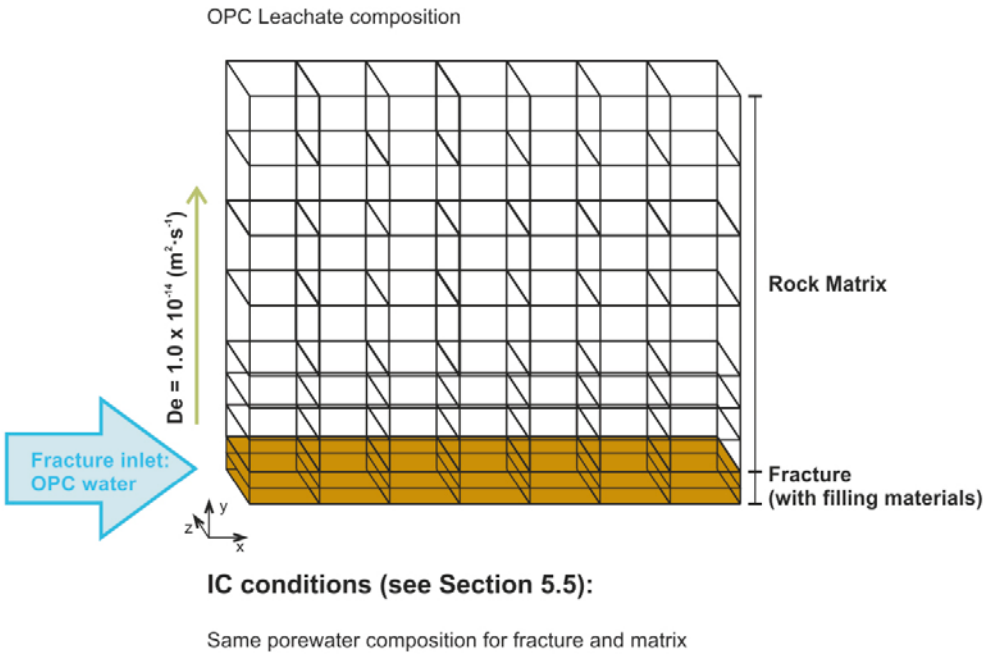

Figure 7-2. *Schematic representation of the numerical model, with the porous rock matrix adjacent to the fracture and the specification of the initial and boundary conditions.*

[18] The rock matrix depth available for diffusion has been limited in this work due to mainly two reasons. On one hand, the idea of the present study has been to obtain conservative estimates of the effect of an alkaline plume. On the other hand, for the effective diffusion coefficient value used here and the time span analysed, the penetration of a tracer in an infinite rock near the fracture inlet by diffusion would roughly be less than 2 m after 1,000 years and less than 5 m after 5,000 years. Therefore, considering much larger rock matrix depths would only increase the computational resources needed for the simulations, while the transport of solute species would not be affected in the time span considered here.

[19] A broader analysis of the sensitivity of the results to this parameter has been left out of the scope of this study due to time constraints. It is thought that it would be very useful that future work aimed at assessing this sensitivity.

With these F-factors, and considering a fixed fracture length of 100 m, the travel times are respectively 200 and 20 y. The corresponding linear velocities are 0.5 and 5 m/y, respectively. The reference case considered in most of the simulations is the one representative of the glacial period (with an F-factor of $4.0 \cdot 10^5$ y/m), unless otherwise stated.

The transport related parameters for the rock matrix are gathered in Table 7-1. The fracture hydraulic conductivity considered is $5 \cdot 10^{-10}$ m/s (Follin et al. 2005). It is noted that this value is only relevant for the simulations in which porosity-permeability coupling has been considered. The porosity of the fracture is equal to 0.5 in all the simulations (see Section 5.5). The dispersivity adopted in all the reactive transport simulations is 0.6 m.

7.3 Transport validation

To verify the calculation of the non-reactive transport of a tracer, different solutions have been compared, including multiple code verification as well as analytical solutions. Two cases have been simulated, with and without rock matrix.

Transport of a conservative tracer through a fracture without rock matrix

Steady state conditions are considered for the flow through the fracture. The fracture length and the linear velocity in the fracture considered are 100 m and 5 m/y, respectively (travel time is 20 years). The porosity of the fracture is equal to 0.5 in all the simulations. For this verification exercise, different reactive transport codes (PFLOTRAN, TOUGHREACT, PHAST) have been compared to an analytical solution (Ogata and Banks 1961). Simulations have been repeated for a case with no dispersion and a second case with a dispersivity of 0.6 m. A numerical dispersivity of 0.25 m is introduced in the simulations since the discretisation of the fracture is 200 grid elements of 0.5 m (as a result of the upstream weighting scheme). The results are thus compared to the analytical solution considering a dispersivity of 0.25 and 0.85 m, respectively. This is shown in Figure 7-3 in terms of the breakthrough curve at the outlet of the fracture (x = 100 m), and in Figure 7-4 in terms of tracer profiles along the fracture. The results correspond to a case with a dispersivity of 0.6 m. TOUGHREACT does not consider dispersivity explicitly in the formulation, although it introduces a numerical dispersivity, which is approximately 0.6 m in the present simulations. It may be observed that the agreement is qualitatively satisfactory, although there are some minor differences in the total dispersivity between the different solutions. The advective term is similar in all cases (given by the points corresponding to $C/C_{max} = 0.5$ in the curves).

Transport of a conservative tracer through a fracture-rock matrix system

A verification case has also been simulated considering the fracture-rock matrix system. Similar conditions to those in the previous section are considered for the flow through the fracture. The fracture width is 0.1 mm. The matrix depth is 1.0 m (distance between parallel fractures is 2.0 m) to simulate a case with an approximately semi-infinite rock matrix depth, for which an analytical solution is available (Tang et al. 1981) to compare with the numerical results. The simulations have been performed with PFLOTRAN and PHAST. The parameters used in this simulation are presented in presented in Table 7-1.

Table 7-1. Model parameters for fracture-rock matrix system.

Description	Value	Unit	Reference
Matrix depth	0 / 0.1 / 0.4	m	This work
Matrix porosity	0.001	–	Sidborn et al. (2010, Section 5.1.1)
Effective diffusivity	$1 \cdot 10^{-14}$	m^2/s	Sidborn et al. (2010, Section 5.1.2)
F-factor	$4 \cdot 10^5$ / $4 \cdot 10^6$	y/m	This work, Chapter 6
Travel time	20 / 200	y	This work
Fracture length	100	m	This work
Fracture width	0.1	mm	This work

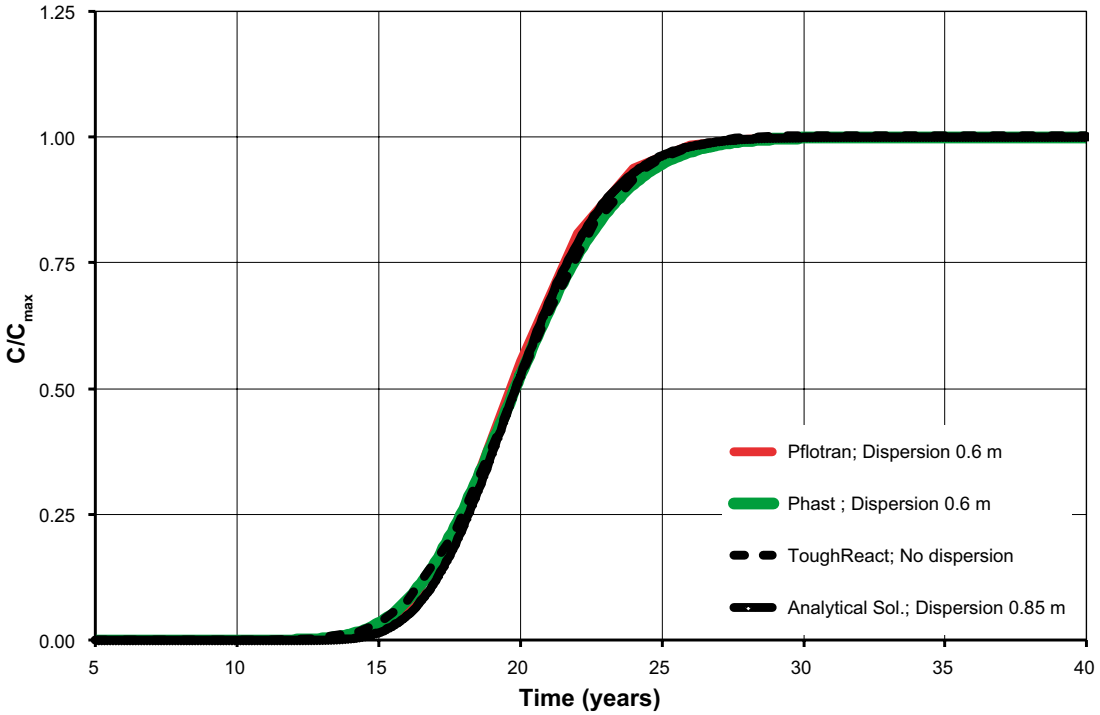

Figure 7-3. *Breakthrough curves of normalized tracer concentration at the fracture outlet (x = 100 m): analytical solution (small circles), PFLOTRAN (in red), TOUGHREACT (dashed line), and PHAST (in green) results.*

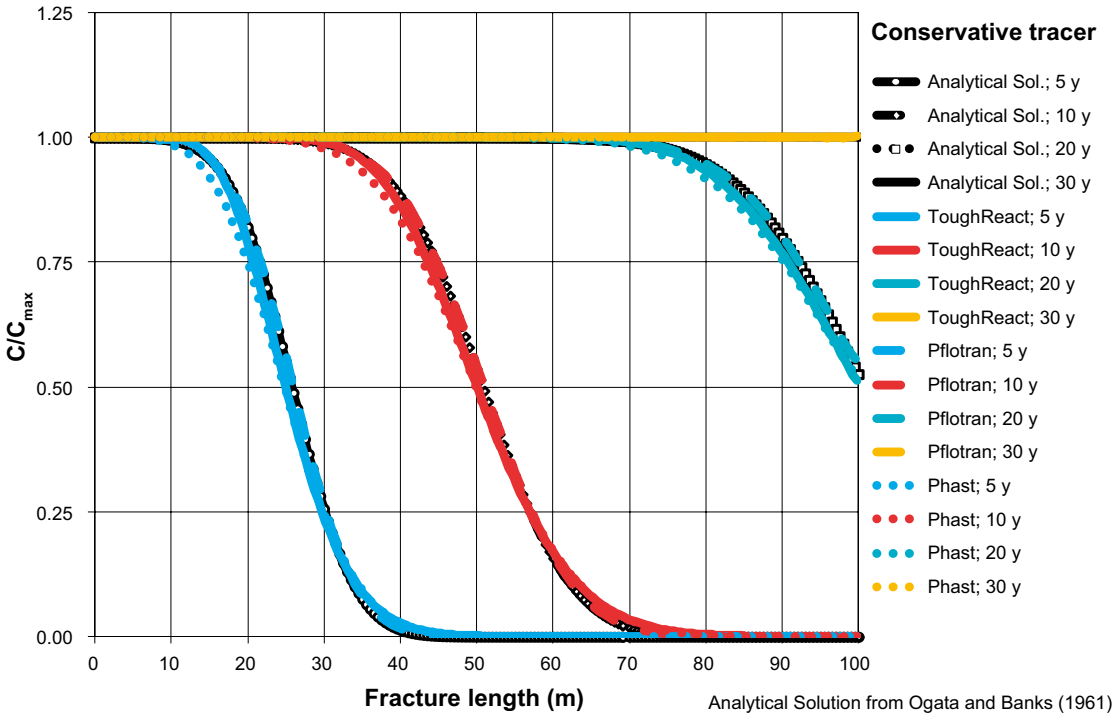

Figure 7-4. *Profiles along the fracture of the normalized tracer concentrations: analytical solution (black lines), PFLOTRAN (dashed lines), TOUGHREACT (solid lines), and PHAST (dotted lines) results.*

The numerical results for the transport of a conservative tracer are compared to the analytical solution in Figure 7-5 in terms of the normalized concentration vs. time at the outlet of the fracture (breakthrough curve). It may be observed that there is a very good quantitative agreement until around 750 years. At this point, the tracer concentration starts to increase significantly at a matrix depth of 1 m. Therefore, the assumption of a semi-infinite rock matrix is not valid anymore, and the numerical solution presents a faster increase of the tracer concentration compared to the analytical solution. It is also observed that there is a very good agreement between the numerical results of PHAST and PFLOTRAN throughout the simulation time.

7.4 Alkaline plume ingress calculations

The results presented in this section correspond to simulation cases in which the boundary OPC water composition is fixed throughout the simulation. The leachates composition, as well as the procedure to calculate it, is summarized in Section 5.4. Unless otherwise stated, the numerical reactive transport code used for the simulations presented in this section is PFLOTRAN. Figure 7-6 to Figure 7-18 present the results obtained with PFLOTRAN.

7.4.1 Reactive transport along a fracture only: worst case scenario

First, reactive transport simulations of the effect of an ADZ in a single fracture have been performed considering that the rock matrix is not available for diffusion. This case would correspond to a situation in which the rock matrix has been sealed from the beginning of the simulation. This case represents the worst case scenario for a given set of parameters because it neglects the positive effect of retardation of the transport and the potential pH buffering capacity of the rock matrix. These simulations have been carried out considering one-dimensional transport along the fracture. The input data considered for the flow and transport has been presented in Section 7.2.

The mineralogy of the fracture (i.e. the primary minerals) has been described in Section 5.5 (based on the work by Sandström et al. 2008). Different mineral surface areas were considered to assess the sensitivity of the results to this crucial parameter (the values used were 3, 30, 300, 1,000, 3,000 m^2/m^3_{min}, where subscript min stands for mineral). In each simulation, the same surface area has been used for the different minerals (with units m^2/m^3_{min}). To express these surface areas in m^2/m^3_{rock} the values are multiplied by the different mineral volume fractions.

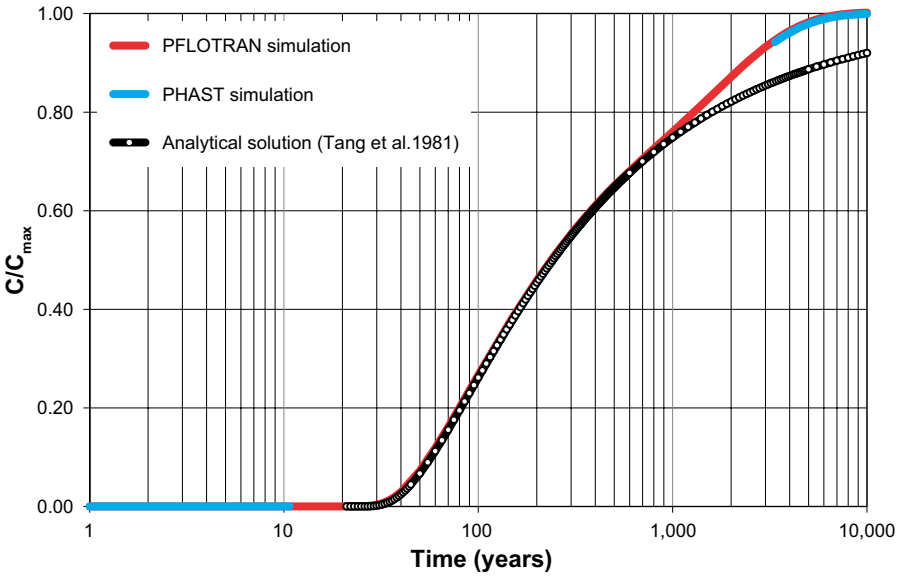

Figure 7-5. *Breakthrough curves of normalized tracer concentration (C/C_{max}) at the fracture outlet (x = 100 m): analytical solution (circles), and numerical results from PFLOTRAN (in red) and PHAST (blue dashed lines).*

Effect of surface area

The results in terms of pH at the fracture outlet versus time are presented in Figure 7-6 for the different reactive surface areas considered for the primary minerals (3, 30, 300, 1,000, and 3,000 m^2/m^3_{min}). It may be observed that assuming values of reactive surface areas of 3 to 30 m^2/m^3_{min} leads to almost no reduction of the pH at the fracture outlet (this is confirmed in both TOUGHREACT and PFLOTRAN simulations, although only PFLOTRAN results are shown here). On the contrary, the cases with a surface area from 300 to 3,000 m^2/m^3_{min} present a significant decrease of the maximum pH at steady state. The maximum pH ranges from around 12.10 for a surface area of 300 m^2/m^3_{min}, to 10.73 for 3,000 m^2/m^3_{min}. It is remarkable that in the case of a large surface area (3,000 m^2/m^3_{min}, corresponding to spherical mineral grains with a radius of 1 mm) the pH is significantly lower than the rest of the cases, and below pH 11, a value below which the degradation of bentonite seems to be much slower than for higher pH levels (see Chapter 2 for more details on experimental observations).

The decrease of the pH is a result of the dissolution of the primary minerals (especially quartz, calcite and albite) and the subsequent precipitation of the following secondary minerals: brucite, amorphous C-S-H with low Ca/Si ratio (= 0.80), prehnite, saponite-Ca, and mesolite. This is shown in Figure 7-7 for the simulations with surface areas of 300 and 3,000 m^2/m^3_{min}. Figure 7-8 presents the kinetic rates of the primary minerals. A significant dissolution of quartz and albite (and to a lesser extent of K-feldspar) releases silica and aluminum into the fracture porewater, leading to the precipitation of C-S-H with Ca/Si of 0.8 and prehnite. A high magnesium concentration in the OPC leachates causes an important precipitation of brucite near the fracture inlet (in the first 4 grid cells in the case with largest surface area).

To gain more insight into the role of brucite on the pH buffering, an additional simulation has been performed. For this purpose, the composition of the OPC leachates has been slightly modified by forcing equilibrium of Mg concentration with brucite, otherwise keeping the rest of the input parameters constant and equal to the case of surface area 3,000 m^2/m^3_{min}. The results (not shown) indicate that the pH at the fracture outlet (and in general the pH profile along the fracture) is almost identical to the previous case (i.e. with the original OPC leachate). The sequence and volume fractions of secondary minerals precipitating are also the same, although the volume of brucite precipitating adjacent to the fracture inlet is much smaller than in the previous case. This is of course consistent with the fact that the OPC leachate composition is in equilibrium with brucite.

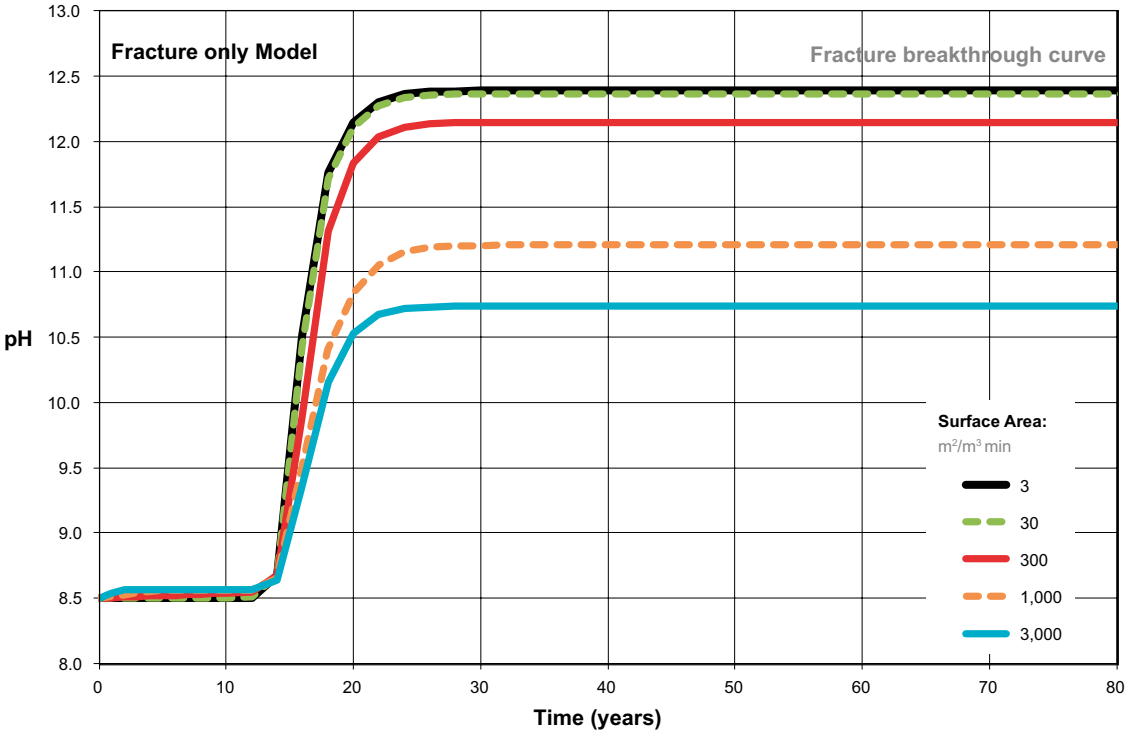

Figure 7-6. *pH values at the fracture outlet for 5 different simulations with PFLOTRAN, with reactive surface areas of: 3, 30, 300, 1,000, and 3,000 m^2/m^3_{min}.*

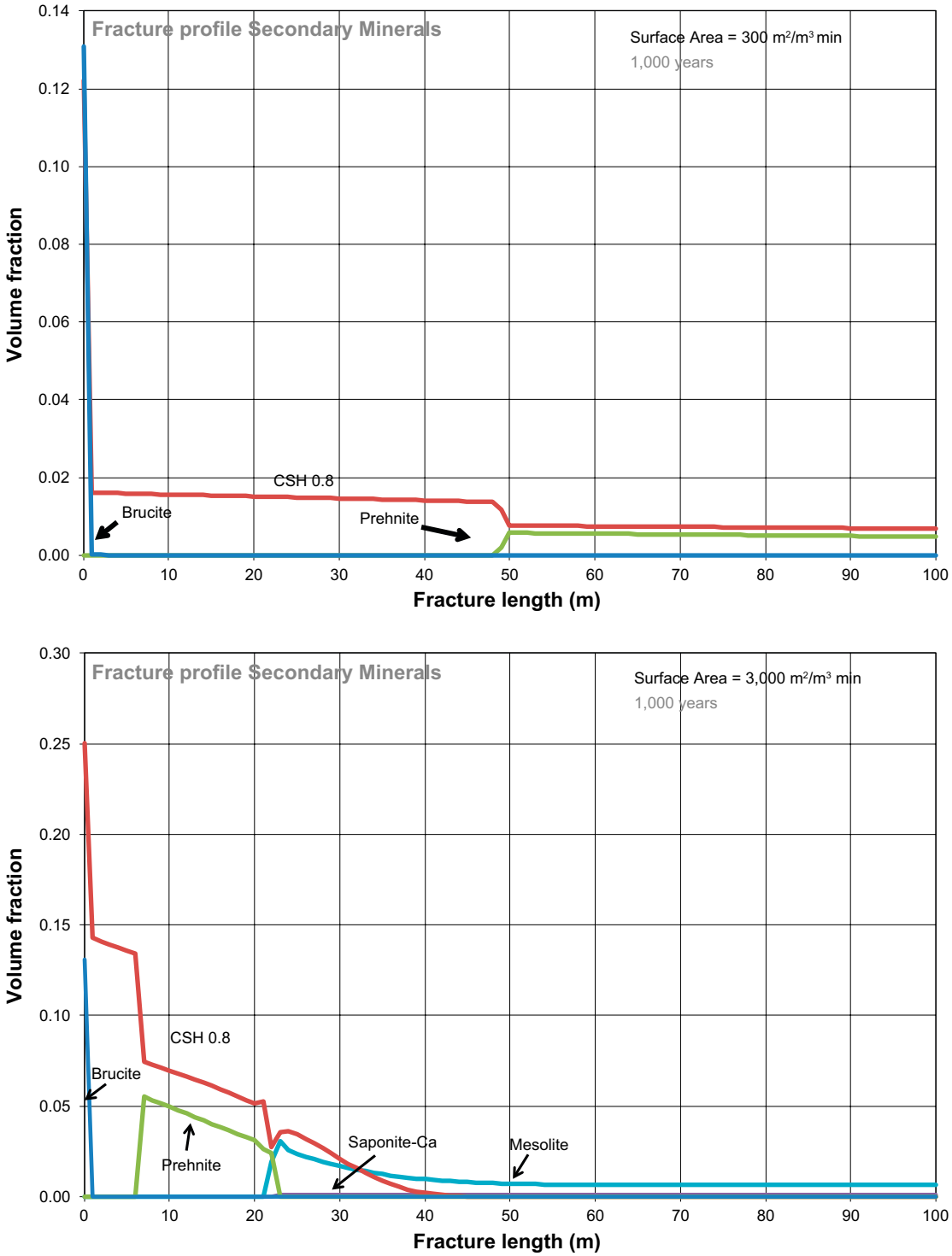

Figure 7-7. *Secondary minerals that precipitate along the fracture in the simulations with surface areas of 300 (top) and 3,000 m^2/m^3_{min} (bottom) after 1,000 years. The case with surface area of 3 m^2/m^3_{min} is not shown because only C-S-H 0.8 and brucite precipitate and in very small amounts (< 0.0002), except at the fracture inlet, where brucite and C-S-H 0.8 reach a volume fraction of 0.12.*

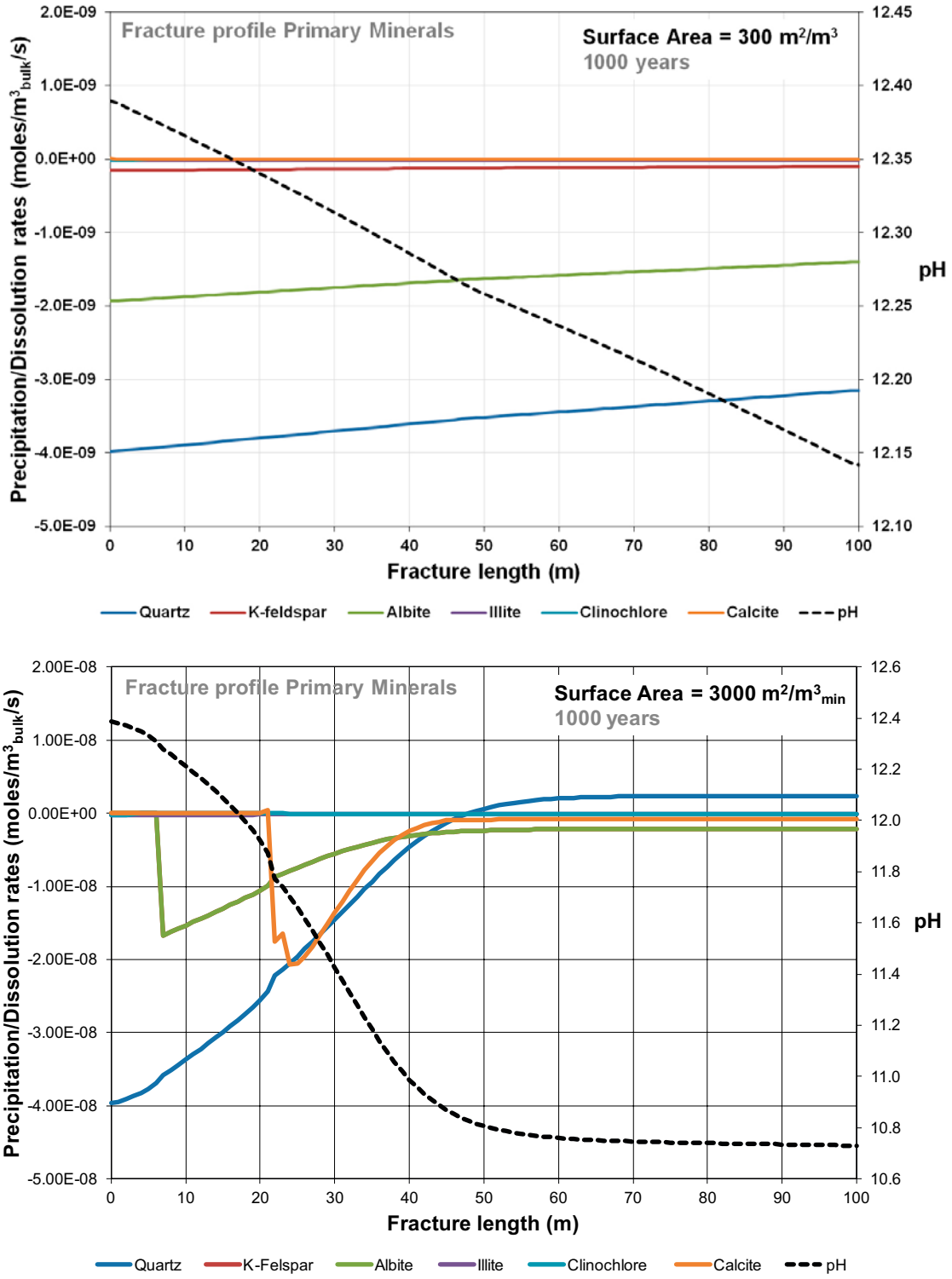

Figure 7-8. *Kinetic rates of the primary minerals along the fracture for the simulations with surface areas of 300 (top) and 3,000 m^2/m^3_{min} (bottom) after 1,000 years.*

Effect of the coupling between porosity changes and transport

The previous simulation cases did not consider any feedback of porosity changes due to dissolution/ precipitation of minerals on the hydraulic conductivity of the fracture. To analyze the potential effect of porosity changes on the pH at the fracture outlet, the simulations were repeated considering the following hydraulic conductivity (K, in m/s) – porosity (ϕ) relation:

$$K = \left(\frac{\phi}{\phi_0} \right)^3 K_0 \qquad 7\text{-}1$$

In this expression, sub-index 0 indicates initial state (0.5 for porosity and $5 \cdot 10^{-10}$ m/s for the hydraulic conductivity, see Follin et al. (2005)). It is noted that in these simulations the constant boundary conditions for the flow are set in terms of pressure gradient, so that changes in permeability affect the water inflow to the fracture. Figure 7-9 presents the pH breakthrough curves at the outlet of the fracture for 3 different surface areas (3, 300, 3,000 m^2/m^3_{min}) in the case where permeability is coupled to porosity evolution. The evolution of porosity and hydraulic conductivity of the fracture in time is depicted in Figure 7-10 for the cases with surface area of 300 and 3,000 m^2/m^3_{min}.

It must be noted that for the current simulations the volume fractions of the infill minerals and the porosity of the fracture have been only qualitatively considered (initially, porosity is 0.5 and total mineral volume fraction is 0.5). Therefore, the time scale in Figure 7-9 and Figure 7-10 should not be considered as a precise estimation of the temporal variations, but is rather indicative of the different stages in the evolution of the system.

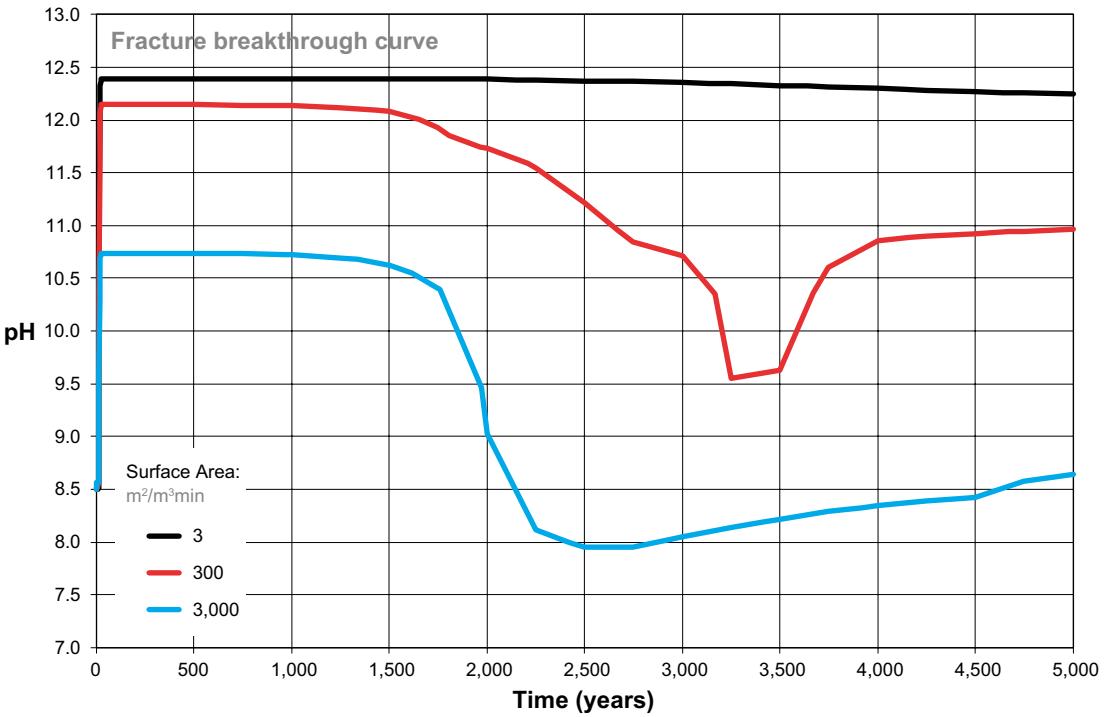

Figure 7-9. *pH values at the fracture outlet (x = 100 m) for 3 different simulations, with reactive surface areas of 3, 300, and 3,000 m^2/m^3_{min}. Porosity-permeability coupling is considered in these simulations.*

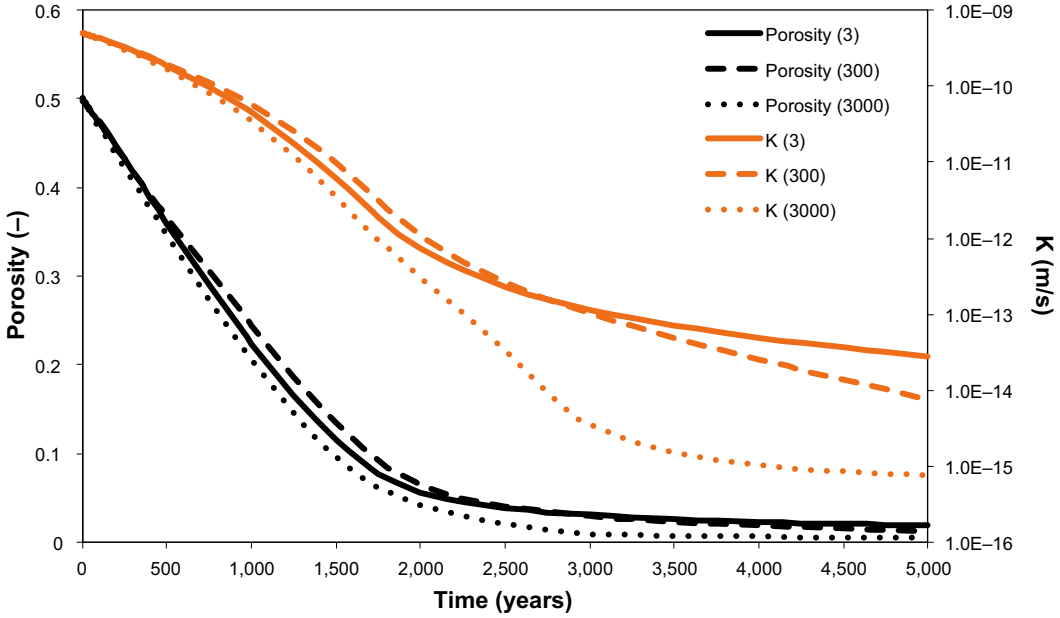

Figure 7-10. *Evolution of the fracture porosity and hydraulic conductivity (m/s) values at the fracture inlet (x = 0 m) for the simulations with a surface area of 3, 300 and 3,000 m^2/m^3_{min}.*

The reduction of the porosity due to the precipitation of secondary minerals (especially brucite and C-S-H with a Ca/Si of 0.8) leads to a gradual decrease of the hydraulic conductivity of the fracture adjacent to the OPC leachates source (Figure 7-10). As a consequence, the ingress of OPC leachates is reduced, leading to a decrease in the pH at the fracture outlet. The pH at the fracture outlet drops significantly for the cases with a surface area of 300 and 3,000 m^2/m^3_{min}, as opposed to the very small pH decrease for the smallest surface area (Figure 7-9). This effect is predicted in all the simulations considering different reactive surface area. However, for the lowest surface area, even though the fracture sealing process is similar to the other two cases, the kinetics of primary mineral dissolution is not fast enough to buffer the pH significantly, even after 5,000 years. Indeed, the decrease in the pH is due to the fact that the OPC leachates have a much longer time to react with the primary minerals along the fracture as the permeability is reduced, and as larger surface areas are considered. In the case of a surface area of 3 m^2/m^3_{min}, the dissolution rates of the primary minerals are so low that the pH reduction at the fracture outlet is not significant even after 5,000 years. However, for the cases that assume a large surface area, the pH drops to values below 11.0. In Figure 7-10 it may be seen that the porosity at the fracture inlet does not clog completely, so that the hydraulic conductivity is not reduced to zero. Therefore, the transport of OPC leachates continues, although at a much slower velocity.

Effect of flow velocity

Finally, the effect on the pH buffering capacity of the flow velocity has also been evaluated in the 1D reactive transport simulations through a fracture. The flow velocities considered in the simulations are the result of the hydrogeological modelling in the previous chapter. In all the previous simulations, a flow velocity of 5 m/y has been used (see Section 7.2). An additional case has been considered, in which a flow velocity of 0.5 m/y has been adopted.

The simulations have been repeated for three different surface areas: 3, 300, and 3,000 m^2/m^3_{min}. The results are shown in Figure 7-11 with respect to the breakthrough curves of pH for the three different cases and for the two flow velocities. As expected, the arrival time of the pH plume is delayed by one order of magnitude in all cases due to the different velocity (from around 20 to 200 years). After 1,000 years, all the simulations have reached steady state conditions. It may be observed that in the case with a slower flow velocity the pH at steady state is lower than the reference case for surface areas larger than 300 m^2/m^3_{min}. The pH value is reduced from 10.7 to 10.4. A larger contact time between the high-pH plume and the fracture infill materials increases the effectiveness of the pH buffering of the fracture due to the dissolution of primary minerals. On the other hand, the case with a surface area of 3 m^2/m^3_{min} does not show any significant pH reduction. This is due to the fact that the flow is still not slow enough to allow significant pH buffering by kinetic dissolution of the primary minerals and precipitation of secondary minerals.

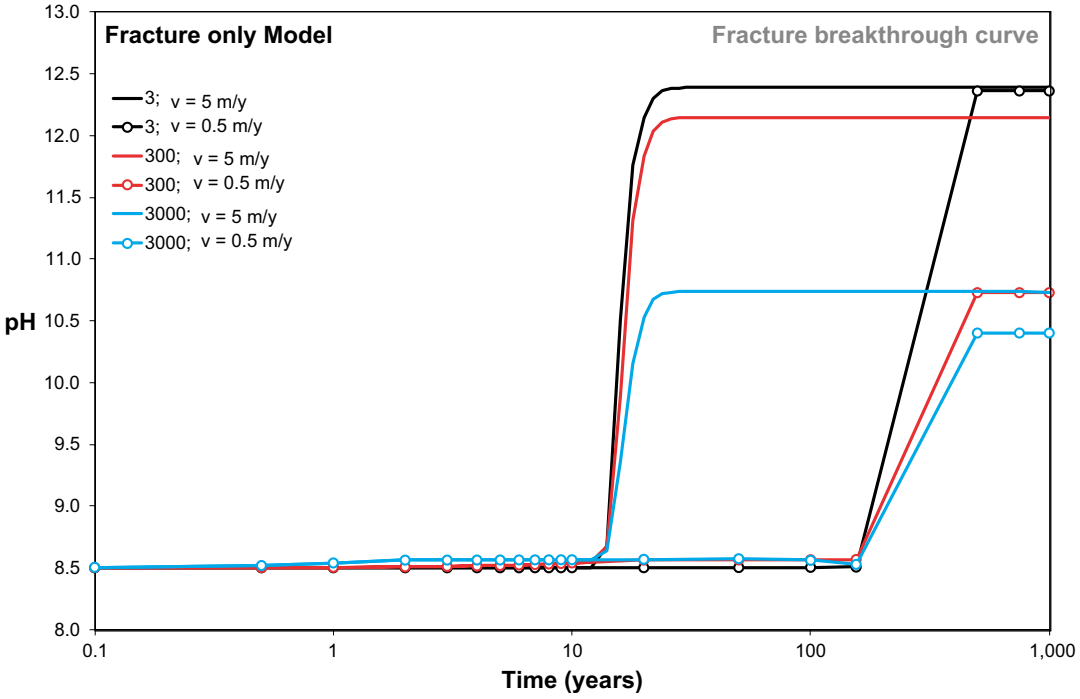

Figure 7-11. *pH breakthrough curves at the fracture outlet for three different cases with surface areas of 3 (black), 300 (red) and 3,000 (blue) m^2/m^3_{min}, and with flow velocities equal to 5 m/y (solid lines) and 0.5 m/y (circles).*

7.4.2 Reactive transport in the fracture—rock matrix system

Next, the different cases considered in the previous section have been repeated considering a rock matrix available for molecular diffusion with a depth of 0.1 m. these simulations do not account for the coupling of porosity with permeability. Again, the flow and transport conditions are gathered in Section 7.2. The initial groundwater composition of the fracture and the rock matrix are assumed identical (Section 5.5). The OPC water is the same as in the previous calculations (described in Section 5.4) and the composition of the rock matrix is depicted in Section 5.5 (from Sandström and Stephens 2009, Table 3-7). Different values of the surface area of the rock matrix have been considered: 3, 300 and 3,000 m^2/m^3_{min}.

The results in terms of pH, reaction rates of primary minerals (at steady state), volume fractions for secondary minerals, and porosity profiles along the fracture are shown from Figure 7-12 to Figure 7-16. The steady state situation is reached when the kinetic rates reach a constant value in each grid cell and provided that primary minerals are not exhausted (for the cases in which porosity update is not accounted for). It can be observed in Figure 7-12 that in the steady state situation the pH at the fracture outlet is around 10.75 for the three cases, which is significantly lower than the values obtained for the same cases without the effect of the matrix diffusion (higher than 12). In fact, this is the case for the simulations with surface areas of 3 and 300 m^2/m^3_{min}. In the third case (surface area of 3,000 m^2/m^3_{min}), the pH is almost the same whether considering 0.1 m of matrix or not (see Figure 7-12).

The pH in the rock matrix is depicted in Figure 7-13 for the case with a surface area of 300 m^2/m^3_{min}. It can be observed that the high-pH plume with a pH larger than 11 is restricted to the first meters adjacent to the fracture inlet (8 meters along the fracture).

It is worth noting that the breakthrough curves for the cases with larger surface areas show a sudden increase in pH from the beginning of the simulation. This is due to the disequilibrium that develops between the fracture and the rock matrix during the first years in the cases with larger surface areas.

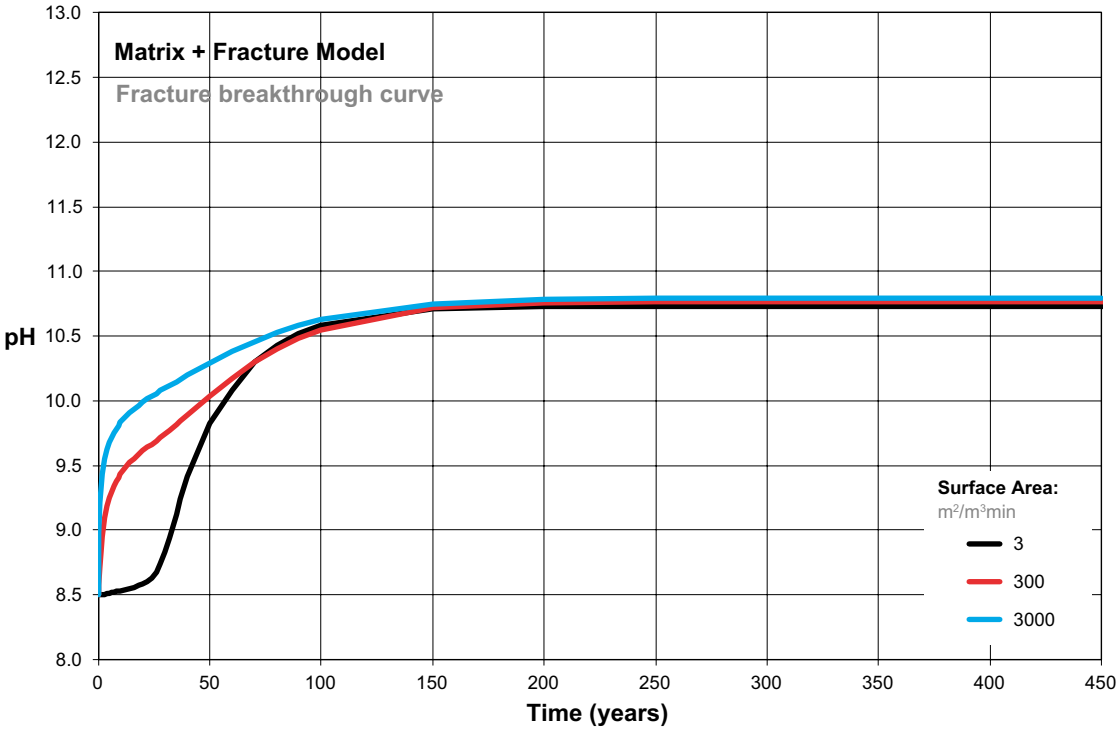

Figure 7-12. *pH values at the fracture outlet (x = 100 m) for 3 different simulations, with reactive surface areas of 3, 300, and 3,000 m^2/m^3_{min}. Porosity-permeability coupling is not considered in these simulations. Rock matrix depth is 0.1 m.*

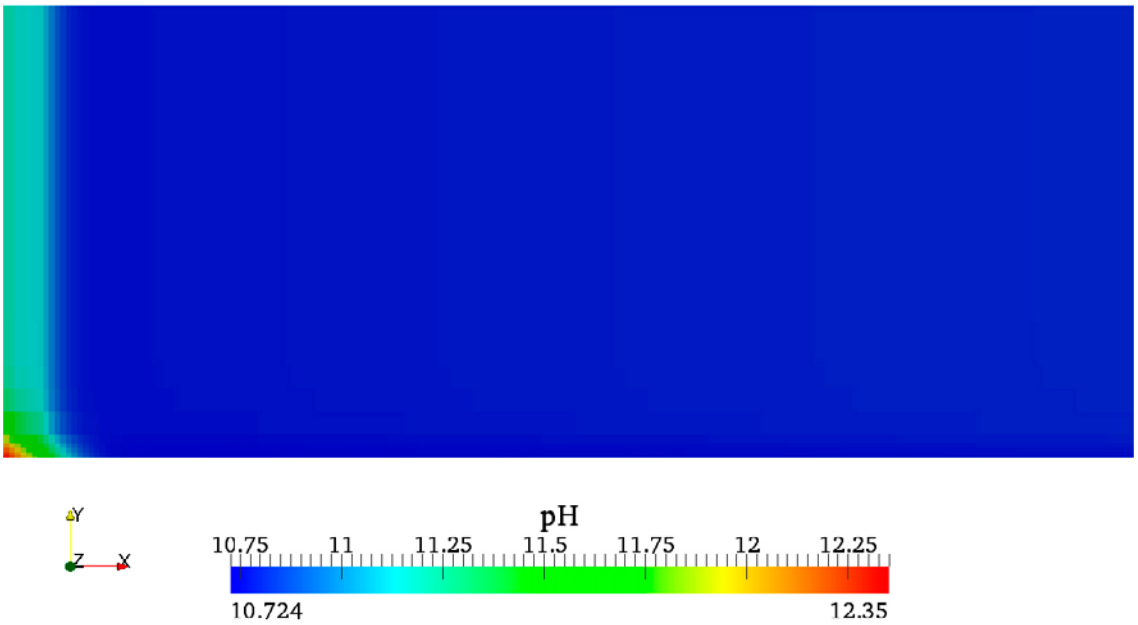

Figure 7-13. *Two dimensional pH in the rock matrix along the fracture length (100 m) at steady state conditions (after 500 years). Results correspond to the case of a rock matrix depth of 0.1 m (magnification factor is 400 in the Y-direction) and a surface area of 300 m^2/m^3_{min}.*

Even though the fracture and rock matrix porewater compositions are initially identical, the primary minerals are different in both cases. As outlined in Section 5.5, the porewater is undersaturated with respect to albite and K-feldspar (both present in the fracture and the rock matrix), and also with respect to clinochlore, illite (only present in the fracture). Therefore, since primary minerals are kinetically constrained, the dissolution of the primary minerals starts from the beginning of the simulation. As a consequence, an even though the solution was initially undersaturated with respect to all the secondary minerals, a small amount of mesolite precipitates in the rock matrix. The process is faster the higher the reactive surface areas, and for the cases with 300 and 3,000 m^2/m^3_{min} precipitation occurs in approximately 0.1 y. This precipitation consumes almost all the calcium in the rock matrix porewater (the porosity is 0.1% so there is a very small amount of water available), inducing a fast disequilibrium between the rock matrix and fracture porewater compositions. This is the cause of the sudden increase in pH for the cases with larger surfaces areas. However, it may be observed that as soon as the high-pH plume reaches a certain point in the fracture or the rock matrix, the pH and the geochemistry of that point is controlled by the alkaline conditions.

Figure 7-14 shows the kinetic rates for the primary minerals and the pH along the fracture for three different cases (differing in surface area). It may be observed that the two simulations with larger surface area (300 and 3,000 m^2/m^3) predict very similar results. In these cases, it is seen that the high-pH region is limited roughly to the first 10 m, and that after this point the pH is buffered to a value that is below 11. The primary minerals are dissolving near the fracture inlet, except clinochlore which precipitates due to the availability of Mg from the OPC leachates. Quartz only dissolves near the inlet, providing the silica for C-S-H 0.8 and mesolite precipitation, as shown in Figure 7-15. However, away from the OPC source it precipitates at a small and almost constant rate along the fracture due to the availability of SiO_2(aq) from the dissolution of silicates and the OPC leachates. In turn, calcite dissolves along the entire fracture length, except very near the fracture inlet, where it precipitates. A significant dissolution in the first fracture meters provides the calcium for the precipitation of C-S-H 0.8 and mesolite (Figure 7-15). Small amounts (less than 0.001) of analcime and prehnite and saponites are also predicted to precipitate but have not been included in Figure 7-15.

In the case with the smallest surface area considered (3 m^2/m^3_{min}), the results show similar trends, but due to the lower kinetic rates the reaction fronts penetrate the fracture length to a much higher degree. As a result, the high-pH region with a value higher than 11 extends to half of the fracture length (50 m). In addition, the second peak of C-S-H 0.8 precipitation, which is due to calcite dissolution (Figure 7-16), now develops between 25 and 60 m away from the fracture inlet (Figure 7-15 top).

The mineralogical and porosity profiles along the rock matrix thickness are presented in Figure 7-17. It may be observed that the porosity of the rock matrix is sealed in the region adjacent to the fracture, and only near the fracture inlet due to the precipitation of C-S-H 0.8, prehnite and mesolite (Figure 7-17 top), but away from the OPC source the porosity has been roughly unaltered by the interaction with the plume (Figure 7-17 bottom). However, it is noted that the simulations considering rock matrix presented in this section do not account for the coupling of porosity with diffusion and permeability changes.

Finally, an additional case with a matrix depth of 0.4 m and a surface area of 300 m^2/m^3_{min} has been simulated, to assess the impact of the matrix depth on the pH buffering capacity of the system. The results in terms of pH at the fracture outlet are compared with two similar previous simulations only differing in the matrix depth: 0, and 0.1 m. It may be observed that the pH at steady state conditions is similar to the case with a matrix depth of 0.1 m, and that the only appreciable effect is the retardation of the high-pH plume arrival at the fracture outlet.

7.5 Summary of reactive-transport modelling results.

In this chapter, the main results of the simulations of the reactive transport of an alkali disturbed zone (ADZ) through a simulated plausible fracture at the Forsmark site have been presented and discussed. Different key variables and parameters have been analysed, such as the reactive surface area of the fractured bedrock, the effect of the rock matrix diffusion-reaction processes, the effect of porosity changes on the reactive transport analysis, and the F-factor.

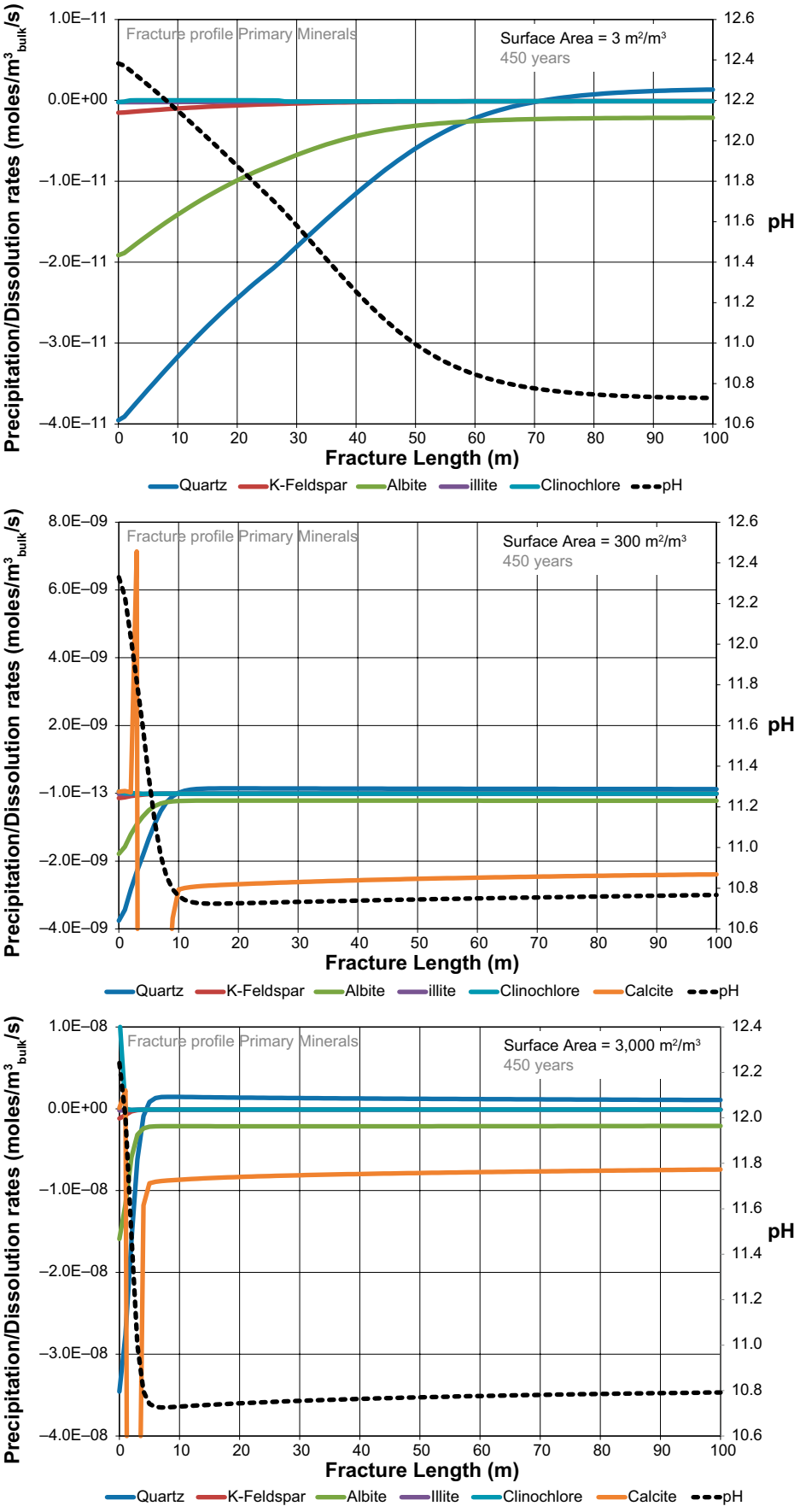

Figure 7-14. *Kinetic rates of the primary minerals (positive means precipitation, and negative is dissolution) and pH along the fracture for the simulations with a surface area of 3 (top), 300 (middle) and 3,000 m^2/m^3_{min} (bottom) after 450 years. The calcite dissolution peaks are (middle) $-1.45 \cdot 10^{-8}$ mol/m³/s and (bottom) $-1.91 \cdot 10^{-7}$ mol/m³/s. Calcite dissolution rate for the case of 3 m^2/m^3_{min} is shown separately in Figure 7-16.*

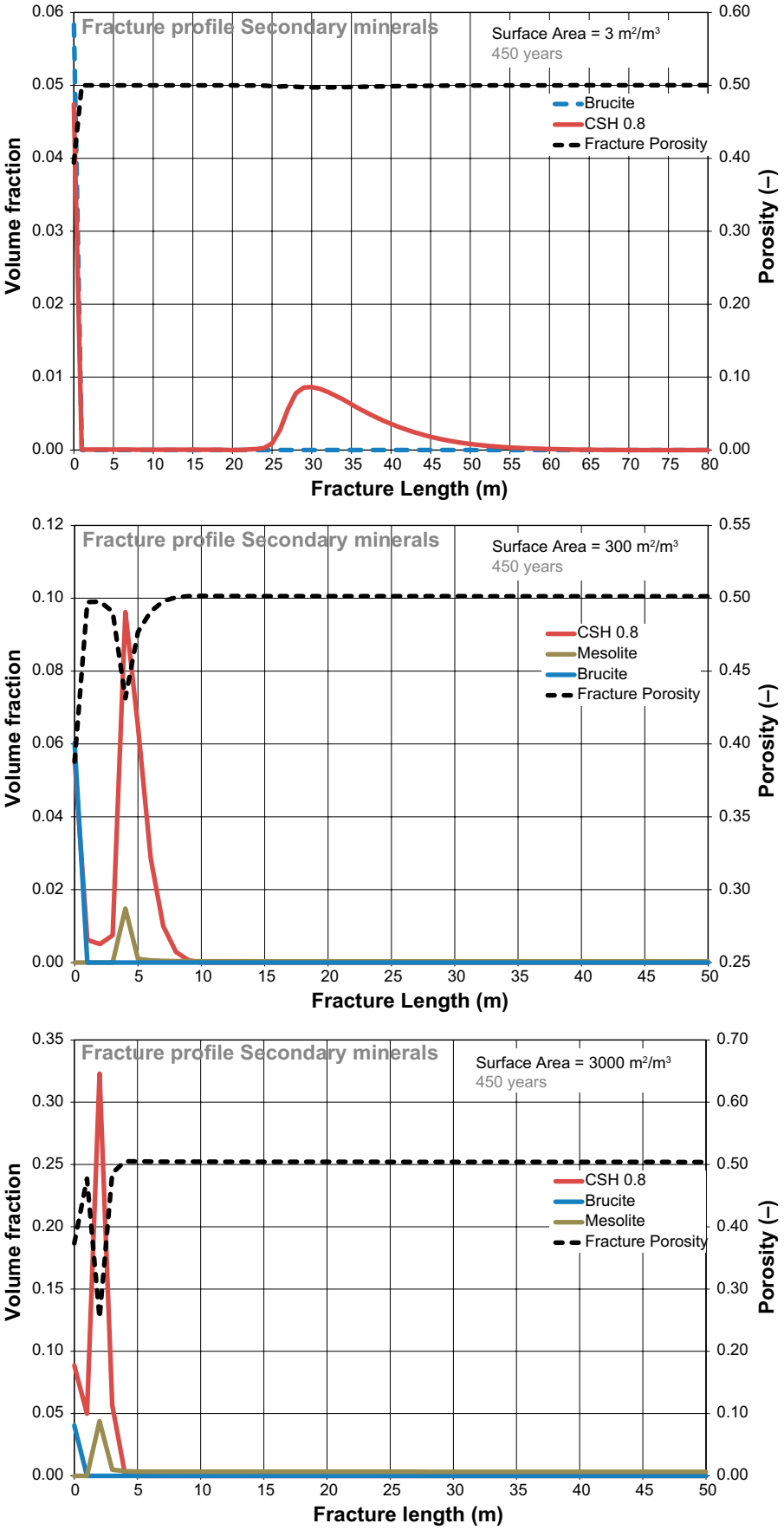

Figure 7-15. *Secondary minerals that precipitate along the fracture in the simulations with surface areas of 300 (top) and 3,000 m^2/m^3_{min} (bottom) after 450 years. Note the different scales in the horizontal axes.*

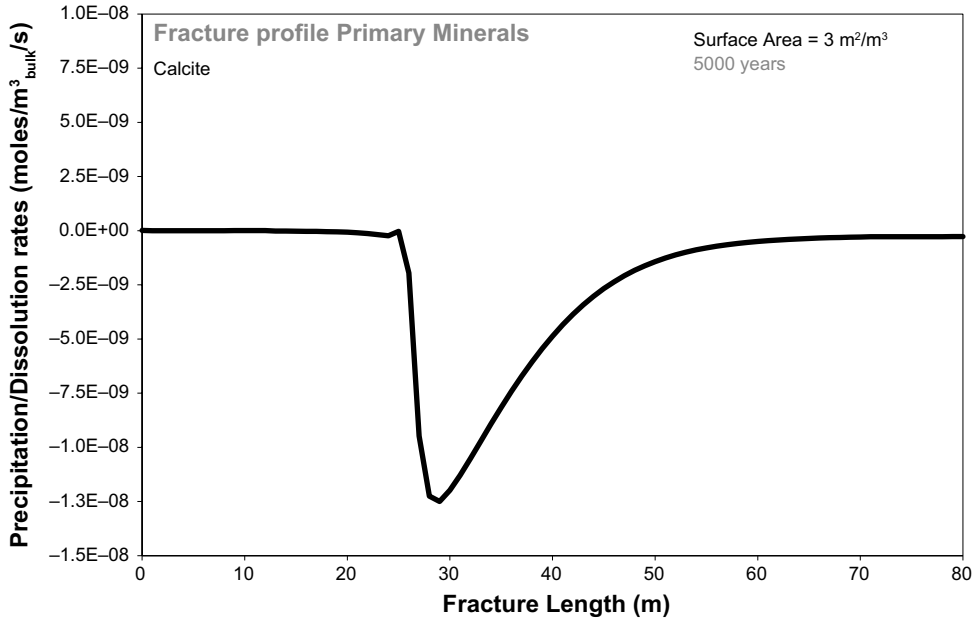

Figure 7-16. *Kinetic rate for calcite (positive means precipitation, and negative is dissolution) along the fracture for the simulation with a surface area of 3 m^2/m^3_{min} after 450 years.*

The conceptual model considers a conservative scenario in which a conservative boundary condition with fixed pH in time (equal to 12.4) is considered while at the same time the potential dilution of the high-pH plume by the interaction with the surrounding fracture groundwater is neglected. Moreover, most of the simulations have assumed a groundwater flow scenario corresponding to the conditions expected during the glacial period, with much faster flows that the present hydrogeological conditions.

With this in mind, the results obtained indicate that in certain cases there is a significant reduction of the pH along the fracture even in the adverse situation considered. However, the pH buffering capacity of the fracture alone, without the effect of the rock matrix diffusion-reaction processes, is not sufficient to reduce the pH to values below 11.0 in the present simulations, unless a high surface area (3,000 m^2/m^3_{min}) is considered. However, if the effect of porosity changes on permeability is taken into account, it is predicted that the sealing of the fracture porosity near the fracture inlet induces a significant reduction of pH to values below or near 11.0 even for the cases with surface areas of 300 m^2/m^3_{min} or larger.

The effect of the flow velocity and the F-factor is translated into a pH decrease for the cases where the F-factor is higher (slower flow velocity). Indeed, when considering the minimum F-factor expected for the period 2000 AD (see Chapter 6), the pH was reduced from above 12 to around 10.7 at the fracture outlet in the case with a surface area of 300 m^2/m^3_{min}, due to a larger contact time between the fracture infill materials and the OPC leachates.

The simulations have shown that the effect of the rock matrix diffusion-reaction processes is remarkable, even for the cases in which the reactive surface area is assumed small (as low as 3 m^2/m^3_{min}). By considering a limited matrix depth of 10 to 40 cm the pH is reduced from a value above 12 to a value between 10 and 11.

The reactive surface area parameter for the fracture infill and the rock matrix minerals is one important source of uncertainty in the simulations presented, at least at the present stage. This is an important aspect due to the relatively large effect on the results regarding pH. Further efforts in this line should be devoted to gain more insight into the expected ranges of the surface area of the different minerals considered.

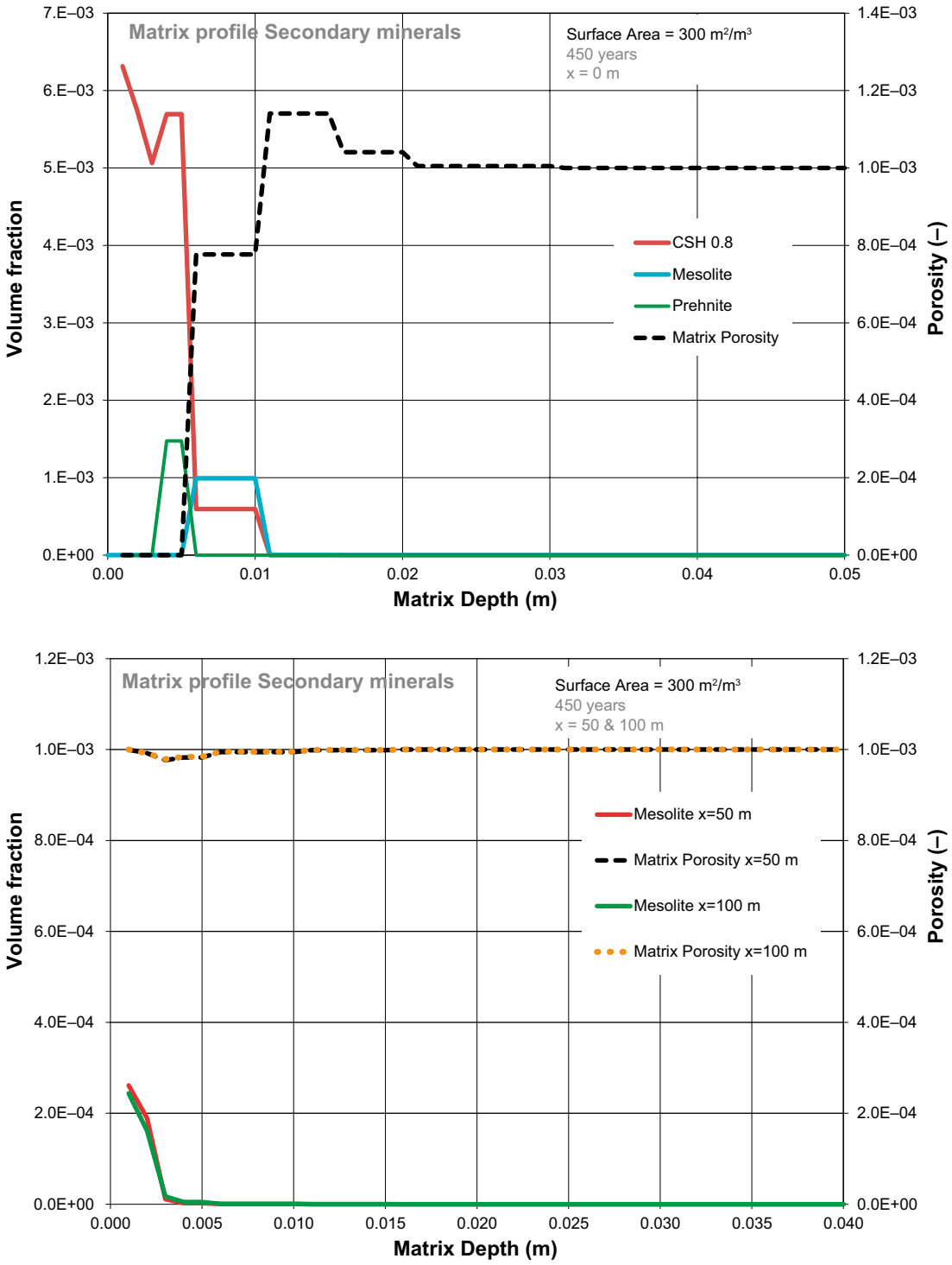

Figure 7-17. *Secondary minerals that precipitate and porosity profiles along the rock matrix at different points in the fracture in the simulation with surface area of 300 m^2/m^3_{min} after 450 years: x = 0 (top), x = 50 and x = 100 m (bottom).*

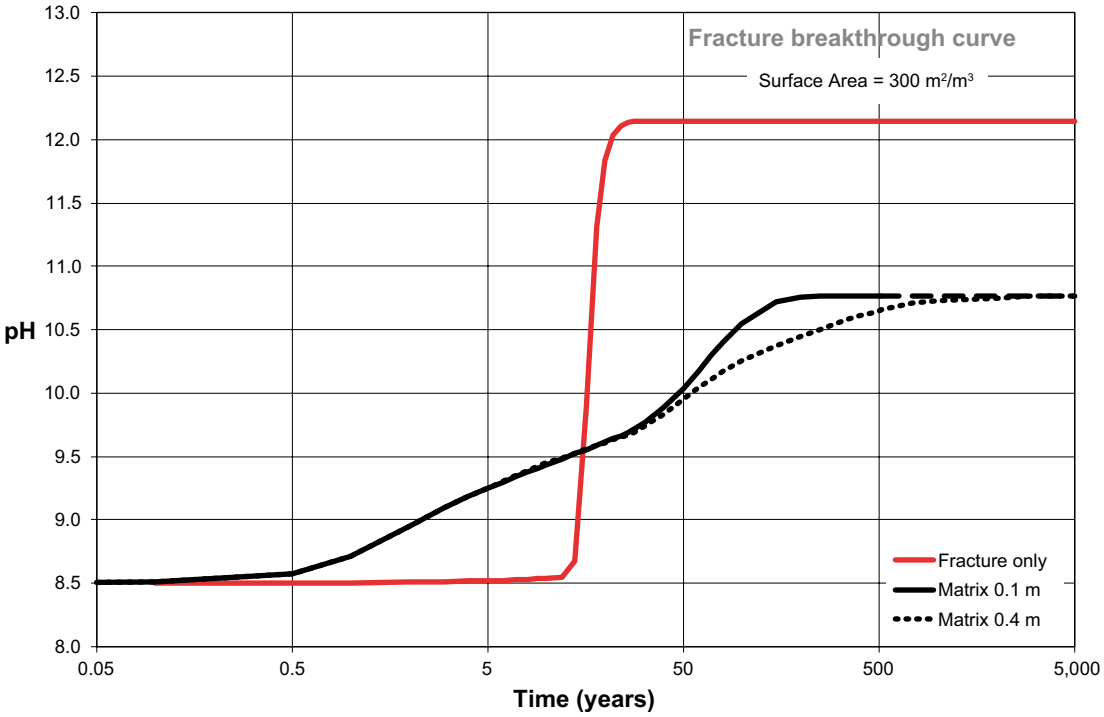

Figure 7-18. *pH values at the fracture outlet (x = 100 m) for 3 different matrix depths, with reactive surface area of 300 m^2/m^3_{min}: 0, 0.1, and 0.4 m of rock matrix. The case with a matrix depth of 0.1 m was only calculated until 500 years, but steady state was reached. Thus, the dashed line for t > 500 years is valid.*

8 Coupling of reactive-transport and hydrogeological model results

In Chapter 7, various aspects of the evolution of the Alkali Disturbed Zone (ADZ) are studied by means of numerical reactive-transport models. Concentration profiles of reacting species and minerals along a single generic flow path with given uniform initial properties along its length are presented. The uniform properties of the generic flow-path studied allows for a direct coupling, or "mapping" of the results onto flow paths obtained from the hydrogeological models in Chapter 6.

The rationale for this is very simple:

In this case, the flow related transport resistance, or F-factor, is linearly proportional to the distance in the flow direction (see Equation 3-1). For x (m) being the distance along the fracture with a uniform aperture width δ (m) carrying flowing groundwater at a velocity v, the F-factor is (Equation 3-1):

$$F = \frac{2x}{Ti} \quad \left(= \frac{2x}{v\delta} \right)$$

This entity, which can be viewed upon as the flow-wetted surface to flow-rate ratio, has a dominating influence on the amount of minerals that can be accessed for reaction and is a direct measure of the extent of interaction between dissolved species in the flowing water and minerals on the fracture surface and in the matrix. This is provided that the porosity in the rock matrix is connected and accessible to a sufficient depth not limiting the availability of the matrix minerals. Note also that any minerals present in the fracture are assumed to line the fracture walls and the amount of fracture minerals per fracture surface is assumed to be constant for all fractures.

Each distance, *x,* along the generic fracture, thus corresponds to a cumulative flow path F-factor, with a linearly dependence between the two parameters.

Let us consider the numerical reactive-transport results after 450 years in Figure 7-14 (top figure) as an example. In this case a very low specific surface of reactive minerals is assumed to be 3 $m^2/m^3_{mineral}$, and the total F-factor for the 100 m long fracture is $4 \cdot 10^5$ y/m according to Equation 3-1. At half the fracture length (50 m), pH has decreased to ~11. This distance then corresponds to a cumulative F-factor of $2 \cdot 10^5$ y/m.

Given that the established steady-state profile in Figure 7-14 is not largely affected by the assumed fracture dispersivity, i.e. the retention is governed by the reaction with matrix minerals, this F-factor may be compared with calculated F-factors for flowpaths obtained from the hydrogeological modelling that intersect and connect grouted volumes with canister positions in the repository (e.g. $F_{min} = 9.164 \cdot 10^4$ y/m for the case of 200 m grouting at 3000 BC in Table 6-11).

In this example the steady-state pH profile along the flow path reaches the canister position ($F = 9.164 \cdot 10^4$ y/m) at a pH of ~11.75 (approximately corresponding to $x = 23$ m in Figure 7-14).

A similar approach for all the different modelled hydrogeological cases in Sections 6.2 (temperate conditions) and 6.4 (glacial conditions) and the reactive-transport cases in Chapter 7 allowed for approximate estimations of the resulting pH in the water reaching canister positions (visually estimated from Figure 7-8 and Figure 7-14). These estimations together with estimations based on the simplified analytical evaluation in Appendix A are given in Table 8-1. It can be seen that when accounting for flow paths that meet the starting criteria, FPC, and EFPC, the flow-related transport resistances (F-factors) for all temperate cases are large, resulting in discharge of leachate water at canister positions that has become equilibrated with the rock minerals (to pH ~10.8 with the mineral assemblage considered). When accounting for all flow paths under temperate conditions (including those that do not meet the criteria), the discharging pH has not reached equilibrium values only for the cases when matrix minerals are not accounted for, or when assuming very limited available specific mineral surface (3 m^2/m^3 mineral). Under glacial conditions however, the discharging water at the canister position has a composition with maximum estimated pH values close to or above 11 in all cases. In several of the glacial cases very little or no pH reduction can safely be accounted for, based on these results.

It could be noted however, that for the case of a specific mineral surface area of 3,000 m^2/m^3 (and also 300 m^2/m^3) the visual estimation of pH in Figure 7-14 is difficult due to the steep profile for short distances (or low F-factors). Under these conditions the high estimated discharging pH values are due to very high flow-rates under the extreme (steady-state) conditions assumed when the glacial ice front is located right above the repository footprint (Ice front location II). The uncertainty of the hydraulic conditions prevailing under glacial conditions combined with the uncertainties related to the chemical state of the grouting at the time for the next glaciation is obviously large, and extremely pessimistic conditions have been assumed in these calculations. In addition, no dilution of the leachates by ambient groundwater due to mixing is accounted for in these calculations (cf. Sections 6.2.2 and 6.4.2 where the ADZ evolution is calculated based on dilution neglecting any chemical reactions). Note also that these estimations are based on the minimum calculated F-factor in each case, and that typical or median F-factors are considerably higher in all cases (which would result in shorter equilibration distances).

Table 8-1. Estimated maximum pH at canister positions after steady-state concentration profiles are developed along recharge pathways between the grouted region and the deposition holes for each case and particle release time. Pessimistic values after including paths not meeting starting criteria, FPC and EFPC are shown in parentheses. Assumed grouting radius is 5 m. Values calculated assuming 20 m grouting radius are included in brackets if they show considerably decreased F-factors. pH values are estimated visually from Figure 7-8 and Figure 7-14, and analytically from Equation A-22. Thus, dilution due to mixing is not considered in these estimations.

Case	Release time	Min F_r (y/m)	Corresponding fracture distance, in Figure 7-8 and Figure 7-14	Fracture only Figure 7-8 SA = 3,000 m^2/m^3	Fracture + Matrix Figure 7-14 SA = 3,000 m^2/m^3	Fracture + Matrix Figure 7-14 SA = 300 m^2/m^3	Fracture + Matrix Figure 7-14 SA = 3 m^2/m^3	Fracture + Matrix Eqn. A-22 SA = 3,000 m^2/m^3
			x (m)	pH	pH	pH	pH	pH[3]
200 m grouting	3000 BC	$5.496 \cdot 10^6$ ($9.164 \cdot 10^4$)	1,374 m[1] (23 m)	~10.72[1] (~11.75)	~10.8[1] (~10.75)	~10.78[1] (~10.72)	~10.72[1] (~11.75)	10.44 (10.45)
	2000 AD	$6.806 \cdot 10^6$ ($4.721 \cdot 10^6$)	1,710 m[1] (1,180 m[1])	~10.72[1]	~10.8[1]	~10.78[1]	~10.72[1]	10.44 (10.44)
	9000 AD	$2.392 \cdot 10^8$ ($5.083 \cdot 10^7$)	>2,000 m [1] (>2,000 m[1])	~10.72[1]	~10.8[1]	~10.78[1]	~10.72[1]	10.44 (10.44)
	Glacial II	$1.309 \cdot 10^4$ ($1.035 \cdot 10^4$)	3.3 m (2.6 m)	~12.35 (~12.4)	~10.9[2] (~11[2])	~11.8[2] (~11.9[2])	~12.3 (~12.35)	10.50 (10.52)
370 m grouting	3000 BC	$5.496 \cdot 10^6$ ($9.164 \cdot 10^4$)	1,374 m[1] (23 m)	~10.72[1] (~11.75)	~10.8[1] (~10.75)	~10.78[1] (~10.72)	~10.72[1] (~11.75)	10.44 (10.45)
	2000 AD	$6.806 \cdot 10^6$ ($4.721 \cdot 10^6$)	1,710 m[1] (1,180 m[1])	~10.72[1]	~10.8[1]	~10.78[1]	~10.72[1]	10.44 (10.44)
	9000 AD	$2.392 \cdot 10^8$ ($5.083 \cdot 10^7$)	>2,000 m [1] (>2,000 m[1])	~10.72[1]	~10.8[1]	~10.78[1]	~10.72[1]	10.44 (10.44)
	Glacial II	$6.622 \cdot 10^3$ [$6.590 \cdot 10^3$]	1.7 m [1.6 m]	~12.4 [~12.4]	~12.1[2] [~12.2[2]]	~12.3[2] [~12.3[2]]	~12.4 [~12.4]	10.58 [10.58]
370 m sealing	3000 BC	$1.570 \cdot 10^6$ ($2.218 \cdot 10^5$)	392 m[1] (55.5 m)	~10.72[1] (~10.80)	~10.8[1] (~10.78)	~10.78[1] (~10.75)	~10.72[1] (~10.90)	10.44 (10.44)
	2000 AD	$6.386 \cdot 10^6$ ($4.734 \cdot 10^6$)	1,596 m[1] (1,184 m[1])	~10.72[1]	~10.8[1]	~10.78[1]	~10.72[1]	10.44 (10.44)
	9000 AD	$1.899 \cdot 10^8$ ($1.294 \cdot 10^7$)	>2,000 m[1] (>2,000 m[1])	~10.72[1]	~10.8[1]	~10.78[1]	~10.72[1]	10.44 (10.44)
	Glacial II	$1.272 \cdot 10^4$ ($4.571 \cdot 10^3$)	3.2 m (1.1 m)	~12.35 (~12.4)	11.0[2] (~12.3[2])	~11.8[2] (~12.35[2])	~12.3 (12.4)	10.50 (10.65)

[1] Presumably pH is at equilibrium. Value is not visible in the figure since the fracture distance (x) corresponding to the F-factor is far outside the axis limits.

[2] Highly uncertain and approximate value due to difficulties in extracting data visually from the figures at their resolution (steep pH profile close to fracture inlet).

[3] Equilibrium pH differs from Figure 7-14 owing to differences in hydrogeochemical model and mode of aqueous phase activity calculation in CrunchFlow.

9 Discussion and conclusions

Source term definition

Although not really addressed in any detail in the modelling carried out here, definition of the likely source term is the logical starting point for any analysis of the potential impact of cement grouts on the repository EBS. From the moment a cement/aggregate mixture hydrates to form concrete, it is subject to attack (i.e. leaching), especially when the concrete is in contact with water. In simple terms, leaching may be viewed as equilibration between the cement minerals/gels/porewater and any percolating groundwaters. This is important to understand as it provides an estimate for the lifetime of the high pH conditions and an idea of the composition of the cement leachates which may impact the repository EBS.

Generally, in SAs, cement leaching is treated by means of a simplistic 'mixing tank' model (e.g. Berner 1990, Neall 1994) which, because it is usually accepted to be highly conservative, is still commonly applied today. However, detailed information on cement leaching does exist (e.g. Bros et al. 2005, Sugiyama et al. 2001) and the review of leaching models by Lagerblad (2001) provides the basis for a more mechanistic approach. Indeed, thermodynamic models of cement hydration have been developed recently (e.g. Lothenbach and Winnefeld 2006). These models can be incorporated into the modelling of grout hydration/leaching and the formation of the high-pH plume (e.g. Soler et al. 2011a, b). Overall, certain parameters define the leaching properties of cements, namely

- the amount and type of binder (OPC, pozzolan etc) – this defines the buffering capacity of the system in response to changed groundwater chemistry,
- the cement/water (c/w) ratio of the cement paste – related to the porosity of the cement paste which, in turn, controls diffusivity in the system (in effect, lower porosity, lower leach rate),
- the degree of hydration of the binder – as more cement is hydrated, the porosity decreases and so leach rate decreases,
- the homogeneity of the material.

Lagerblad (2001) noted that, after initial dissolution of primary phases (such as CH and C-S-H) and concomitant precipitation of secondary phases (such as calcite), concrete/cement degradation is diffusion controlled (e.g. case 2 in Figure 1-4). Variations of note include:

- cements with higher porosity (as in the case of grouts) leach at a much faster rate (e.g. case 1 in Figure 1-4),
- cements with a c/w ratio of 0.4 and less are leach resistant,
- the leach rate basically depends on the Ca gradient in the cement,
- the presence of HCO_3^-, Cl^- etc in the groundwater significantly increases leach rates, but high Ca content groundwaters (e.g. saline waters) will decrease the rates,
- groundwaters containing moderate levels of SO_4^{2-} (e.g. seawater) will probably induce blocking of cement porosity by the formation of ettringite and/or thaumasite,
- a carbonated 'shell' will develop on the cement surface which will reduce diffusion into the fresh cement beneath,
- this shell can be encouraged by ensuring that the cement paste is as homogenous and dense as possible (as is not the case in grouts),
- pozzolan cements or those made with with blast furnace slag (such as low alkali cements) will have a higher initial leach rate (due to greater porosity) but a lower long-term leach rate,
- pozzolan and blast furnace slag cements will produce a more resistant shell,
- physical aggradation can physically remove previously leached layers, so opening up a fresh surface of cement to further leaching.

Overall, however, the long-term stability of most grouts remains unclear (cf. comments in Smith 2004) due to the fact that a range of potential mechanisms have not yet been examined closely enough to provide a definitive picture. These include:

Carbonation: if carbonation of the cement grout does armour the cement against significant reaction with the groundwater, then the ADZ will probably be of a much more limited extent as diffusive transport will limit the movement of reactants. However, to date, no thorough assessment of the potential impact of carbonation of cements has been carried out. Normally, the reaction proceeds as groundwater HCO_3^- and CO_2 diffuse into the cement from the surface, so producing a reaction front characterised by a lower pH. At the front, groundwater HCO_3^-, CO_2 and cement Ca^{2+} will be at a minimum due to the low solubility of calcite and so free ions in the cement porewater will diffuse down the concentration gradient to the front. In saturated cements (e.g. in a grout), Ca^{2+} will diffuse much faster than HCO_3^-, so the front tends to be very near to the cement surface. In cements reacted in groundwaters with "High contents of Mg and/or HCO_3^- in the (*ground*)water leads to a more dense outer shell...." (Lagerblad 2005) of secondary precipitates on the cement which leads to more rapid sealing of the cement and reduced leaching.

To investigate carbonation processes more quantitatively in a cementitious repository in a sedimentary host rock, Pfingsten (2001) modelled data from small cement discs using a 2-D coupled hydraulic and reactive transport code (2D-MCOTAC). Although the physical parameters modelled are of no direct relevance to Forsmark, the approach is of interest and could be applied to scope potential changes to the grouts from carbonation reactions. This could be followed up by a short series of focussed laboratory experiments to assess carbonation on the actual grout formulation to be used in Forsmark. If necessary to increase confidence in the long-term behavior of the carbonated grout, support can be obtained from study of the natural cements in Jordan where evidence already exists of carbonation reactions (Clark et al. 1994).

Seismically induced degradation of grout: as noted in Chapter 2, the seismic characteristics of the Forsmark area has already been investigated and the data to provide a preliminary assessment of potential seismically induced grout degradation currently exists. Although an assessment of grout leaching in the Äspö URL is ongoing, it could be profitable to support these data with information from older grouted tunnels across the Fennoscandian Shield, especially where related seismic records exist. For a worse case scenario, examination of seismic degradation of grouts in tunnels in seismically active areas could also be useful. For example, the deep ore mines in South Africa where the great depths (currently, the deepest is the TauTona gold mine in Carltonville, SA, which reaches 3.9 km) mean that the shafts and tunnels are actually reaching into the zones of earthquake focus (Brandt and Saunders 2011, Reches 2006). With a typical deep-level mine recording about 1,000 (predominantly mining induced) seismic events each day (SAWDIS 2011), these sites offer the possibility of observing accelerated seismic degradation of the grouts not possible in other more 'normal' grouted tunnels.

Hydrogeological DFN model pathways

Performance measures for a set of flow paths are calculated assuming a steady-state flow field resulting in flow path properties representative for a "snap-shot" in time, neglecting dynamic flow-field changes. In the real system, not only would flow rates be expected to change with time but also the flow pattern would be different upon the transient changes in hydraulic head gradients. In extreme hydraulic situations, such as during a glacial ice front passage, recharge flow paths may become discharge flow paths and previously inactive parts of fractures with practically stagnant water may become important flow channels. The diversion of the flow into parts of fractures that previously have been inactive may also result from changes in the transmissivity distribution within the flow channels due to secondary mineral precipitation as a consequence of reactions with the alkaline leachates. This would imply that the mineral surfaces exposed to the alkaline leachates would change accordingly, minimising the gradual loss in pH buffering capacity with time. Neglecting these transient effects is therefore considered to be a cautious approach since it contributes to underestimating the pH buffering capacity.

The DFN model is based on a network of fractures comprising a combination of deterministic and stochastic fractures. Flow path properties are calculated based on a so-called particle tracking procedure, in which imaginary particles are released in the calculated flow field and performance measures are recorded along the paths taken within the fracture network. For a large number of released particles, this procedure yields a statistical distribution of F-factors that may be representative for the overall variability of this set of flow paths on that scale. However, caution should be taken in making far-reaching conclusions for the individual flow paths in that set, being a result of a stochastic

representation of fractures. The degree of uncertainty for the individual flow paths and their corresponding performance measures may be reduced by generating several realisations of the underlying stochastic fracture network, although this is time consuming.

The ECPM models for temperate and glacial conditions have been used also for evaluating ADZ evolution as a result of mixing of waters from different flow paths with different properties and pH. These results, where reactions with minerals along the paths are neglected, can thus be compared with the coupled hydrogeological DFN and reactive transport results presented in Chapter 8, where interaction with fracture and matrix minerals is included, but mixing/dilution is neglected.

Reactive-transport modelling

Large uncertainties exist in the assumed specific reactive surface area of minerals that participate in the buffering of pH along the flow paths. The reactive surface area ultimately determines the rate at which reactions occur, and thus the distance over which steady-state equilibrium conditions are attained. In the numerical models, the uncertainty is reflected in that a range of specific surfaces are used in order to evaluate the impact of this uncertainty on the extent of alkaline leachate ingress. The chosen range encompass relatively small specific surface areas as compared with the analysis in Appendix A. One could argue that this is a cautious approach in that it underestimates the actual surface reaction rates. However, the slow reaction rate also implies that precipitation of secondary minerals occur over a larger distance in the pores of the rock matrix, prolonging the time for pore clogging and ultimately sealing of the rock matrix porosity. A high reaction rate on the other hand implies that precipitation may occur in a thin shell effectively sealing the available buffering capacity in the bulk of the matrix minerals in a relatively short time. Precipitation of secondary minerals in the fractures may also induce a redistribution of the flow as discussed above, potentially resulting in a decrease in overall flow rates or even complete sealing of available flow paths. The optimum reaction rate, minimising both the extent of the ADZ ingress along the flow path and the time persistence of this mitigation would be somewhat intermediate. A cautious approach in the choice of reactive surface area is therefore difficult to define due to this ambiguous behaviour of the system.

In the simplified calculations in Appendix A, the pH buffering effect is shown to be governed by the approach to equilibrium of the primary mineral dissolution reaction (quartz in the simplified case studies) when the secondary minerals precipitate sufficiently fast to be considered in local equilibrium. It is furthermore found that the dissolution characteristics of quartz and the reactive transport of silica along a flowpath can be uniquely described by a dimensionless Damköhler number which combines the main hydrodynamic and material property parameters describing the system. The Damköhler number is essentially the ratio of the effective rate of primary mineral dissolution and the rate of advective transport of dissolved reaction products. Although the calculations are based on a number of simplifying assumptions, the relation between the various parameters comprising the Damköhler number and the physical process they describe suggests that general inferences can be drawn for more complex reaction systems concerning the spatial scaling of the pH profile along a flowpath in response to variations in these uncertain parameters (i.e. F-factor, far-from-equilibrium rate of primary mineral dissolution, reactive surface area, effective diffusivity).

Coupling of hydrogeological and reactive-transport models

In the case of the open-repository period (Section 6.1) and the periglacial period with permafrost (Section 6.3) no flow paths intersecting and connecting grouted volumes and canister positions in the repository were found in the modelling. Based on these results, any perturbation of the bentonite barrier function due to alkaline OPC leachates is deemed to be negligible during these periods, which therefore are excluded in the coupled hydrogeological and reactive-transport modelling evaluation. The results of the hydrogeological DFN models for temperate and glacial conditions (Sections 6.2 and 6.4 respectively) provided F-factors for complete individual flow paths intersecting and connecting grouted areas with canister positions in the repository. These results were coupled in Chapter 8 with steady-state results from the generic reactive-transport models using the F-factor as the coupling variable. The coupled results thus assume the most pessimistic hydraulic conditions (minimum F-factors are considered from steady-state flow field DFN calculations, and any mixing/dilution between different paths are neglected). These results should therefore be considered as pessimistic in particular with respect to the flow path properties and are therefore not appropriate for predicting actual discharging

pH at canister positions. They should rather be suited for pessimistic safety assessment purposes with the cautious assumptions in mind. Notable from the estimated results in Table 8-1 is that, even for these pessimistically chosen flow paths, equilibrium pH is reached in almost all temperate cases. The only exceptions during temperate conditions are for the assumption of a very small (3 m^2/m^3) specific mineral surface or a completely sealed matrix in combination with the inclusion of all flow paths (including those that do not meet the above mentioned criteria). During glacial conditions, the estimations in Table 8-1 may indicate that pH at the canister positions possibly exceed equilibrium conditions, for these rapid flow paths, although the pH values are highly uncertain. It may be noted that, based on the simplified analytical evaluation in Appendix A, equilibrium or close to equilibrium conditions are expected for all calculated F-factors in Table 8-1.

Host rock buffering capacity

In general, considering the likely changes to the flowpaths with time noted above, it would be useful focussing on the likely buffer capacity of the real system (rather than the 'artificial' mineralogy modelled here). In this case, it is suggested that the following could be carried out:

- alkaline leachate interaction with Forsmark site fracture material: this will define the likely secondary phases which will be produced *in situ*, so focussing future modelling effort on real phases,
- alkaline leachate interaction with Forsmark site rock matrix: as above, this will focus the modelling effort and will give a better indication of the likelihood of matrix sealing. In both cases, it would be useful beginning with a constantly buffered leachate solution to simplify data interpretation.

It is suggested that simple batch leaching experiments are carried out first to scope the likely reactions in the host rock and that these are followed by core infiltration experiments which more closely reflect true *in situ* conditions. Combining the information from these two sets of carefully designed experiments will allow an overall appreciation of the host rock buffer capacity and provide preliminary information on fracture sealing, rates of change in the fracture hydrology, mineral dissolution rates, surface areas of primary and secondary mineral phases and many other parameters which are currently open to speculation in the modelling effort.

Bentonite buffering capacity

Although not covered in any detail in the modelling to date, it is worth noting that a range of relevant experiments and natural analogue studies are currently ongoing. As such, it is worth maintaining a watching brief in this area and data mining relevant data as and when they are made available. Focus should, however, be on data produced by studies of reaction of compacted, massive bentonite, rather than dispersed material as this has less relevance to the *in situ* repository environment.

Final recommendation

The results from the modelling in this report suggests that OPC can be used at least down to 200 m depth taking into account hydrodynamic dispersion, dilution, buffering capacity, reactions and OPC durability. However, more studies are recommended to further decrease the level of uncertainty (see Table 9-1).

Table 9-1. Open actions for further consideration (with priority noted).

Process	Comment	Priority
Durability of grout	needs to be addressed to obtain a better idea of the likely degree of leachability of the cementitious material (and so the likely source term)	1
Alteration of host rock mineralogy:		
data-mine the existing literature in an exhaustive fashion to provide information of direct relevance to the Forsmark site	would allow a more detailed assessment of the likely impact of using grouts at Forsmark and could provide test cases for code testing	1
limited experimental examination of alkaline leachate/flow system mineralogy interaction (fresh water)	would allow a site-specific assessment of the likely impact of using grouts. Would also allow direct comparison with data-mining effort above	1
limited experimental examination of alkaline leachate/flow system mineralogy interaction (saline water)	as above, but lower priority as previous studies suggest alteration in saline waters is less than in fresh waters	2
mineralogical thermodynamic databases	probably the limiting factor to any detailed modelling of leachate/host rock interaction. SKB could consider participation in an international joint programme of fundamental laboratory research to produce the necessary data	3
Host rock hydrogeology	current coupled codes cannot model the detailed changes in flow systems as fractures begin to seal (following reaction of the rock with cement leachates) with any great precision. Questionable if the effort involved is worth the investment, certainly at the moment	3
Dilution of the alkaline leachate	data mining the existing extensive database could provide an indication of the applicability of this mechanism at Maqarin and so, by analogy, at Forsmark	2
Carbonation (groundwater HCO_3^{2-} and atmospheric CO_2 during ventilation)	would be worth conducting scoping calculations to assess if carbonation could play a significant role in minimising alkaline leachate production	1
Bentonite buffer:		
mineralogical thermodynamic databases	probably the limiting factor to any detailed modelling of leachate/bentonite interaction. Ongoing studies should improve this situation, but SKB could also consider participation in an international joint programme of fundamental laboratory research to produce the necessary data	3
focussed NA study	further work at the Khushaym Matruk site in Jordan, focussed on clay/alkaline fluid interaction would provide significant supporting data	2
leachate interaction with compacted bentonite	further laboratory work on leachate interaction with compacted bentonite buffer as too few studies have been carried out to date to be statistically meaningful. SKB should maintain a watching brief on ongoing studies	3

References

SKB's (Svensk Kärnbränslehantering AB) publications can be found at www.skb.se/publications.

Adenot F, 1992. Durabilité du béton: Caractérisation et modélisation des processus physiques et chimiques de dégradation du ciment. PhD thesis. Université d'Orléans. (In French.)

Adler M, 2001. Interaction of claystone and hyperalkaline solutions at 30°C: a combined experimental and modelling study. PhD thesis, University of Berne, Switzerland.

Adler M, Mäder U K, Waber H N, 2001. Core infiltration experiments investigating high pH alteration of low permeability argillaceous rock at 30°C. In Cidu R (ed). Water–rock interaction: proceedings of the Tenth International Symposium on Water–Rock Interaction WRI-10, Villasimius, Italy, 10–15 July 2001. Rotterdam: Balkema, 1299–1302.

Ahokas H, Hellä P, Ahokas T, Hansen J, Koskinen K, Lehtinen A, Koskinen L, Löfman J, Mészáros F, Partamies S, Pitkänen P, Sievänen U, Marcos N, Snellman M, Vieno T, 2006. Control of water inflow and use of cement in ONKALO after penetration of fracture zone R19. Posiva Working Report 2006-45, Posiva Oy, Finland.

Alexander W R (ed), 1992. A natural analogue study of the Maqarin hyperalkaline groundwaters. I. Source term description and thermodynamic database testing. Nagra Technical Report NTB 91-10, Nagra, Switzerland.

Alexander W R, 1995. Natural cements: How can they help us safely dispose of radioactive waste? Radwaste Magazine 2, 61–69.

Alexander W R, 2012. The impact of a (hyper)alkaline plume on (fractured) crystalline rock. In Cementitious materials in safety cases for geological repositories for radioactive waste: role, evolution and interactions: a workshop organised by the OECD/NEA Integration Group for the Safety Case and hosted by ONDRAF/NIRAS. NEA/RWM/R(2012)3/REV, NEA/OECD, 81–84.

Alexander W R, McKinley I G, 1999. The chemical basis of near-field containment in the Swiss high-level radioactive waste disposal concept. In Metcalfe R, Rochelle C A (eds). Chemical containment of wastes in the geosphere. Bath: The Geological Society. (Geological Society Special Publication No. 157), 47–69.

Alexander W R, Milodowski A E (eds), 2011. Cyprus Natural Analogue Project (CNAP). Phase II Final report. Posiva Working Report 2011-08, Posiva Oy, Finland.

Alexander W R, Möri A, 2003. Cementitious colloids: integration of laboratory, natural analogue and in situ field data. Geochimica et Cosmochimica Acta 67, Suppl. 11, 159–160.

Alexander W R, Neall F B, 2007. Assessment of potential perturbations to Posiva's SF repository at Olkiluoto from the ONKALO facility. Posiva Working Report 2007-35, Posiva Oy, Finland.

Alexander W R, Smellie J A T, 1998. Maqarin natural analogue project. ANDRA, CEA, Nagra, Nirex and SKB synthesis report on Phases I, II and III. Nagra Project Report NPB 98-08, Nagra, Switzerland.

Alexander W R, Gautschi A, Zuidema P, 1998. Thorough testing of performance assessment models: the necessary integration of in situ experiments, natural analogue studies, and laboratory work. In McKinley I G, McCombie C (eds). Scientific basis for nuclear waste management XXI: symposium held in Davos, Switzerland, 23 September–3 October 1997. Warrendale, PA: Materials Research Society. (Materials Research Society Symposium Proceedings 506), 1013–1014.

Alexander W R, McKinley I G, Arcilla C A, Takahashi Y, Kawamura H, Yamakawa M, Aoki K, 2008a. Hyperalkaline natural analogue potential in the Philippines. In Proceedings of the 2nd East Asia Forum on Radwaste Management (EAFORM) Conference, Tokyo, 20–23 October 2008.

Alexander W R, Arcilla C A, McKinley I G, Kawamura H, Takahashi Y, Aoki K, Miyoshi S, 2008b. A new natural analogue study of the interaction of low-alkali cement leachates and the bentonite buffer. In Lee W E (ed). Scientific basis for nuclear waste management XXXI: symposium held in Sheffield, United Kingdom, 16–21 September 2007. Warrendale, PA: Materials Research Society. (Materials Research Society Symposium Proceedings 1107), 493–500.

Alexander W R, Milodowski A E, Pitty A F (eds), 2012. Cyprus Natural Analogue Project (CNAP) Phase III Final report. Posiva Working Report 2011-77, Posiva Oy, Finland.

André M, Malmström M E, Neretnieks I, 2009. Specific surface area determinations on intact drillcores and evaluation of extrapolation methods for rock matrix surfaces. Journal of Contaminant Hydrology 110. doi: 10.1016/j.jconhyd.2009.05.003.

Arcilla C A, Pascua C S, Vargas E, Honrado M L L, Alexander W R, Namiki K, Fujii N, Yamakawa M, Sato T, McKinley I G, 2009. Reaction pathways for rising hyperalkaline groundwater in a bentonite mine in the Philippines. Geochimica et Cosmochimica Acta Supplement 73, A50.

Arenius M, Hansen J, Juhola P, Karttunen P, Koskinen K, Lehtinen A, Lyytinen T, Mattila J, Partamies S, Pitkänen P, Raivio P, Sievänen U, Vuorinen U, Vuorio M, 2008. R20 Summary report: the groundwater inflow management in ONKALO – the future strategy. Posiva Working Report 2008-44, Posiva Oy, Finland.

Atkinson A, 1985. The time-dependence of pH within a repository for radioactive waste disposal. Report AERE-R11777, United Kingdom Atomic Energy Authority.

Balay S, Gropp W D, Curfman McInnes L, Smith B F, 1997. Efficient management of parallelism in object-oriented numerical software libraries. In Arge E, Bruaset A M, Langtangen H P (eds). Modern software tools for scientific computing. Boston, MA: Birkhäuser, 163–202.

Bateman K, Coombs P, Noy D J, Pearce J M, Wetton P D, 2001a. Nagra/Nirex/SKB column experiments: Fluid chemical and mineralogical studies, Phase II. Report WE/99/5, British Geological Survey.

Bateman K, Coombs P, Pearce J M, Wetton P D, 2001b. Nagra/Nirex/SKB column experiments: Fluid chemical and mineralogical studies. Report WE/95/26, British Geological Survey.

Bauer A, Berger G, 1998. Kaolinite and smectite dissolution rate in high molar KOH solutions at 35° and 80°C. Applied Geochemistry 13, 905–916.

Bechtel/Parsons Brinckerhoff, 2005. Water intrusion in the I-93 tunnels: causes and cures. Bechtel Corporation/Parsons Brinckerhoff Joint Venture report to the Massachusetts Turnpike Authority. Bechtel Corporation.

Benbow S, Robinson P, Savage D, 2002. Buffering capacity of pH in backfill. SKI Report 02:39, Statens kärnkraftinspektion (Swedish Nuclear Power Inspectorate).

Berner U, 1987. Modelling porewater chemistry in hydrated cement. In Bates J K, Seefeldt W B (eds). Scientific basis for nuclear waste management X: symposium held in Boston, Massachusetts, USA, 1–4 December 1986. Pittsburgh, PA: Materials Research Society. (Materials Research Society Symposium Proceedings 84), 319–330.

Berner U, 1990. A thermodynamic description of the evolution of pore water chemistry and uranium speciation during degradation of cement. PSI-Bericht 62, Paul Scherrer Institute, Switzerland.

Bérubé M-A, Choquette M, Locat J, 1990. Effects of lime on common soil and rock forming minerals. Applied Clay Science 5, 145–163.

Blanc P, Lassin A, Piantone P, 2007. THERMODDEM: a thermodynamic database for modelling the alteration of waste minerals. Orléans, France: BRGM. Available at: http://thermoddem.brgm.fr/index.asp?langue=GB

Bodén A, Sievänen U (eds), 2006. Low-pH injection grout for deep repositories. Summary report from a co-operation project between NUMO (Japan), Posiva (Finland) and SKB (Sweden). Posiva Working Report 2005-24, Posiva Oy, Finland.

Bradbury M H, Baeyens B, 2003. Near-field sorption data bases for compacted MX-80 bentonite for performance assessment of a high-level radioactive waste repository in Opalinus clay host rock. Nagra Technical Report NTB 02-18, Nagra, Switzerland.

Brandt M B C, Saunders I, 2011. New regional moment tensors in South Africa. Seismological Research Letters 82, 69–80.

Brantberger M, Janson T, 2009. Underground design Forsmark, Layout D2. Grouting. SKB R-08-114, Svensk Kärnbränslehantering AB.

Brantley S L, Kubicki J D, White A F (eds), 2008. Kinetics of water–rock interaction. New York: Springer Science.

Bros R, Kanai Y, Okusawa K, Seki Y, Suzuki M, Watanabe Y, 2005. Immersion experiment of commercial concrete in groundwater (Kanamaru, Japan). In AGU 2005 Fall Meeting abstracts, H21B-1330. Washington, DC: American Geophysical Union.

Brown P W, Taylor H F W, 1999. The role of ettringite in external sulfate attack. In Marchand J, Skalny J P (eds), Materials science of concrete, Special volume: Sulfate attack mechanisms. Westerville, OH: The American Ceramic Society, 73–98.

Brydsten L, Strömgren M, 2010. A coupled regolith-lake development model applied to the Forsmark site. SKB TR-10-56, Svensk Kärnbränslehantering AB.

Byegård J, Selnert E, Tullborg E-L, 2008. Bedrock transport properties. Data evaluation and retardation model. Site descriptive modelling, SDM-Site Forsmark. SKB R-08-98, Svensk Kärnbränslehantering AB.

Cama J, Dávila M G, Soler J M, 2012. Experimental study of the interaction between low-pH grout and gneiss from ONKALO. Posiva Working Report 2012-02, Posiva Oy, Finland.

Cassagnabère A, Parneix J C, Sammartino S, Griffault L, Maeder U, Milodowski A E, 2001. Mineralogical evolution of bituminous marl adjacent to an alkaline water conducting feature at the Maqarin analogue site. In Cidu R (ed). Water–rock interaction: proceedings of the Tenth International Symposium on Water–Rock Interaction WRI-10, Villasimius, Italy, 10–15 July 2001. Rotterdam: Balkema, 367–370.

Chermak J A, 1992. Low temperature experimental investigation of the effect of high pH NaOH solutions on the Opalinus shale, Switzerland. Clays and Clay Minerals 40, 650–658.

Chermak J A, 1993. Low temperature experimental investigation of the effect of high pH KOH solutions on the Opalinus shale, Switzerland. Clays and Clay Minerals 41, 365–372.

Claesson L, Skelton A, Graham C, Dietl C, Mörth M, Torssander P, Kockum I, 2004. Hydrogeochemical changes before and after a major earthquake. Geology 32, 641–644.

Clark I D, Dayal R, Khoury H N, 1994. The Maqarin (Jordan) natural analogue for ^{14}C attenuation in cementitious barriers. Waste Management 14, 467–477.

Crawford J, 2008. Bedrock transport properties Forsmark. Site descriptive modelling, SDM-Site Forsmark. SKB R-08-48, Svensk Kärnbränslehantering AB.

Crawford J, 2010. Bedrock K_d data and uncertainty assessment for application in SR-Site geosphere transport calculations. SKB R-10-48, Svensk Kärnbränslehantering AB.

Crawford J, Sidborn M, 2009. Bedrock transport properties Laxemar. Site descriptive modelling, SDM-Site Laxemar. SKB R-08-94, Svensk Kärnbränslehantering AB.

Cronstrand P, 2007. Modelling the long-time stability of the engineered barriers of SFR with respect to climate changes. SKB R-07-51, Svensk Kärnbränslehantering AB.

Degnan P, Milodowski A E, et al. 2011. Tectonic setting, geology and hydrogeology of Maqarin. In Pitty A F, Alexander W R (eds). A natural analogue study of cement buffered, hyperalkaline groundwaters and their interaction with a repository host rock IV: an examination of the Khushaym Matruk (central Jordan) and Maqarin (northern Jordan) sites. Moor Row, UK: NDA.

Diamond S, White J L, Dolch W L, 1963. Transformation of clay minerals by calcium hydroxide attack. Clays and Clay Minerals 12, 359–379.

Duerden S L, 1992. Review of the interactions between bentonite and cement. Report DOE/HMIP/RR/92/031, Department of the Environment, Her Majesty's Inspectorate of Pollution.

ECOCLAY, 2005. ECOCLAY II: effects of cement on clay barrier performance – Phase II. Final report. EUR 21921 EN, European Commission.

Ekman M, 1996. A consistent map of the postglacial uplift of Fennoscandia. Terra Nova 8, 158–165.

Emmelin A, Brantberger M, Eriksson M, Gustafson G, Stille H, 2007. Rock grouting. Current competence and development for the final repository. SKB R-07-30, Svensk Kärnbränslehantering AB.

Ewart F T, Sharland S M, Tasker P W, 1985. The chemistry of the near-field environment. In Werme L O (ed). Scientific basis for nuclear waste management IX: symposium held in Stockholm, Sweden, 9–11 September 1985. Pittsburgh, PA: Materials Research Society. (Materials Research Society Symposium Proceedings 50), 539–546.

Fogler H S, 1992. Elements of chemical reaction engineering. 2nd ed. Englewood Cliffs, NJ: Prentice Hall.

Follin S, 2008. Bedrock hydrogeology Forsmark. Site descriptive modelling, SDM-Site Forsmark. SKB R-08-95, Svensk Kärnbränslehantering AB.

Follin S, Stigsson M, Svensson U, 2005. Regional hydrogeological simulations for Forsmark – numerical modelling using DarcyTools. Preliminary site description Forsmark area – version 1.2. SKB R-05-60, Svensk Kärnbränslehantering AB.

Follin S, Levén J, Hartley L, Jackson P, Joyce S, Roberts D, Swift B, 2007. Hydrogeological characterisation and modelling of deformation zones and fracture domains, Forsmark modelling stage 2.2. SKB R-07-48, Svensk Kärnbränslehantering AB.

Fransson Å, 2008. Grouting design based on characterization of the fractured rock. Presentation and demonstration of a methodology. SKB R-08-127, Svensk Kärnbränslehantering AB.

Fälth B, Hökmark H, Munier R, 2010. Effects of large earthquakes on a KBS-3 repository. Evaluation of modelling results and their implications for layout and design. SKB TR-08-11, Svensk Kärnbränslehantering AB.

Galíndez J M, Molinero J, 2010. Assessment of the long-term stability of cementitious barriers of radioactive waste repositories by using digital-image-based microstructure generation and reactive transport modelling. Cement and Concrete Research 40, 1278–1289.

Gaucher E, Tournassat C, Nowak C, 2005. Modelling the geochemical evolution of the multi-barrier system of the Silo of the SFR repository. Final report. SKB R-05-80, Svensk Kärnbränslehantering AB.

Gautier J-M, Oelkers E H, Schott J, 2001. Are quartz dissolution rates proportional to B.E.T. surface areas? Geochimica et Cosmochimica Acta 65, 1059–1070.

Grandia F, Galíndez J-M, Arcos D, Molinero J, 2010. Quantitative modelling of the degradation processes of cement grout. Project CEMMOD. SKB TR-10-25, Svensk Kärnbränslehantering AB.

Hallsworth C R, Knox R W O'B, 1999. BGS rock classification scheme. Volume 3: Classification of sediments and sedimentary rocks. Research Report RR 99-03, British Geological Survey.

Hammond G E, Lichtner P C, 2010. Field-scale model for the natural attenuation of uranium at the Hanford 300 Area using high-performance computing. Water Resources Research 46. doi: 10.1029/2009WR008819.

Hammond G, Lichtner P, Lu C, 2007. Subsurface multiphase flow and multicomponent reactive transport modeling using high-performance computing. Journal of Physics: Conference Series 78, 012025. doi: 10.1088/1742-6596/78/1/012025.

Hedenström A, Sohlenius G, Strömgren M, Brydsten L, Nyman H, 2008. Depth and stratigraphy of regolith at Forsmark. Site desprictive modelling, SDM-Site Forsmark. SKB R-08-07, Svensk Kärnbränslehantering AB.

Heikola T, 2008. Dynamic leach testing of low- and medium-pH injection grouts to be used in deep repositories. Cementitious materials in deep geological repositories. Posiva Working Report 2008-92, Posiva Oy, Finland.

Helgeson H C, 1969. Thermodynamics of hydrothermal systems at elevated temperatures and pressures. American Journal of Science 267, 729–804.

Helgeson H C, Kirkham D H, Flowers G C, 1981. Theoretical prediction of the thermodynamic behavior of aqueous electrolytes by high pressures and temperatures: IV. Calculation of activity coefficients, osmotic coefficients, and apparent molal and standard and relative partial molal properties to 600°C and 5 KB. American Journal of Science 281, 1249–1516.

Hobbs D W, 2003. Thaumasite sulfate attack in field and laboratory concretes: implications for specifications. Cement and Concrete Composites 25, 1195–1202.

Hodgkinson D P, Robinson P C, 1987. Nirex near-surface repository project. Preliminary radiological assessment: Summary. Nirex Safety Studies Report NSS/RA100, UK Nirex.

Holgersson S, Albinsson Y, Engkvist I, Rochelle C, Pierce J, 1998. Interactions of cement pore fluids with host rock and the effects on HTO, Na and Cs diffusion. Radiochimica Acta 82, 197–203.

Holt E, 2008. Durability of low pH injection grout. A literature survey. Posiva Working Report 2007-57, Posiva Oy, Finland.

Huertas F J, Caballero E, Jiménez de Cisneros C, Huertas F, Linares J, 2001. Kinetics of montmorillonite dissolution in granitic solutions. Applied Geochemistry 16, 397–407.

Idiart A E, López C M, Carol I, 2011. Chemo-mechanical analysis of concrete cracking and degradation due to external sulfate attack: a meso-scale model. Cement and Concrete Composites 33, 411–423.

JAEA, 2007. Second progress report on research and development for TRU waste disposal in Japan: repository design, safety assessment and means of implementation in the generic phase. JAEA-Review 2007-010, Japan Atomic Energy Agency.

Joyce S, Simpson T, Hartley L, Applegate D, Hoek J, Swan D, Marsic N, Follin S, 2010. Groundwater flow modelling of periods with temperate climate conditions – Forsmark. SKB R-09-20, Svensk Kärnbränslehantering AB.

Jull S P, Lees T P, 1990. Studies of historic concrete: final report. EUR 12972 EN, European Commission.

Kamei G, Alexander W R, Smellie J A T, 2005. Overview of the Maqarin Natural Analogue Project: results from the Phase I to III. JNC TN8400 2005-005, Japan Nuclear Cycle Development Institute. (In Japanese.)

Kamei G, Alexander W R, Clark I D, Degnan P, Elie M, Khoury H, Milodowski A E, Pitty A F, Salameh E, Smellie J A T, 2010. Natural analogues of cement: overview of the unique systems in Jordan. In Proceeding of the 13th International Conference on Environmental Remediation and Radioactive Waste Management, Tsukuba, Japan, 3–7 October 2010, Volume 2, 141–147. doi: 10.1115/ICEM2010-40063.

Karlsson F, Lindgren M, Skagius K, Wiborgh M, Engkvist I, 1999. Evolution of geochemical conditions in SFL 3-5. SKB R-99-15, Svensk Kärnbränslehantering AB.

Karnland O, Muurinen A, Karlsson F, 2003. Bentonite swelling pressure in NaCl solutions – Experimentally determined data and model calculations. In Alonso E E, Ledesma A (eds). Advances in understanding engineered clay barriers: proceedings of the International Symposium on Large Scale Field Tests in Granite, Barcelona, Spain, 12–14 November 2003. Leiden: Balkema, 241–256.

Karnland O, Nilsson U, Olsson S, Sellin P, 2004. Experimental study on changes of bentonite mineralogy and physical properties as a result of exposure to high pH solutions. In Metcalfe R, Walker C (eds). Proceedings of the International Workshop on Bentonite–Cement Interaction in Repository Environments, Tokyo, 14–16 April 2004. NUMO-TR-04-05, Nuclear Waste Management Organization of Japan (NUMO), A3-42–A3-46.

Karnland O, Olsson S, Nilsson U, Sellin P, 2007. Experimentally determined swelling pressures and geochemical interactions of compacted Wyoming bentonite with highly alkaline solutions. Physics and Chemistry of the Earth, Parts A/B/C 32, 275–286.

Kawano M, Tomita K, 1997. Experimental study on the formation of zeolites from obsidian by interaction with NaOH and KOH solutions at 150 and 200°C. Clays and Clay Minerals 45, 365–377.

Kipp K L, 1997. Guide to the revised heat and solute transport simulator: HST3D – Version 2. Water-Resources Investigations Report 97-4157, U.S. Geological Survey, Denver, Colorado.

Knight W C, 1898. Bentonite. Engineering and Mining Journal 66, 491.

Kuwahara Y, 2008. In situ observations of muscovite dissolution under alkaline conditions at 25–50 C by AFM with an air/fluid heater system. American Mineralogist 93, 1028–1033.

Lagerblad B, 2001. Leaching performance of concrete based on studies of samples from old concrete constructions. SKB TR-01-27, Svensk Kärnbränslehantering AB.

Lagerblad B, 2005. Mechanism and mode of carbonation of cementitious materials. In Book of abstracts, International Workshop on mechanisms and modelling of waste/cement interactions, Meiringen, Switzerland, 8–12 May 2005. Dübendorf, Switzerland: EMPA.

Lagerblad B, Trägårdh J, 1995. Conceptual model for concrete long time degradation in a deep nuclear waste repository. SKB TR 95-21, Svensk Kärnbränslehantering AB.

Laine H, Karttunen P, 2010. Long-term stability of bentonite. A literature review. Posiva Working Report 2010-53, Posiva Oy, Finland.

Lambeck K, Purcell A, 2003. Glacial rebound and crustal stress in Finland. Posiva 2003-10, Posiva Oy, Finland.

La Pointe P, Hermanson J, 2002. Estimation of rock movements due to future earthquakes at four candidate sites for a spent fuel repository in Finland. Posiva Report 2002-02, Posiva Oy, Finland.

Lasaga A C, 1981. Rate laws in chemical reactions. In Lasaga A C, Kirkpatrick R J (eds). Kinetics of geochemical processes. Blacksburg: Mineralogical Society of America. (Reviews in Mineralogy 8), 135–169.

Lasaga A C, 1984. Chemical kinetics of water–rock interactions. Journal of Geophysical Research 89, 4009–4025.

Le Bellégo C, Pijaudier-Cabot G, Gérard B, Dubé J-F, Molez L, 2003. Coupled mechanical and chemical damage in calcium leached cementitious structures. Journal of Engineering Mechanics 129, 333–341.

Le Bescop P, Solet C, 2006. External sulphate attack by ground water. Experimental study on CEM I cement pastes. Revue Européenne de Génie Civil 10, 1127–1145.

Lee S-T, Park D-W, Ann K-Y, 2008. Mitigating effect of chloride ions on sulfate attack of cement mortars with or without silica fume. Canadian Journal of Civil Engineering 35, 1210–1220.

Lehikoinen J, 2004. Cement–bentonite interaction issues, buffering capacity of bentonite. In Metcalfe R, Walker C (eds). Proceedings of the International Workshop on Bentonite–Cement Interaction in Repository Environments. Posiva Working Report 2004-25, Posiva Oy, Finland, 137–144.

Levenspiel O, 1972. Chemical reaction engineering. 2nd ed. New York: Wiley.

Lichtner P C, 2001. FLOTRAN user's manual: two-phase nonisothermal coupled thermal-hydrological-chemical (THC) reactive flow & transport code, version 1.0. Technical Report LA-UR-01-2349, Los Alamos National Laboratory, New Mexico.

Lichtner P C, Eikenberg J, 1994. Propagation of a hyperalkaline plume into the geological barrier surrounding a radioactive waste repository. Nagra Technical Report NTB 93-16, Nagra, Switzerland.

Lichtner P C, Hammond G E, 2012. Quick reference guide: PFLOTRAN 2.0 (LA-CC-09-047) Multiphase-multicomponent-multiscale massively parallel reactive transport code. Report LA-UR-06-7048, Los Alamos National Laboratory, New Mexico.

Lindborg T (ed), 2010. Landscape Forsmark – data, methodology and results for SR-Site. SKB TR-10-05, Svensk Kärnbränslehantering AB.

Linklater C M (ed), 1998. A natural analogue study of cement-buffered, hyperalkaline groundwaters and their interaction with a repository host rock. Phase II. Nirex Science Studies Report S/98/003, UK Nirex.

Lipson D S, McCray J E, Thyne G D, 2007. Using PHREEQC to simulate solute transport in fractured bedrock. Ground Water 45, 468–472.

Lothenbach B, Winnefeld F, 2006. Thermodynamic modelling of the hydration of Portland cement. Cement and Concrete Research 36, 209–226.

Lothenbach B, Matschei T, Möschner G, Glasser F P, 2008. Thermodynamic modelling of the effect of temperature on the hydration and porosity of Portland cement. Cement and Concrete Research 38, 1–18.

Luttge A, 2011. Experimental techniques for cement hydration studies. Studia Universitatis Babes-Bolyai, Geologia 56, 3–15.

Lönnqvist M, Hökmark H, 2010. Assessment of potential for glacially induced hydraulic jacking at different depths. SKB R-09-35, Svensk Kärnbränslehantering AB.

MacQuarrie K T B, Mayer K U, 2005. Reactive transport modeling in fractured rock: a state-of-the-science review. Earth-Science Reviews 72, 189–227.

Malinowski R, Garfinkel Y, 1991. Prehistory of concrete. Concrete International 13, 62–68.

McEwen T, Andersson J, 2009. Stable tectonic settings: designing site investigations to establish the tectonic basis for design and safety evaluation of geological repositories in Scandinavia. In Conner C B, Chapman N A, Conner L J (eds). Volcanic and tectonic hazard assessment for nuclear facilities. Cambridge: Cambridge University Press, 527–547.

McKinley I G, Alexander W R, 2009. Issues for coastal sites. In Connor C B, Chapman N A, Conner L J (eds). Volcanic and tectonic hazard assessment for nuclear facilities. Cambridge: Cambridge University Press, 509–526.

Metcalfe R, Walker C (eds), 2004. Proceedings of the International Workshop on Bentonite–Cement Interaction in Repository Environments, Tokyo, 14–16 April 2004. NUMO-TR-04-05, Nuclear Waste Management Organization of Japan (NUMO).

Miller W M, Alexander W R, Chapman N A, McKinley I G, Smellie J A T, 2000. Geological disposal of radioactive wastes and natural analogues: lessons from nature and archaeology. Amsterdam: Pergamon. (Waste management series 2).

Miller W M, Hooker P, Smellie J, Dalton J, Degnan P, Knight L, Nosek U, Ahonen L, Laciok A, Trotignon L, Wouters L, Hernán P, Vela A, 2006. Network to review natural analogue studies and their applications to repository safety assessment and public communication (NAnet). EUR 21919, European Commission.

Milodowski A E, Nancarrow P H A, Spiro B, 1989. A mineralogical and stable isotope study of natural analogues of ordinary Portland cement (OPC) and $CaO–SiO_2–H_2O$ (CSH) compounds. Safety Studies Report, NSS/R240, UK Nirex.

Milodowski A E, Khoury H N, Pearce J M, Hyslop E K, 1992. Results: source/sink terms. In Alexander W R (ed). A natural analogue study of the Maqarin hyperalkaline groundwaters. I. Source term description and thermodynamic database. Nagra Technical Report NTB 91-10, Nagra, Switzerland, 41–83.

Milodowski A E, Pearce J M, Hyslop E K, Hughes C R, Inglethorpe S D J, Strong G E, Wheal N, Mckenzie A B, Karnland O, Khoury H N, 1998a. Mineralogy and petrology. In Linklater C M (ed), A natural analogue study of analogue cement buffered, hyperalkaline groundwaters and their interaction with a repository host rock II Nirex Science Report, S-98-003. Harwell, UK: NDA, Chapter 6.

Milodowski A E, Hyslop E K, Pearce J M, Wetton P D, Kemp S J, Longworth G, Hodginson E, Hughes C R, 1998b. Mineralogy, petrology and geochemistry. In Smellie J A T (ed), MAQARIN natural analogue study: Phase III. SKB TR 98-04, Svensk Kärnbränslehantering AB.

Milodowski A E, Hyslop E K, Khoury H N, Hughes C R, Mader U, Griffault L Y, Trotignon L, 2001. Mineralogical alteration by hyperalkaline groundwaters in northern Jordan. In Cidu R (ed). Water–rock interaction: proceedings of the Tenth International Symposium on Water–Rock Interaction WRI-10, Villasimius, Italy, 10–15 July 2001. Rotterdam: Balkema,1347–1350.

Milodowski A E, Lacinska A, Wagnera D, 2009. A natural analogue study of CO_2-cement interaction: carbonate alteration of calcium silicate hydrate-bearing rocks from Northern Ireland. Report CR/09/096N, British Geological Survey.

Milodowski A E, Rochelle C A, Lacinska A, Wagner D, 2011. A natural analogue study of CO_2 – cement interaction: carbonation of calcium silicate hydrate-bearing rocks from Northern Ireland. Energy Procedia 4, 5235–5242.

Montori J, Saaltink M W, Soler J M, 2008. Reactive transport modeling of the effect of hyperalkaline solutions along a fracture at the ONKALO site. Posiva Working Report 2008-14, Posiva Oy, Finland.

Moody J B, 1976. Serpentinization: a review. Lithos 9, 125–138.

Moranville M, Kamali S, Guillon E, 2004. Physicochemical equilibria of cement-based materials in aggressive environments – experiment and modeling. Cement and Concrete Research 34, 1569–1578.

Moyce E B A, Rochelle C, Morris K, Milodowski A E, Chen X, Thornton S, Small J S, Shaw S, 2014. Rock alteration in alkaline cement waters over 15 years and its relevance to the geological disposal of nuclear waste. Applied Geochemistry, 50, 91–105. doi:10.1016/j.apgeochem.2014.08.003.

Mäder U K, Ekberg C, 2006. GTS/HPF Project: Geochemical evolution of porewater in the granitic shear zone AU-126 during 3 years of interaction with a hyperalkaline fluid, and its interpretation. Nagra Arbeitsbericht NAB 06-08, Nagra, Switzerland.

Mäder U K, Traber D, 2005. Reactive transport model of cement clay stone interaction with application to a HLW repository in Opalinus Clay. In Micheau N (ed). ECOCLAY-II: Effects of Cement on Clay Barrier Performance Phase II (Eurpean Union Project FIKW-CT-2000-00028), Final Report. External Document C.RP.ASCM.04.009, Andra, 283–289.

Mäder U K, Frieg B, Puigdomenech I, Decombarieu M, Yui M, 2004. Hyperalkaline cement leachate-rock interaction and radionuclide transport in a fractured host rock (HPF Project). In Oversby V M, Werme L O (eds). Scientific basis for nuclear waste management XXVII: symposium held in Kalmar, Sweden, 15–19 June 2003. Warrendale, PA: Materials Research Society. (Materials Research Society Symposium Proceedings 807), 861–866.

Mäder U K, Fierz T, Frieg B, Eikenberg J, Rüthi M, Albinsson Y, Möri A, Ekberg S, Stille P, 2006. Interaction of hyperalkaline fluid with fractured rock: field and laboratory experiments of the HPF project (Grimsel Test Site, Switzerland). Journal of Geochemical Exploration 90, 68–94.

NEA, 2012. Cementitious materials in safety cases for geological repositories for radioactive waste: role, evolution and interactions: a workshop organised by the OECD/NEA Integration Group for the Safety Case and hosted by ONDRAF/NIRAS. NEA/RWM/R(2012)3REV, Nuclear Energy Agency.

Nakayama S, Sakamoto Y, Yamaguchi T, Akai M, Tanaka T, Sato T, Iida Y, 2004. Dissolution of montmorillonite in compacted bentonite by highly alkaline aqueous solutions and diffusivity of hydroxide ions. Applied Clay Science 27, 53–65.

Neal C, Shand P, 2002. Spring and surface water quality of the Cyprus ophiolites. Hydrology and Earth System Sciences 6, 797–817.

Neal C, Stanger G, 1983. Hydrogen generation from mantle source rocks in Oman. Earth and Planetary Science Letters 66, 315–320.

Neall F B, 1994. Modelling of the near-field chemistry of the SMA repository at the Wellenberg site: **:** application of the extended cement degradation model. Nagra Technical Report NTB 94-03, Nagra, Switzerland.

Neall F B, Johnson L (eds), 2006. Proceedings of the NUMO workshop on near-field processes (Tokyo, 7–9 December 2005). Nagra Project Report NPB 06-06, Nagra, Switzerland.

Neall F, Pastina B, Smith P, Gribi P, Snellman M, Johnson L, 2007. Safety assessment for a KBS-3H spent nuclear fuel repository at Olkiluoto. Complementary evaluations of safety report. Posiva Report 2007-10, Posiva Oy, Finland.

Nguyen V H, Colina H, Torrenti J M, Boulay C, Nedjar B, 2007. Chemo-mechanical coupling behaviour of leached concrete. Part I: Experimental results. Nuclear Engineering and Design 237, 2083–2089.

Nilsson A-C, Tullborg E-L, Smellie J, Gimeno M J, Gómez J, Auqué L, Sandström B, Pedersen K, 2011. SFR site investigation. Bedrock hydrogeochemistry. SKB R-11-06, Svensk Kärnbränslehantering AB.

Ogata A, Banks R B, 1961. A solution of the differential equation of longitudinal dispersion in porous media. USGS Professional Paper 411-A. U.S. Geological Survey, Denver, Colorado.

Orantie K, Kuosa H, 2008. Durability 2007. Injection grout investigations. Background description. Posiva Working Report 2008-54, Posiva Oy, Finland.

Palandri J L, Kharaka Y K, 2004. A compilation of rate parameters of water–mineral interaction kinetics for application to geochemical modeling. Open File Report 2004-1068, U.S. Geological Survey, Denver, Colorado.

Parkhomenko E I, 1967. Electrical properties of rocks. New York: Plenum Press. (Monographs in geoscience).

Parkhurst D L, Appelo C A J, 1999. User's guide to PHREEQC (version 2): a computer program for speciation, batch-reaction, one-dimensional transport, and inverse geochemical calculations. Water-Resources Investigations Report 99-4259, U.S. Geological Survey, Denver, Colorado.

Parkhurst D L, Kipp K L, Charlton S R, 2010. PHAST version 2 – A program for simulating groundwater flow, solute transport, and multicomponent geochemical reactions. U.S. Geological Survey Techniques and Methods 6–A35, U.S. Geological Survey, Denver, Colorado.

Pastina B, Hellä P, 2010. Models and data report 2010. Posiva 2010-01, Posiva Oy, Finland.

Pate S M, McKinley I G, Alexander W R, 1994. Use of natural analogue test cases to evaluate a new performance assessment TDB. Report EUR 15176 EN, European Commission.

Pearce J M, 2006. What can we learn from natural analogues? In Lombardi S, Altunina L K, Beaubien S E (eds) Advances in the geological storage of carbon dioxide: international approaches to reduce anthropogenic greenhouse gas emissions. Dordrecht: Springer. (NATO Science Series: IV: Earth and Environmental Sciences 65), 127–139.

Pfingsten W, 2001. Indications for self-sealing of a cementitious L/ILW repository. PSI Bericht 01-09, Paul Scherrer Institute, Switzerland.

Pfingsten W, Paris B, Soler J M, Mäder U K, 2006. Tracer and reactive transport modelling of the interaction between high-pH fluid and fractured rock: field and laboratory experiments. Journal of Geochemical Exploration 90, 95–113.

Piqué À, Grandia F, Sena C, Arcos D, Molinero J, Duro L, Bruno J, 2010. Conceptual and numerical modelling of radionuclide transport in near-surface systems at Forsmark. SR-Site Biosphere. SKB R-10-30, Svensk Kärnbränslehantering AB.

Pitty A F, Alexander W R (eds), 2011. A natural analogue study of cement buffered, hyperalkaline groundwaters and their interaction with a repository host rock IV: an examination of the Khushaym Matruk (central Jordan) and Maqarin (northern Jordan) sites. Bedrock Geosciences contractor's report for NDA-RWMD. NDA.

Posiva, 2012. Safety case for the disposal of spent nuclear fuel at Olkiluoto – Complementary considerations 2012. Posiva 2012-11, Posiva Oy, Finland.

Pruess K, Oldenburg C, Moridis G, 1999. TOUGH2 user's guide, version 2. Report LBNL-43134, Lawrence Berkeley National Laboratory, Berkeley, California.

Ramirez S, Parnieix J-C, 2005. The effect of high-pH cement pore waters on the mineral stability of Callovo-Oxfordian Clay. In ECOCLAY II: Effects of Cement on Clay Barrier Performance – Phase II. Final Report. CEC Report EUR 21921 EN, European Commission, Section 8.2.

Rassineux F, Griffault L Y, Smellie J A T, Trotignon L, Raynal J, Khoury H, Mercier F, 2001. Mineralogical evolution of clay-bearing rock during alkaline alteration (Khushaym Matruk, Central Jordan). In Cidu R (ed). Water–rock interaction: proceedings of the Tenth International Symposium on Water–Rock Interaction WRI-10, Villasimius, Italy, 10–15 July 2001. Rotterdam: Balkema, 1363–1366.

Rautio T, 2005. Core drilling of boreholes ONK-KR1, ONK-KR2, ONK-KR3, ONKKR4 and ONK-PVA1 in ONKALO at Olkiluoto 2005. Posiva Working Report 2005-66, Posiva Oy, Finland.

Reches Z, 2006. Building a Natural Earthquake Laboratory at Focal Depth (DAFSAM-NELSAM Project, South Africa). Scientific Drilling 3, 30–33.

Reiman M, Pöllänen J, Väisäsvaara J, 2006. Flow measurements in ONKALO at Olkiluoto. Probe holes and ONK-KR1 – ONK-KR4, ONK-PVA1 and ONK-YPPL18. Posiva Working Report 2006-65, Posiva Oy, Finland.

Rhén I, Follin S, Hermanson J, 2003. Hydrological Site Descriptive Model – a strategy for its development during Site Investigations. SKB R-03-08, Svensk Kärnbränslehantering AB.

Romer M, Holzer L, Pfiffner M, 2003. Swiss tunnel structures: concrete damage by formation of thaumasite. Cement and Concrete Composites 25, 1111–1117.

Rowe G L, Brantley S L, 1993. Estimation of the dissolution rates of andesitic glass, plagioclase and pyroxene in a flank aquifer of Poás Volcano, Costa Rica. Chemical Geology 105, 71–87.

Rozalen M, Huertas F J, Brady P V, 2009. Experimental study of the effect of pH and temperature on the kinetics of montmorillonite dissolution. Geochimica et Cosmochimica Acta 73, 3752–3766.

Saaltink M W, Carrera J, Ayora C, 2001. On the behavior of approaches to simulate reactive transport. Journal of Contaminant Hydrology 48, 213–235.

Salas J, Gimeno M J, Auqué L F, Molinero J, Gómez J, Juárez I, 2010. SR-Site – hydrogeochemical evolution of the Forsmark site. SKB TR-10-58, Svensk Kärnbränslehantering AB.

Sandström B, Stephens M, 2009. Mineralogy, geochemistry, porosity and redox properties of rocks from Forsmark. Compilation of data from the regional model volume for SR-Site. SKB R-09-51, Svensk Kärnbränslehantering AB.

Sandström B, Tullborg E-L, Smellie J, MacKenzie A B, Suksi J, 2008. Fracture mineralogy of the Forsmark site. SDM-Site Forsmark. SKB R-08-102, Svensk Kärnbränslehantering AB.

Santhanam M, Cohen M D, Olek J, 2002. Mechanism of sulfate attack: a fresh look. Part 1: Summary of experimental results. Cement and Concrete Research 32, 915–921.

Sato T, Kuroda M, Yokoyama S, Tsutsui M, Fukushi K, Tanaka T, Nakayama S, 2004. Dissolution mechanism and kinetics of smectite under alkaline conditions. In Metcalfe R, Walker C (eds). Proceedings of the International Workshop on Bentonite–Cement Interaction in Repository Environments, Tokyo, 14–16 April 2004. NUMO-TR-04-05, Nuclear Waste Management Organization of Japan (NUMO), A3-38–A3-41.

Savage D, 1998. Zeolite occurrence, stability and behaviour. Implications for Performance assessment. In Smellie J A T (ed). Maqarin natural analogue study: Phase III. SKB TR 98-04, Svensk Kärnbränslehantering AB.

Savage D, 2006. Appendix B.4.4 Topic 4. In Neall F B, Johnson L (eds). Proceedings of the NUMO workshop on near-field processes (Tokyo, 7–9 December 2005). Nagra Project Report NPB 06-06, Nagra, Switzerland.

Savage D, 2011. A review of analogues of alkaline alteration with regard to long-term barrier performance. Mineralogical Magazine 75, 2401–2418.

Savage D, Rochelle C, Moore Y, Milodowski A E, Bateman K, Bailey D, Mihara M, 2001a. Experimental and modelling studies to assess cement–bentonite interaction. In Cidu R (ed). Water–rock interaction: proceedings of the Tenth International Symposium on Water–Rock Interaction WRI-10, Villasimius, Italy, 10–15 July 2001. Rotterdam: Balkema, 1379–1382.

Savage D, Rochelle C, Moore Y, Milodowski A, Bateman K, Bailey D, Mihara M, 2001b. Analcime reactions at 25–90°C in hyperalkaline fluids. Mineralogical Magazine 65, 571–587.

Savage D, Noy D, Mihara M, 2002. Modelling the interaction of bentonite with hyperalkaline fluids. Applied Geochemistry 17, 207–223.

Savage D, Walker C, Arthur R, Rochelle C, Oda C, Takase H, 2007. Alteration of bentonite by hyperalkaline fluids: a review of the role of secondary minerals. Physics and Chemistry of the Earth, Parts A/B/C 32, 287–297.

Savage D, Watson C, Wilson J, Benbow S, 2010a. Modelling support to the LCS experiment phase I. Contribution to the LCS partners' joint report. QRS-1378S-R2 Version 1.2, Quintessa Ltd., UK.

Savage D, Benbow S, Watson C, Takase H, Ono K, Oda C, Honda A, 2010b. Natural systems evidence for the alteration of clay under alkaline conditions: an example from Searles Lake, California. Applied Clay Science 47, 72–81.

Savage D, Soler J M, Yamaguchi K, Walker C, Honda A, Inagaki M, Watson C, Wilson J, Benbow S, Gaus I, Rueedi J, 2011. A comparative study of the modelling of cement hydration and cement–rock laboratory experiments. Applied Geochemistry 26, 1138–1152.

SAWDIS, 2012. South Africa Weather and Disaster Information Service. Available at: http://sawdis1.blogspot.ch/search/label/Earthquakes%20South%20Africa/ [28 May 2012].

Schmidt T, 2010. Sulfate attack and the role of internal carbonate on the formation of thaumasite. PhD thesis. École Polytechnique Fédérale de Lausanne, Switzerland.

Sellin P, Karlsson F, Werme L, Spahiu K, Puigdomenech I, 2003. Effect of pH on the safety of KBS-3 deep repository and the confidence in safety assessments. In Proceedings of a workshop on Qualification of Low pH Cement for a Geological Repository, Stockholm, 15–16 October 2003. Svensk Kärnbränslehantering AB.

Sena C, Salas J, Arcos D, 2010. Thermo-hydro-geochemical modelling of the bentonite buffer. LOT A2 experiment. SKB TR-10-65, Svensk Kärnbränslehantering AB.

Serco, 2011. CONNECTFLOW Release 10.3 Technical summary document. SA/ENV/CONNECTFLOW/15, Serco Assurance, UK.

Sidborn M, Sandström B, Tullborg E-L, Salas J, Maia F, Delos A, Molinero J, Hallbeck L, Pedersen K, 2010. SR-Site: Oxygen ingress in the rock at Forsmark during a glacial cycle. SKB TR-10-57, Svensk Kärnbränslehantering AB.

Sievänen U, Syrjänen P, Ranta-aho S, 2005. Injection grout for deep repositories – low-pH cementitious grout for larger fractures field testing in Finland, pilot tests. Posiva Working Report 2004-47, Posiva Oy, Finland.

Sievänen U, Raivio P, Vuorinen U, Hansen J, Norokallio J, Syrjänen P, 2006. Optimisation of technical properties of low pH cementitious injection grout. Laboratory tests and pilot field test 3. Posiva Working Report 2006-85, Posiva Oy, Finland.

Singer A, 1979. Palygorskite in sediments: detrital, diagenetic or neoformed — A critical review. Geologische Rundschau 68, 996–1008.

SKB, 2004. RETROCK Project. Treatment of geosphere retention phenomena in safety assessments. Scientific basis of retention processes and their implementation in safety assessment models (WP2). Work package 2 report of the RETROCK concerted action. SKB R-04-48, Svensk Kärnbränslehantering AB.

SKB, 2006. Initial state report for the safety assessment SR-Can. SKB TR-06-21, Svensk Kärnbränslehantering AB.

SKB, 2008. Safety analysis SFR 1. Long-term safety. SKB R-08-130, Svensk Kärnbränslehantering AB.

SKB, 2010a. Design, production and initial state of the closure. SKB TR-10-17, Svensk Kärnbränslehantering AB.

SKB, 2010b. Climate and climate-related issues for the safety assessment SR-Site. SKB TR-10-49, Svensk Kärnbränslehantering AB.

SKB, 2010c. Biosphere analyses for the safety assessment SR-Site – synthesis and summary of results. SKB TR-10-09, Svensk Kärnbränslehantering AB.

SKB, 2010d. Design, production and initial state of the buffer. SKB TR-10-15, Svensk Kärnbränslehantering AB.

SKB, 2011. Äspö Hard Rock Laboratory. Annual report 2010. SKB TR-11-10, Svensk Kärnbränslehantering AB.

SKI, 2005. Engineered barrier system - Long-term stability of buffer and backfill. Report from a workshop in Lund, Sweden, November 15–17, 2004. Synthesis and extended abstracts. SKI Report 2005-48, Statens kärnkraftinspekton (Swedish Nuclear Power Inspectorate).

Slunga R, 1990. Swedish earthquakes and fault movements (abstract). Geologiska Föreningen i Stockholm Förhandlingar 112, 326.

Smellie J A T (ed), 1998. Maqarin natural analogue study: Phase III, vol. I and II. SKB TR 98-04, Svensk Kärnbränslehantering AB.

Smellie J A T, Karlsson F, Alexander W R, 1997. Natural analogue studies: present status and performance assessment implications. Journal of Contaminant Hydrology 26, 3–17.

Smith B, 2004. What the DOE knows it doesn't know about grout: serious doubts remain about the durability of concrete proposed to immobilize high-level nuclear waste in the tank farms at the Savannah River site and other DOE sites. Institute for Energy and Environmental Research, Takoma Park, Maryland. Available at: http://ieer.org/wp/wp-content/uploads/downloads/reports/grout.pdf (see also http://www.ieer.org/reports/srs).

Smith P, Neall F, Snellman M, Pastina B, Hjerpe T, Nordman H, Johnson L, 2008. Safety assessment for a KBS-3H spent nuclear fuel repository at Olkiluoto. Summary report. SKB R-08-39, Svensk Kärnbränslehantering AB.

Soler J M, 2010. Reactive transport modeling of grout–rock interaction at the ONKALO site. Posiva Working Report 2010-73, Posiva Oy, Finland.

Soler J M, 2011. Reactive transport modeling of grout–water interaction in a fracture at the ONKALO site. Effect of different potential groundwater compositions. Posiva Working Report 2011-83, Posiva Oy, Finland.

Soler J M, Mäder U K, 2007. Mineralogical alteration and associated permeability changes induced by a high-pH plume: modeling of a granite core infiltration experiment. Applied Geochemistry 22, 17–29.

Soler J M, Mäder U K, 2010. Cement-rock interaction: infiltration of a high-pH solution into a fractured granite core. Geologica Acta 8, 221–233.

Soler J M, Pfingsten W, Paris B, Mäder U K, Frieg B, Neall F, Källvenius G, Yiu M, Yoshida Y, Shi P, Rochelle C A, Noy D J, 2006. Grimsel Test Site Investigation Phase V. HPF-experiment: Modelling report. Nagra Technical Report NTB 05-01, Nagra, Switzerland.

Soler J M, Vuorio M, Hautojärvi A, 2011a. Reactive transport modelling of the interaction between water and a cementitious grout in a fracture. Extended abstract. In EGU Conference, April 2011, Vienna, Austria.

Soler J M, Vuorio M, Hautojärvi A, 2011b. Reactive transport modeling of the interaction between water and a cementitious grout in a fractured rock. Application to ONKALO (Finland). Applied Geochemistry 26, 1115–1129.

Steadman J A, 1986. Archaeological concretes as analogues. In Côme B, Chapman N A (eds). Natural analogue working group, second meeting, Interlaken, June 1986. CEC Nuclear Science and Technology Report EUR 10671, Commission of the European Communities, 165–171.

Steefel C I, 2009. CrunchFlow. Software for modeling multicomponent reactive flow and transport. User's manual. Lawrence Berkeley National Laboratory, Berkeley, California.

Steefel C I, Lichtner P C, 1994. Diffusion and reaction in rock matrix bordering a hyperalkaline fluid-filled fracture. Geochimica et Cosmochimica Acta 58, 3595–3612.

Steefel C I, Lichtner P C, 1998. Multicomponent reactive transport in discrete fractures: I. Controls on reaction front geometry. Journal of Hydrology 209, 186–199.

Steefel C I, DePaolo D J, Lichtner P C, 2005. Reactive transport modeling: an essential tool and a new research approach for the Earth sciences. Earth and Planetary Science Letters 240, 539–558.

Stumm W, Morgan J, 1996. Aquatic chemistry: chemical equilibria and rates in natural waters. 3rd ed. New York: John Wiley & Sons.

Sugiyama D, Fujita T, Nakanishi K, 2001. Chemical alteration of cement material in a radioactive waste repository I – thermodynamic modelling for the dissolution and precipitation of CSH. CRIEPI Report T01007. Komae, Japan: CRIEPI. (In Japanese.)

Svensson U, Follin S, 2010. Groundwater flow modelling of the excavation and operational phases – Forsmark. SKB R-09-19, Svensk Kärnbränslehantering AB.

Svensson U, Ferry M, Kuylenstierna H-O, 2010. DarcyTools version 3.4 – Concepts, methods and equations. SKB R-07-38, Svensk Kärnbränslehantering AB.

Swanton S, Alexander W R, Berry J A, 2010. Review of the behaviour of colloids in the near field of a cementitious repository. Report to NDA RWMD. Serco/TAS/000475/01. Serco, UK.

Swedenborg S, Dahlström L-O, 2003. Rock mechanics effects of cement grouting in hard rock masses. In Johnsen L, Bruce D A, Byle M J, Grouting and ground treatment: proceedings of the Third International Conference, New Orleans, Louisiana, 10–12 February 2003. New York: American Society of Civil Engineers, 1089–1102.

Tajima T, Fujii K, Kubo H, Mihara M, 2003. Alteration of bentonite by hyperalkaline fluids. Geochimica et Cosmochimica Acta Supplement 67, 467.

Tang D H, Frind E O, Sudicky E A, 1981. Contaminant transport in fractured porous media: analytical solution for a single fracture. Water Resources Research 17, 555–564.

Techer I, Fourcade S, Elie M, Martinez L, Boulvais P, Claude C, Clauer N, Pagel M, Hamelin B, Lancelot J, 2004. Contribution des analogues naturels à la compréhension du comportement à long terme des milieux argileux vis-à-vis de la circulation de fluides hyper-alcalins: Etude du site de Khushaym Matruk en Jordanie Centrale-Géochimie Isotopique du Sr, C, O, datatio. FORPRO Report 2004/01 Rf. GdR FORPRO. (In French.)

Tester J W, Worley W G, Robinson B A, Grigsby C O, Feerer J L, 1994. Correlating quartz dissolution kinetics in pure water from 25 to 625°C. Geochimica et Cosmochimica Acta 58, 2407–2420.

Thiery M, Villain G, Dangla P, Platret G, 2007. Investigation of the carbonation front shape on cementitious materials: effects of the chemical kinetics. Cement and Concrete Research 37, 1047–1058.

Thomassin J H, Rassineux F, 1992. Ancient analogues of cement-based materials: stability of calcium silicate hydrates. Applied Geochemistry 7, 137–142.

Torres S M, Lynsdale C J, Swamy R N, Sharp J H, 2003. Thaumasite formation in limestone filler cement mortar under sulfate and chloride exposure. In International Seminar on the thaumasite form of sulfate attack of concrete, University of Sheffield, UK. Available at: http://www.shef.ac.uk/polopoly_fs/1.142966!/file/08.pdf

Trotignon L, Rose J, Khoury H, Milodowski A, Bienvenu P, Provitina O, Mercier F, Susini J, 2006. Rhenium migration at the Maqarin natural analogue site (Jordan). Radiochimica Acta 94, 755–761.

Vidstrand P, Follin S, Zugec N, 2010. Groundwater flow modelling of periods with periglacial and glacial climate conditions – Forsmark. SKB R-09-21, Svensk Kärnbränslehantering AB.

Vieno T, Lehikoinen J, Löfman J, Nordman H, Mészáros F, 2003. Assessment of disturbances caused by construction and operation of ONKALO. Posiva 2003-06, Posiva Oy, Finland.

Vuorinen U, Lehikoinen J, Luukkonen A, Ervanne H, 2003. Effects of salinity and high pH on crushed rock and bentonite – experimental work and modelling in 2001 and 2002. Posiva Working Report 2003-22, Posiva Oy, Finland.

Vuorinen U, Luukkonen A, Lehikoinen J, Ervanne H, 2004. Effects of saline alkaline attack on bentonite and crushed rock – experimental and modelling studies – ECOCLAY II. In Metcalfe R, Walker C (eds). Proceedings of the International Workshop on Bentonite–Cement Interaction in Repository Environments, Tokyo, 14–16 April 2004. NUMO-TR-04-05, Nuclear Waste Management Organization of Japan (NUMO), A3-47–A3-53.

Vuorinen U, Lehikoinen J, Luukkonen A, Ervanne H, 2006. Effects of salinity and high pH on crushed rock and bentonite – experimental work and modelling. Posiva Report 2006-01, Posiva Oy, Finland.

Wang L, Moors P, De Cannière P, 2005. Migration of an alkali plume in Boom Clay cores: a six years experiment. In Book of abstracts, International Workshop on mechanisms and modelling of waste/cement interactions, Meiringen, Switzerland, 8–12 May 2005. Dübendorf, Switzerland: EMPA.

Wang L, Jacques D, De Cannière P, 2010. Effects of an alkaline plume on the Boom Clay as a potential host formation for geological disposal of radioactive waste. External Report SCK•CEN-ER-28, SCK•CEN, Belgium.

Watson C, Hane K, Savage D, Benbow S, Cuevas J, Fernandez R, 2009. Reaction and diffusion of cementitious water in bentonite: results of "blind" modelling. Applied Clay Science 45, 54–69.

White A F, Brantley S L, 2003. The effect of time on the weathering of silicate minerals: why do weathering rates differ in the laboratory and field? Chemical Geology 202, 479–506.

White A F, Peterson M L, 1990. Role of surface area characterization in geochemical models. In Melchior R L, Bassett R (eds). Chemical modeling of aqueous systems II. Washington: American Chemical Society, 461–475.

Wieland E, Tits J, Bradbury M H, 2004. The potential effect of cementitious colloids on radionuclide mobilisation in a repository for radioactive waste. Applied Geochemistry 19, 119–135.

Winberg A, Andersson P, Byegård J, Poteri A, Cvetkovic V, Dershowitz W, Doe T, Hermanson J, Gómez-Hernández J J, Hautojärvi A, Billaux D, Tullborg E-L, Holton D, Meier P, Medina A, 2003. Final report of the TRUE Block Scale project. 4. Synthesis of flow, transport and retention in the block scale. SKB TR-02-16, Svensk Kärnbränslehantering AB.

Wolery T J, 1992. EQ3/6. A software package for geochemical modeling of aqueous systems. UCRL-MA-110662, Lawrence Livermore National Laboratory (LLNL).

Wolery T, Jove-Colon C, 2004. Qualification of thermodynamic data for geochemical modelling of mineral-water interactions in dilute systems. Report ANL-WIS-GS-000003 REV00, Bechtel SAIC Company, Las Vegas, NV.

Xu T, Pruess K, 2001. On fluid flow and mineral alteration in fractured caprock of magmatic hydrothermal systems. Journal of Geophysical Research 106, 2121–2138.

Xu T, Sonnenthal E, Spycher N, Pruess K, 2008. TOUGHREACT user's guide: a simulation program for non-isothermal multiphase reactive geochemical transport in variably saturated geologic media. Lawrence Berkeley National Laboratory, Berkeley, CA.

Yamaguchi T, Sakamoto Y, Akai M, Takazawa M, Tanaka T, Nakayama S, Sato T, 2004. Experimental study on dissolution of montmorillonite in compacted sand-bentonite mixture under Na-Cl-OH pore-water conditions. In Metcalfe R, Walker C (eds). Proceedings of the International Workshop on Bentonite–Cement Interaction in Repository Environments, Tokyo, 14–16 April 2004. NUMO-TR-04-05, Nuclear Waste Management Organization of Japan (NUMO), A3-54–A3-58.

Yamamoto T, Nishida T, Hironaga M, Suzuki S, Ueda H, 2008. Release of superplasticizers and other organic additives from altered cement. NUMO- TR-08-01, Nuclear Waste Management Organization of Japan (NUMO).

Yokozeki K, Watanabe K, Sakata N, Otsuki N, 2004. Modeling of leaching from cementitious materials used in underground environment. Applied Clay Science 26, 293–308.

Zevenberg C, Bradley J P, van Reeuwijk L P, Shyam A K, 1999. Clay formation during weathering of alkaline coal fly ash. In Proceedings of 1999 International Ash Utilisation Symposium. Centre for Applied Energy Research, University of Kentucky.

Zuber B, Marchand J, 2000. Modeling the deterioration of hydrated cement systems exposed to frost action: Part 1: Description of the mathematical model. Cement and Concrete Research 30, 1929–1939.

Öhman J, Follin S, 2010. Site investigation SFR. Hydrogeological modelling of SFR. Model version 0.2. SKB R-10-03, Svensk Kärnbränslehantering AB.

Appendix A

Simplified scoping calculations

The geochemical system studied in this report involves a complex set of mineral reactions and equilibria. In this appendix a simplified system is modelled with the purpose to gain insights and mechanistic understanding of the fundamental processes involved. The calculations and results in this appendix are therefore of important value in the interpretation of the main results and aid understanding of the more complex calculations in the main sections of the report.

Author: James Crawford

A1 Background and case definitions

It was understood from simplified reaction path calculations that hydroxyl promoted dissolution of quartz from the rock matrix combined with precipitation of a crystalline Ca-silicate secondary phase would likely buffer pH levels to somewhat less than the initial pH of OPC leachate, possibly mitigating some of the problems associated with high pH in the repository volume. Since there is an effectively unlimited amount of quartz in the rock matrix relative to the alkaline "carrying capacity" of the OPC leachate, this would suggest that propagation of a highly alkaline pH plume to repository level would be unlikely, all other things being equal.

If, however, a significant amount of precipitation occurs within the advective flow space this might reduce the transmissivity of the fracture and eventually seal off the fracture from subsequent advective flow. Although this would undoubtedly be favourable for mitigation of alkaline plume transport, no special consideration was given to this process in the modelling work by appealing to arguments of caution. In practice this meant that the flow velocity along the advective transport path was considered fixed even though the transport aperture could potentially decrease.

An unresolved question, however, was the extent to which precipitation of secondary mineral phases might reduce the matrix porosity in the immediate vicinity of fracture surfaces. Since the proposed secondary phase, gyrolite has a specific volume greater than the quartz which it replaces in the rock matrix, this process could conceivably reduce the accessible quartz reactive surface area and eventually allow breakthrough of the alkaline plume if matrix porosity were to be significantly reduced along much of the transport pathway. To address this issue, complementary reactive transport calculations of a simplified nature were performed where the impact of various simulation parameters were studied. As was the case for the detailed reactive transport calculations described in previous chapters, no additional credit was taken for dilution or attenuation of the alkaline plume at source or mixing neutralisation with non-affected advective groundwater streams along the advective transport path. Only neutralisation reactions involving simple 1D matrix diffusive mixing along the transport path and pH buffering via the quartz/gyrolite reaction mechanism were considered.

In order to simplify the calculations as much as possible, a very simple groundwater recipe was assumed to represent both the initial groundwater and the OPC affected groundwater. The composition of the initial groundwater was obtained by assuming equilibration of pure water with calcite and a fixed partial pressure of CO_2 of $10^{-3.5}$ atm giving a pH of 8.28. For the initial state of the rock matrix and fracture water, quartz equilibrium was additionally assumed. The OPC affected groundwater was obtained by imposing Portlandite equilibrium on the initial groundwater, giving a pH of 12.38. Calculations were made using the CrunchFlow program (Steefel 2009) which uses an extended Debye-Hückel aqueous phase activity model and a custom database with key reactions taken directly from the Yucca mountain database (ther_ympR4d.dat). To preserve internal consistency in the modelling work, all calculations were made assuming a temperature of 25°C. In order to control for numerical artefacts relating to discretisation, two non-reactive tracer components (A and B) were defined as an internal standard. The tracer concentrations were set at arbitrarily low levels in order to avoid influencing the aqueous phase activities. The composition of the initial groundwater in the aquifer and the infiltrating OPC-affected groundwater is given in Table A-1.

Table A-1. Chemical composition of simplified fracture/matrix groundwater and OPC-affected groundwater in SRTBC simulations. Groundwater compositions for RTTC cases are approximately the same although $SiO_{2\ (aq)}$ is absent. Component concentrations are given as total concentrations (mol/kg H_2O).

	Initial fracture & matrix porewater	OPC-affected infiltrate
pH	8.277	12.380
Ca^{2+}	$5.0142 \cdot 10^{-4}$	$1.6622 \cdot 10^{-2}$
HCO_3^-	$9.9057 \cdot 10^{-4}$	$8.2077 \cdot 10^{-6}$
$SiO_{2\ (aq)}$	$1.8119 \cdot 10^{-4}$	$1.0 \cdot 10^{-20}$
Tracer A	$1 \cdot 10^{-30}$	$1 \cdot 10^{-6}$
Tracer B	$1 \cdot 10^{-6}$	$1 \cdot 10^{-30}$
Ionic strength	0.001	0.045

Reactive transport simulations were made using the global implicit, one-step solver (GIMRT) available within CrunchFlow rather than using the solver based on operator splitting (OS3D) since the very small transport aperture would otherwise severely limit time stepsize by way of the Courant criterion and require unreasonably long simulation times. A Péclet number of 10 was chosen as being approximately representative of a customary amount of hydrodynamic dispersion (i.e. corresponding to a dispersion length equivalent to 10% of the flowpath length). Although an arbitrary choice, the use of a Péclet number of this magnitude tends to avoid many of the numerical issues associated with the simulation of advectively dominated flow systems. The physical parameters relevant to the simulations are detailed in Table A-2.

Two sets of simulations were performed:

- Reactive transport test case (RTTC) – neutralisation of alkaline pH plume by matrix diffusive mixing of initial and OPC-affected groundwater (calcite precipitation allowed although initially absent from aquifer).
- Simplified reactive transport base case (SRTBC) – neutralisation of alkaline pH plume by reactive dissolution of quartz coupled with gyrolite precipitation and matrix diffusive mixing (calcite and gyrolite precipitation allowed although initially absent from aquifer).

Table A-2. Physical parameters for simplified simulation cases.

Parameter	Description	Value	Units
L	flowpath length	100	m
δ_m	matrix depth	1.0	m
δ_t	transport aperture	$1 \cdot 10^{-4}$	m
ε_p	matrix porosity	0.001	-
t	matrix tortuosity	0.01	-
D_w	free solute diffusivity	$1 \cdot 10^{-9}$	m^2/s
D_e	effective diffusivity	$1 \cdot 10^{-14}$	m^2/s
F	F-factor	$4 \cdot 10^5$	y/m
v	fluid velocity	5	m/y
t_w	advective travel time	20	y
Pe	Peclet number	10	-
n_a	advective cells	100	-
n_d	matrix diffusive cells	31-61	-
$V_{m\ (calcite)}$	molar volume of calcite	36.934	cm^3/mol
$V_{m\ (SiO2)}$	molar volume of quartz	22.688	cm^3/mol
$V_{m\ (gyrolite)}$	molar volume of gyrolite	136.069	cm^3/mol

Since the amount of calcite precipitated was expected to be very low, the matrix porosity was considered fixed in the RTTC simulations. In the SRTBC simulations, on the other hand, the effective diffusivity was allowed to evolve as a function of the changing porosity of the rock matrix. To simplify the interpretation of results, no minerals were assumed to be initially present in the advective flowspace, even though calcite and secondary clay minerals are known to be present as fracture coatings in flow-bearing fractures at Forsmark site.

The simulated matrix depth was 1 m which was found to be sufficient to capture the main reactive transport phenomena without introducing spurious boundary effects and it is only the hypothetical, non-reactive tracer components which exhibit partial saturation effects at long simulation times. The choice of 1 m is somewhat arbitrary and selected partly to ensure that results should be comparable with simulations made by the other groups involved in the project. It should be noted that the choice of matrix depth is largely a modelling convenience to avoid unnecessarily top-heavy numerical calculations and does not reflect any physical limitation on the depth of connected porosity. As discussed in some detail in Crawford (2008) and Crawford and Sidborn (2009) there is compelling evidence to suggest that the rock matrix porosity is effectively unbounded.

There are a number of different ways of defining effective diffusivity in CrunchFlow. It can be fixed through the use of a constant tortuosity, definition of a constant formation factor, or definition of a cementation exponent for use with a power law expression (Archie's law). Since the use of a constant formation factor does not permit updating of the effective diffusivity, this option was not used. The power law expression used in CrunchFlow does not include a pre-factor to scale the effective diffusivity which makes it of limited usefulness in the current case owing to the dominant tortuosity/constrictivity effect on effective diffusivity in granitic media. In principle, it is possible to include a pre-factor by re-scaling the free component diffusivity, although for reasons of data transparency the most appropriate means of modelling the evolving effective diffusivity in this work was deemed to be through the use of a constant tortuosity factor. The effective matrix diffusivity is thus defined as:

$$D_e = \varepsilon_p \tau D_w \tag{A-1}$$

For the SRTBC cases where effective diffusivity was allowed to evolve along with matrix porosity, this gives a linear dependency between porosity and effective diffusivity. Although the linearity of this dependency could be questioned, it is considered sufficiently accurate for the scoping calculations presented in this appendix. The relation between formation factor (D_e/D_w) implied by Equation A-1 is shown in Figure A-1 together with some other relations reported in the literature for comparative purposes. The work by Soler (2010), also using CrunchFlow, assumed a cementation exponent of 2 and no pre-multiplier in 1D grout rock calculations (although other 2D calculations use Equation A-1). Also shown is the original Archie's law expression given by Parkhomenko (1967) for low porosity igneous rock, as well as an expression derived by Byegård et al. (2008) for Forsmark specific rock types. It is noted that the use of an Archie's law type expression for Forsmark site-specific rock has low predictive power for porosities on the order of 0.5% and lower, due to a dominant tortuosity-constrictivity effect (This is discussed in more detail in Crawford (2008)). The regression derived by Byegård et al. (2008), on the other hand, includes a number of data points for Vuggy granite with porosities ranging from 2–20% and seems to give a better fit at higher porosities than the power law expression from Parkhomenko (1967).

For the hydrodynamic and material property data specified in Table A-2, no matrix diffusion saturation effects are expected until ~80-90% breakthrough fraction of the non-reactive solute is achieved. The analytical solution for solute transport provided by Tang et al. (1981) can therefore be used to compare with the simulated solute breakthrough for recovery times up to at least 800 y for the assumed Peclét number of 10 (i.e. a dispersion length equal to 10% of flowpath length).

The dissolution of quartz was modelled using a standard rate law expression derived from transition state theory (TST) (Lasaga 1981, 1984) with far from equilibrium kinetic rates described using the expression given by Palandri and Kharaka (2004). At the reference temperature of 25°C, the resultant rate law for quartz dissolution is of the form:

$$R_m = \left(k_1 + k_2 a_{H^+}^{-0.5}\right) A_m \left(1 - \Omega\right) \tag{A-2}$$

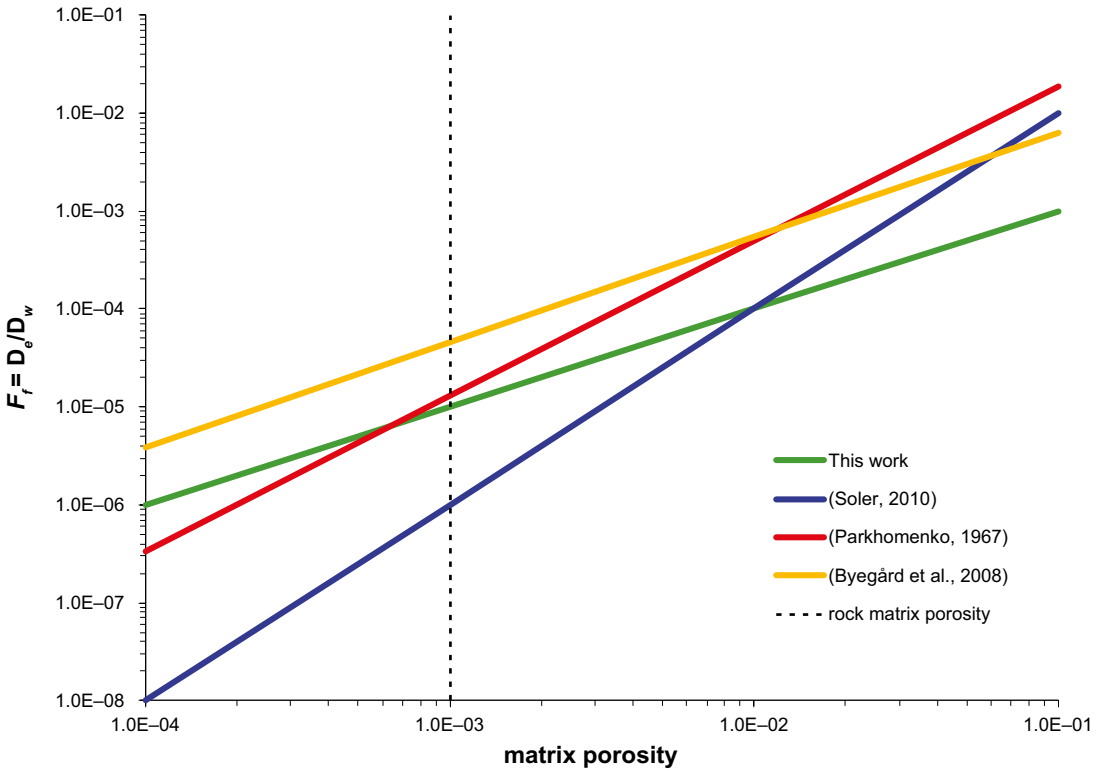

Figure A-1. *Variation of formation factor ($F_f = D_e/D_w$) as a function of rock matrix porosity. The green line (corresponding to Equation A-1) gives the linear relation between formation factor and porosity assumed in the calculations presented in this appendix. Other formation factor vs. porosity relations are plotted in the figure for comparative purposes.*

Where A_m is the mineral surface area per volume of porous medium (m^2/m^3), Ω is the ratio of the ion activity product and the equilibrium constant for the dissolution reaction, k_1 and k_2 are the far-from equilibrium kinetic rate constants given by Palandri and Kharaka (2004) and the term $a_{H^+}^{-0.5}$ accounts for the enhanced rate of dissolution (hydroxyl promoted) at alkaline pH levels. The pH-dependent, far from equilibrium rate of quartz dissolution is plotted in Figure A-2. It is noted that the kinetic dissolution rate predicted with this model is somewhat less than that predicted by some other models published in the literature (also plotted in Figure A-2 for comparative purposes). Compared to the other kinetic models, the Palandri and Kharaka expression would predict a slightly longer quartz equilibration distance along the advective flowpath, which for the overall purposes of the study might be considered a cautious assumption (all other things being equal). Given that quartz dissolution is the rate limiting process for the mineral dissolution/precipitation, it may also slightly under-predict the extent of secondary mineral precipitation in the immediate vicinity of the fracture surface.

The bulk surface area for undisturbed matrix rock was estimated in SR-Site (Crawford 2010) to be 0.018 m^2/g based on BET surface area measurements on intact monoliths reported by André et al. (2009). The initial volume fraction of quartz in the rock matrix was taken to be 34.6% which is the average volumetric quartz content of Forsmark metagranite (SKB rock code 101057). Assuming that the reactive surface area of quartz is roughly proportional to its volumetric fraction in the rock and based on a molar volume of 22.688 cm^3/mol, the surface area of quartz per unit volume of porous medium is estimated to be:

$$A_m = \frac{\phi_m A_{BET} M_w}{V_m} = \frac{0.346(0.018)60.084}{22.6880 \cdot 10^{-6}} \approx 1.65 \cdot 10^4 \ \mathrm{m^2/m^3} \qquad \text{(A-3)}$$

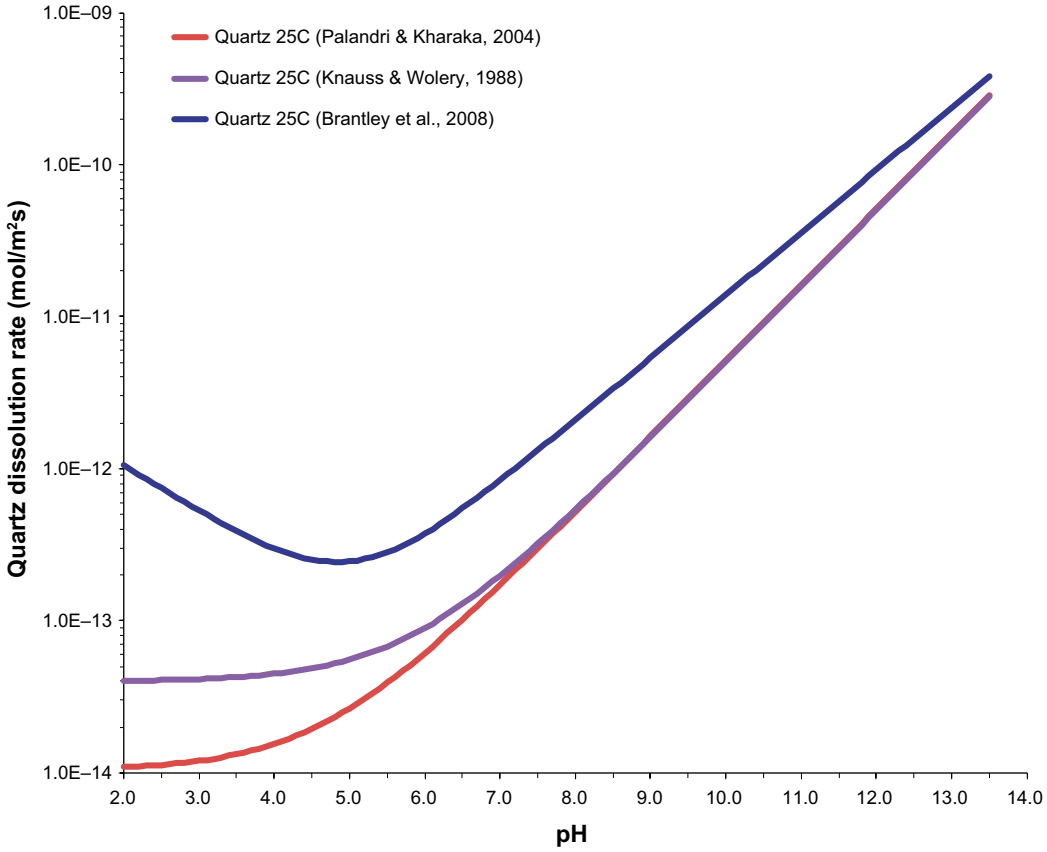

Figure A-2. *Far from equilibrium quartz dissolution rate as a function of pH at 25°C. The rate expression used in the reactive transport simulations is taken from Palandri and Kharaka (2004) and is normalised with respect to BET surface area. For comparative purposes, some other kinetic expressions for quartz dissolution reported in the open literature are also plotted.*

Where, ϕ_m (-) is the mineral volume fraction, A_{BET} (m^2/g) is the bulk surface area of the rock matrix, M_w (g/mol) is the molar mass of quartz, and V_m (m^3/mol) is its molar volume. It is thought that the BET surface area of quartz and feldspar minerals may not be representative of reactive surface area owing to the predominance of relatively non-reactive crystal faces relative to a smaller number of reactive sites corresponding to crystal dislocation and etch-pit cores (see e.g. Gautier et al. 2001, Tester et al. 1994). In spite of this, the estimate for intact rock given by Equation A-3 is considered a reasonable proxy for reactive surface area since the quartz reaction rate data given by Palandri and Kharaka (2004) is BET surface area normalised rather than being based on geometric surface area. Any discrepancy in the magnitude of the reactive surface area relative to BET surface area should already be accounted for in the kinetic parameters.

In order to obtain a sense of geometric scale for the reactive surface area estimated using Equation A-3, it is useful to consider the equivalent diameter of spherical particle required to give the same specific surface area. The relation between specific external surface area, A_g and diameter of a sphere of equivalent volume with surface roughness factor, λ is given by:

$$A_g = \frac{6\lambda}{\rho_s d_p} \qquad \text{(A-4)}$$

Where, ρ_s (kg/m^3) is the mineral density and d_p (m) is the grain diameter. A perfectly smooth sphere has the lowest surface area to volume ratio physically possible which implies that λ is always greater than unity. Surface roughness factors are typically estimated on the basis of regression analysis of sieve size fractions of crushed rock and are usually in the range of about 7–15 for non-weathered silicate minerals typically found in granite (White and Brantley 2003, White and Peterson 1990).

Based on regression analysis of measured BET surface areas of crushed rock samples from Forsmark, André et al. (2009) have estimated the surface roughness of crushed bulk rock to be on the order of 6–7. Interestingly, a surface roughness factor of ~8 corresponds to an equivalent diameter of about 1 mm for a BET surface area of 0.018 m^2/g which is roughly the same size as tectosilicate phenocrysts typically found in fine- to medium-grained granites. Although the surface roughness of crushed mineral sieve size fractions may not be the same as that of pristine matrix grains, it is probably a reasonable approximation given that mechanical failure during crushing is likely to occur along existing zones of weakness in the rock (along grain boundaries). This should firstly lead to decompaction of individual mineral grains and grain aggregates from the matrix sample before brittle failure of intact grains is likely to occur. An additional, although related issue is that given the very small porosity of the rock matrix, a large proportion of minerals grains will be in direct contact and likely not be porewater accessible. Although the measured BET surface area of intact monoliths already accounts for this, it does complicate the direct comparison of physical dimensions of crushed mineral grains and phenocrysts emedded in intact rock.

Estimated equivalent spherical diameters for a range of specific surface areas and surface roughness values are shown in Figure A-3 in the form of a bubble plot for comparative purposes. From the figure, specific surface areas less than 1/10 the base case value appear to be unlikely given the relevant size range of quartz grains likely to be encountered in Forsmark site specific rocks.

The rate of calcite precipitation/dissolution was set at an arbitrarily high level of 10^{-3} mol/m^2s to ensure approximately local equilibrium conditions for this mineral. For gyrolite precipitation an arbitrarily high kinetic far-from-equilibrium rate of precipitation was assumed (10^{-6} mol/m^2s) also formulated using a TST-type expression. The rate was chosen to simulate fast precipitation of gyrolite in order that the kinetic dissolution of quartz would be the limiting constraint on the pH buffering and mineral precipitation dynamics. The particular value of 10^{-6} mol/m^2s was chosen since it was found in preliminary calculations that rates any higher than this gave rise to significant numerical difficulties. Since the appropriate surface area for secondary precipitates in the rock matrix is unknown, default values for surface area of calcite and gyrolite (100 m^2/m^3 of porous medium) were assumed in the simulations. It is also noted that the formulation of the kinetic rates of dissolution and precipitation cannot take into account armouring effects where secondary minerals precipitate over the reactive surface of the primary dissolving quartz. It is unclear how this would affect the results if it were possible to simulate this process. It is speculated, however, that the main effect might be a smearing out of the active region of dissolution/precipitation in the rock matrix owing to that armouring would lead to a less effective dissolution of the primary quartz. It is also relevant to note that the diminishing reactive surface area and porosity of the rock matrix during reactive transport should effectively result in termination of the precipitation process at some point just short of full porosity closure. This would mean that some residual connected porosity should always exist even when the pore spaces are, for all practical purposes, fully clogged.

In the CrunchFlow program, the reactive surface areas (i.e. specific surface area) of minerals are assumed to vary in accordance with a simple 2/3 power law scaling relation involving porosity and mineral volume fraction. The actual form of the scaling relation depends on whether the mineral is initially present (i.e. a primary mineral) or considered to be a secondary mineral. The surface area scaling relations are:

$$A_m = A_m^0 \left(\left(\frac{\varepsilon_p}{\varepsilon_p^0} \right) \cdot \left(\frac{\phi_m}{\phi_m^0} \right) \right)^{2/3} \quad \text{(primary mineral dissolution)} \tag{A-5}$$

$$A_m = A_m^0 \left(\left(\frac{\varepsilon_p}{\varepsilon_p^0} \right) \cdot \phi_m \right)^{2/3} \quad \text{(secondary mineral dissolution)} \tag{A-6}$$

$$A_m = A_m^0 \left(\frac{\varepsilon_p}{\varepsilon_p^0} \right)^{2/3} \quad \text{(precipitation – all minerals)} \tag{A-7}$$

where the superscript zero denotes the initial state for specific surface area (A_m), porosity (ε_p), and mineral volume fraction (ϕ_m).

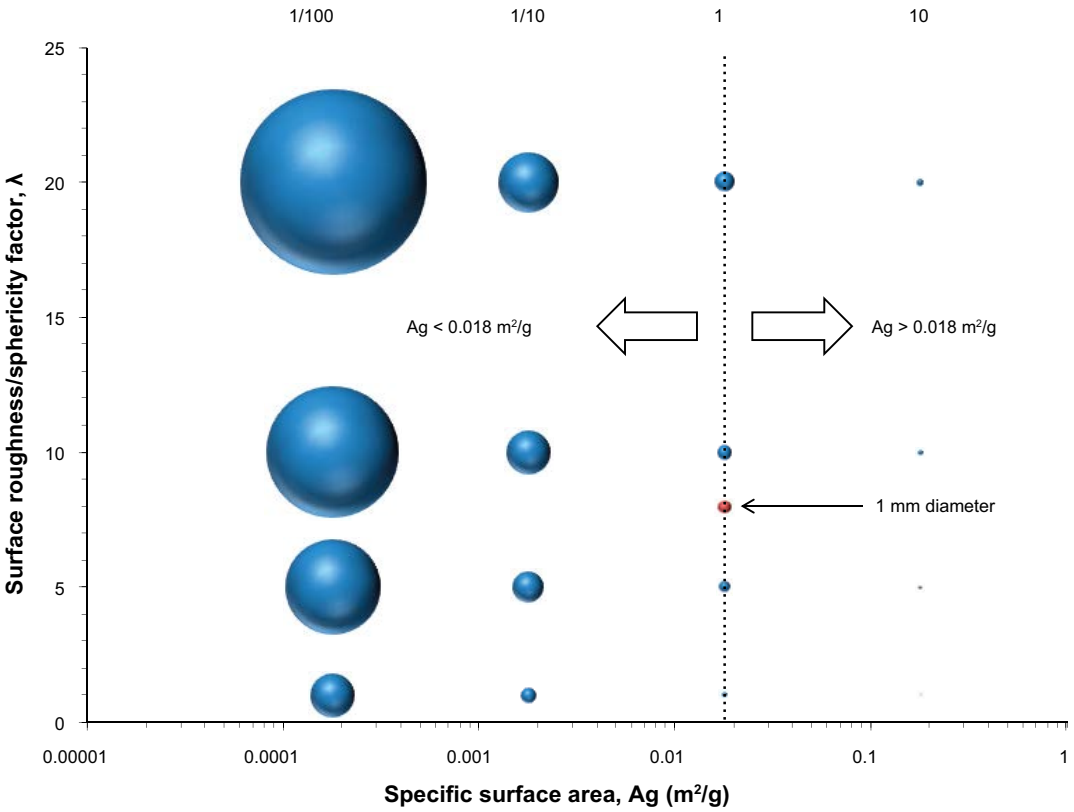

Figure A-3. *Equivalent diameter of quartz crystal grains as a function of specific (geometric) surface area, A_g (m^2/g) and surface roughness/sphericity factor, λ (-) visualised as a bubble plot. The red bubble indicates the λ value required to obtain an equivalent diameter of 1 mm for a BET surface area of 0.018 m^2/g.*

In order to examine the impact of discretisation of the rock matrix, a number of different grid discretisation variants were defined for each of the RTTC and SRTBC simulation cases. The grid discretisation variants for the RTTC simulations are plotted in Figure A-4 and for the SRTBC simulations in Figure A-5. For the RTTC case studies, little or no difference was noted in the breakthrough curve results (aqueous phase concentrations) obtained for the different refinements of matrix grid discretisation. For the SRTBC simulation case studies, on the other hand, a relatively strong impact of matrix discretisation was observed which is why the most finely discretised case study (SRTBC_73486161323) assumes µm size for the first group of 10 diffusive cells.

A2 Reactive transport test case (RTTC) simulation results

The case study corresponding to the most refined grid took roughly 3.5 days of CPU time to simulate 1,000 years of reactive transport. For this a Dell Optiplex 745 (Intel Core 2 Duo processor, 2 GB physical memory) was used running a Windows XP, 32 bit operating system. For the non-reactive tracer components A and B, near perfect agreement was obtained with the analytical solution described by Tang et al. (1981) indicating the absence of numerical artefacts related to grid discretisation for the breakthrough of non-reactive components in the aqueous phase. The result for the non-reactive tracers also shows that the rock matrix can be safely assumed to be effectively infinite on the timescale of transport for the chosen hydrodynamic conditions (i.e. no matrix saturation effects are apparent related to the maximum diffusion depth of 1 m).

Although the aqueous phase concentrations show virtually no impact of differing matrix grid discretisation, the mineral mass balance does exhibit oscillations increasing with the coarseness of the grid (see Figure A-8 to Figure A-10). It is interesting to note that in spite of the oscillatory behaviour of the mineral mass balance, the baseline amount of precipitated calcite appears to be approximately the same in each case and approaches a value of ~$4.1 \cdot 10^{-8}$ m^3/m^3 porous medium. Decreasing the maximum allowable time stepsize by a factor of 100 (from 0.1 y to 0.001 y) did not improve the smoothness of the mineral mass balance. There was insufficient time to study this further although it appears that it could be related to the use of a non-uniform grid discretisation.

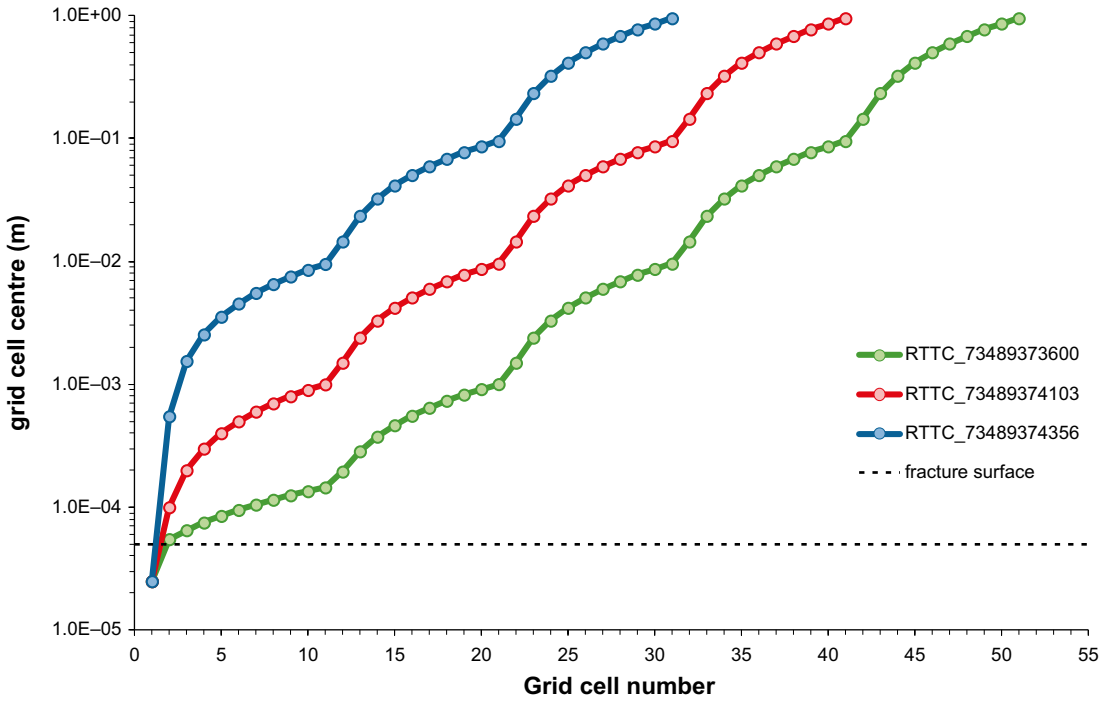

Figure A-4. *Matrix grid discretisation for the reactive transport test case simulations (RTTC). The discretisation is based on a nested logarithmic series of arithmetically spaced grid cells. The first cell in the sequence corresponds to the advective pore space (fracture half-aperture) which is* $5 \cdot 10^{-5}$ *m.*

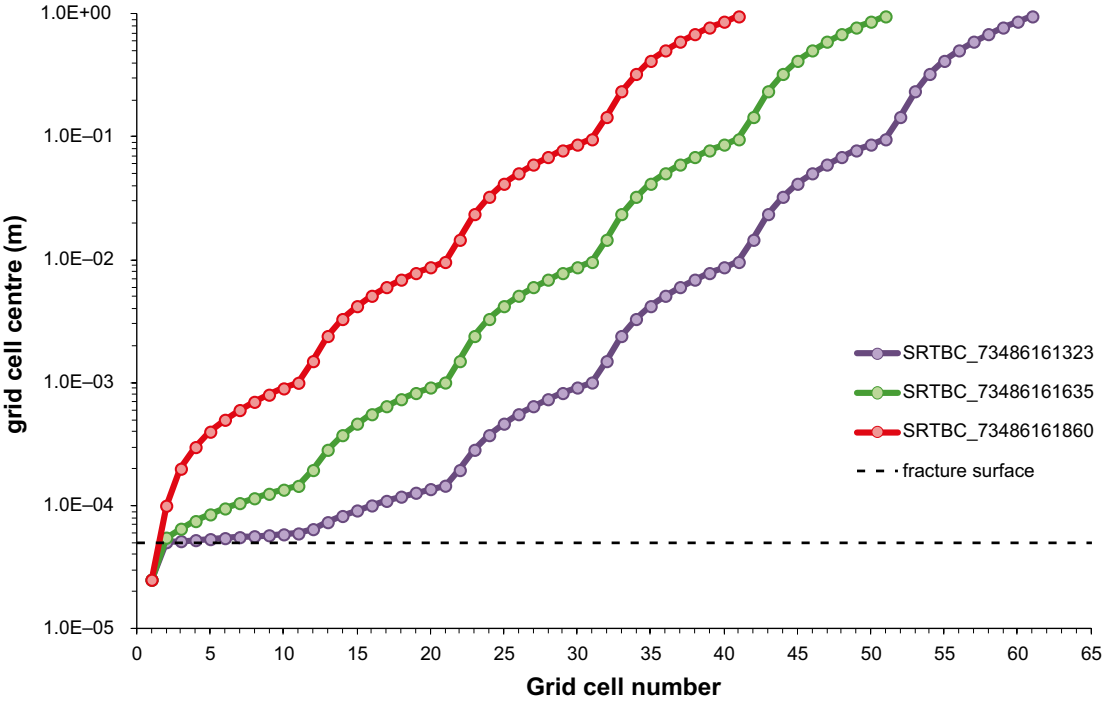

Figure A-5. *Matrix grid discretisation for the simplified reactive transport base case simulations (SRTBC). The discretisation is based on a nested logarithmic series of arithmetically spaced grid cells. The first cell in the sequence corresponds to the advective pore space (fracture half-aperture) which is* $5 \cdot 10^{-5}$ *m.*

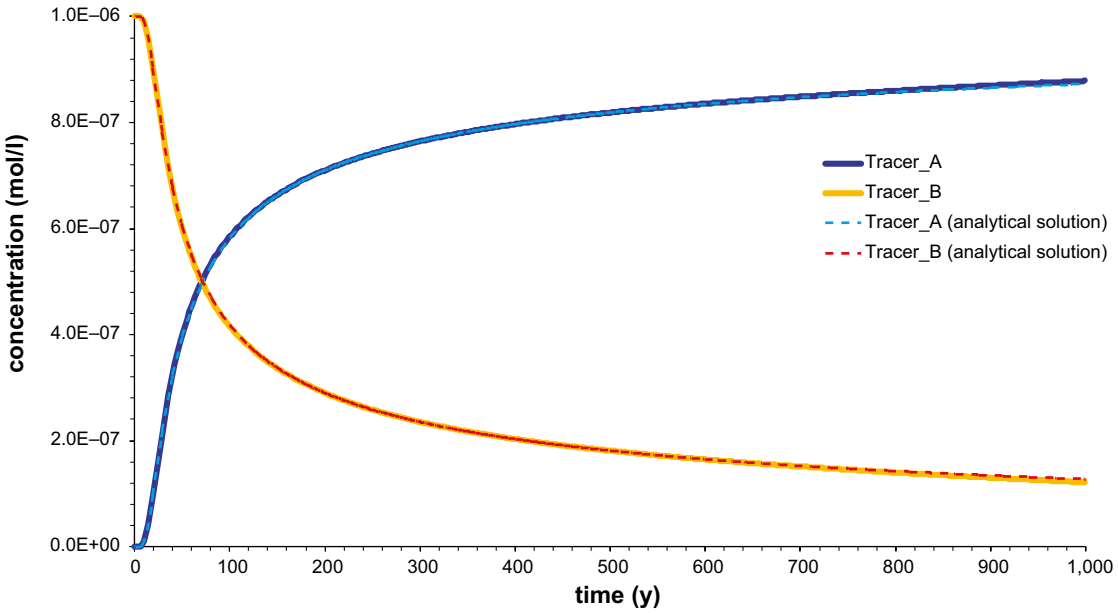

Figure A-6. *Breakthrough of tracer components at L = 100 m simulated using CrunchFlow compared to the analytical solution described by Tang et al. (1981) for an infinite rock matrix (simulation case RTTC_73489373600). Near perfect agreement is obtained with the analytical solution over the entire breakthrough curve up to at least 800–900 y.*

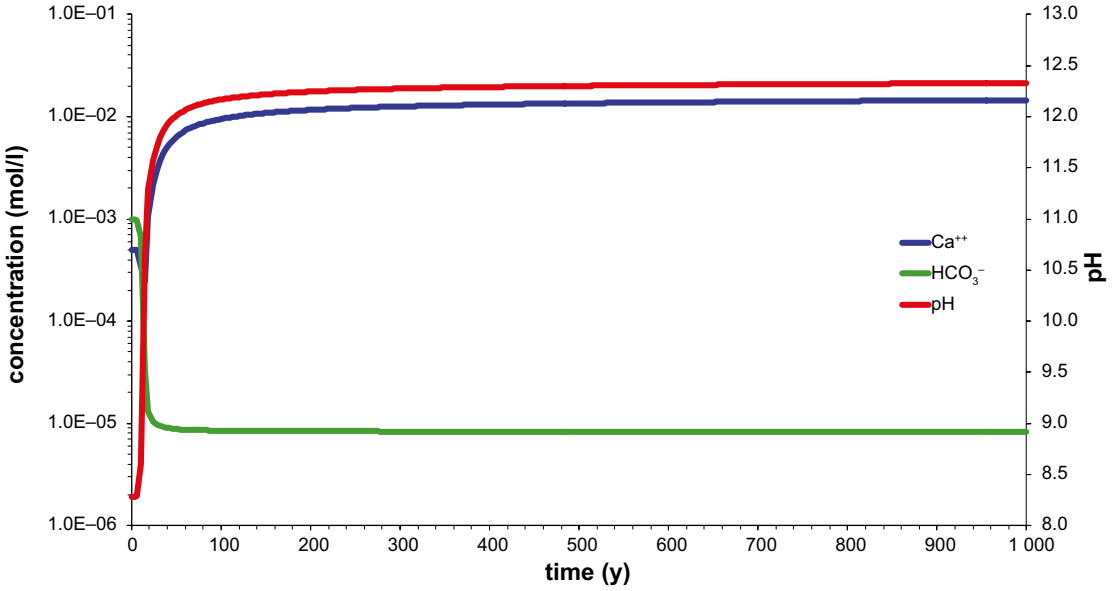

Figure A-7. *Breakthrough for pH, total Ca^{2+}, and HCO_3^- concentration at L = 100 m simulated using CrunchFlow (simulation case RTTC_73489373600).*

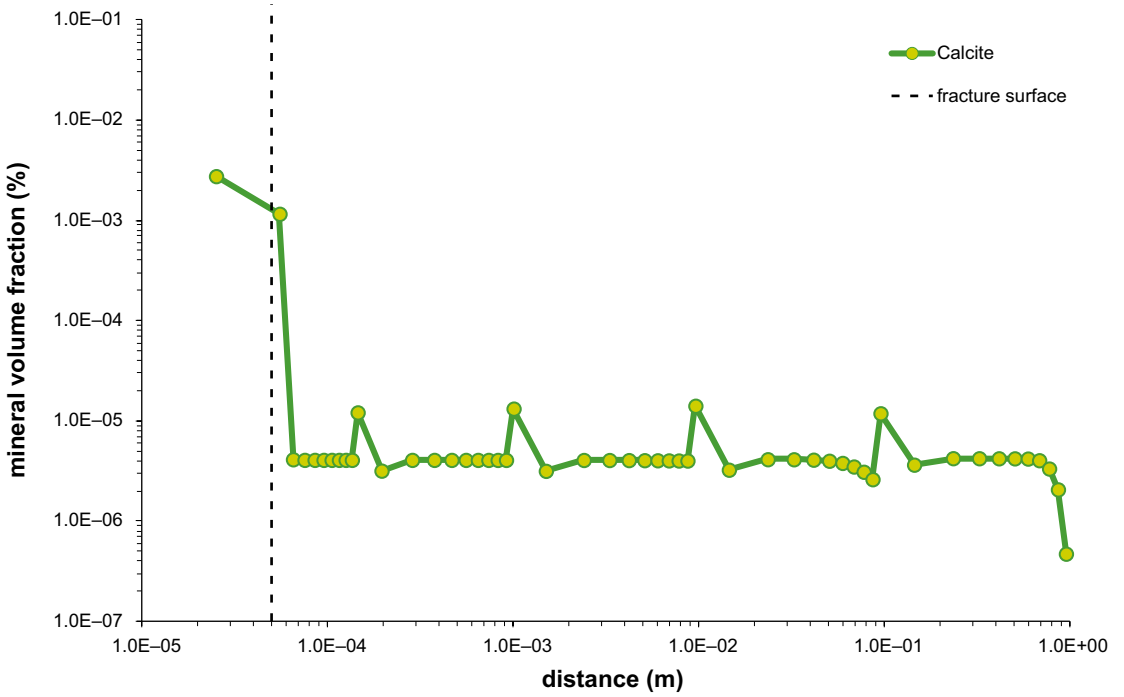

Figure A-8. *Calcite mineral volume fraction (%) plotted versus matrix distance for the advective cell centred at L = 50.5 m and t = 1000 y simulated using CrunchFlow (simulation case RTTC_73489373600). The matrix distance includes the transport half-aperture of the fracture and thus the first grid cell boundary is at $5 \cdot 10^{-4}$ m (corresponding to the fracture surface as indicated in the figure). Oscillations in the calculated mass of calcite precipitated at the boundaries of the nested grid appear to be related to the matrix discretisation.*

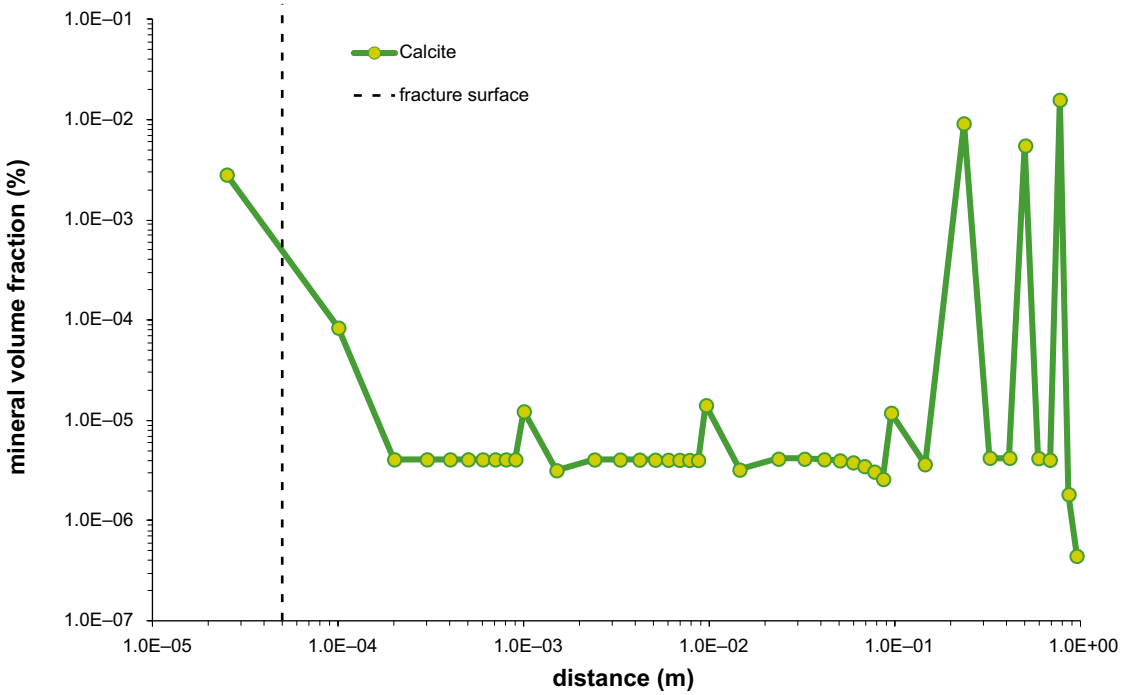

Figure A-9. *Calcite mineral volume fraction plotted versus matrix distance for the advective cell centred at L = 50.5 m and t = 1000 y simulated using CrunchFlow (simulation case RTTC_73489374103). The matrix distance includes the transport half-aperture of the fracture and thus the first grid cell boundary is at $5 \cdot 10^{-4}$ m (corresponding to the fracture surface as indicated in the figure). Oscillations in the calculated mass of calcite precipitated at the boundaries of the nested grid appear to be related to the matrix discretisation.*

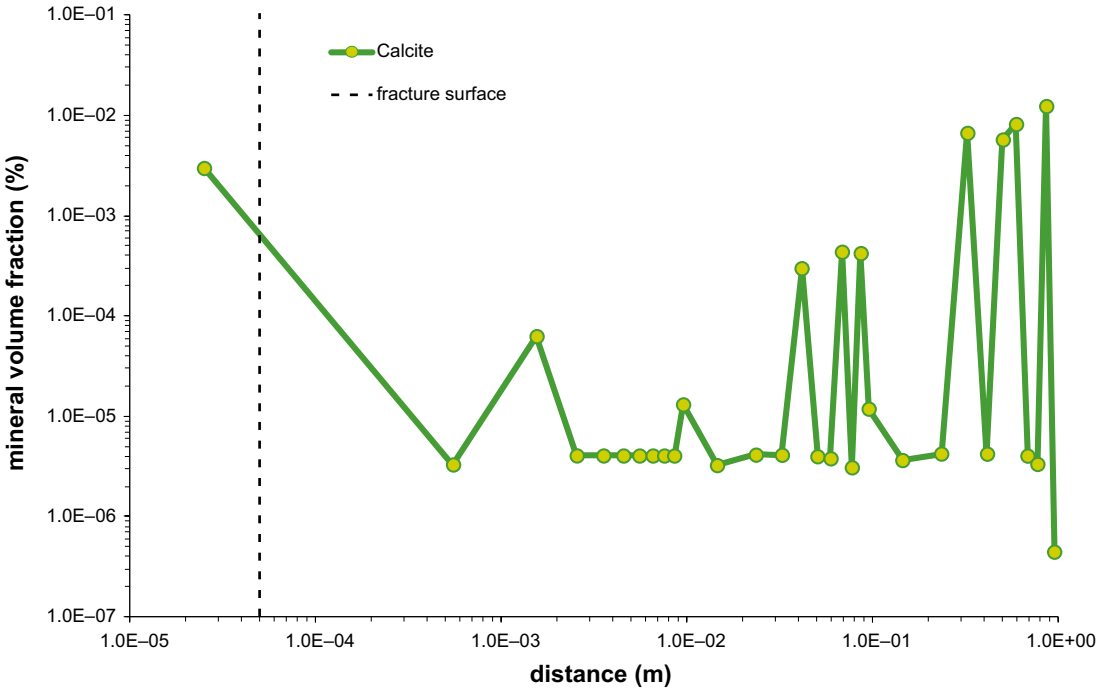

Figure A-10. *Calcite mineral volume fraction plotted versus matrix depth for the advective cell centred at L = 50.5 m and t = 1000 y simulated using CrunchFlow (simulation case RTTC_73489374356). The matrix distance includes the transport half-aperture of the fracture and thus the first grid cell boundary is at $5 \cdot 10^{-4}$ m (corresponding to the fracture surface as indicated in the figure). Oscillations in the calculated mass of calcite precipitated at the boundaries of the nested grid appear to be related to the matrix discretisation.*

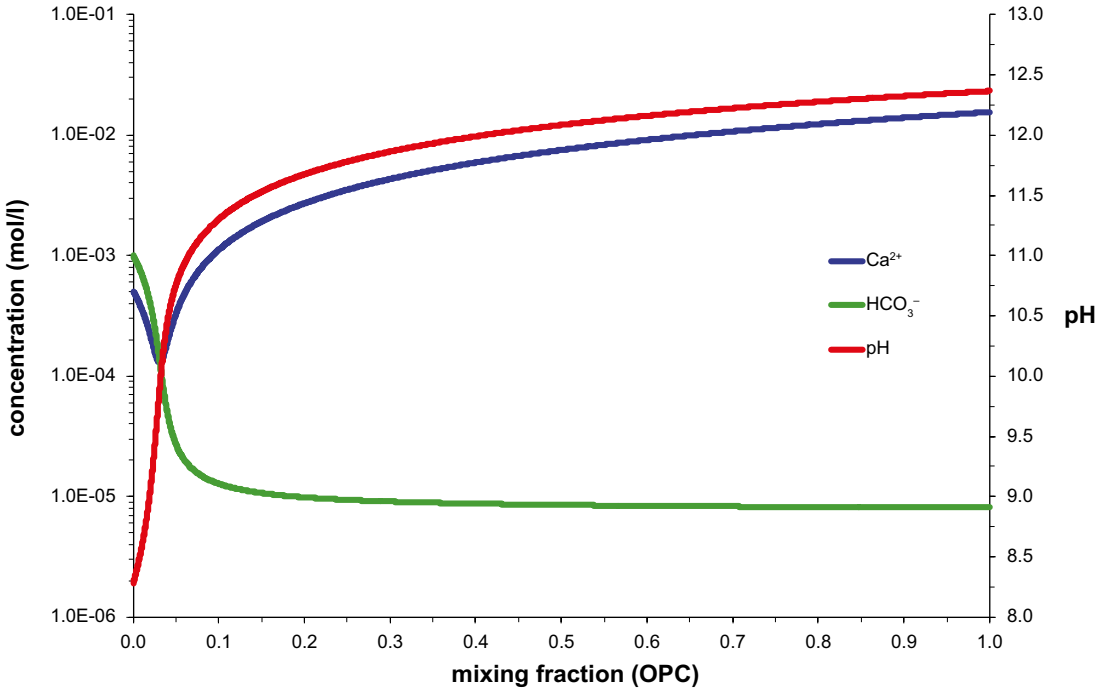

Figure A-11. *Total concentration of Ca^{2+} and HCO_3^- and pH plotted as a function of mixing fraction (i.e. fraction of OPC affected leachate in groundwater). Data were calculated using PHREEQC and the Yucca mountain thermodynamic database and assuming ubiquitous calcite equilibrium.*

The amount of calcite precipitated appears to be limited by the initial inventory of Ca^{2+} and HCO_3^- contained in the matrix porewater and that of the infiltrating OPC affected groundwater. The amount precipitated does not change with time, although the precipitation front progresses into the rock matrix at a rate consistent with the penetration depth of the diffusive mixing front. This result suggests that clogging of the matrix porosity with calcite does not occur for the simplified chemical boundary and initial conditions considered in the calculation (and for the assumed effective diffusivity rock matrix). Although a slightly larger amount of calcite is found to precipitate in the advective pore space and first matrix cell, the amount of precipitated calcite is still at least 2–3 orders of magnitude less than what would be required to cause pore clogging.

The simulation results for the reactive components H^+, Ca^{2+}, and HCO_3^- were found to agree to a high degree of precision with a PHREEQC-based mixing model using the transport of the non-reactive, internal standard components as a proxy for the mixing fraction (Figure A-12). Very small deviations appear to be related to minor differences in the methods used to calculate aqueous phase activity coefficients in the different programs and the results can be considered, for all practical purposes, to be identical.

A3 Simplified reactive transport base case (SRTBC) simulation results

1 µm initial matrix grid spacing

The case study for the most finely discretised grid with 1 µm initial matrix grid cell spacing (SRTBC_73486161323) took 26 days of CPU time to simulate 1,000 years of reactive transport. Precipitation of gyrolite in the rock matrix leading to pore closure was found to have a significant impact on the breakthrough of the non-reactive tracer components A and B. As shown in Figure A-13, deviations are apparent in the breakthrough curve already after the first 20 years of transport when compared with the analytical solution described by Tang et al. (1981). The breakthrough of reactive components (Figure A-14) exhibits a slow approach to the quartz/gyrolite equilibrium pH with an abrupt breakthrough of high pH OPC leachate at roughly 750 years. The small notch in the breakthrough curve at this time appears to be related to numerical oscillation which is typical in the vicinity of sharp reaction fronts when using global implicit solution methods. In 1D advective simulations, the oscillation can be made to disappear by using a lower Péclet number (Pe ~ 5, corresponding to a hydrodynamic dispersion distance of 20 m). The rock matrix porosity is completely clogged along the entire flowpath at 750 years thereby allowing the breakthrough of non-buffered OPC leachate.

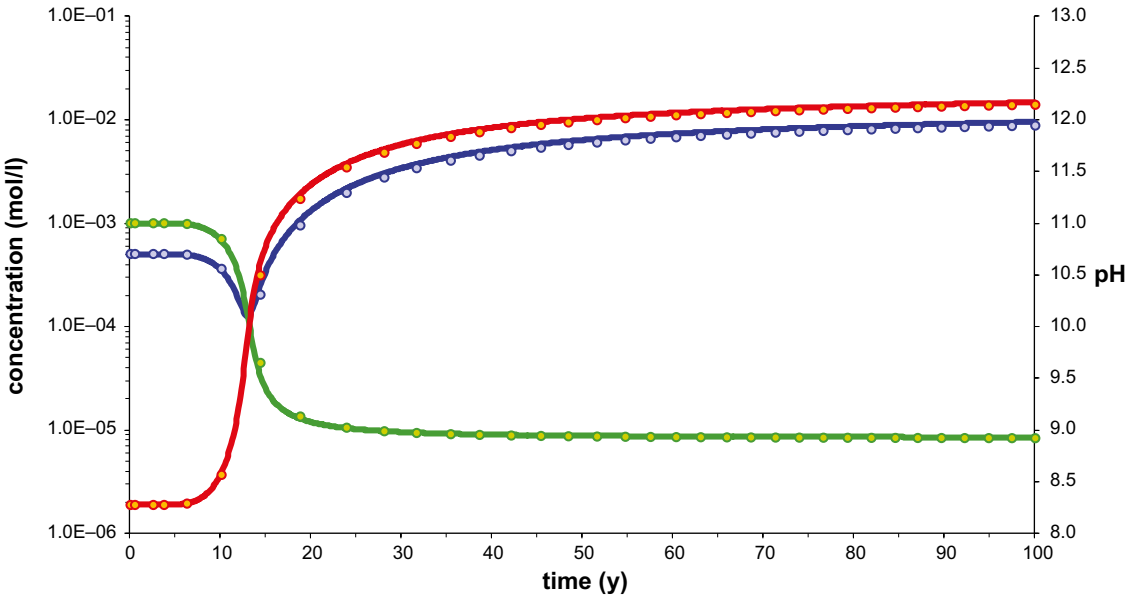

Figure A-12. *Comparison of results from CrunchFlow reactive transport simulations (solid lines) and data interpolated from the PHREEQC mixing model (circular markers) assuming tracer component A as a proxy for the OPC mixing fraction. Slight deviations between the values calculated using the two models are due to differences in the calculation of aqueous phase activities in PHREEQC and CrunchFlow.*

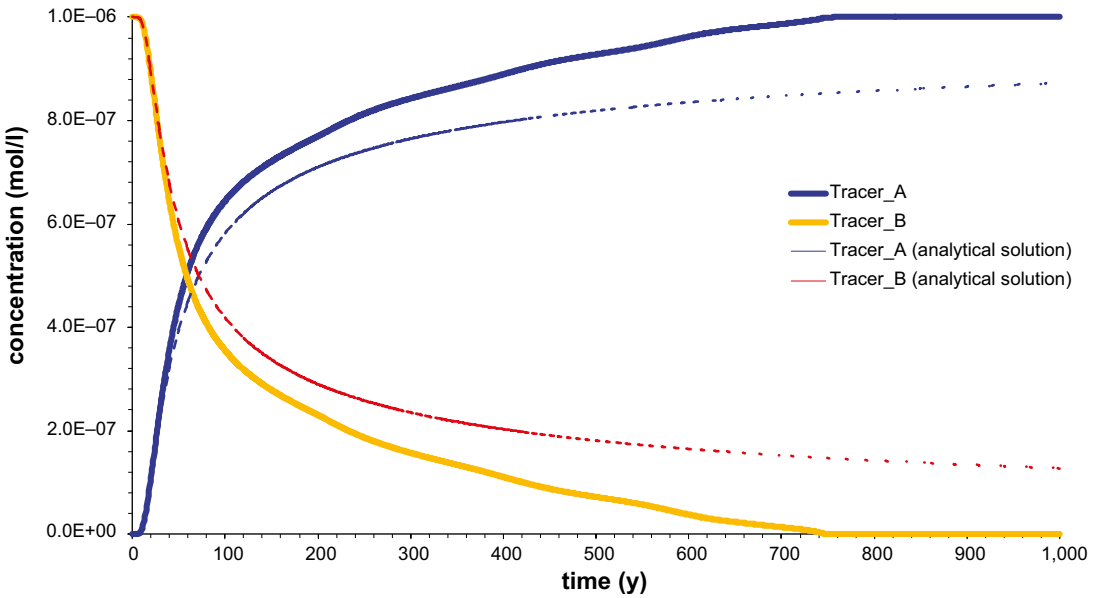

Figure A-13. *Breakthrough of tracer components at L = 100 m simulated using CrunchFlow compared to the analytical solution described by Tang et al. (1981) for an infinite rock matrix (simulation case SRTBC_73486161323). Significant deviations relative to the analytical solution are apparent from very early in the breakthrough curve.*

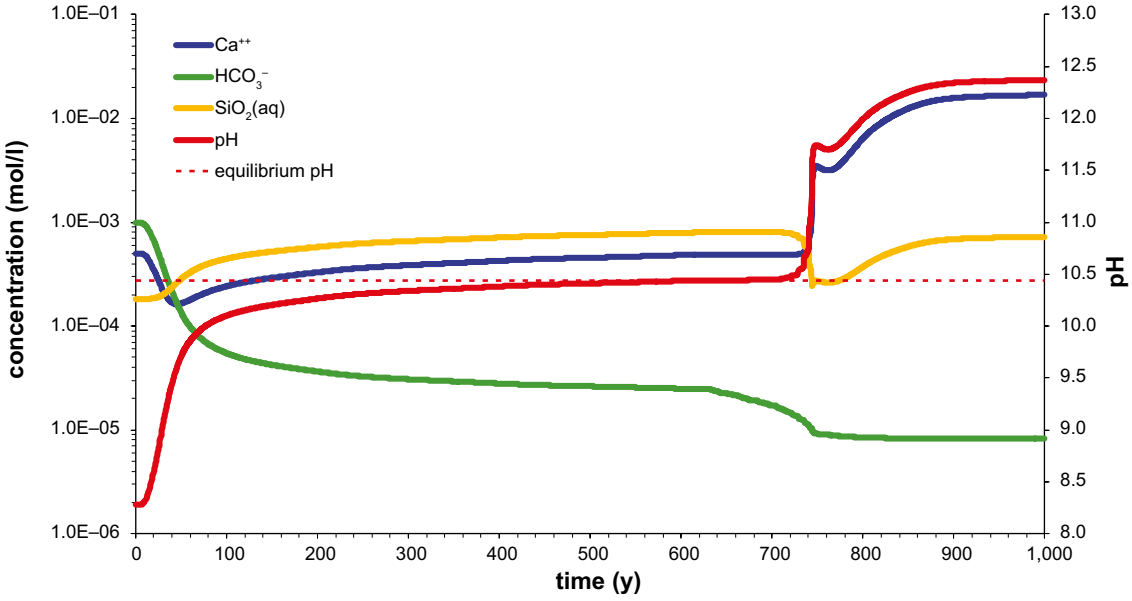

Figure A-14. *Breakthrough for pH, total Ca^{2+}, HCO_3^-, and dissolved SiO_2 concentration at L = 100 m simulated using CrunchFlow (simulation case SRTBC_73486161323). The effluent concentrations at t = 1000 y correspond to the initial OPC leachate composition. The broken line indicates the quartz/gyrolite equilibrium pH level of 10.44.*

A small amount of gyrolite precipitation occurs in the advective flowspace. Most of the gyrolite precipitation in the rock matrix is confined in a narrow band in the first 0.1 mm adjacent to the fracture surface (Figure A-15). Precipitation of calcite exhibits a high degree of spatial variability which may be, at least in part, artefactual. It is noted, however, that the amounts of calcite precipitated are extremely low and the variability may be due to the level of precision of the mass balance. The first few grid cells of the rock matrix exhibit increased porosity as the volume of quartz lost by dissolution is greater than the net volume of gyrolite precipitated. Very little alteration occurs further into the rock matrix than about 0.2 mm from the fracture surface for the simulated material properties. Figure A-16 shows a map of the porosity change ($\log_{10}$ transformed data) relative to the initial matrix porosity of 0.1%. Artefacts in the calculated porosity distribution are most likely due to the interplay between steep reaction fronts, grid discretisation and time stepsize used by the CrunchFlow. Given the long CPU time required to obtain a solution, it does not seem practical to run simulations with timestep sizes much smaller than those currently used. The maximum allowable timestep was set to 0.1 y in the simulations, although the maximum timestep actually used by the program was on the order of $\sim 9 \cdot 10^{-3}$ y (timestep size is chosen automatically by the GIMRT solver) and it is therefore not clear whether reducing the timestep size further would necessarily improve the mineral mass balance.

10 µm initial matrix grid spacing

The case study considering an initial matrix grid cell spacing of 10 µm (SRTBC_73486161635) took 23 days of CPU time to simulate 1,000 years of reactive transport. For this case study, precipitation of gyrolite in the rock matrix leading to pore closure was also found to have a significant impact on the breakthrough of the non-reactive tracer components A and B (Figure A-17). Similarly to the 1 µm grid case described in the previous section, deviations are apparent in the breakthrough curve already after the first 20 years of transport when compared with the analytical solution. The deviation for the non-reactive tracers does not appear to be as great as that observed for the 1 µm grid case suggesting a less effective pore clogging effect for the coarser matrix grid.

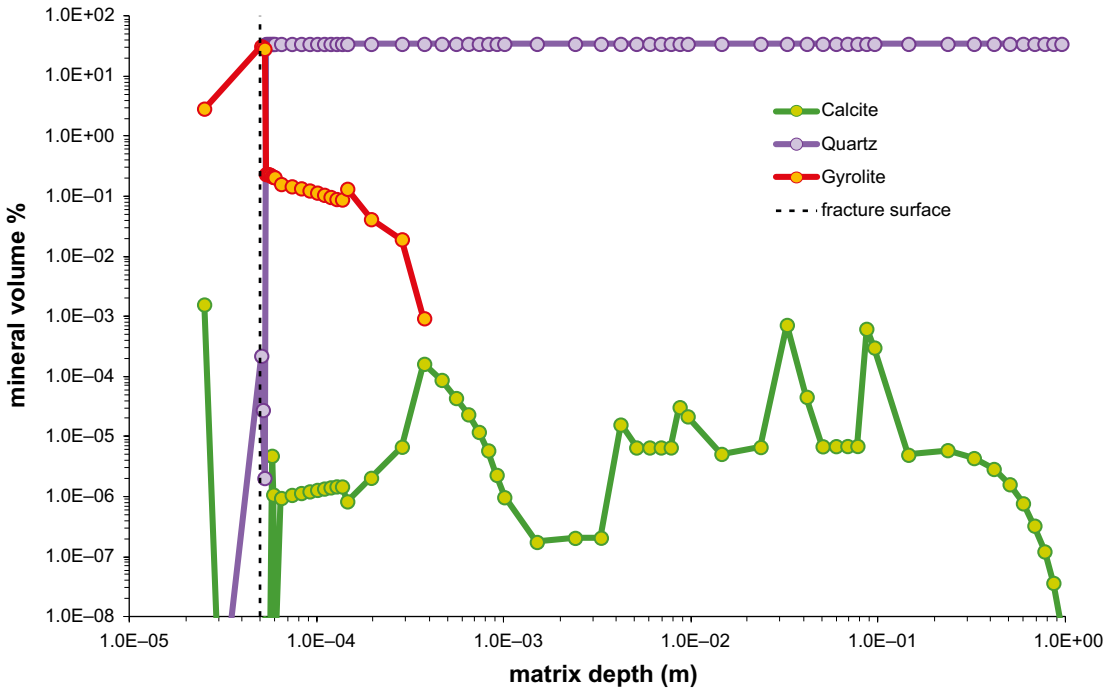

Figure A-15. *Mineral volume fraction (%) plotted versus matrix depth for the advective cell centred at L = 50.5 m and t = 1000 y simulated using CrunchFlow (simulation case SRTBC_73486161323). The matrix distance includes the transport half-aperture of the fracture and thus the first grid cell boundary is at $5 \cdot 10^{-4}$ m (corresponding to the fracture surface as indicated in the figure).*

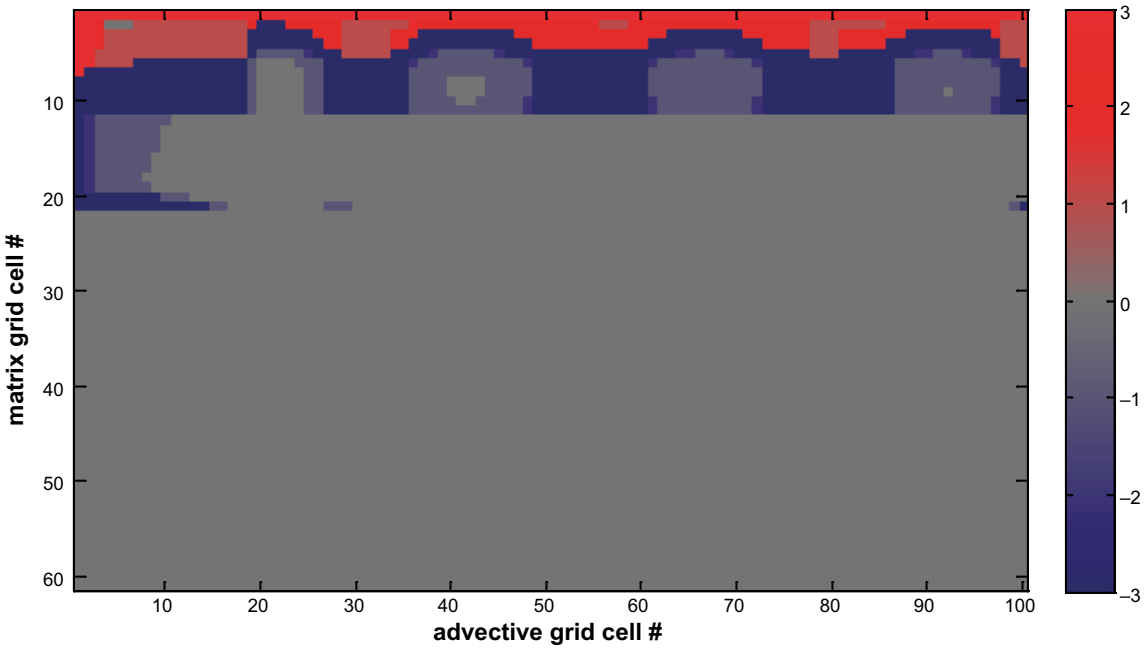

Figure A-16. *Porosity of grid cells (log_{10} transformed values) relative to the initial matrix porosity of 0.1% at t = 1000 y simulated using CrunchFlow (simulation case SRTBC_73486161323). There appears to be an initial increase in porosity in the first few matrix grid cells followed by a steep decrease. The rock matrix is completely clogged by gyrolite precipitate at this time. Artefacts in the porosity distribution (and mineral mass balance) are likely to be related to the interplay between steep reaction fronts, grid discretisation, and discrete timestepping used by the program.*

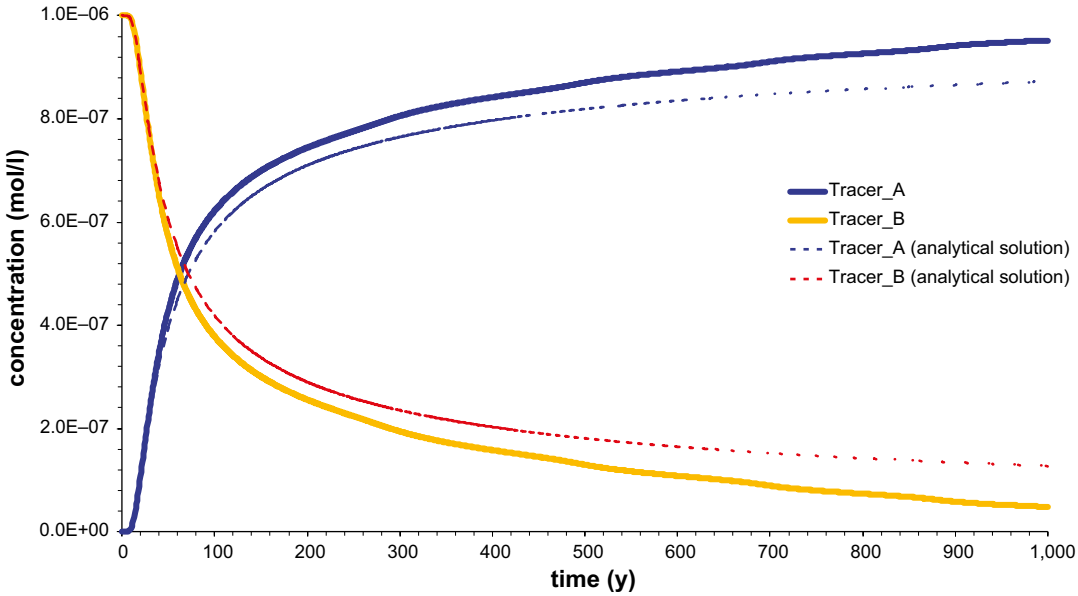

Figure A-17. *Breakthrough of tracer components at L = 100 m simulated using CrunchFlow compared to the analytical solution described by Tang et al. (1981) for an infinite rock matrix (simulation case SRTBC_73486161635). Significant deviations relative to the analytical solution are apparent from very early in the breakthrough curve.*

The breakthrough of reactive components (Figure A-18) exhibits a slow approach to the quartz/gyrolite equilibrium pH although there is no breakthrough of high pH OPC leachate in this case. The main features of quartz dissolution and gyrolite precipitation are similar to the 1 µm grid case, although the matrix porosity only becomes clogged along roughly 65% of the flowpath. The distribution of gyrolite precipitate suggests a time to non-buffered OPC breakthrough of ~1,540 y which is roughly double the pore closure time obtained for the 1 µm grid case.

100 µm initial matrix grid spacing

The case study for the coarsest matrix grid cell spacing of 100 µm (SRTBC_73486161860) took 19 days of CPU time to simulate 1,000 years of reactive transport. For this case study, precipitation of gyrolite in the rock matrix leading to pore closure was found to have a significant impact on the breakthrough of the non-reactive tracer components A and B (Figure A-22), although to a much lesser degree than either the 1 µm or 10 µm cases. Deviations are apparent in the breakthrough curve after roughly 50 years of transport when compared with the analytical solution. The results suggest a progressively less effective pore clogging effect for increasing coarseness of the matrix grid.

The breakthrough of reactive components (Figure A-23) exhibits similar features to the previously studied 10 µm case and there is no breakthrough of high pH OPC leachate. The distribution of gyrolite precipitate and changes in matrix porosity are similar to the 10 µm grid case, with the matrix porosity becoming clogged along roughly 65% of the flowpath. The results suggest a time to non-buffered OPC breakthrough of roughly the same magnitude as the 10 µm grid case.

A4 1D Exploratory Calculations (SRTBC)

As shown in the previous section the rate of porosity closure of the rock matrix appears to be sensitive to the rock matrix discretisation. For this reason, additional 1-dimensional diffusion calculations have been made to explore various issues related to the set up of the diffusive reactive transport problem. In these calculations, the most finely discretised grid (corresponding to simulation case SRTBC_73486161323) has been assumed while the other parameters have been studied in an interactive fashion to understand the dynamics of porosity alteration. In the 1D simulations, the fracture aperture is not included and a Dirichlet type (i.e. constant concentration) boundary condition is assumed at the fracture surface.

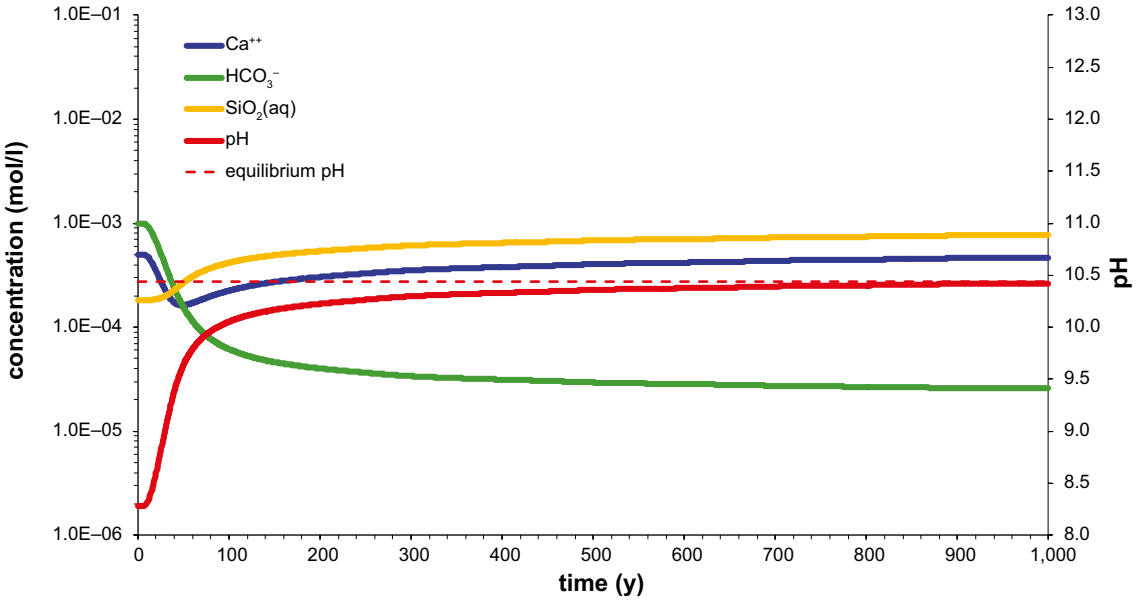

Figure A-18. *Breakthrough for pH, total Ca^{2+}, HCO_3^-, and dissolved SiO_2 concentration at L = 100 m simulated using CrunchFlow (simulation case SRTBC_73486161635).*

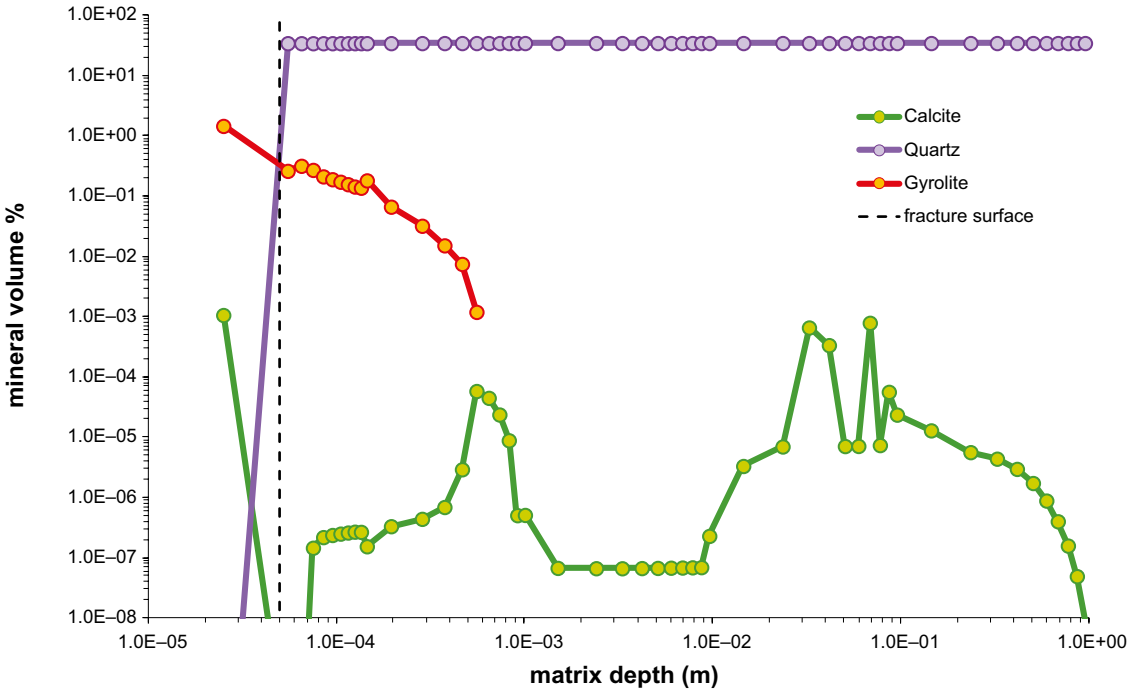

Figure A-19. *Mineral volume fraction (%) plotted versus matrix depth for the advective cell centred at L = 50.5 m and t = 1000 y simulated using CrunchFlow (simulation case SRTBC_73486161635). The matrix distance includes the transport half-aperture of the fracture and thus the first grid cell boundary is at $5 \cdot 10^{-4}$ m (corresponding to the fracture surface as indicated in the figure).*

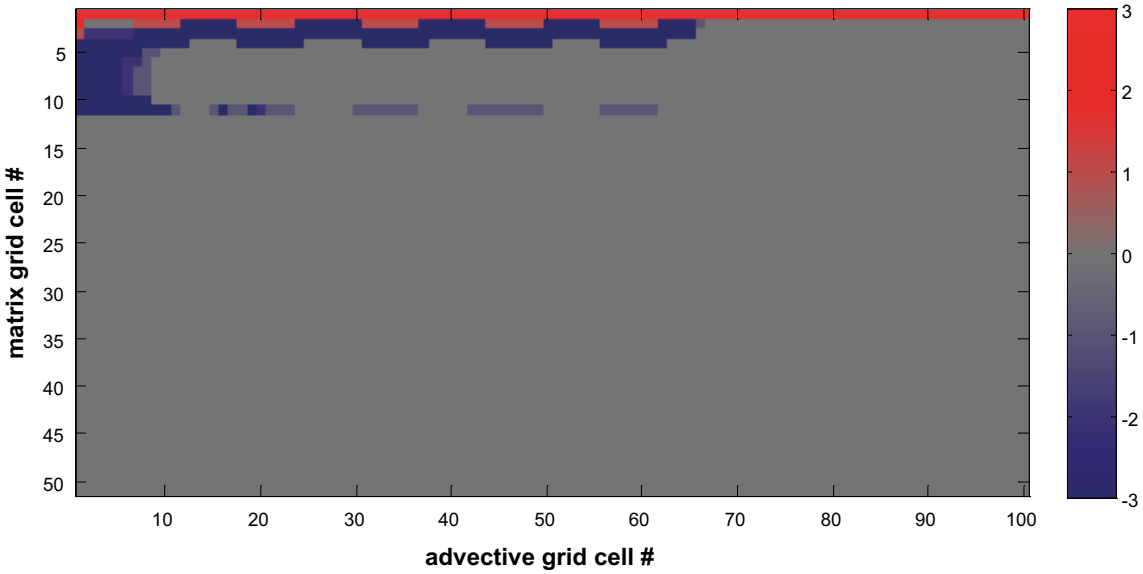

Figure A-20. *Porosity of grid cells (log_{10} transformed values) relative to the initial matrix porosity of 0.1% at t = 1000 y simulated using CrunchFlow (simulation case SRTBC_73486161635). There appears to be an initial increase in porosity in the first few matrix grid cells followed by a steep decrease. The rock matrix along at least half the flowpath is completely clogged by gyrolite precipitate at this time. Artefacts in the porosity distribution (and mineral mass balance) are likely to be related to the interplay between steep reaction fronts, grid discretisation, and discrete timestepping used by the program.*

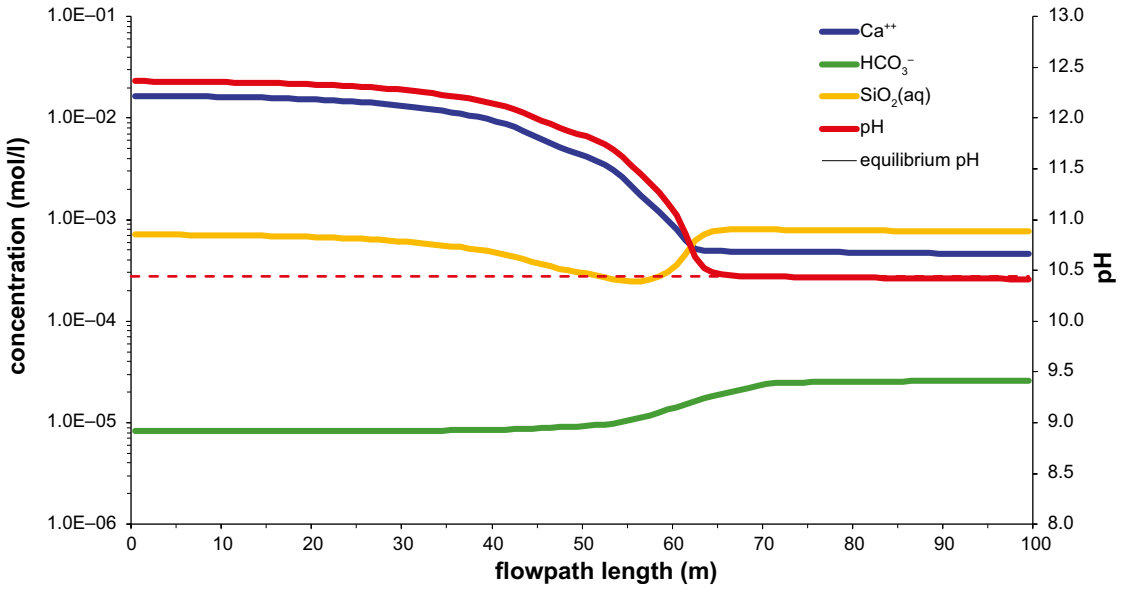

Figure A-21. *Flowpath concentration profiles for pH, total Ca^{2+}, HCO_3^-, and dissolved SiO_2 concentration at t = 1000 y simulated using CrunchFlow (simulation case SRTBC_73486161635). The rock matrix along at least half the flowpath is completely clogged by gyrolite precipitate at this time thereby preventing effective pH buffering of the infiltrating OPC affected leachate.*

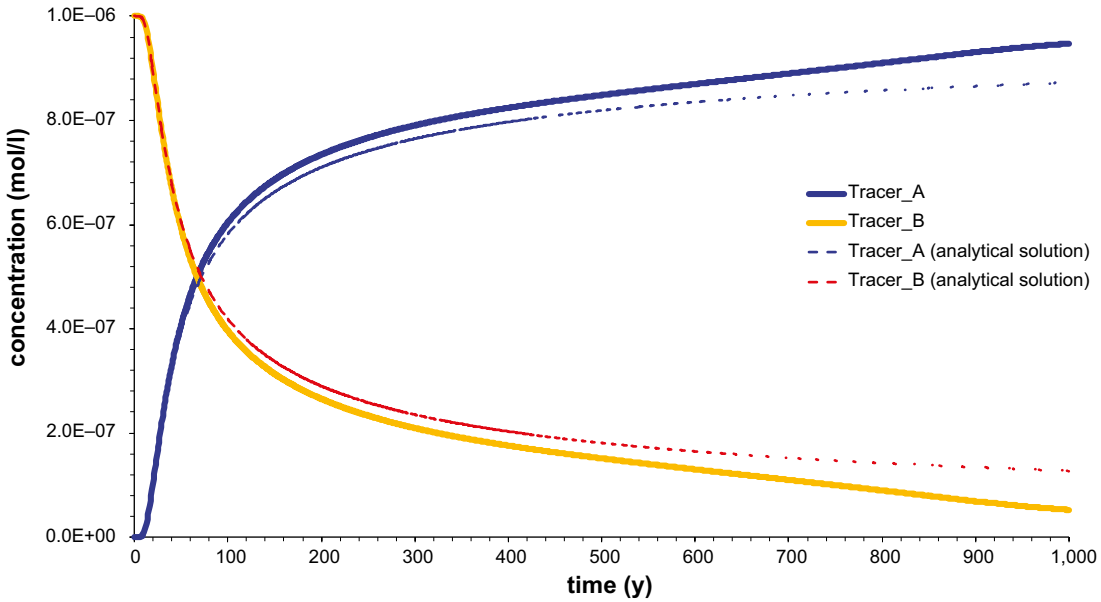

Figure A-22. *Breakthrough of tracer components at L = 100 m simulated using CrunchFlow compared to the analytical solution described by Tang et al. (1981) for an infinite rock matrix (simulation case SRTBC_73486161860). Significant deviations relative to the analytical solution are apparent from very early in the breakthrough curve.*

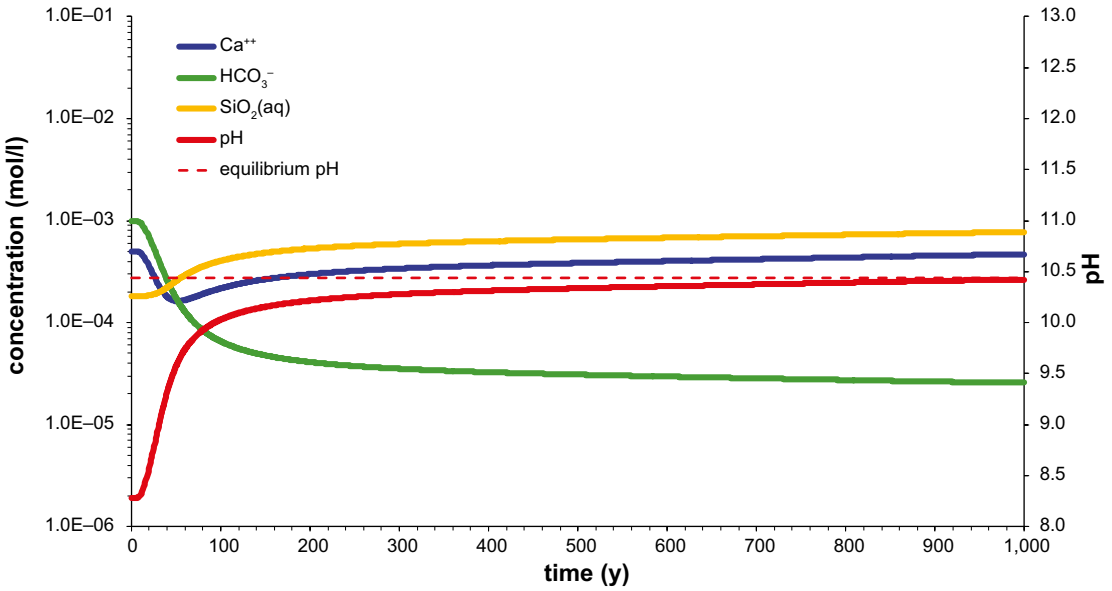

Figure A-23. *Breakthrough for pH, total Ca^{2+}, HCO_3^-, and dissolved SiO_2 concentration at L = 100 m simulated using CrunchFlow (simulation case SRTBC_73486161860).*

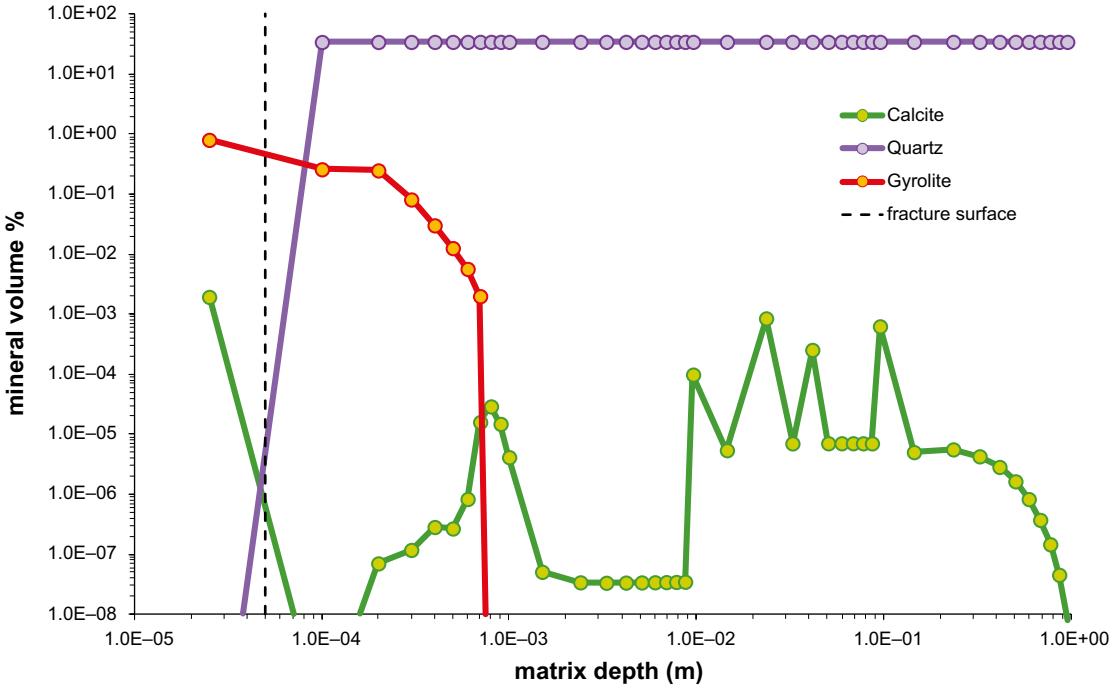

Figure A-24. *Mineral volume fraction (%) plotted versus matrix depth for the advective cell centred at L = 50.5 m and t = 1000 y simulated using CrunchFlow (simulation case SRTBC_73486161860). The matrix distance includes the transport half-aperture of the fracture and thus the first grid cell boundary is at $5 \cdot 10^{-4}$ m (corresponding to the fracture surface as indicated in the figure).*

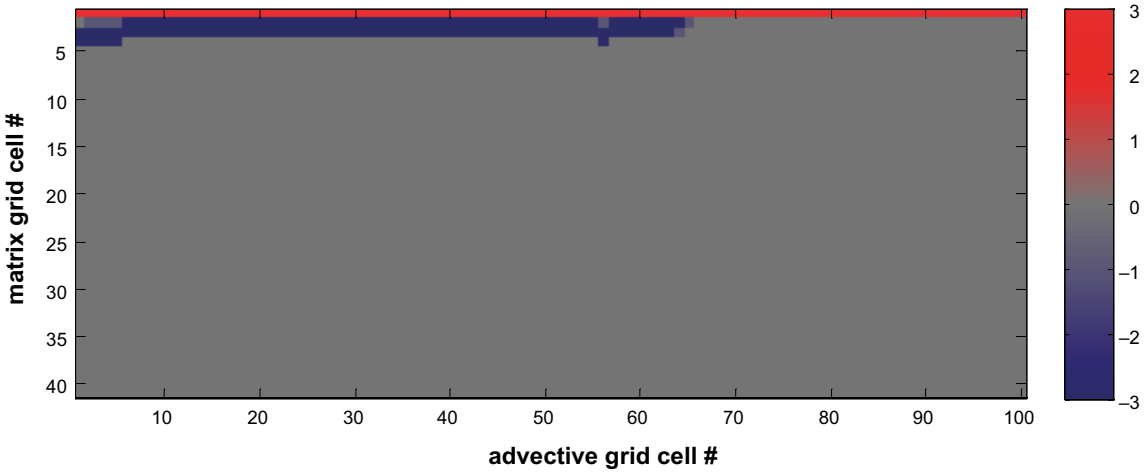

Figure A-25. *Porosity of grid cells (log_{10} transformed values) relative to the initial matrix porosity of 0.1% at t = 1000 y simulated using CrunchFlow (simulation case SRTBC_73486161860). In this case only a steep decrease in the fracture porosity is seen in the first few matrix grid cells. The rock matrix along at least half of the flowpath is completely clogged by gyrolite precipitate at this time. Artefacts in the porosity distribution (and mineral mass balance) are likely to be related to the interplay between steep reaction fronts and discrete timestepping in the program.*

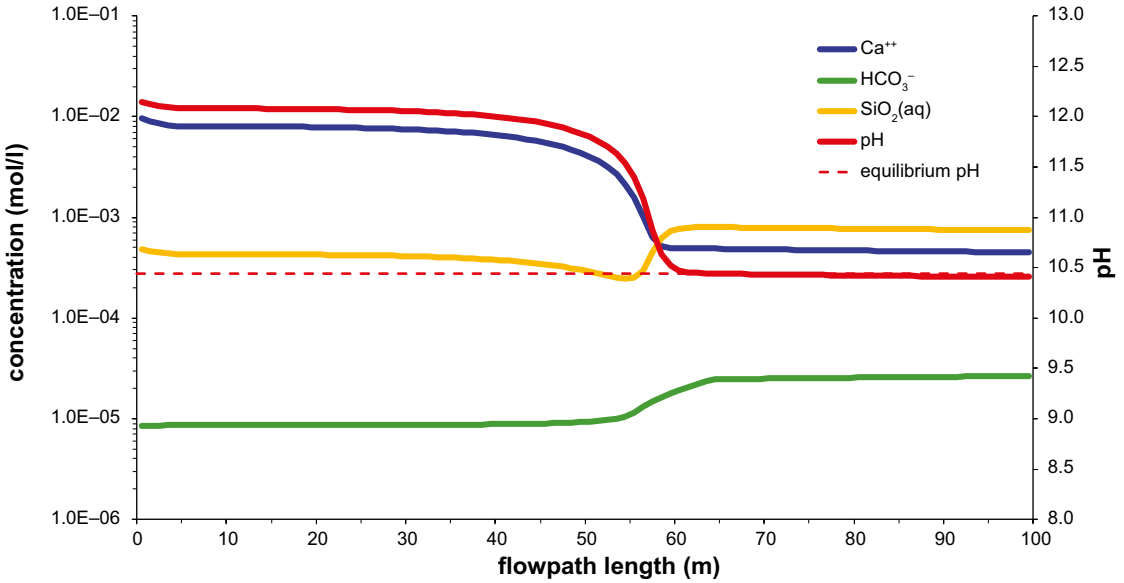

Figure A-26. *Flowpath concentration profiles for pH, total Ca^{2+}, HCO_3^-, and dissolved SiO_2 concentration at t = 1000 y simulated using CrunchFlow (simulation case SRTBC_73486161860). The rock matrix along at least half the flowpath is completely clogged by gyrolite precipitate at this time thereby preventing effective pH buffering of the infiltrating OPC affected leachate.*

Assuming (for the moment) a single component mass balance description of quartz dissolution and approximately constant porosity, the reactive transport of dissolved silica in the matrix is described by:

$$\varepsilon_p \frac{\partial C^*}{\partial t} - D_e \frac{\partial^2 C^*}{\partial z^2} = k_+ A_m \left(1 - \frac{C}{C_{eq}}\right) \qquad \text{(A-8)}$$

Here, the variable C^* is used to denote the total concentration, whereas C represents the free concentration of non-complexed $SiO_{2\,(aq)}$. The parameter C_{eq} is the free concentration at equilibrium. The total concentration is always higher than the free concentration on account of aqueous complexation reactions and the relation between free and total concentration may be expected to vary along a migration path as a function of groundwater composition. In the SRTBC simulations discussed

previously, the free concentration of $SiO_{2\,(aq)}$ was typically found to comprise anywhere between 2–98% of the total concentration when tracked along a migration path. To account for the speciation of $SiO_{2\,(aq)}$, we therefore define the following relation:

$$\zeta = C/C^* \tag{A-9}$$

A rigorous solution of Equation A-8 would require the spatial variability of ξ to be accounted for. For the purposes of the current discussion, however, we make an approximation by assuming a conservatively low (constant) value of ξ that would tend to underestimate the rate of quartz equilibrium approach. Although the far-from-equilibrium kinetic constant, k_+ (mol/m^{2}y) also varies along a flowpath (i.e. it is dependent on pH), it is also sufficient to consider it as a constant in the current discussion and set to a conservatively low value for the pH range under consideration. On the basis of these approximations and assuming steady-state conditions, Equation A-8 simplifies to:

$$\frac{\partial^2 C}{\partial z^2} \approx -\frac{k_+ A_m}{D_e}\zeta\left(1-\frac{C}{C_{eq}}\right) \tag{A-10}$$

For a Dirichlet boundary condition ($C\,(z = 0) = C_0$), the solution to Equation A-10 is:

$$C(z) = C_{eq} + \left(C_0 - C_{eq}\right)\exp\left(-\phi z\right) \tag{A-11}$$

where,

$$\phi = \sqrt{\frac{k_+ A_m}{D_e C_{eq}/\zeta}} \tag{A-12}$$

For a rock matrix of limited extent, δ_m the solution to Equation A-10 would be:

$$C(z) = C_{eq} + \left(C_0 - C_{eq}\right)\frac{\cosh\left(-\phi\left(\delta_m - z\right)\right)}{\cosh\left(-\phi\delta_m\right)} \tag{A-13}$$

The parameter ϕ occurs frequently in the chemical engineering literature where is is often referred to as the Thiele modulus. Equation A-10 (or A-13) essentially describes the distance over which the quartz dissolution reaction approaches an equilibrium state in the rock matrix. For our current purposes it is sufficient to note that the dynamics of the coupled reactive transport problem (neglecting changes in porosity) is closely related to this parameter group. On the basis of this analysis, we might expect the case of reduced reactive surface area, A_m to exhibit similarities to that of increased diffusivity, D_e provided ϕ is constant in both cases. Although this is not necessarily true for multicomponent systems in general, it is a useful place to start when attempting to deconstruct the dynamics of the present system as it has been modelled. This is mainly because the kinetic rates of secondary mineral precipitation-dissolution have been chosen to be sufficiently fast relative to quartz dissolution that the quartz dissolution is the rate limiting step in the reactive transport calculations.

The Thiele modulus, however, does not tell the full story since the dimensionless mass balance for the transport of dissolved silica says nothing about the rate of porosity closure or increase. In our case, quartz is dissolved and replaced by gyrolite which occupies a greater specific volume than quartz per mole of Si content. Gyrolite and quartz are initially undersaturated at the fracture surface owing to the imposed Dirichlet boundary condition of constant component concentrations (corresponding to the OPC leachate). As the primary mineral quartz dissolves, the porewater concentration of $SiO_{2\,(aq)}$ increases over a small distance until gyrolite reaches saturation, at which point it begins to precipitate. Since the rate of gyrolite precipitation is set high relative to the quartz dissolution rate, the rate of quartz dissolution governs the rate of gyrolite precipitation which is maintained approximately at its equilibrium saturation level.

The rate of porosity closure is related to the magnitude of the kinetic rate and reactive surface area product, k_+A_m for the quartz dissolution. Close to the fracture surface where gyrolite is undersaturated, there is a net loss of Si from the rock matrix giving an increase in porosity. In the zone where gyrolite precipitates, the amount of Si in the rock matrix is roughly constant since the gyrolite precipitation consumes all available Si from the quartz dissolution. The specific volume of gyrolite is roughly twice that of quartz (per mole of Si) giving a net decrease in porosity. In the 1D simulations, a gyrolite

precipitation front forms a short distance into the rock matrix rather than at the fracture surface itself as appears to be the case in the 2D reactive transport simulations described in the previous section. This is due to the Dirichlet (constant concentration) boundary condition in the 1D simulations which forces undersaturation of gyrolite at the fracture surface.

To understand these interacting processes in more detail, a number of different case studies have been defined to examine the relation between effective diffusivity (D_e), the limiting far-from equilibrium kinetic rate of quartz reaction (k_+A_m), and fractional equilibrium approach at the fracture surface (boundary condition). These cases are listed in Table A-3. Based on the discussions above, three characteristic performance measures were selected as being relevant to the sensitivity analysis, these were:

- Distance from fracture surface to the onset of gyrolite precipitation front.
- Width of gyrolite precipitation front.
- Time to pore closure resulting from gyrolite precipitation.

These performance measures are relevant to the current discussion since they relate to the choice of grid discretisation and also since they provide an insight into how the key processes are affected by changes in the underlying model parameters.

In addition to the parameter variation case studies listed in Table A-3, two additional simulation cases were defined where the impact of grid discretisation was assessed. In these simulations, the base case parameter set (Case 1) was run with the coarse grid discretisation of 10 µm and 100 µm initial cell sizes (i.e. analogous to the matrix grid settings of the SRTBC_73486161635 and SRTBC_73486161860 simulations presented in the previous sections).

A useful additional performance measure is the total amount of mineral dissolved or precipitated within the rock matrix per unit area of fracture surface, Δm (mol/m^2). This is given by the integral:

$$\Delta m = \frac{\delta_m}{V_m}\int_0^1 \left(\phi_m - \phi_m^0\right) d\zeta \qquad \text{(A-14)}$$

The integral can be readily evaluated using the tabulated mineral volumes output by CrunchFlow. For the simple four component system discussed here, alkalinity can be defined as (e.g. Stumm and Morgan 1996):

$$\begin{aligned}\left[\mathrm{Alk}\right] &= \left[\mathrm{HCO_3^-}\right] + 2\left[\mathrm{CO_3^{2-}}\right] + \left[\mathrm{OH^-}\right] - \left[\mathrm{H^+}\right] + \left[\mathrm{HSiO_3^-}\right] \\ &= 2\left[\mathrm{Ca^{2+}}\right]\end{aligned} \qquad \text{(A-15)}$$

Since two moles of Ca^{2+} are consumed for each mole of gyrolite precipitated, the total rate of alkalinity consumption (mol/m^{2}y) in the rock matrix would then be given by:

$$R_{Alk} = \frac{\delta_m}{V_m}\cdot\frac{d}{dt}\int_0^1 \left(\phi_m - \phi_m^0\right) d\zeta \qquad \text{(A-16)}$$

The rate of alkalinity consumption is also a useful performance measure in that it can be used to make inferences about the efficiency of pH buffering along a flowpath in response to parameter variations studied in this section.

Results for base case (Case 1) parameter settings

Figure A-27 shows the distribution of gyrolite at different contact times ranging from 4 days to 10 years for the base case parameter values (Case 1). The case where porosities are updated in each time step and the case of constant matrix porosity are shown in the figure to illustrate the impact of pore space closure. Since the amount of quartz dissolved at short times is quite small relative to the initial inventory in the rock matrix, it is more useful to plot the change in quartz volume in the system. Figure A-28 shows the absolute change in quartz mineral volume (% dissolved) as a function of distance in the rock matrix at different times. Also shown is the total amount of mineral dissolved or precipitated in the rock matrix.

Table A-3. Transport and reaction parameters assumed in 1D exploratory case studies. The shading in the far right-hand column is colour-coded to indicate cases which should exhibit dynamic similarity with regard to equilibration distance for the coupled reactive transport problem. Simulations have been made for variable material properties (i.e. feedback between porosity, effective diffusivity, and reactive surface area) as well as for the limiting case of constant porosity fixed at its initial value (0.1%).

Case #	C_0 (mol/L)	k (mol/m²s)	Am (m²)	D_e (m²/s)	k A_m/D_eC_{eq} (1/m²)
1	$1\cdot10^{-20}$	$5.14\cdot10^{-12}$	$1.65\cdot10^{4}$	$1\cdot10^{-14}$	$2.7\cdot10^{4}$
2	$1\cdot10^{-20}$	$5.14\cdot10^{-12}$	$1.65\cdot10^{4}$	$1\cdot10^{-13}$	$8.5\cdot10^{3}$
3	$1\cdot10^{-20}$	$5.14\cdot10^{-12}$	$1.65\cdot10^{2}$	$1\cdot10^{-14}$	$2.7\cdot10^{3}$
4	$1\cdot10^{-20}$	$5.14\cdot10^{-12}$	$1.65\cdot10^{3}$	$1\cdot10^{-14}$	$8.5\cdot10^{3}$
5	$1\cdot10^{-4}$	$5.14\cdot10^{-12}$	$1.65\cdot10^{4}$	$1\cdot10^{-14}$	$2.7\cdot10^{4}$
6	$1\cdot10^{-4}$	$5.14\cdot10^{-12}$	$1.65\cdot10^{4}$	$1\cdot10^{-15}$	$8.5\cdot10^{4}$
7	$1\cdot10^{-4}$	$5.14\cdot10^{-12}$	$1.65\cdot10^{4}$	$1\cdot10^{-12}$	$2.7\cdot10^{3}$
8	$1\cdot10^{-20}$	$5.14\cdot10^{-12}$	$1.65\cdot10^{4}$	$1\cdot10^{-12}$	$2.7\cdot10^{3}$
9	$1\cdot10^{-20}$	$5.14\cdot10^{-12}$	$1.65\cdot10^{4}$	$1\cdot10^{-15}$	$8.5\cdot10^{4}$
10	$1\cdot10^{-20}$	$5.14\cdot10^{-12}$	$1.65\cdot10^{3}$	$1\cdot10^{-13}$	$2.7\cdot10^{3}$
11	$1\cdot10^{-20}$	$5.14\cdot10^{-12}$	$1.65\cdot10^{2}$	$1\cdot10^{-13}$	$8.5\cdot10^{2}$

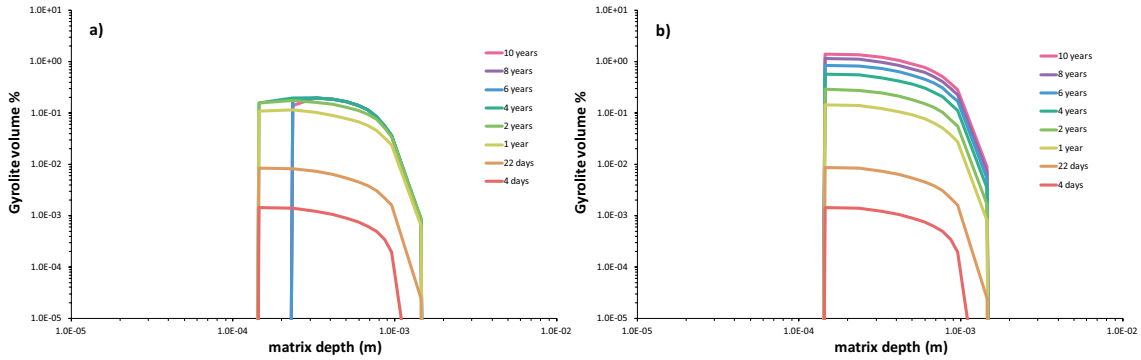

Figure A-27. *Distribution of gyrolite at different times for a) variable material properties, and b) assumed fixed porosity. Plotted data correspond to Case 1 in Table A-3 (base case material properties).*

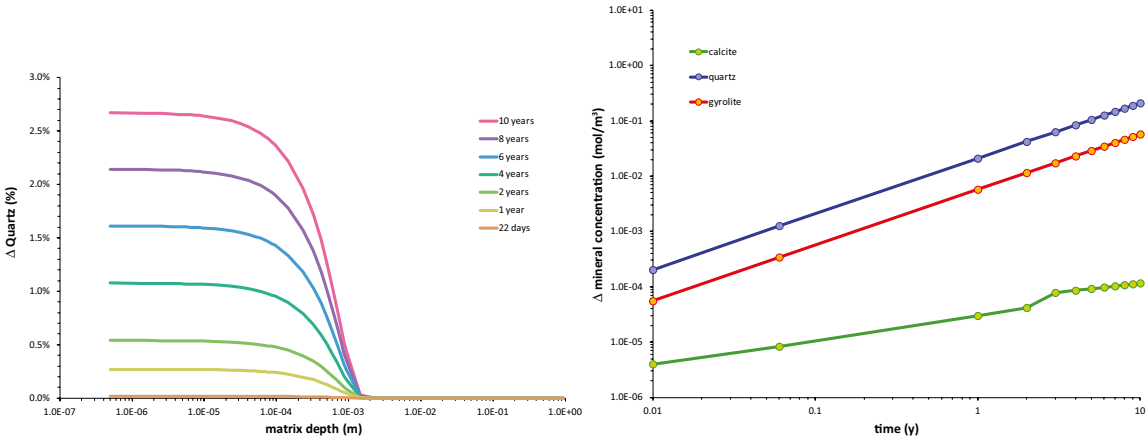

Figure A-28. *a) absolute change in quartz distribution (% dissolved) relative to initial inventory as a function of distance in the rock matrix at different times, and b) total change in mineral inventory (absolute values) as a function of time estimated using Equation A-14 (broken lines show the corresponding results for the non-updated porosity case). Plotted data correspond to Case 1 in Table A-3 (base case material properties).*

It is interesting to note that the amount of quartz dissolved continues to increase even after the precipitation of gyrolite reaches a plateau due to pore closure. This is due to the quartz remaining on the fracture side of the pore blockage which continues to dissolve with the dissolved silica back-diffusing to the fracture boundary. A slight decrease in the amount of gyrolite in the system also occurs at later times (after the blockage event). This seems to be due to a redistribution of gyrolite at the leading and trailing edges of the gyrolite precipitation zone. Most of the change occurs on the fracture side of the blockage, although a small amount may also dissolve and be redistributed on the matrix side (this is not visible in Figure A-27 although it can be inferred from the mineral reaction rates).

To understand why this occurs it is useful to plot the saturation index for the reactive minerals at different times to illustrate the regions where precipitation and dissolution are actively occurring. The saturation index for calcite, quartz and gyrolite is shown in Figure A-29 as a function of matrix depth for a contact time of 22 days and 10 years, respectively which illustrates the redistribution of the minerals during this time period. On the leading edge of the gyrolite precipitation zone, there is continuing depletion of quartz as can be inferred from the changing saturation index profile in the matrix. The corresponding matrix concentration profiles of reactive components are shown in Figure A-30. The highly variable total concentration of $SiO_{2\,(aq)}$ in the vicinity of the reaction front is related to the predominance of different complexed forms of $SiO_{2\,(aq)}$ at different pH levels. The discontinuity in the concentration profiles at the interface of the pore blockage is clearly evident at 10 years.

Figure A-31 shows the distribution of matrix porosity as a function of distance in the rock matrix at different times plotted on both log-log and log-linear axes to illustrate the relevant changes relating to porosity increase near the fracture surface and decrease at the gyrolite precipitation front.

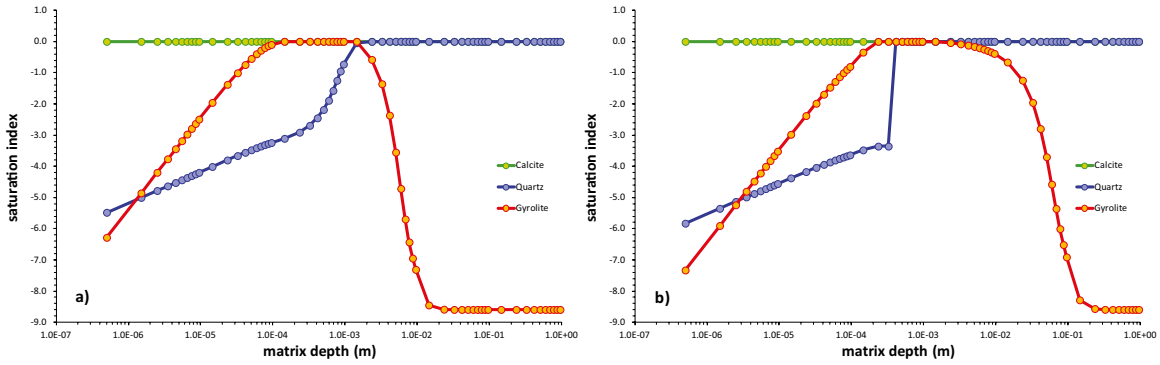

Figure A-29. *a) saturation index for calcite, quartz and gyrolite plotted as a function of distance in the rock matrix at 22 days contact time, and b) 10 years contact time. Plotted data correspond to Case 1 in Table A-3 (base case material properties).*

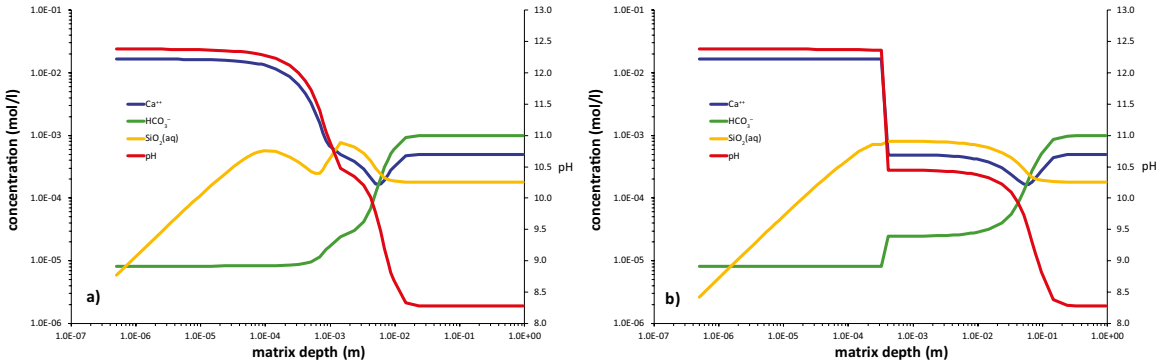

Figure A-30. *Concentration profiles of reactive components (total concentrations) in the rock matrix for a) a contact time of 22 days, and b) a contact time of 10 years. The discontinuity in aqueous phase concentrations at the blockage is clearly apparent in b).*

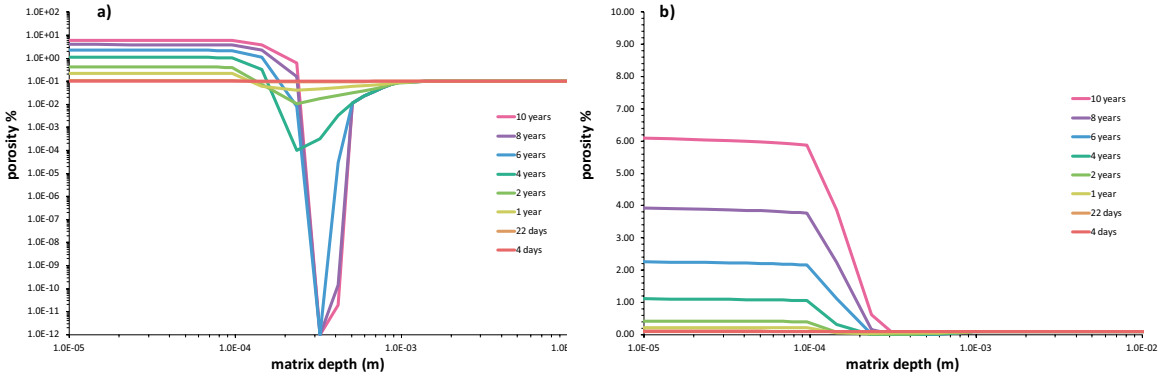

Figure A-31. *Distribution of porosity at different times for the variable material properties case shown on a) log-log axes, and b) log-linear axes. Plotted data correspond to Case 1 in Table A-3 (base case material properties).*

Impact of varied reactive surface area, A_m

For the sensitivity case studies where reactive surface area is reduced, while the effective diffusivity is held constant at the base case value (10^{-14} m^2/s), the main effect is an increase in the time required for pore closure to occur. There is also an increase in the depth to the onset of gyrolite precipitation, an increase in the precipitation zone width, and a decrease in both the peak amount and total amount of gyrolite precipitated. Figure A-32 shows the impact on the location and size of the gyrolite precipitation front.

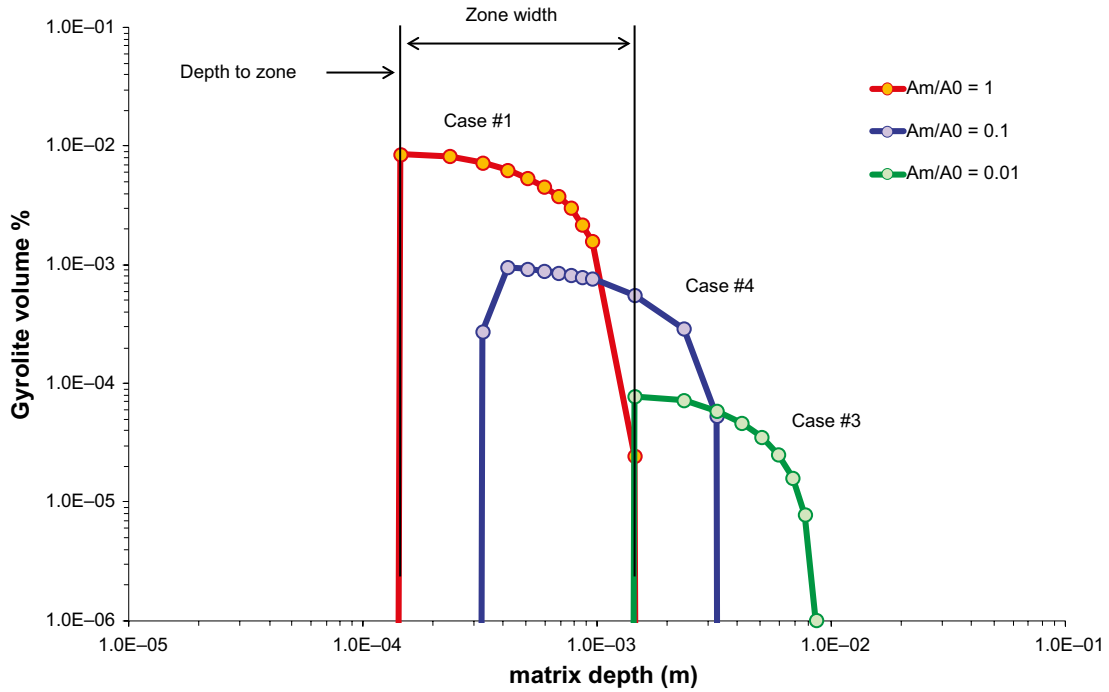

Figure A-32. *Impact of varying reactive surface area (A_m) relative to the base case reactive surface area (A_0) at 22 days contact time. The reduced rate of quartz dissolution at lower surface area causes the gyrolite precipitation zone to recede further into the rock matrix and also results in a larger band of gyrolite precipitation. A reduction in reactive surface area also results in a lower overall rate of gyrolite precipitation and consequently longer pore closure times.*

Impact of varied effective diffusivity, D_e

When the effective diffusivity is varied while reactive surface area is held constant, the pore closure time is not affected significantly. Increasing effective diffusivities, however, cause the gyrolite precipitation front to retreat further into the rock matrix and also increases the precipitation zone width. It is interesting to note that the total amount of gyrolite precipitated increases as a function of increasing effective diffusivity, although the peak mineral volume is approximately constant which explains why closure time is not affected.

Impact of varied boundary condition

Varying the magnitude of initial quartz disequilibrium at the fracture surface was found to have no discernable impact on the closure time, on the shape, or location of the gyrolite precipitation zone for boundary concentrations of $SiO_{2\,(aq)}$ in the range 10^{-20}–10^{-4} mol/l. This, however, is a highly artificial boundary condition since the concentrations of the other reactive components were held constant. In actuality, they are also expected to vary along a flowpath in response to the saturation state of quartz. In order to account for this, an additional set of 1D matrix diffusion simulations were performed where the Dirichlet boundary condition was assigned from flowpath concentration profiles obtained from an independent 1D advective simulation (without matrix diffusion). Figure A-34 shows the variation of the reactive component total concentrations and pH as a function of quartz saturation index achieved along the 1D flowpath. The 17 circular markers indicate the specific cases studied.

Varying the concentrations of the other reactive components together with the initial $SiO_{2\,(aq)}$ concentration was found to have a relatively large impact on the behaviour observed in the 1D diffusive simulations. Matrix profiles of precipitated gyrolite are shown in Figure A-35. Interestingly, the initial gap in the rock matrix before onset of gyrolite precipitation was only observed for the lowest quartz saturation index (–4.5). In all the other cases studied where gyrolite precipitation occurred, theprecipitation zone was found to initiate already at the fracture surface in a similar fashion to the 2D SRTBC simulations described in previous sections. The corresponding rates of steady-state alkalinity consumption are shown in Figure A-36.

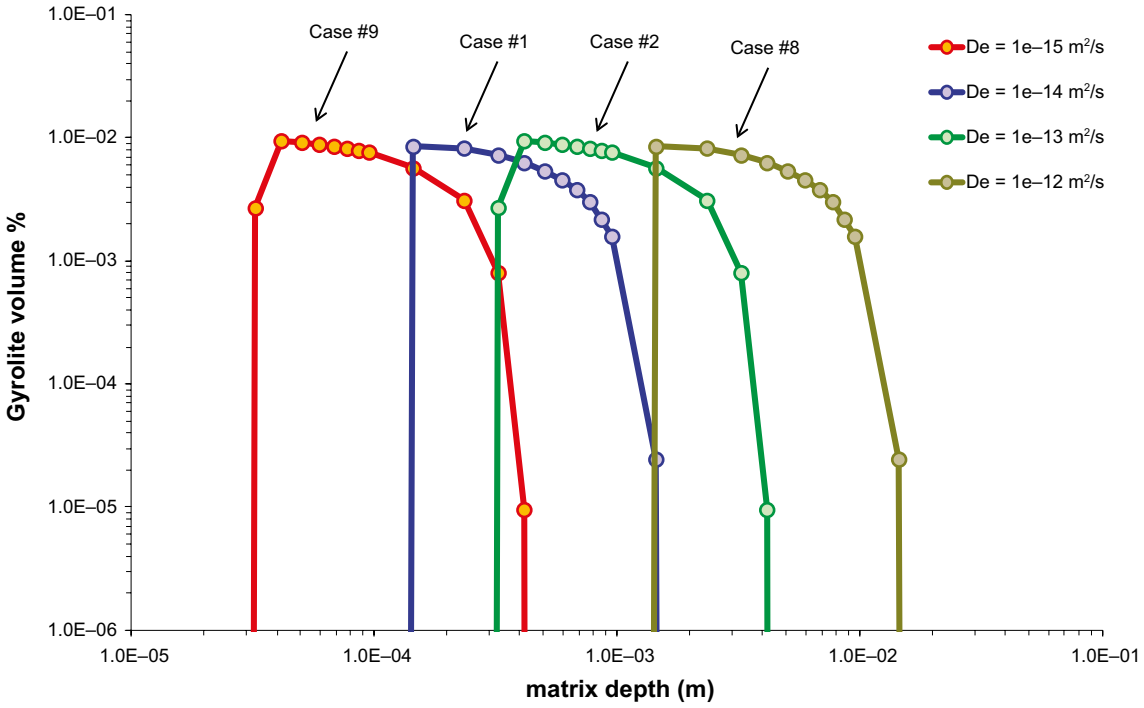

Figure A-33. *Impact of varying the effective diffusivity (D_e) at 22 days contact time. The main effect is to cause the gyrolite precipitation zone to recede further into the rock matrix and also results in a larger band of gyrolite precipitation. Although the total amount of gyrolite precipitated increases with increasing D_e, the peak mineral volume remains approximately constant.*

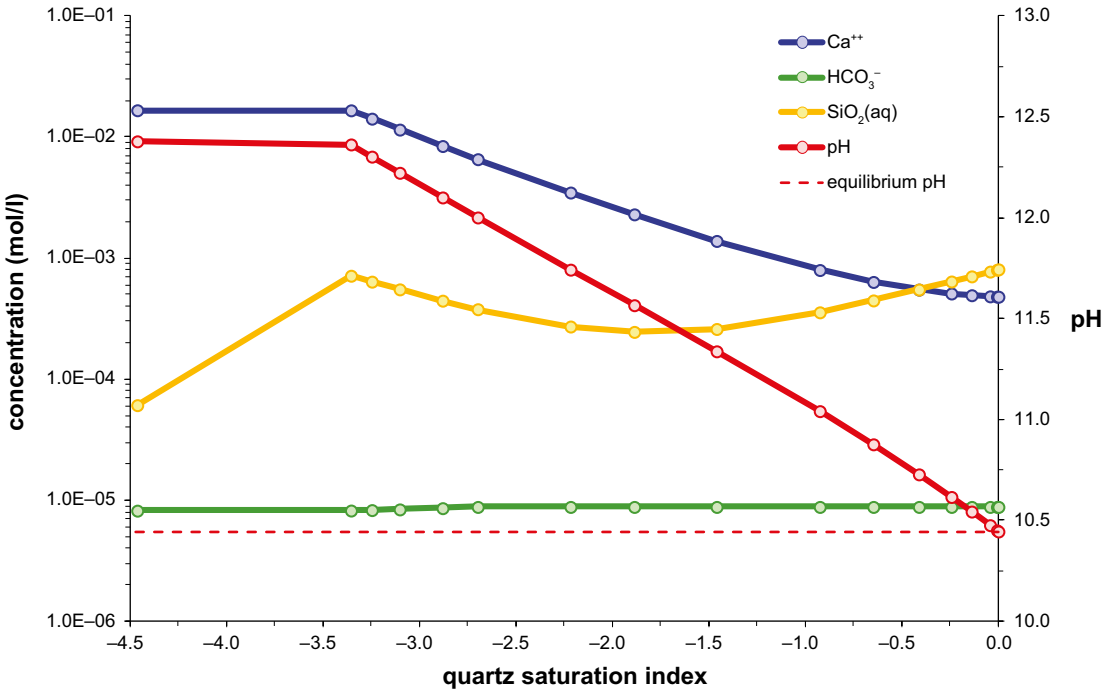

Figure A-34. *Variation of total Ca^{2+}, HCO_3^-, $SiO_{2\,(aq)}$ concentration and pH of groundwater as a function of quartz saturation index along a 1D advective flowpath calculated using CrunchFlow. Circular markers indicate compositions for the 17 additional 1D matrix diffusion simulations performed to investigate the role of the fracture boundary condition.*

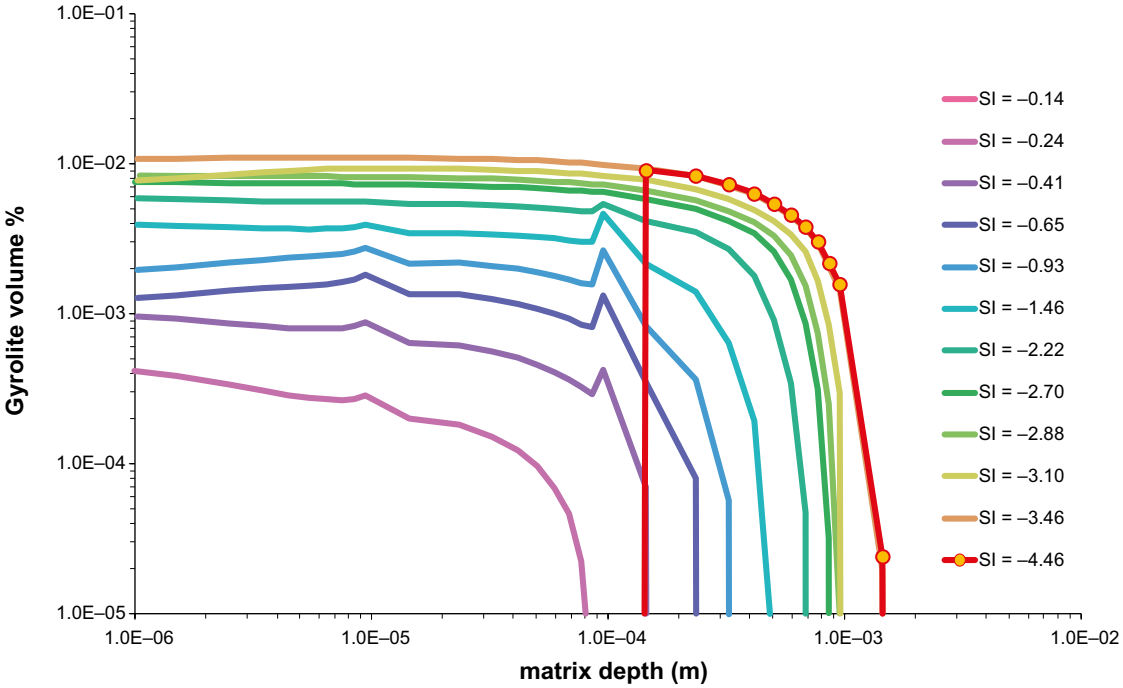

Figure A-35. *Distribution of gyrolite precipitate as a function of matrix depth for different quartz saturation indices at the fracture boundary (boundary concentrations of other reactive component are interpolated from the data in Figure A-34). The plotted data are for a contact time of 22 days.*

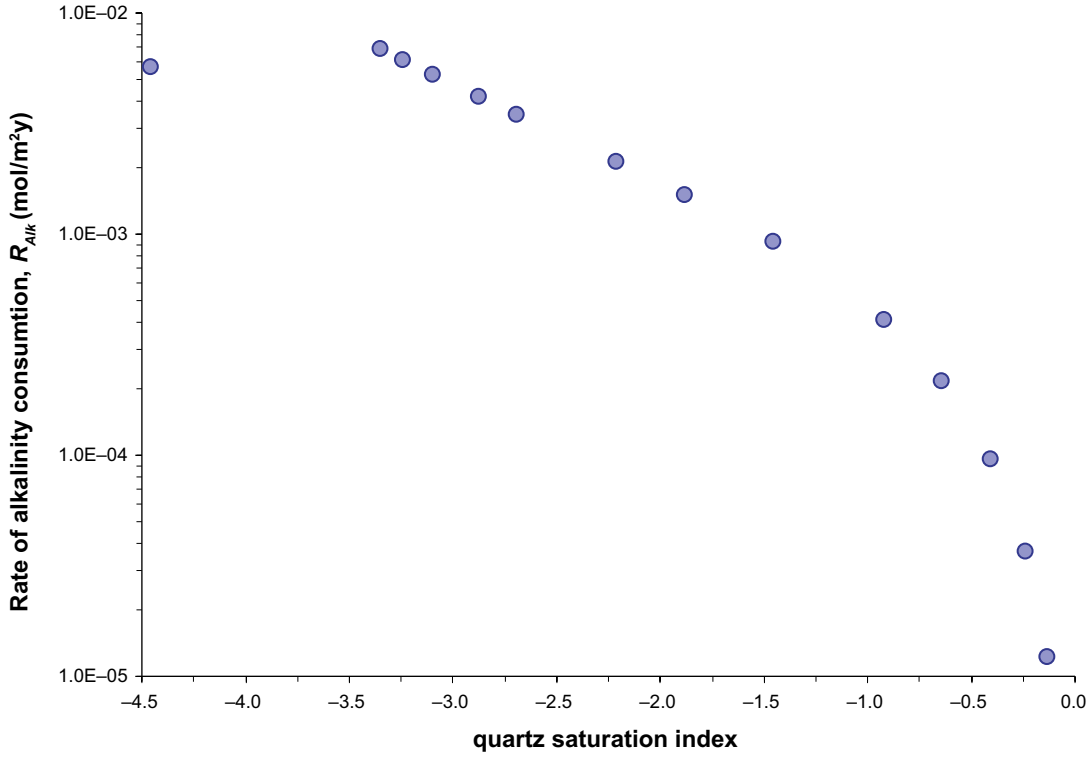

Figure A-36. *Steady-state rate of alkalinity consumption for different quartz saturation indices at the fracture boundary (boundary concentrations of other reactive components were interpolated from the data in Figure A-34).*

Impact of grid discretisation

In the 1D matrix diffusion simulations, the choice of grid discretisation with initial cell dimensions of 1 µm, 10 µm, or 100 µm (corresponding to the 2D grid discretisation cases) had no discernable impact on the closure time, on the shape, or location of the gyrolite precipitation zone.

Impact of combined parameter variations

When the different performance measures for the 1D matrix diffusion simulations are plotted as a function of the ϕ parameter (Equation A-12), clear systematic behavior can be discerned. Both the depth to the onset of gyrolite precipitation and the width of the gyrolite precipitation zone are shown to be approximately inversely correlated with ϕ (see Figure A-37 and Figure A-38). The time to pore closure, on the other hand, was found to be more or less independent of the effective diffusivity although strongly correlated with reactive surface area. Regression analysis of the data indicated a power law relation between time to pore closure and reactive surface area with an exponent of –0.75. Decreasing the reactive surface area by a factor of 10 therefore gives an increase in the pore closure time of about a factor of 6.

A5 On the rate of steady state alkalinity consumption and a possible “short cut” method

When the rate of alkalinity consumption in the 1D matrix diffusion simulations is numerically evaluated using Equation A-16, it is generally found that the rate approaches an approximately constant value after a brief initial transient period. In the simulations described in the previous section, the steady state was usually observed to occur by about 22 days contact time. The rate of alkalinity consumption then only starts to plateau when sufficient gyrolite has precipitated that the porosity starts to decrease significantly. In the simulations assuming a constant porosity, no such plateau occurs and the rate of alkalinity consumption remains constant with increasing time. In these cases, however, the results might be considered physically non-meaningful given that this would imply negative porosities.

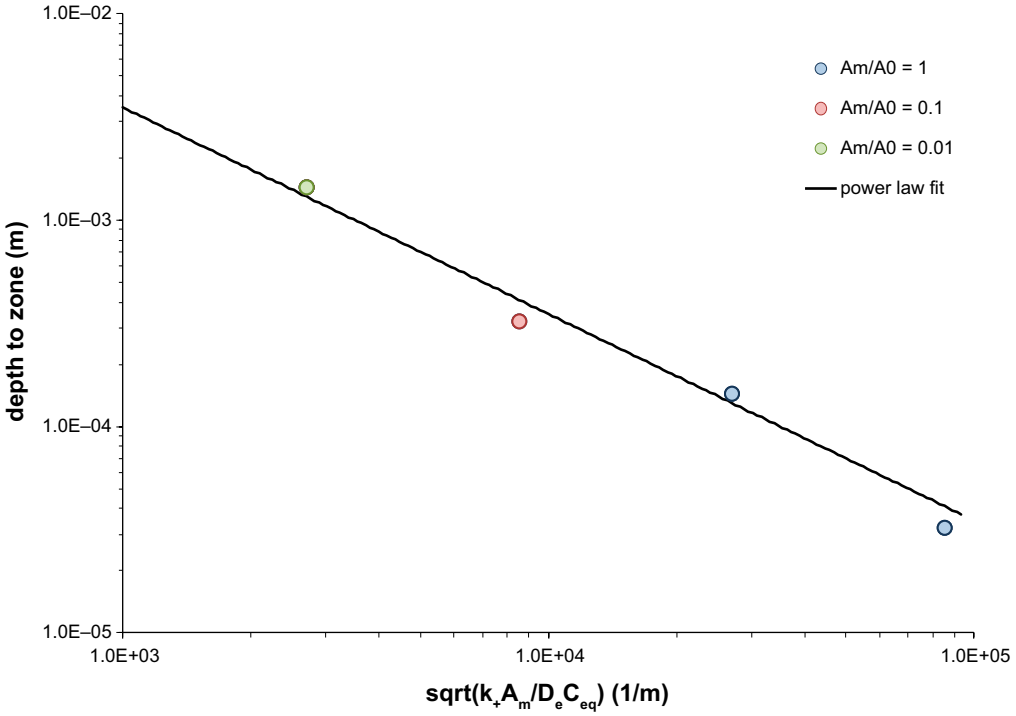

Figure A-37. *Depth to onset of gyrolite precipitation zone for the different cases studies listed in Table A-3 as a function of the reaction parameter ϕ (Equation A-12). The power law curve fit has an exponent of –1 indicating an approximately inverse relation between the precipitation zone width and ϕ.*

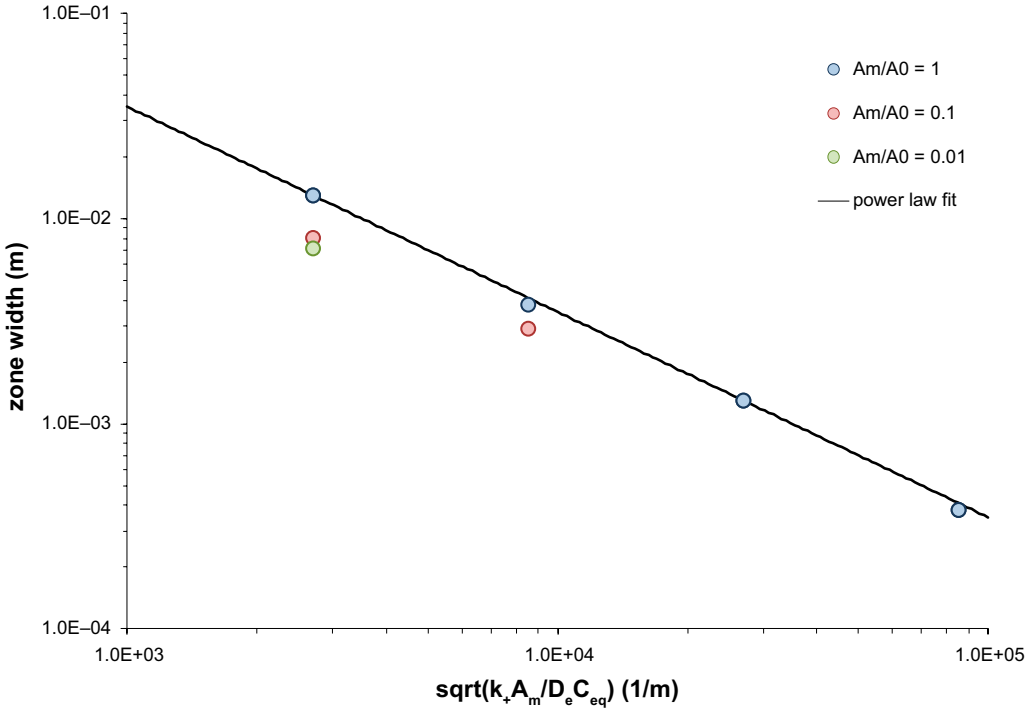

Figure A-38. *Gyrolite precipitation zone width for the different cases studies listed in Table A-3 as a function of the reaction parameter ϕ (Equation A-12). The power law curve fit has an exponent of –1 indicating an approximately inverse relation between the precipitation zone width and ϕ.*

The approximately constant rate of alkalinity consumption for the constant concentration boundary condition suggests that the zone of gyrolite precipitation achieves a quasi stationary state, and does not change significantly until pore closure starts to have a significant impact on the transport properties of the rock matrix. Regression analysis of the data suggested that the steady-state rate of alkalinity consumption could be correlated with effective diffusivity and reactive surface area in the following fashion:

$$R_{Alk} \propto \sqrt{\frac{D_e k_+ A_m}{C_{eq}}} \ \text{(mol/m}^2\text{y)} \tag{A-17}$$

The steady-state rate of alkalinity consumption is plotted in Figure A-40 together with a regression line confirming the empirical correlation with the diffusion-reaction parameter group (Equation A-17). Interestingly, the parameter dependency exhibited by the correlation Equation A-17 is identical to what we would expect if the quartz dissolution is the primary rate controlling variable in the system.

If it is assumed that the steady-state concentration profile given by Equation A-11 is approximately valid, the steady-state flux of total dissolved silica at the fracture surface can be shown to be:

$$N_{Si} = -\left(C_0 - C_{eq}\right)\frac{1}{\zeta}\sqrt{\frac{D_e k_+ A_m}{C_{eq}/\zeta}} \tag{A-18}$$

In the case of a rock matrix of limited extent, we would have instead:

$$N_{Si} = -\left(C_0 - C_{eq}\right)\frac{1}{\zeta}\sqrt{\frac{D_e k_+ A_m}{C_{eq}/\zeta}} \cdot \tanh\left(\delta_m \sqrt{\frac{k_+ A_m}{D_e\, C_{eq}/\zeta}}\right) \tag{A-19}$$

The form of the equation describing silica flux at the fracture surface and its similarity to the empirical relation describing alkalinity consumption (Equation A-17) indicates that there is a direct correspondence between the rate of quartz dissolution and the rate of pH buffering. This also suggests that it is only necessary to know the saturation state of quartz to be able to compute the pH of groundwater being transported in a fracture by advective flow (given that the secondary minerals gyrolite and calcite react sufficiently fast that they can be assumed to be in equilibrium). The correlation between Ca^{2+}, pH and quartz saturation index is shown in Figure A-34 for the quartz/gyrolite/calcite system.

Although the 1D simulations consider a fixed concentration boundary condition, the linear form of the flux Equation A-18 (or A-19) implies that the steady-state differential mass balance of free silica along a flowpath can be written as:

$$v\frac{dC}{dx} - D_L\frac{d^2C}{dx^2} + \frac{2}{\delta_t}\sqrt{\frac{D_e k_+ A_m}{C_{eq}/\zeta}}\left(C - C_{eq}\right) = 0 \tag{A-20}$$

This can also be written in terms of the overall flowpath F-factor as:

$$\frac{dC}{\partial\theta} - \frac{1}{\mathrm{Pe}}\frac{d^2C}{d\theta^2} + F\sqrt{\frac{D_e k_+ A_m}{C_{eq}/\zeta}}\left(C - C_{eq}\right) = 0 \tag{A-21}$$

Where, Pe is the Péclet number for dispersive mixing, F (y/m) is the flowpath F-factor, and θ is the fractional distance along the flowpath of length L (i.e. $\theta = x/L$). The analytical solution to Equation A-21 can be given by analogy with the solution described in Fogler (1992) and Levenspiel (1972) for a first-order chemical reaction:

$$\chi = \frac{4a\exp\left(\mathrm{Pe}/2\right)}{\left(1+a\right)^2\exp\left(a\,\mathrm{Pe}/2\right) - \left(1-a\right)^2\exp\left(-a\,\mathrm{Pe}/2\right)} \tag{A-22}$$

where, the equilibrium approach χ is defined as:

$$\chi = \frac{C(z) - C_{eq}}{C_0 - C_{eq}} \tag{A-23}$$

and,

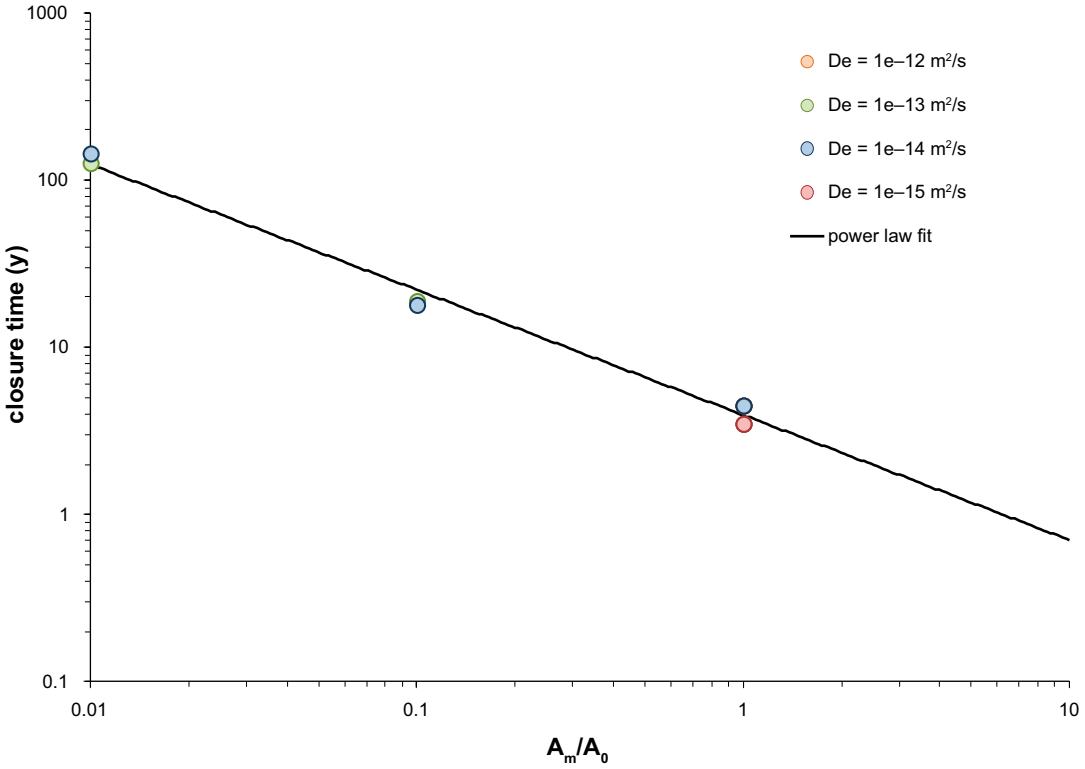

Figure A-39. *Porosity closure time estimated for the different cases studies listed in Table A-3 as a function of reactive surface area plotted relative to the base case value $A_0 = 1.65 \cdot 10^4$ m^2/m^3. The power law curve fit has an exponent of –0.75. An order of magnitude decrease in the reactive surface area therefore increases the time to pore closure by roughly a factor of 6.*

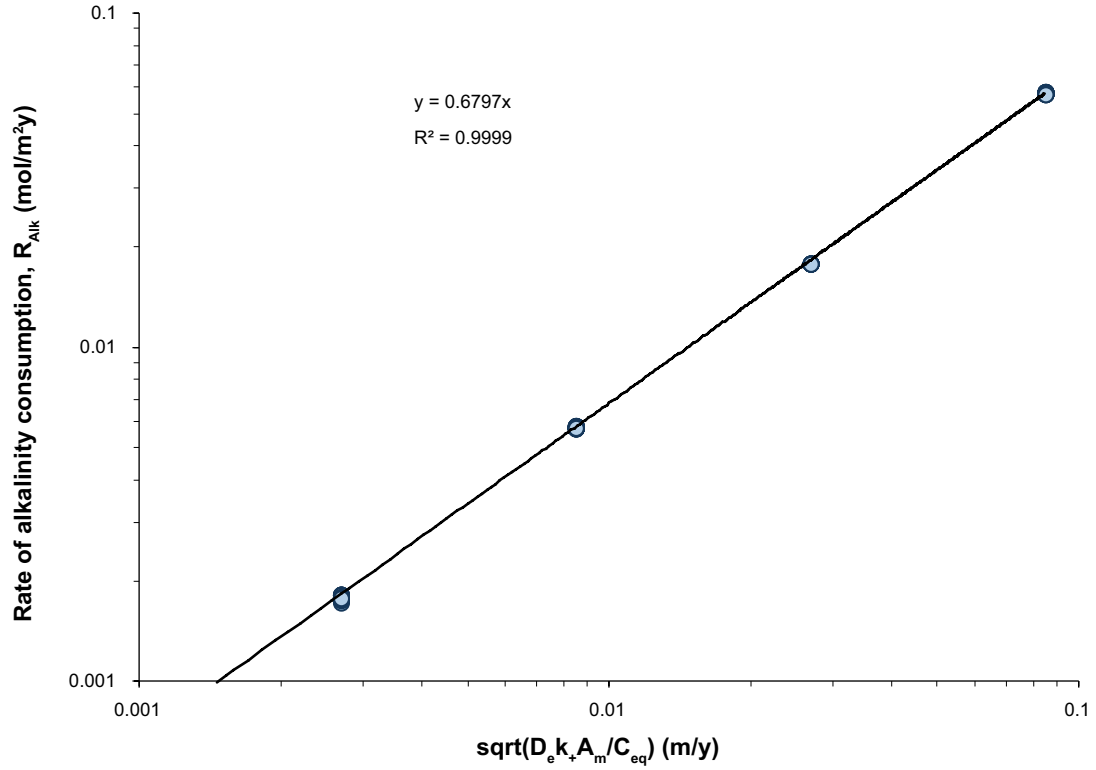

Figure A-40. *Steady-state rate of alkalinity consumption (contact time ≥ 1 year) estimated for the different 1D matrix diffusion case studies listed in Table A-3 and plotted as a function of the diffusion-reaction parameter group.*

$$a = \sqrt{1 + \left(\frac{4}{\mathrm{Pe}} \mathrm{Da} \right) \frac{x}{L}} \tag{A-24}$$

The dimensionless parameter Da in Equation A-24 is referred to as the Damköhler number in the chemical engineering literature (e.g. Fogler 1992) and essentially describes the ratio of the effective reaction rate to the rate of advective transport:

$$\mathrm{Da} = F \sqrt{\frac{D_e k_+ A_m}{C_{eq} / \zeta}} \tag{A-25}$$

The corresponding definition of the *a*-parameter for a rock matrix of limited extent is not given here, although it follows directly from Equation A-19. For high Péclet number flow (i.e. very little dispersion), the analytical solution for an unbounded rock matrix is:

$$\chi = \exp\left(-\mathrm{Da} \cdot \frac{x}{L} \right) \tag{A-26}$$

The saturation index of quartz can then be obtained from the expression:

$$SI_{quartz} = \log_{10}\left(1 + \frac{\left(C_0 - C_{eq} \right)}{C_{eq}} \chi \right) \tag{A-27}$$

If the inlet concentration, C_0 of dissolved silica is very small relative to the equilibrium concentration and there are only low to moderate levels of hydrodynamic dispersion, equation A-27 simplifies to:

$$SI_{quartz}(x) \approx \log_{10}\left(1 - \exp\left(-\mathrm{Da} \cdot \frac{x}{L} \right) \right) \tag{A-28}$$

Provided that the groundwater chemistry is dominated by quartz dissolution, the steady-state pH profile along the flowpath can be estimated by interpolation of the porewater chemistry profiles given in Figure A-34. Although neither Equation A-22 nor A-26 consider pore closure, they may be sufficiently accurate to use in screening calculations to identify situations where the material properties of the rock matrix would give rise to unacceptably poor pH buffering of the OPC leachate plume. For sufficiently high matrix effective diffusivity and reactive surface area this may not be an issue, although for low rock matrix effective diffusivities and low reactive surface area relative to the hydrodynamic conditions, the pH of groundwater reaching canister positions may exceed what might be considered acceptable.

As noted previously, the main assumptions in this derivation are:

- The variable ζ describing the ratio of free and total silica concentration can be treated as a constant and set to a low value ($\zeta \sim 0.02$) which conservatively overestimates the equilibration distance for quartz dissolution;
- The pH-dependent, far-from-equilibrium kinetic constant k_+, can be treated as a constant and set to a low value ($k_+ \sim 2.7 \cdot 10^{-4}$ mol/m^{2}y at pH 10.44) which conservatively overestimates the equilibration distance for quartz dissolution.

Taken together, these simplifications give rise to a greater quartz equilibration distance (by about an order of magnitude) than what would be obtained if these parameters were correctly integrated over the migration path. An additional assumption implicit in this treatment is the requirement that gyrolite is present everywhere downstream (along the flowpath) from the reaction front where quartz reaches equilibrium. In reality, the precipitation of gyrolite will cease downstream of the quartz equilibration front although matrix diffusion will continue for some time to deplete the fracture concentration of Ca^{2+} along the flowpath thereby giving transient downstream pH values slightly lower than the nominal gyrolite equilibrium value of pH 10.44.

Figure A-41 shows the dependency of the steady-state pH profile on the reactive surface area for the base case F-factor of $4 \cdot 10^5$ y/m and a Péclet number of 10. The pH values were calculated by interpolation of the chemistry data in Figure A-34 using Equations A-22 and A-27 to estimate the quartz saturation index along the flowpath. Dispersion appears to have very little impact on the calculated pH profiles with the results for Pe = 10 being indistinguishable from the limiting case of no dispersion (Equation A-26). The pH profiles show that decreasing the reactive surface area by a factor of 10, increases the equilibration distance roughly by a factor of 3 (i.e. $\sqrt{10} \approx 3.16$). Figure A-42 shows the dependency of the steady-state pH profile on the flowpath F-factor for the base case reactive surface area of $1.65 \cdot 10^4$ m^2/m^3 and Pe = 10. Since the equilibration distance is inversely proportional to the F-factor, a factor of 10 decrease in the F-factor gives a commensurate increase in the equilibration distance.

A6 Summary of main results

In this appendix chapter, calculations of a simplified nature have been made in support of the detailed simulation studies documented in the main report. The aim of this work was twofold:

1. To explore the role of discretisation in both the advective and diffusive domains with the aim of improving confidence in the accuracy of the numerical results for the more detailed calculation cases documented in the main report.
2. To examine the performance of the numerical models for simplified, limiting cases where analytical solutions could be derived independently and compared. The main focus here was to improve overall process understanding and enhance the transparency of results for more complex simulation cases featuring more detailed chemistry.

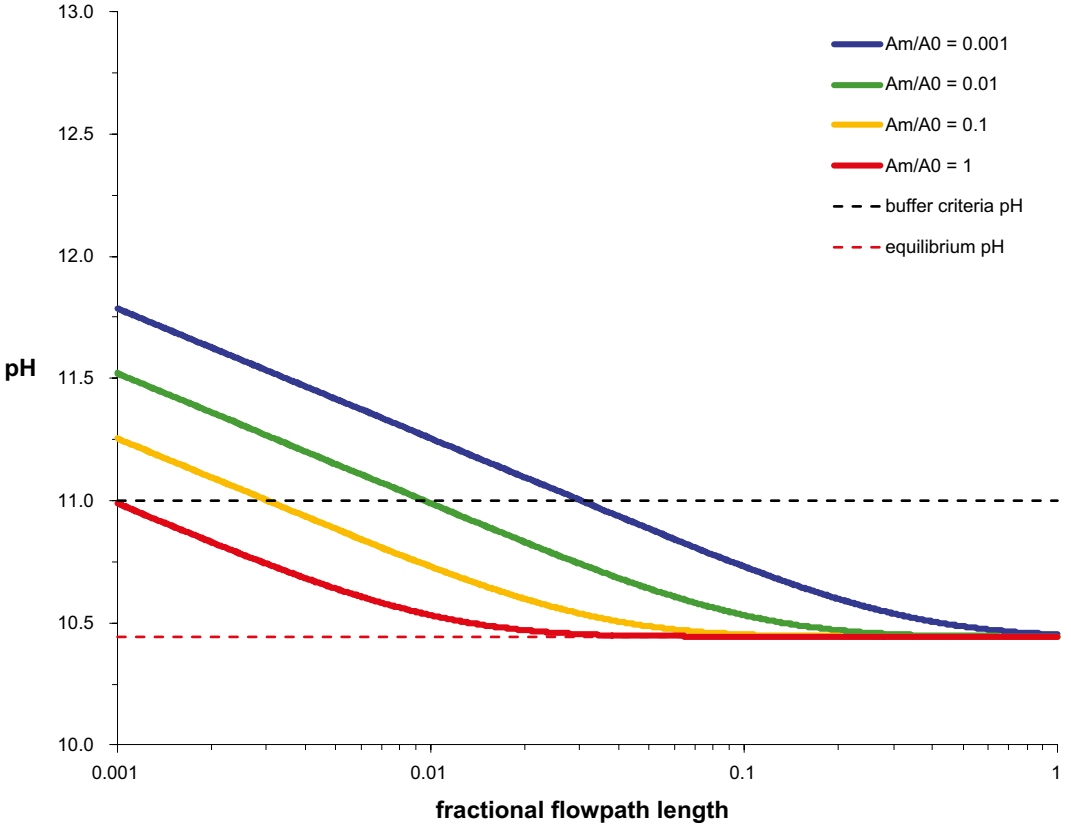

Figure A-41. *Steady-state pH plotted as a function of flowpath length for different reactive surface areas (A_m) relative to the base case ($A_0 = 1.65 \cdot 10^4$ m^2/m^3). Results are calculated using the analytical expression (Equation A-22) for the base case flowpath F-factor of $4 \cdot 10^5$ y/m and Pe = 10.*

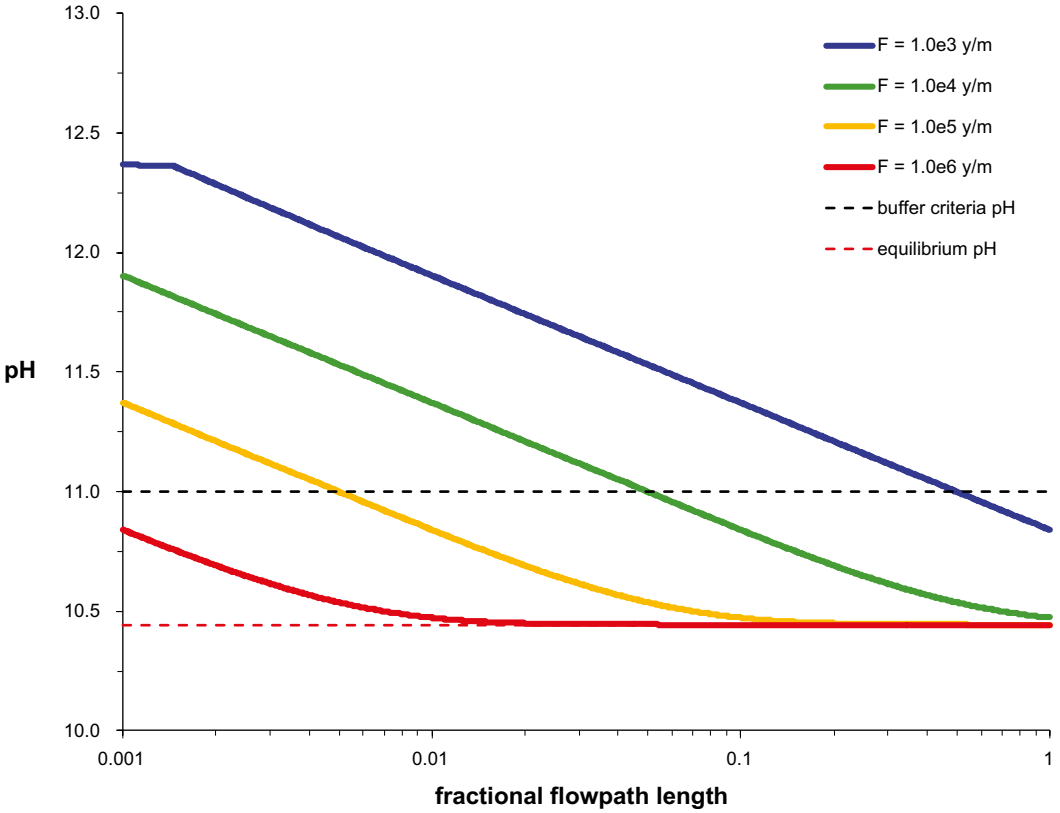

Figure A-42. *Steady-state pH plotted as a function of flowpath length for different flowpath F-factors. Results are calculated using the analytical expression (Equation A-22) assuming the base case reactive surface area $A_m = 1.65 \cdot 10^4$ m^2/m^3 and Pe = 10.*

The main outcomes of the work are summarised as follows:

- A reactive transport test case (RTTC) was defined to investigate the pH buffering effect that can be obtained by matrix diffusive mixing assuming calcite equilibrium in the absence of additional dissolution-precipitation reactions. Simulations using the CrunchFlow program (Steefel 2009) were made for a 100 m flowpath featuring advective cells of 1 m size and a nested logarithmic sequence of arithmetically spaced diffusive grid cells used to represent the rock matrix. Three different levels of rock matrix discretisation have been studied (with initial matrix grid cell sizes of 10 µm, 100 µm, 1 mm).
- Very close agreement was achieved for the transport of non-reactive components (used as internal standards) with an analytical result described by Tang et al. (1981). The results for the reactive components H^+, Ca^{2+}, and HCO_3^- indicate that very little pH buffering effect can be realised by way of matrix diffusive mixing only and breakthrough of the alkaline OPC-leachate plume is roughly the same as the advective travel time.
- The simulation results for the reactive components H^+, Ca^{2+}, and HCO_3^- were found to agree to a high degree of precision with a PHREEQC-based mixing model using the transport of the non-reactive, internal standard components as a proxy for the mixing fraction (Figure A-12). Very small deviations appear to be related to minor differences in the methods used to calculate aqueous phase activity coefficients in the different programs and the results can be considered, for all practical purposes, to be identical.
- The mineral mass balance for calcite in the RTTC simulations made with CrunchFlow was sensitive to the coarseness of the matrix grid discretisation. More refined grids were found to result in less "jitter" in the calculated spatial distribution of precipitated calcite. It is noted that the amount of calcite precipitated in the initially calcite-free rock matrix was very small (on the order of ~10^{-6} mol/L) and may not be of great significance.

- A simplified reactive transport base case (SRTBC) was defined to investigate the pH buffering effect obtained by enhanced dissolution of quartz in the basic pH range together with the precipitation of a secondary crystalline Ca-silicate phase, here assumed to be gyrolite. Simulations using the CrunchFlow program (Steefel 2009) were made for a 100 m flowpath featuring advective cells of 1 m size and a nested logarithmic sequence of arithmetically spaced diffusive grid cells used to represent the rock matrix. Three different levels of rock matrix discretisation have been studied (with initial matrix grid cell sizes of 1 μm, 10 μm, 100 μm).
- The CrunchFlow simulation results indicate effective buffering of pH over a short distance of, at most, a few tens of metres to the level determined by quartz/gyrolite/calcite equilibrium (pH~10.44). The steady state pH downstream of the reaction front was found to be stable for some period of time, although clogging of the first 0.1 mm of the rock matrix porosity with gyrolite eventually leads to breakthrough of non-buffered OPC leachate once the entire flowpath has become affected.
- The main uncertainty with regard to material properties appears to be the reactive surface area of quartz assumed in the model. The base case material properties assume a reactive surface area proportional to the volume percent of quartz in Forsmark metagranite and a measured BET surface area of 0.018 m^2/g of intact monolithic samples taken from the site.
- The results indicate an apparent sensitivity to the coarseness of the rock matrix grid discretisation, with the most refined grid (initial cell size of 1 μm) exhibiting breakthrough of high pH OPC leachate after roughly 750 years of flow. Coarser levels of matrix grid discretisation give longer times to pore closure (by about a factor of two or more) and breakthrough of the OPC front was not observed during the 1,000 year simulation time. All cases studied exhibited artefacts in the mineral mass balance which is speculated to be the result of interaction between steep reaction fronts, the coarseness of grid discretisation, and discrete time stepping.
- In order to understand the underlying mechanisms governing the behaviour observed in the SRTBC simulations, additional 1D diffusive simulations were made also using CrunchFlow. In these 1D simulations, parameters assumed to play an important role in the reactive transport problem were varied in a sensitivity analysis to study the impact on the distribution of secondary mineral precipitates in the rock matrix and time to pore closure (i.e. clogging of matrix porosity).
- The behaviour of the 1D system was found to be highly consistent with a quartz dissolution control mechanism with equilibrium precipitation of secondary minerals. The consumption of alkalinity was also found to correlate strongly with a well-known material property parameter group which could be derived by independent theoretical reasoning.
- The results suggested the possibility of a "shortcut" method to predict steady-state pH profiles for the quartz/gyrolite/calcite system based on a simple analytical model of quartz dissolution. It was found that the approach to quartz equilibrium along a flowpath can be described using a simple formula of the form

$$SI_{quartz}(x) \approx \log_{10}\left(1-\exp\left(-\mathrm{Da}\cdot\frac{x}{L}\right)\right)$$

where the dimensionless Damköhler number, Da is defined as:

$$\mathrm{Da} = F\sqrt{\frac{D_e k_+ A_m}{C_{eq}/\zeta}}$$

The steady-state pH can then be calculated using a suitable geochemical model (e.g. PHREEQC, CrunchFlow, or similar) as a function of the quartz saturation index assuming contemporaneous gyrolite and calcite equilibrium along the migration path. Small to moderate amounts of dispersion (Pe~10) was found to have almost no impact on the steady state profiles calculated. The analytical model can be used to screen hydrodynamic and material property parameter combinations which would likely lead to unacceptable pH buffering characteristics.

A7 Custom thermodynamic database for simplified scoping calculations

Since the CrunchFlow program utilizes a different database structure to that of TOUGHREACT and Pflotran, a custom written database was used for the simplified calculations. The database contained a reduced set of groundwater components and secondary species considered most important for the simulation of the reactive transport test case (RTTC) and simplified reactive transport base case (SRTBC) described in previous sections. Thermodynamic data were taken from the TOUGHREACT thermodynamic database "ther_ympR4d.dat". This, in turn, was based on reaction data contained in the EQ3/6 database used in the Yucca Mountain Project (Wolery and Jove-Colon 2004). Since the present calculations are for low temperature conditions, data were tabulated for the 0.01°C–35°C temperature range rather than the 0.01°C–300°C range in the original reference. Equilibrium constants for the seconday species, gas, and mineral reactions were calculated at 5°C intervals in the relevant temperature range using the interpolation equation (Xu et al. 2008):

$$\log_{10} K = a \cdot \ln(T) + b + c \cdot T + d/T + e/T^2 \qquad \text{(A-29)}$$

where T is the absolute temperature (K) and the polynomial coefficients $\{a,b,c,d,e\}$ are as defined in the TOUGHREACT database. Aqueous phase activities in CrunchFlow are calculated using the B-dot equation for activity coefficients described by Helgeson (1969):

$$\log_{10} \gamma_i = -\frac{A_{\gamma,10}\, z_i^2 \sqrt{I}}{1 + \text{å}_i B_\gamma \sqrt{I}} + \dot{B} I \qquad \text{(A-30)}$$

where I is the ionic strength, å_i is the hard core diameter of the species i, $A_{\gamma,10}$ and B_γ are the Debye-Hückel A and B parameters, and $\dot{B}$ is the characteristic B-dot parameter. The A and B parameters ("adh" and "bdh" in CrunchFlow) are given by:

$$A(T) = \frac{1.8246 \cdot 10^6 \left(10^{-3} \rho_w(T)\right)^{1/2}}{\left(\varepsilon_w(T) \cdot T\right)^{3/2}} \qquad \text{(A-31)}$$

$$B(T) = \frac{50.29 \left(10^{-3} \rho_w(T)\right)^{1/2}}{\left(\varepsilon_w(T) \cdot T\right)^{1/2}} \qquad \text{(A-32)}$$

where $\rho_w(T)$ is the density of water and $\varepsilon_w(T)$ is the dielectric constant of water. The B-dot parameter, $\dot{B}$ was interpolated for the relevant temperature range using a simple cubic polynomial fitted to the corresponding data in the 0.01°C–100°C range in the EQ3/6 database. This treatment gives a smoother interpolation for temperatures in the 0.01°C–35°C range rather than the original tabulated data in the EQ3/6 database for the much wider temperature range. It should be noted that in the EQ3/6 database dummy values (i.e. equilibrium constants) are used to suppress formation of secondary species at temperatures other than 25°C for species where temperature correction data are not available (mainly to ensure internal consistency of calculations). The approach in the custom database, however, was to assume that the equilibrium constant for 25°C was also applicable at other temperatures (i.e. constant values independent of temperature). Although this results in an internal inconsistency in the custom database, this was considered advisable since the formation of all secondary species involving silica would otherwise be suppressed at temperatures other than 25°C which could conceivably lead to incorrect conclusions concerning temperature effects if in situ temperatures below 25°C were to be simulated in the case studies. Given that all calculations were made at 25°C, specific details of the temperature corrections are superfluous in the context of the present report although are described here for traceability since the original intention was to make simulations for in situ temperatures of ~15°C. The custom database used in the simplified calculations is listed below in the CrunchFlow format (Steefel 2009):

```
'temperature points'  8  0.01  5.0  10.0  15.0  20.0  25.0  30.0  35.0
'Debye-Huckel adh'    0.4911  0.4942  0.4975  0.5012  0.5051  0.3283  0.5137  0.5185
'Debye-Huckel bdh'    0.3247  0.3254  0.3261  0.3268  0.3276  0.3283  0.3291  0.3300
'Debye-Huckel bdt'    0.0374  0.0382  0.0390  0.0397  0.0404  0.0410  0.0416  0.0421

'H2O' 0.00  0 18.0150
'Ca++'  2.87  2 40.0780
'Cl-' 1.81  -1  35.4530
'H+'  3.08  1 1.0080
'HCO3-' 2.10  -1  61.0170
'Na+' 1.91  1 22.9900
'SiO2(aq)'  0.00  0 60.0840
'O2(aq)'  0.00  0 31.9990
'Tracer'  0.00  0 0.0000
'Tracer_A'  0.00  0 0.0000
'Tracer_B'  0.00  0 0.0000

'End of primary'  0.0 0.0 0.0

'CO2(aq)' 3 -1  'H2O' 1 'H+'  1 'HCO3-'       -6.5817 -6.5157 -6.4596 -6.4124 -6.3733
-6.3414 -6.3161 -6.2966 0.00  0 44.0100
'CO3--' 2 -1  'H+'  1 'HCO3-'           10.6257 10.5498 10.4826 10.4233 10.3710 10.3249
10.2844 10.2490 2.81  -2  60.0090
'Ca(H3SiO4)2(aq)' 4 -2  'H+'  1 'Ca++'  2 'SiO2(aq)'  4 'H2O'   15.0530 15.0530 15.0530
15.0530 15.0530 15.0530 15.0530 15.0530 0.00  0 230.2900
'CaCl+' 2 1 'Ca++'  1 'Cl-'           0.6712  0.6886  0.6996  0.7048  0.7050  0.7009
0.6929  0.6816  2.31  1 75.5310
'CaCl2(aq)' 2 1 'Ca++'  2 'Cl-'           0.4484  0.5126  0.5638  0.6035  0.6330  0.6538
0.6667  0.6728  0.00  0 110.9840
'CaH2SiO4(aq)'  4 -2  'H+'  1 'Ca++'  1 'SiO2(aq)'  2 'H2O'   18.5620 18.5620 18.5620
18.5620 18.5620 18.5620 18.5620 18.5620 0.00  0 134.1760
'CaH3SiO4+' 4 -1  'H+'  1 'Ca++'  1 'SiO2(aq)'  2 'H2O'   8.7920  8.7920  8.7920  8.7920
8.7920  8.7920  8.7920  8.7920  2.31  1 135.1840
'CaHCO3+' 2 1 'Ca++'  1 'HCO3-'           -1.0966 -1.0716 -1.0547 -1.0448 -1.0411
-1.0428 -1.0493 -1.0600 2.31  1 101.0950
'CaCO3(aq)' 3 -1  'H+'  1 'Ca++'  1 'HCO3-'       7.5019  7.3973  7.2955  7.1967  7.1012
7.0089  6.9198  6.8340  0.00  0 100.0870
'CaHSiO3+'  4 -1  'H+'  1 'Ca++'  1 'SiO2(aq)'  1 'H2O'   8.7796  8.7518  8.7155  8.6721
8.6229  8.5689  8.5110  8.4501  2.31  1 117.1700
'CaOH+' 3 -1  'H+'  1 'Ca++'  1 'H2O'       14.0848 13.8162 13.5569 13.3071 13.0663
12.8341 12.6100 12.3937 2.31  1 57.0850
'H2SiO4--'  3 -2  'H+'  1 'SiO2(aq)'  2 'H2O'       23.9071 23.6952 23.4890 23.2893
23.0963 22.9103 22.7313 22.5594 3.00  -2  94.0980
'H4(H2SiO4)4-4' 3 -4  'H+'  4 'SiO2(aq)'  8 'H2O'       35.7460 35.7460 35.7460 35.7460
35.7460 35.7460 35.7460 35.7460 5.60  -4  380.4240
```

```
'H6(H2SiO4)4-2' 3 -2  'H+'  4 'SiO2(aq)'  8 'H2O'       13.4460 13.4460 13.4460 13.4460
13.4460 13.4460 13.4460 13.4460 3.00  -2  382.4400

'HCl' 2 1 'H+'  1 'Cl-'           0.6501  0.6700  0.6839  0.6930  0.6981  0.7001  0.6996
0.6973  0.00  0 36.4610

'HSiO3-'  3 -1  'H+'  1 'H2O' 1 'SiO2(aq)'        10.3267 10.2482 10.1700 10.0928
10.0168 9.9423  9.8694  9.7983  1.81  -1  77.0910

'NaCl(aq)'  2 1 'Cl-' 1 'Na+'           0.8270  0.8244  0.8180  0.8085  0.7964  0.7822
0.7662  0.7489  0.00  0 58.4430

'NaCO3-'  3 -1  'H+'  1 'HCO3-' 1 'Na+'       9.8140  9.7993  9.7925  9.7933  9.8012
9.8159  9.8369  9.8640  1.81  -1  82.9990

'NaHCO3(aq)'  2 1 'HCO3-' 1 'Na+'           -0.3662 -0.3306 -0.2925 -0.2526 -0.2116
-0.1698 -0.1276 -0.0854 0.00  0 84.0070

'NaOH(aq)'  3 -1  'H+'  1 'H2O' 1 'Na+'       15.1311 14.9292 14.7358 14.5511 14.3745
14.2057 14.0441 13.8895 0.00  0 39.9970

'NaHSiO3(aq)' 4 -1  'H+'  1 'H2O' 1 'Na+' 1 'SiO2(aq)'    8.4158  8.4015  8.3816  8.3571
8.3291  8.2984  8.2658  8.2319  0.00  0 100.0810

'OH-' 2 -1  'H+'  1 'H2O'           14.9413 14.7281 14.5273 14.3382 14.1598 13.9912
13.8315 13.6803 1.40  -1  17.0070


'End of secondary'  1 0.0 '0' 0.0 0.0 0.0 0.0 0.0 0.0 0.0 0.0 0.0 0.0 0.0


'CO2(g)'  0 3 -1  'H2O' 1 'H+'  1 'HCO3-'     -7.6782 -7.6990 -7.7229 -7.7496 -7.7784
-7.8092 -7.8414 -7.8749 44.01

'O2(g)' 0 1 1 'O2(aq)'              -2.6563 -2.7164 -2.7703 -2.8184 -2.8612 -2.8993
-2.9330 -2.9628 31.999


'End of gases'  0.0 1 1.0 '0' 0.0 0.0 0.0 0.0 0.0 0.0 0.0 0.0 0.0


'Calcite' 36.9340 3 -1  'H+'  1 'Ca++'  1 'HCO3-'     2.2235  2.1525  2.0794  2.0051
1.9299  1.8542  1.7784  1.7027  100.0870

'Portlandite' 33.0560 3 -2  'H+'  1 'Ca++'  2 'H2O'     24.6082 24.1669 23.7402 23.3282
22.9302 22.5456 22.1737 21.8141 74.0930

'Gyrolite'  136.0669  4 -4  'H+'  2 'Ca++'  3 'SiO2(aq)'  4.5 'H2O' 25.3873 25.0389
24.6920 24.3488 24.0103 23.6775 23.3513 23.0322 337.4460

'Quartz'  22.6880 1 1 'SiO2(aq)'              -4.1600 -4.0660 -3.9788 -3.8978 -3.8223
-3.7517 -3.6853 -3.6227 60.0840

'Inert_matrix' 100.0 1 1 'Tracer'              -30.0 -30.0 -30.0 -30.0 -30.0 -30.0 -30.0
-30.0 0.0


'End of minerals' 0.0 1 0.0 '0' 0.0 0.0 0.0 0.0 0.0 0.0 0.0 0.0 0.0

Begin surface complexation

End of surface complexation

Begin aqueous kinetics

End of aqueous kinetics
```

```
Begin mineral kinetics
+--------------------------------------------------
Calcite
  label = default
  type  = tst
  rate(25C) = -6.19
  activation = 15.0  (kcal/mole)
  dependence :
  1.0 Calcite + 1.0 H+ =  1.0 Ca+2 + 1.0 HCO3-
+--------------------------------------------------
Calcite
  label = h+
  type  = tst
  rate(25C) = -3.00
  activation = 15.0  (kcal/mole)
  dependence :     H+  1.0
  1.0 Calcite + 1.0 H+ =  1.0 Ca+2 + 1.0 HCO3-
+--------------------------------------------------
Gyrolite
  label = default
  type  = tst
  rate(25C) = -13.00
  activation = 15.0  (kcal/mole)
  dependence :
+--------------------------------------------------
Portlandite
  label = default
  type = tst
  rate(25C) = -9
  activation = 0.0 (kcal/mole)
  dependence :
+--------------------------------------------------
Quartz
  label = default
  type  = tst
  rate(25C) = -13.0
  activation = 15.0  (kcal/mole)
  dependence :
+--------------------------------------------------
Quartz
  label = Brantley_H+
  type  = tst
  rate(25C) = -11.3625
  activation = 0.0  (kcal/mole)
  dependence :     H+  0.309
```

```
+------------------------------------------------
Quartz
  label = Brantley_OH-
  type  = tst
  rate(25C) =  -9.2175
  activation = 0.0  (kcal/mole)
  dependence :    OH-  0.411
+------------------------------------------------
Quartz
  label = PK04_OH-
  type  = tst
  rate(25C) = -16.290
  activation = 25.9  (kcal/mole)
  dependence :     H+  -0.500
+------------------------------------------------
Quartz
  label = PK04_H2O
  type  = tst
  rate(25C) = -13.9842
  activation = 20.96  (kcal/mole)
  dependence :
+------------------------------------------------
Quartz
  label = KW88_OH-
  type  = tst
  rate(25C) = -16.300
  activation = 25.9  (kcal/mole)
  dependence :     H+  -0.500
+------------------------------------------------
Quartz
  label = KW88_H2O
  type  = tst
  rate(25C) = -13.400
  activation = 21.8  (kcal/mole)
  dependence :
+------------------------------------------------
Inert_matrix
  label = default
  type  = tst
  rate(25C) = -15.000
  activation = 0.0  (kcal/mole)
  dependence :
+------------------------------------------------
End of mineral kinetics

Begin exchange
End of exchange
Begin surface complexation parameters
End surface complexation parameters
```